Compteur de photon basé sur une mesure dispersive multiplexée

Antoine Essig

To cite this version:

Antoine Essig. Compteur de photon basé sur une mesure dispersive multiplexée. Quantum Physics [quant-ph]. Université de Lyon, 2021. English. NNT : 2021LYSEN089 . tel-03602821

HAL Id: tel-03602821
https://theses.hal.science/tel-03602821
Submitted on 9 Mar 2022

Numéro National de Thèse : 2021LYSEN089

THESE DE DOCTORAT DE L'UNIVERSITE DE LYON
opérée par
l'Ecole Normale Supérieure de Lyon

Ecole Doctorale N° 52
Physique et Astrophysique de Lyon (PHAST)

Discipline : Physique

Soutenue publiquement le 14/12/2021, par :
Antoine ESSIG

Photon counting with a multiplexed dispersive readout

Compteur de photon basé sur une mesure dispersive multiplexée

---

Devant le jury composé de :

HACOHEN-GOURGY, Shay	Professeur, Israel Institute of Technology	Rapporteur
WISEMAN, Howard	Professeur, Griffith University	Rapporteur
DEVORET, Michel	Professeur, Yale University	Examinateur
ROCH, Nicolas	Docteur, Institut Néel	Examinateur
CALLARD, Ségolène	Professeure des Universités, Ecole centrale de Lyon	Présidente
SARLETTE, Alain	Docteur, INRIA	Invité
HUARD, Benjamin	Professeur des Universités, ENS de Lyon	Directeur de thèse

PHOTON COUNTING WITH A MULTIPLEXED DISPERSIVE READOUT

ANTOINE ESSIG

Directed by Benjamin HUARD

École Normale Supérieure

december 2021

ABSTRACT

When a two-level system – a qubit – is used to probe a larger system, it naturally leads to answering a single yes-no question about the system state. Identifying what is the state of a system thus comes down to ask a series of binary questions iteratively to refine our knowledge. However, this approach leads to long measurement times for large systems, such as a resonator containing a large number of photons. In this thesis, we propose a new approach which enables us to make a measurement in a time, which is independent of the system size. This new measurement uses the qubit as an encoder of information about the system state into the many propagating modes of a transmission line.

Assuming an ideal detector, we show that photon counting can then be implemented in a fixed time whatever the number of photons. We demonstrate the practicality of this approach by counting the number of photons in a microwave resonator coupled dispersively to a single superconducting qubit.

In a first instance, we observe the qubit fluorescence dependence on the resonator photon number when the qubit is driven by a microwave monochromatic tone. Using the backaction of this dispersive measurement and post-selection, we evidence the photon counting ability of the measurement. The dephasing rate between two Fock states induced by the photon number measurement is measured and compared to theory. The latter allows us to study the non-linear dependence of the dephasing rate on the microwave drive amplitude.

In a second instance, the qubit fluorescence is probed using a frequency comb. Multiplexed heterodyne detections are simultaneously performed at each comb frequency and allow us to measure the photon number in the microwave resonator. This multiplexed measurement benefits from the recent bandwidth improvements of near quantum limited amplifiers. The limited cavity lifetime and detector efficiency prevented us from reaching single shot readout of the photon number in this proof-of-principle experiment. However, unlike in sequential measurement schemes, a single run of our experiment does provide, in parallel, partial information about the occupancy of each Fock state. Besides, we manage to observe the multiplexed measurement backaction on the resonator using direct Wigner tomography, which allowed us to measure the decoherence rate of the resonator induced by the measurement. We evidence an optimal qubit drive amplitude for information extraction, which matches the expected dynamics of a qubit under a multifrequency drive.

RÉSUMÉ

Lorsque l'on utilise un bit quantique (qubit) pour sonder l'état d'un système, la stratégie habituelle consiste à poser une série de questions binaires, chaque question améliorant notre connaissance de l'état du système. Cependant, cette stratégie nécessite de longs temps de mesure lorsque l'on considère un grand système, comme par exemple un résonateur électromagnétique peuplé d'un grand nombre de photons, car chaque question ne peut extraire qu'un bit d'information. Dans cette thèse, nous proposons une nouvelle stratégie qui permet d'obtenir un temps de mesure indépendant de la taille du système. Cette nouvelle approche est basée sur l'utilisation d'un qubit comme routeur, ce qui permet d'encoder l'information sur l'état du système dans les nombreux modes d'une ligne de transmission.

Dans le cas d'un détecteur idéal, nous montrons à l'aide d'une expérience de pensée que cette stratégie permet de mesurer le nombre de photons contenu dans une cavité en un temps constant, indépendant de la taille du système. Pour démontrer la faisabilité de cette mesure idéale, nous appliquons cette stratégie à la mesure du nombre de photons contenu dans un résonateur micro-onde couplé dispersivement à un qubit supraconducteur.

Dans un premier temps, la fluorescence du qubit est mesurée lorsque ce dernier est sondé à l'aide d'un ton micro-onde monochromatique. L'action en retour de cette mesure dispersive est étudiée, nous démontrons à travers la post-sélection que la fluorescence du qubit encode effectivement le nombre de photons contenu dans le résonateur. Nous mesurons le taux de déphasage induit par la mesure entre deux états de Fock du résonateur et le comparons à un modèle théorique. Ce dernier nous permet alors d'étudier le comportement non-linéaire du taux de déphasage induit par la mesure avec l'amplitude du ton micro-onde.

Dans un deuxième temps, la fluorescence du qubit est sondée à l'aide d'un peigne de fréquence. Des mesures hétérodynes multiplexées à tous les tons du peigne de fréquence nous permettent alors de mesurer le nombre de photons contenus dans le résonateur. Cette mesure multiplexée est rendue possible grâce aux récentes améliorations sur la bande passante des amplificateurs limités quantiquement. Le temps de vie du résonateur et une efficacité de mesure limités nous empêchent d'atteindre un rapport signal sur bruit permettant de décoder toute l'information contenue dans notre mesure hétérodyne multiplexée. Cependant, contrairement à une mesure séquentielle, notre approche fournit en parallèle une information partielle sur la population de chaque état de Fock. L'action en retour de cette mesure dispersive multiplexée est étudiée à l'aide de tomographies de Wigner du résonateur. Nous sommes ainsi capables de mesurer le taux de déphasage induit pas la mesure multiplexée et mettons en évidence une amplitude optimale du peigne de fréquence qui maximise le taux de déphasage. Un modèle théorique basé sur l'approximation que le peigne de fréquence est infini nous permet de prédire l'amplitude optimale du peigne, et ce en accord avec l'expérience.

REMERCIEMENTS

Ces presque quatre années de thèse ont été pour moi une belle aventure et ceux grâce aux nombreuses personnes que j'ai pu rencontrer et côtoyer. Toutes ces personnes ont contribué de manière directe ou indirecte à la naissance de ce manuscrit. Cette partie de ma thèse leur est dédiée pour les remercier de tout ce qu'ils m'ont apporté.

Mes premiers remerciements vont naturellement à mon directeur de thèse Benjamin Huard. Lorsque je t'ai rencontré pour la première fois, mes connaissances sur les circuits supraconducteurs étaient nulles et je me suis présenté à toi alors que je cherchais initialement une thèse sur les mesures de transport. Tu n'as pas mis longtemps à éveiller ma curiosité puis à me rendre passionné de ce domaine. Tu m'as fait confiance et m'as permis de passer quatre années exceptionnelles pour lesquelles je te remercie. J'aimerais te remercier en particulier pour ta présence quotidienne et toutes les discussions que tu as pris le temps d'avoir avec moi. A travers elles, tu as grandement changé ma compression de la mécanique quantique mais aussi ma conception du métier de chercheur et de la rigueur qui lui est propre. J'aimerais te remercier pour ce qui est à mes yeux ta plus belle force : l'intérêt que tu portes à chaque individu. Il ne t'a pas fallu longtemps pour connaître mes centres d'intérêt et lorsque je suis venu te voir au début de ma thèse pour t'annoncer que je souhaitais écrire un livre de physique, j'ai mentionné que cela risquait de diminuer ma présence au laboratoire et pourtant tu ne m'as montré que du soutien pour ce projet. Pendant ces 4 ans, tu as fait bien plus qu'être un encadrant, j'ai eu la chance de côtoyer trois de tes facettes : l'encadrant, le physicien et l'humain. Je souhaite toutes les trois remercier pour tous ce qu'elles m'ont apporté.

Au milieu de ma thèse, j'ai eu la chance d'obtenir un second encadrant en la personne d'Audrey Bienfait. J'aimerais te remercier pour toutes nos discussions sur la physique, elles m'ont permis d'élargir mon champ des possibles et m'ont fait découvrir de nouveaux beaux aspect de la mécanique quantique. Tu m'as apporté ton aide sur bien d'autre sujet (simulation, design, fabrication, ...) et j'aimerai te remercier pour tous ce que tu as fait lors de l'installation des nouveaux réfrigérateurs et de la nouvelle salle de manipulation. Plus récemment, j'aimerais te remercier, en particulier, pour toutes les discussions que l'on a eues à propos du métier de chercheur et de la recherche académique, elles m'ont été d'une grande aide lorsque j'ai dû décider de mon après thèse.

Durant cette thèse, je n'ai jamais été seul car j'ai toujours été entouré des membres du Quantum Circuit Group. J'aimerais remercier ceux qui m'ont si bien accueillie et m'ont enseigné les bases du domaine : Quentin Ficheux, Nathanaël Cottet et Théau Peronnin. Ils m'ont fait comprendre que le Quantum Circuit Group était avant tout une grande famille. J'aimerais remercier tout particulièrement Quentin qui fut le premier à travailler sur mes travaux de thèse et avec qui j'ai eu la chance de travailler pendant presque 1 an. Notre amour partagé des incertitudes et notre propension à appeler tous nos instruments Michel ont rendu notre travail d'équipe des plus agréables. J'aimerais ensuite remercier ceux qui m'ont accompagné tout au long de ma thèse :

Rémy Dassonneville, Réouven Assouly, Daniel Szombati et Jeremy Stevens. J'aimerais les remercier pour toutes les discussions, les bons moments partagés aux Ninkasi, à Aussois ou ailleurs. J'aimerais en particulier remercier Jeremy, mon camarade de "promo" de thèse. Pendant ces trois années j'ai découvert en toi bien plus qu'un simple collègue, grâce à nos expériences partagées de la thèse mais surtout grâce à notre passion pour la montagne. Je te remercie pour toutes nos discussions pendant lesquelles on s'exclamait sur la beauté d'une montagne ou sur une trace de ski dans la poudreuse, pour toutes les conférences et écoles d'été qu'on a faits ensemble, et pour toutes les bières et tous les verres de génépi qu'on a pu partager. Nous n'aurons eu que deux désaccords pendant nos thèses : "Faut-il skier les pieds collés avec style ? " et "Lequel de nous deux est le meilleur skieur ? ". Si la seconde question ne prête pas à débat (sauf peut-être en télémark), la première reste une question ouverte ... Je suis heureux de savoir que je pourrai continuer à profiter de ta bonne humeur et de ton rire contagieux chez Alice&Bob. J'aimerais aussi remercier les "nouveaux" : Alexis Jouan, Arne Bahr, Antoine Marquet et Hector Hutin. Alexis pour toutes nos discussions, qu'elle ait portées sur la physique, la recherche ou sur le monde, Alexis et Arne pour nos séances d'escalade, Arne et Antoine pour nos soirées jeux de société ou jeux vidéo et Hector Hutin pour continuer mes travaux de thèse qui me tienne tant à cœur et qui sont maintenant ses travaux de thèse. Pour finir j'aimerais remercier tous ceux qui sont passés dans le groupe que ce soit pendant quelques semaines ou quelques mois, en particulier Stephan Zeppetzauer, avec qui j'ai pu commencer un nouveau projet de recherche, et Sébastien Jezouin pour toutes les discussions d'ingénierie micro-onde. Le Quantum Circuit group est à mes yeux un environnement fantastique pour mener une thèse et c'est pourquoi j'aimerais remercier, encore une fois, Benjamin Huard qui l'a créé et qui a su rassembler les bonnes personnalités.

En plus du Quantum Circuit Group, j'aimerais remercier nos amis parisiens du groupe Quantic : Zaki Leghtas, Raphaël Lescannes, Pierre Rouchon et Alain Sarlette. J'aimerais les remercier pour toutes les discussions de physique que nous avons eu et en particulier Alain qui, à travers nos échanges d'emails, m'a énormément appris sur l'information quantique.

Cette thèse n'aurait pas pu commencer sans le soutien de quelques personnes. J'aimerais remercier mes parents qui m'ont toujours soutenu pendant mes études et ont cru en moi. Vous m'avez permis de savoir très jeune ce que je voulais faire et vous m'avez donné tous les outils pour réussir. Vous avez été tout le long de mes études une source de motivation. J'aimerais remercier aussi mes frères et sœurs : Marion, Agathe, Paul et Nicolas. Nous avons tous mené des études et des projets différents mais chacune de vos réussites a été un élan me poussant à aller au bout des miens. Je n'aurai pas fait une thèse sans mon père, Paul et Marion qui ont su cultiver ma curiosité scientifique et m'inculper les bases de la rigueur et de la démarche scientifique. J'aimerais remercier spécifiquement ma soeur Marion, qui a "testé" avant moi le chemin de la thèse et qui m'a partagé son expérience à travers nos nombreuses discussions.

Pour finir j'aimerais remercier celle qui m'a accompagnée durant toutes mes études, Anaïs Moravia. Tu n'as jamais cessé de m'encourager et tu as été un soutien à chaque situation difficile. Tu as accepté de me suivre à Lyon pour que je puisse faire cette thèse et pendant ces trois ans tu as montré un véritable intérêt pour celle-ci malgré son sujet pour le moins difficile. Avoir pu partager cela avec toi était merveilleux. Cette thèse ne serait pas ce qu'elle est sans toi.

CONTENTS

I INTRODUCTION

II PHOTOCOUNTING

III TOWARD THE SINGLE SHOT MEASUREMENT

IV APPENDIX

V BIBLIOGRAPHY

LIST OF FIGURES

LIST OF TABLES

Part I

INTRODUCTION

1

INTRODUCTION

1.1 BACKGROUND

Quantum and classical measurements differ significantly from one another. When performing a quantum measurement, the quantum state of a system is modified depending on the results of the measurement - an effect called measurement *back-action*. A classical measurement can also have a back-action on a system, for example by draining part of its internal energy and thus decreasing its temperature, but this effect is not systematic. For a quantum measurement, the back-action exists as soon as *information* about the quantum state is extracted. Therefore, quantum mechanics can be seen partly as an information theory.

It is difficult to describe quantum measurement without the notion of *entanglement*. It was first introduced by Einstein, Podolsky and Rosen in 1935 with the EPR paradox [1]. The question was to know if there are *hidden local variable* [2] in quantum mechanics or if the theory is intrinsically *non-local*. Bell came in 1964 with a proposal to test it quantitatively [3]. This was measured by Alain Aspect et al. [4] who concluded that there is no hidden local variable. Thus, entanglement and non-locality are intrinsic concept to the quantum mechanics, whatever is our interpretation of the quantum mechanics.

The first description of the back-action was the *collapse* of the quantum state introduced by W. Heisenberg [5] and used by J. von Neumann to describe the *von Neumann measurement* [6]. However this first description treated the measurement as an instantaneous and discrete phenomenon which is a poor approximation as instantaneous is unphysical, since it would require an infinite amount of energy. The *generalized measurement* description [7] solves this issue by describing the measurement as an entanglement of the system with a *probe* which is measured by a measurement apparatus. The entanglement between the system and the probe is a key part of the measurement as it limits the type and the amount of information one can recover from the measurement. With this formalism, a *continuous measurements* and its back-action can be described. The back-action of a continuous measurement is not described by an instantaneous collapse of the quantum state but rather by its continuous *decoherence* [7]. Because of the *Heisenberg uncertainty principle*, the *information extraction rate* of the continuous measurement is bounded by the *decoherence rate* induced by the measurement [8].

Entanglement and quantum measurements are now routinely used in experiments measuring and manipulating individual quantum systems, following pioneering works from the 2012 Nobel Prize laureates, Haroche and Wineland [9]. A part of the work of Haroche was dedicated to the measurement of the number of excitations, called *photons*, residing into the stationary electromagnetic mode of a microwave cavity using a quantum two-level system, or *quantum bit* (qubit) as a probe. Each measurement was revealing at most 1 bit of information about the number of photons in the cavity mode and a sequence of various and successive measurements was needed to measure the photon number. However, is it the best use of a qubit to determine an observable of an individual quantum state with many possible outcomes such as a photon number? This is the question this thesis aims to answer. It will lead us to investigate the back-action of *multiple and simulatenous measurements* performed on an individual quantum state.

1.2 INDIVIDUAL QUANTUM STATE

Before measuring or manipulating an individual quantum state, one has to understand what are the necessary conditions for its existence. As Zurek explains [10], classicality is a property which emerges from a quantum system when it interacts with an environment. Thus, one can see quantum mechanics as a theory describing "isolated" systems. Of course a system can not be rigorously isolated otherwise it would be impossible to observe. Here, we consider a system *sufficiently isolated* from the environment such that its quantum state can be manipulated and measured before being reduced to a simple classical state by the coupling to the environment. So far, no maximal size has been identified for the existence of a quantum system. For example, the most massive systems showing degrees of freedom described by quantum mechanics are the 40 kg LIGO and VIRGO mirrors [11, 12]. These mirrors are pendulums sufficiently isolated from the earth's vibrations to have mechanical degrees of freedom that follow the rules of quantum mechanics. The motion and position of the mirrors are thus described similarly to a quantum mechanical harmonic oscillator.

Nowadays, numerous systems were successfully "isolated" such that their individual quantum state could be manipulated. One can cite trapped ions [13], nitrogen-vacuum centers [14], quantum dots [15], Rydberg atoms [16] and electromagnetic fields or mechanical waves in cavity quantum electrodynamics [16], cavity optomechanics [17], and circuit quantum electrodynamics [18].

In this thesis, we develop a new measurement approach to measure the number of photons contained in a stationary electromagnetic mode. Our experimental testbed relies on *superconducting circuits*. These circuits are made of resonators and transmission lines that can be easily combined to a Josephson junction in order to create *artificial atoms*. They host collective excitations of the electromagnetic field and the superconducting condensate which are described by electromagnetic resonant modes. These modes can be considered as "isolated" and one can manipulate and measure their quantum states. One of the main advantages of superconducting circuits is that their parameters can be adjusted by design.

1.3 PHOTON-COUNTING WITH THE DISPERSIVE INTERACTION

We want to measure in the pohoton number basis the state of a superconducting microwave resonant mode - that we dub storage - using a superconducting artifical atom called the *transmon* (see Fig. 1.1). When both are cooled down to millikelvin temperature, they exhibit quantum behaviors and the transmon can be considered as a *quantum bit* (qubit). The storage state is described by the number of photons it contains; the state of the qubit is described by only two states: ground and excited. The macroscopic

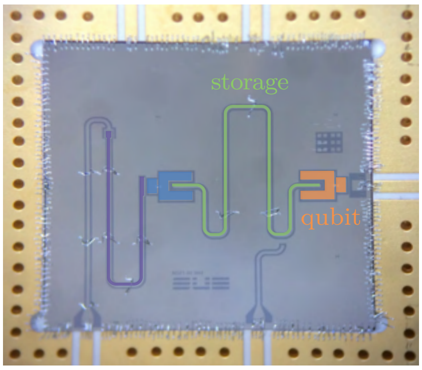

Figure 1.1: Optical picture of the circuit. The storage mode (green) is coupled to a transmon artificial atom or qubit (orange). An additional qubit (blue) and its dedicated readout resonator (purple) are used as a reference photon counter and storage tomography.

size of the qubit allows us to operate in a regime where the coupling rate with the storage is higher than the dissipation rate of the qubit and the storage mode [19]. The detuning between the resonant frequencies of the qubit and the storage is designed to be much larger than the coupling rate leading to an interaction which red-shifts the qubit frequency for each photons in the resonator, also called a *dispersive interaction* [20]. In order to photon count, the dispersive interaction is designed to be in the *number-resolved regime*, in which the frequency red-shift is larger than the decoherence rate of the qubit [21]. Thus, the qubit frequency depends on the number of photons occupying the storage mode.

This system is in fact analogous to the one used by Haroche in his Nobel Prize works and this thesis follows up on his microwave photon-counting works [22, 23, 24, 25] and their implementations in circuit quantum electrodynamics (circuit QED) [21, 26, 27, 28]. In those circuit QED works, the number-resolved regime is used to manipulate the qubit such that its state encodes information about the storage photon number. This information can be recovered by measuring the qubit state using a dedicated readout resonator dispersively coupled to the qubit. This qubit state readout is called a qubit *dispersive readout*. In this case, the qubit readout answers a yes-no question about the system state. Identifying what is the state of a system thus comes down to playing a game of “Guess Who?”. A series of binary questions are asked iteratively to refine our knowledge about the state. Unlike the classical game, each answer disturbs the state of the system due to the measurement back-action. Determining an arbitrary number of photons in the cavity between 0 and $2^m - 1$ takes at least m consecutive qubit measurements since each answer provides at most one bit of information about the system state. This limitation originates from the encoding of the extracted information into the quantum state of the qubit.

Our approach uses the fact that photon number is already encoded in the qubit frequency owing to the dispersive coupling. Thus, probing the qubit fluorescence with a transmission line enables us to readout the qubit frequency and thus to extract information about the storage photon number [29]. This measurement is the reverse of the usual qubit dispersive readout, and can be viewed as the *storage dispersive readout*.

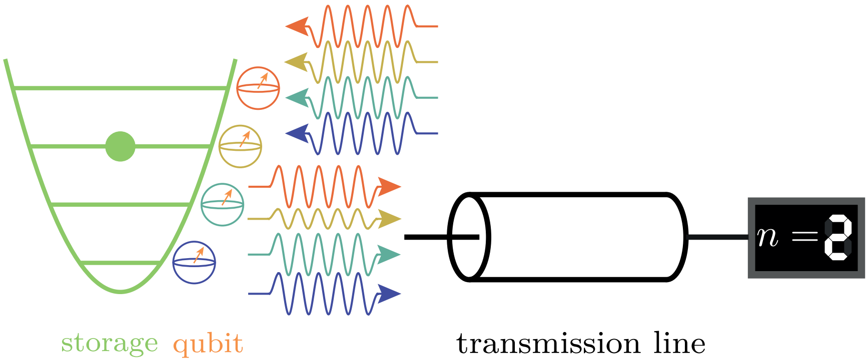

Figure 1.2: The photon number of the storage is encoded in the qubit frequency or color. The qubit is probed with a frequency comb trough a transmission line. The amplitude of the reflected frequency comb enable to measure the photon number, here 2.

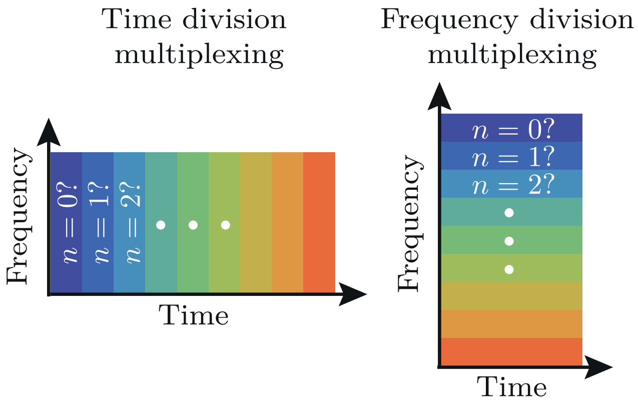

Figure 1.3: Time domain–division multiplexing takes place one question at a time, while frequency-division multiplexing simultaneously retrieves multiple answers.

When probing at a single frequency, the qubit fluorescence encodes at most 1 bit of information, however, thanks to the recent bandwidth improvements of near quantum limited amplifiers [30], we can probe simultaneously the qubit fluorescence at multi-frequencies using a frequency comb (see Fig. 1.2). Here, the qubit is used as an encoder of information about the storage state into the many propagating modes of a transmission line which can, together, encode much more than 1 bit of information. Daring an analogy with communication protocols [31], previous measurement schemes with time series of binary questions used time division multiplexing while our experiment demonstrates the analogous of frequency division multiplexing, where the qubit alone acts as the frequency multiplexing transducer (Fig. 1.3).

Assuming an ideal detector, we show that photon counting can then be implemented in a time independent of the number of photons. We demonstrate the practicality of this approach in an experiment where information about 9 possible photon numbers (more than 3 bits) in the storage mode is simultaneously extracted by a single superconducting qubit into 9 propagating modes of a transmission line. When driving the qubit at 9 test frequencies by multiplexing, the qubit simultaneously emits 9 microwave signals that

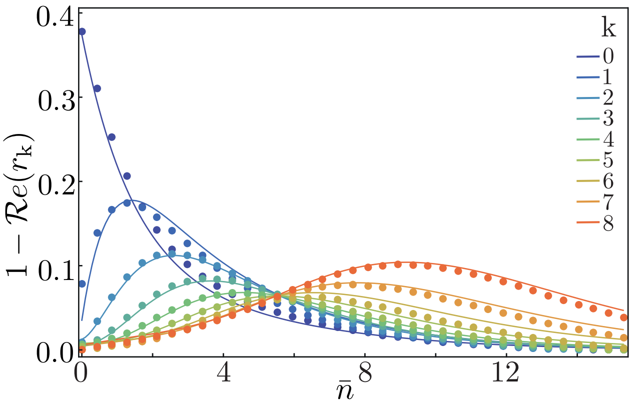

Figure 1.4: Multiplexed photon-counting. Dots: simultaneously measured average emission coefficients corresponding to every photon number k from 0 to 8 as a function of the initial mean photon number $\bar{n}$ in the storage mode. r_k is here the reflection coefficient of the qubit at its frequency corresponding to k photons in the storage mode. Solid lines: prediction based on a master equation without free parameters.

each reveals information about the photon number ranging from 0 to 8 (see Fig. 1.4), implementing a multiplexed dispersive readout of the storage mode.

1.4 MEASUREMENT BACK-ACTION

The measurement back-action of the storage dispersive readout and of the storage multiplexed dispersive readout are observed using *direct Wigner tomographies* of the storage [32], which allows us to measure the decoherence rate of the storage induced by the measurement.

The dephasing between two storage Fock states induced by the storage dispersive readout is measured and reproduced with a theory based on the *adiabatic elimination* of the qubit. We observe a strong non-linear dependence of the measurement-induced dephasing rate on the amplitude of the drive probing the qubit. The drive frequency leading to the largest dephasing rate depends non-linearly on the drive amplitude. This is a major difference compared to the back-action of a qubit dispersive readout.

The dephasing of the storage mode induced by the storage multiplexed dispersive readout is measured and shows a non-linear dependence on the amplitude of the multi-frequency drive. We evidence an optimal qubit drive amplitude for information extraction, which matches the expected dynamics of a qubit under a multi-frequency drive (see Fig. 1.5). In this case, the qubit undergoes periodic and almost instantaneous rotations in the Bloch sphere around the x-axis. At the optimal amplitude, each rotation corresponds to a π-pulse, thus maximizing the emission of the qubit and the information extraction rate.

1.5 OUTLINE

This thesis is not written in a chronological order. Almost all the measurements were performed during the first half of the thesis whereas the theory and models where

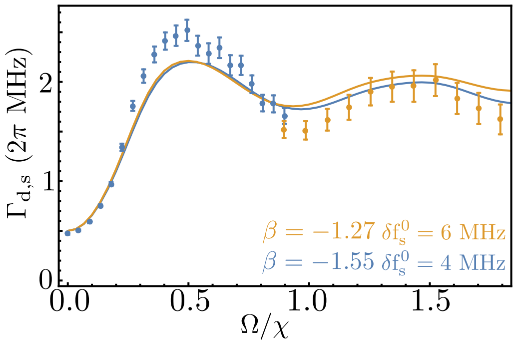

Figure 1.5: Dephasing rate measured (dots) and simulated (line) as a function of qubit drive amplitude Ω in units of χ. The evolution of the dephasing rate are strongly non linear with drive amplitude. β is the initial coherent state in the storage and δf_s^0 the detuning with which the storage is probed.

derived during the second half. This means most experiments were performed with an understanding of the phenomenon below what is explained in this manuscript. To discuss the results in a logical and pedagogical order, we show measurements and theories together.

The three first chapters introduce the basic concepts needed to understand this thesis. Chap. 2 gives a quantum description of superconducting circuits. It discusses the master equation of an open quantum system, the basic controls one can apply on the circuit modes and the dispersive coupling. Chap. 3 shows how a superconducting circuit can be simulated to refine its design and reach the targeted circuit parameters. It focuses on the coupling between the circuits modes and the transmission line and the unavoidable resulting coupling to the environment - the *Purcell effect*. Chap. 4 introduces the notion of quantum measurement, the relevant parameters to classify quantum measurements and the different types of quantum measurements. It discusses in details heterodyne detection and the role of quantum-limited amplifiers. This chapter finishes with a characterization of the Josephson travelling wave parametric amplifier used in this thesis.

The four next chapters discuss the microwave photon-counting experiments and the main results of this thesis. Chap. 5 describes standard photon-counting protocols and their limitations and how a multiplexing approach can improve the measurement speed. In Chap. 6, we discuss the photon-counting of a resonator coherent state using the fluoresence of a dispersively coupled qubit. The measured back-action is studied and discussed with regards to the back-action of the qubit dispersive readout. Chap. 7 explores the photon-counting of a coherent state using a frequency comb to probe the qubit fluorescence in a multiplexing way. The photon spectral density of the reflected comb is measured and related to the dynamics of a qubit driven by a infinite frequency comb. Finally, Chap. 8 discusses the measurement back-action of the resonator multiplexed dispersive readout. The measured dephasing rate induced by the measurement is explained using the resonator-qubit dynamics when the qubit is probed by an infinite frequency comb. The last chapter, Chap. 9, is dedicated to the work performed at the end of this thesis to reach a *single-shot* photon number measurement. It concludes with the perspectives of this thesis work.

2

CIRCUIT QUANTUM ELECTRODYNAMICS

The field of circuit quantum electrodynamics concerns the control, the measurement and the study of quantum electromagnetic modes based on superconducting devices. As said in the introduction, a degree of freedom is described by quantum mechanics if one can consider it as “isolated”, i. e. if one can control and measure it on a time scale smaller than the one with which the degree of freedom and the environment interact. For circuit quantum electrodynamics, the degrees of freedom are the electric and magnetic field[1]. The two fields are coupled together as described by the Maxwell equations and the result is the existence of electromagnetic modes. Those modes are the ones studied in the circuit quantum electrodynamics. The superconductivity of the devices enables one to confine the electric and magnetic fields, to impose the resonant condition (the resonant frequency of the modes is around 5 GHz), and to remove the Joule effect which would destroy the mode quantum state. Interestingly, the use of a superconductor enables coupling these modes to a Josephson junctions which can be built to have mode resonating in the GHz regime. Thus superconductors and Josephson junctions enable one to design and fabricate low-dissipation elements and to couple them strongly in the microwave regime.

The use of superconductors is not enough to ensure the existence of a quantum state on a time scale long enough to manipulate this state. Electromagnetic shielding and filtering, and low temperature are needed to protect the quantum state in these systems. The low temperature plays two roles. First, it freezes the environment dynamics and fluctuations. Second, it cools down the system into its ground state. The energy of the thermal fluctuations $k_B T$, where k_B is the Boltzmann constant, has to be small compared to the energy of a photon of the electromagnetic mode, which is given by hf_r with h the Planck constant and f_r the resonant frequency of the mode. For a mode resonating at 20 GHz, the energy of a photon is equal to the energy of the thermal fluctuations at 1 K. With resonant frequencies around 5 GHz, temperatures of 10 mK, which are reachable with dilution refrigeration [33], are sufficient.

Compared to optical light experiments, which show quantum behaviors even at room temperature, the requirement of a dilution fridge to cool down the microwave modes is a drawback. However, to control, probe, and simulate the system, the circuit quantum electrodynamics community can use microwave equipment and simulation softwares that are already well developed by the microwave industry.

This chapter will describe the nature of the electromagnetic modes used in circuit quantum electrodynamics and derive the formalism to describe them. As said, even if the system is “isolated”, meaning one can control and measure it before that the decoherence happens, it is still an open system interacting with its environment. We will see how we can describe this interaction and derive a master equation describing the dynamics of the system’s quantum state.

---

[1] Either their free version in vacuum or their dressed version in the matter.

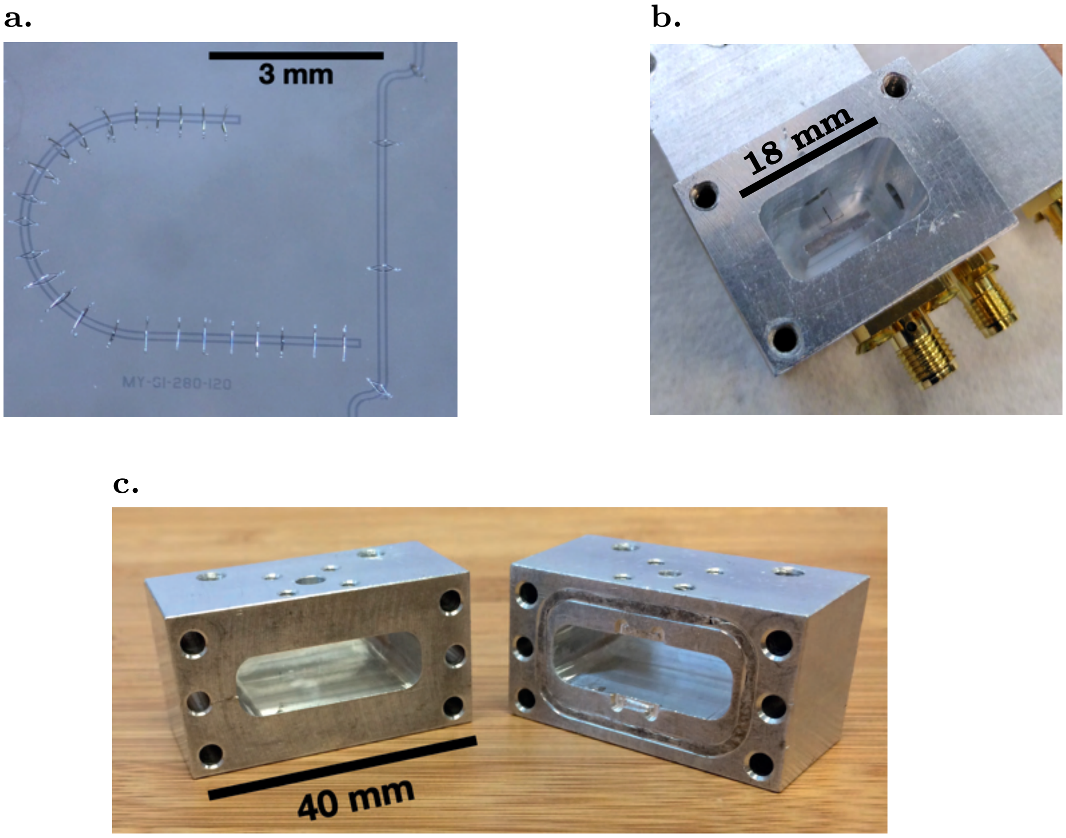

Figure 2.1: **a.** Optical picture of a $\lambda/2$ superconducting resonator in niobium. The vertical coplanar waveguide is a transmission line used to probe the resonator. **b.** Optical picture of a rectangular $\lambda/4$ superconducting post cavity in aluminum. One can see a sapphire wafer with the two antennas of a transmon qubit in tantalum. **c.** Optical picture of an open rectangular cavity. The groove in the right piece is used for an indium seal.

2.1 CIRCUIT QUANTIZATION

2.1.1 *About resonators and cavities*

The field of cavity quantum electrodynamics (cavity QED) was born to study the quantum state dynamics of a light mode confined in a superconducting cavity. By coupling light to matter (e.g., atoms, spins, electrons), the field has led to a large number of ground-breaking experiments [7, 16, 34]. In 1999, the first superconducting qubit was created [35], followed, in 2004, by the first demonstration of the regime of strong coupling between a superconducting qubit and a resonator [19], leading to the birth of a new branch called *circuit* QED. While the cavity QED field uses cavities to confine light modes and make them interact with various kinds of matter, the circuit QED field uses cavities and 2D resonators to confine light and the Josephson junction non-linearities to create and engineer interactions. Thanks to the large range of accessible parameters, the circuit QED field can be used to study and exploit various phenomena like quantum thermodynamics [36, 37, 38], quantum sensors [39], quantum measurement and quantum back-action [40, 41], and quantum computing [18, 42].

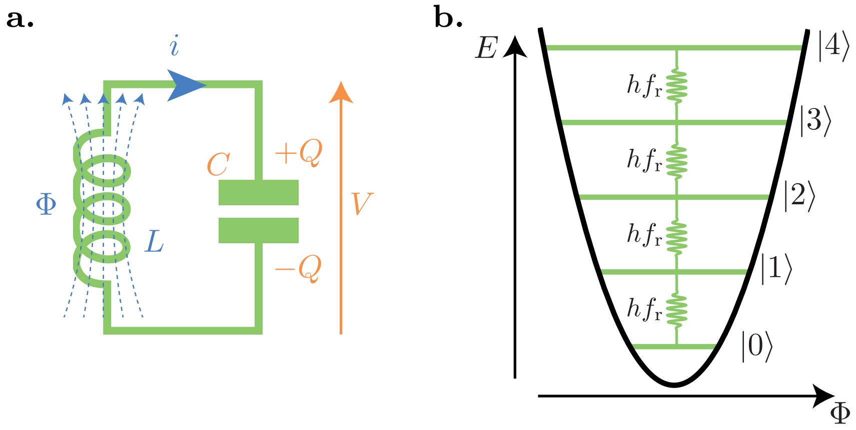

Figure 2.2: **a.** Representation of a resonator or cavity mode by an LC electromagnetic resonator. The relation between the flux Φ through the inductor and the charge Q of the capacitor to the current i and the voltage V is given by Eq. (2.2). **b.** Harmonic potential of a harmonic oscillator as a function of the flux Φ. Fock state $|n\rangle$ levels are equally spaced by hf_r, the energy of a photon at the mode resonance frequency f_r.

Resonators can take many forms: the most common is the $\lambda/2$ coplanar waveguide [43] made of superconductors (see Fig. 2.1a). It behaves as a Fabry-Perot cavity with a first resonance for a wavelength equal to twice its length. Superconducting cavities are bulk 3D superconductors designed to have a stationary resonant electromagnetic mode. The two most used are the rectangular cavity for readout [44], and the coaxial $\lambda/4$ cavity for high Q cavity [45, 46]. The resonant frequencies of a rectangular cavity of dimensions l_x, l_y, l_z are given by

$$f_{k,l,m} = \frac{c}{2\pi}\sqrt{\left(\frac{k\pi}{l_x}\right)^2 + \left(\frac{l\pi}{l_y}\right)^2 + \left(\frac{m\pi}{l_z}\right)^2} \tag{2.1}$$

with k, l, and m, the number of anti-nodes along the x, y, and z direction. For a $\lambda/4$ cavity, the resonant frequency is mainly given by the height h of the cavity central post; the wavelength of the first mode is equal to about $4h$. All those resonators and cavities have an infinite number of resonant modes, which can all be described by an LC circuit [47, 48] (see Fig. 2.2a). As they are made of superconductors, we first ignore the dissipation and model the circuit without a resistor[2]. One can define the generalized flux Φ through the inductor and the generalized charge Q of the capacitor, which are related to the current i and the voltage V by [48].

$$\begin{cases} \Phi(t) = \displaystyle\int_{-\infty}^{t} \mathrm{d}t' V(t') \\ Q(t) = \displaystyle\int_{-\infty}^{t} \mathrm{d}t' i(t') \end{cases} . \tag{2.2}$$

---

[2] To be more precise, there is no DC resistance, but the superconductors still have an AC resistance which can first be neglected.

We can define the classical Lagrangian $\mathcal{L}$ of the system

$$\mathcal{L} = \frac{C\dot{\Phi}^2}{2} - \frac{\Phi^2}{2L} \tag{2.3}$$

with C the capacitance, and L the inductance of the mode studied. Here the capacitor and inductor energies play kinetic and potential energy roles, respectively. One can derive the conjugate variable of Φ, which is equal to $C\dot{\Phi}$, and identify it to the charge Q thanks to the capacitor characteristic. Thus Φ plays the role of position and Q plays the role of momentum. The classical Hamiltonian of the system can be written

$$H = \frac{\partial \mathcal{L}}{\partial \dot{\Phi}}\dot{\Phi} - \mathcal{L} = \frac{Q^2}{2C} + \frac{\Phi^2}{2L}. \tag{2.4}$$

As expected, this Hamiltonian describes a harmonic oscillator with two degrees of freedom, which are the flux Φ and the charge Q. It is identical to a mechanical harmonic oscillator describing a mass-spring system with a mass C and a spring constant $1/L$. The resonant frequency of the LC oscillator is given by $f_\mathrm{r} = 1/\sqrt{LC}$ and its impedance by $Z = \sqrt{L/C}$. The quantum Hamiltonian of the circuit is the same as the classical one, with Q and Φ, replaced by quantum operator charge $\hat{Q}$ and flux $\hat{\Phi}$ that obey the canonical commutation relation $[\hat{\Phi}, \hat{Q}] = i\hbar$.

$$\hat{H} = \frac{\hat{Q}^2}{2C} + \frac{\hat{\Phi}^2}{2L}. \tag{2.5}$$

One can diagonalize this Hamiltonian using the annihilation operator $\hat{a}$ defined as

$$\hat{a} = \frac{1}{\sqrt{2\hbar Z}}(\hat{\Phi} + iZ\hat{Q}). \tag{2.6}$$

Thus, the Hamiltonian takes the form

$$\hat{H} = hf_\mathrm{r}(\hat{a}^\dagger\hat{a} + 1/2) \tag{2.7}$$

with the canonical commutation relation $[\hat{a}, \hat{a}^\dagger] = 1$. We recognize the diagonal form of a quantum harmonic oscillator with $\hat{a}$, the operator which annihilates one mode quantum, $\hat{a}^\dagger$ the creation operator which creates one mode quantum, and $\hat{a}^\dagger\hat{a}$ the number operator that gives the number of quanta in the mode. Those quanta, called *photons*, are collective excitations of the superconducting fluid made of Coopers pairs and of the electromagnetic field. The basis that diagonalizes the Hamiltonian is the Fock basis $\{|n\rangle\}_{n\geq 0}$ [48], where n is the number of quanta of the mode (see Fig. 2.2b).

The flux and charge operators can be expressed using the annihilation and creation operators as

$$\begin{cases} \hat{\Phi} = \Phi_\mathrm{ZPF}(\hat{a} + \hat{a}^\dagger) \\ \hat{Q} = Q_\mathrm{ZPF}(\hat{a} - \hat{a}^\dagger)/i \end{cases}, \tag{2.8}$$

with $\Phi_\mathrm{ZPF} = \sqrt{\frac{\hbar Z}{2}}$ and $Q_\mathrm{ZPF} = \sqrt{\frac{\hbar}{2Z}}$, the *zero-point fluctuations*. One can notice that their product saturates the Heisenberg uncertainty principle: $\Phi_\mathrm{ZPF}Q_\mathrm{ZPF} = \hbar/2$.

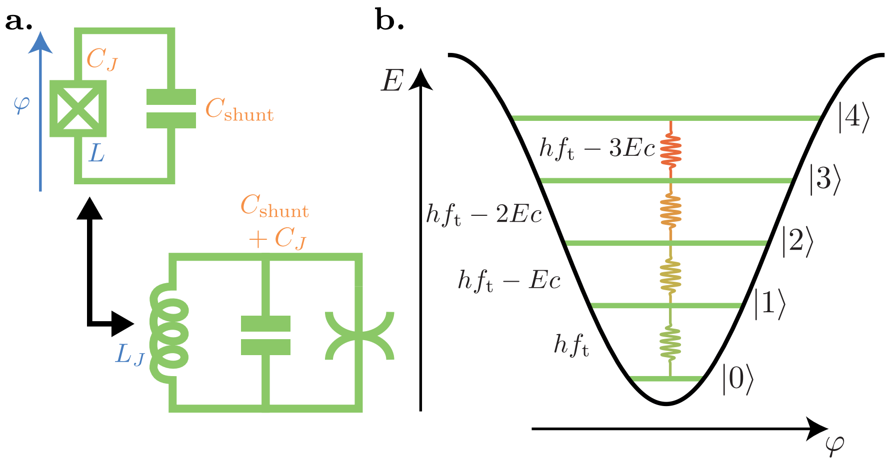

Figure 2.3: **a.** Equivalent circuit of a transmon qubit. The crossed box represents a Josephson junction including the intrinsic junction capacitor. We can separate the linear part from the non-linear one and thereby describe the transmon qubit as an LC resonator in parallel with a non-linear element, represented by the "spider" symbol. **b.** The cosine potential of the transmon qubit with its low energy levels. In the transmon regime, the frequency is independent of the charge n_g and decreases proportionally to the anharmonicity (which is equal to the charge energy E_C) when we climb the energy levels.

Those resonators and cavities cannot be used alone for two reasons. First, as the frequency of the mode is independent of the state (see Fig. 2.2b), the only state one can generate with a classical source is a coherent state $|\alpha\rangle = \exp\left(-|\alpha|^2/2\right)\sum_{n\geq 0}\alpha^n/\sqrt{n!}\,|n\rangle$. Second, as we will see in Sec. 2.5.1 if we couple two light modes capacitively or inductively, we obtain two hybrid modes that are uncoupled. Thus, to have greater control and coupling between our light modes, we need to add non-linearities in the circuit, which is the role of the Josephson junction. From now on, we will not write the hat on a quantum operator except if the classical or quantum nature of the operator is ambiguous.

2.1.2 *The transmon qubit*

A simple way to add non-linearity in the circuit, to have control of it, and to achieve coupling between the modes is to use a Josephson junction (JJ). The JJ has the advantage of working in the microwave regime and shows small amounts of dissipation. It is possible to build either a parametric coupler based on JJ [49, 50, 51, 52] or a resonant mode that can be used as a quantum bit (qubit)[49]. Here, we will focus on the qubit type used in this thesis: the transmon qubit.

The transmon qubit is made from a JJ shunted by a capacitor made of two superconducting islands (the fabrication process is detailed in App. a). As we will see below, the capacitance and the junction properties make the transmon a charge-protected qubit based on a Cooper-pair box. The transmon is currently the most used qubit, particularly in multi-qubit experiments[53, 54]. Before considering it further, we will first describe a JJ.

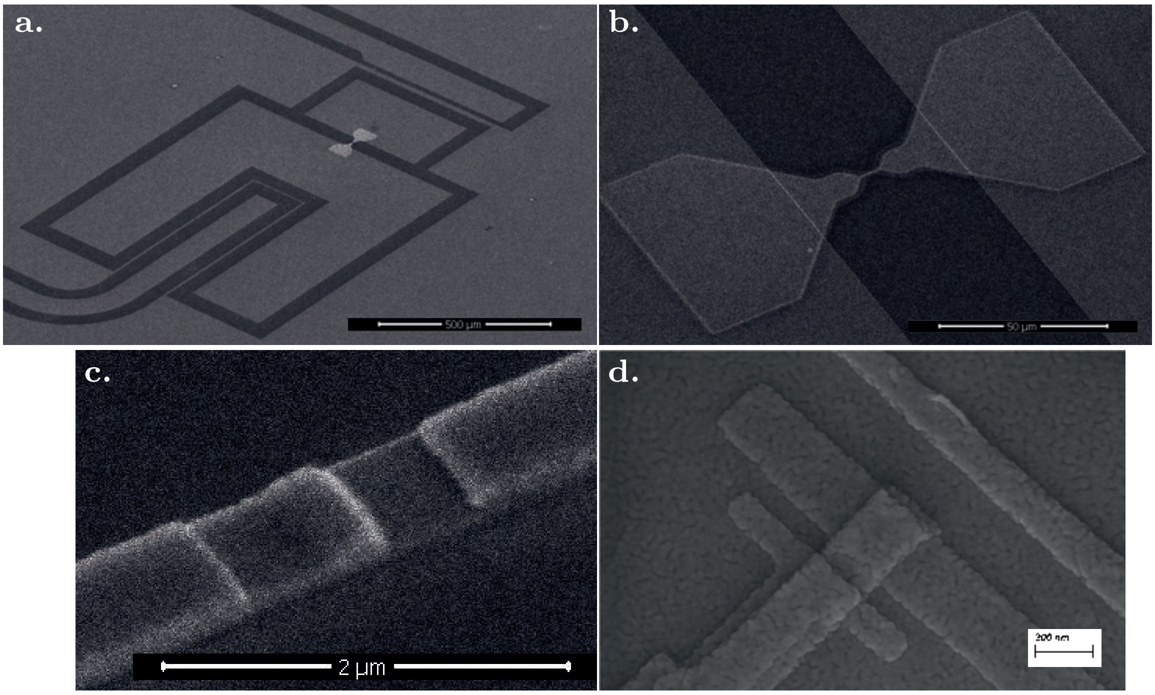

Figure 2.4: **a.** Scanning electron microscope (SEM) image of a transmon qubit. The bright element at the center is the aluminum part of the qubit. The two gray pads on each side of the aluminum part are the two superconducting islands in niobium. At the top and at the bottom, one can see the beginning of $\lambda/2$ resonators capacitively coupled to the transmon. **b.** Aluminum part of the transmon. Here, we can see the galvanic contact, which corresponds to the large area shared by the niobium superconducting islands and the aluminum in order to obtain a small amount of electrical resistance between the two. **c.** SEM image of the JJ, which is the bump at the center. The junction is evaporated using an inline Dolan bridge (see Sec. a). **d.** An SEM image of another JJ in Al/AlO$_x$/Al using a 90° Dolan bridge (see Sec. a). The visible grains are due to the layer of aluminum that was used to image the device.

A JJ is comprised of a weak link between two superconducting islands. In the circuit QED field, the weak link is usually an oxide barrier in AlO$_x$ between two superconducting Al wires. Up until now, only junctions that have aluminum oxide barriers have shown good coherence properties and an almost reproducible fabrication process. In this thesis, the superconducting islands of the transmon are either made of niobium, aluminum or tantalum, and have a galvanic contact with the aluminum junction wires. The dynamics of a JJ can be described by the phase difference φ between the Bose–Einstein condensates of the two superconducting islands [55]. The Josephson Hamiltonian reads

$$H_{\mathrm{JJ}} = -E_J \cos\varphi, \tag{2.9}$$

with $E_{\mathrm{J}}/2 \sim h \times 20\,\mathrm{GHz}$ is the energy associated with a coherent tunneling of a Cooper pair through the junction. The phase φ can be related to a flux Φ across the junction using $\varphi = \dfrac{\Phi}{\varphi_0}(\mathrm{mod}\ 2\pi)$ [3], with $\varphi_0 = \hbar/(2e)$ being the reduced flux quantum. In order

---

[3] If the junction is shunted by an inductance, then the phase φ is defined over $\mathbb{R}$ rather than $]-\pi,\pi]$

to describe the transmon qubit, we need to take into account the capacitance between the two superconducting islands and the capacitance of the JJ. The full Hamiltonian is written as [56]

$$H_{\text{transmon}} = 4E_C(n_c - n_g)^2 - E_J \cos\varphi, \tag{2.10}$$

with n_c the quantum operator giving the difference between number of Copper pairs of the two superconducting islands, $E_C = \dfrac{e^2}{2(C_{\text{shunt}} + C_J)}$ being the charging energy, e the electrical charge, and $C_{\text{shunt}} \sim 0.1\,\text{pF}$ and $C_J \sim 1\,\text{fF}$ the capacitance of the superconducting islands and of the junction, respectively. Finally, n_g is a charge offset either due to a voltage source or to an asymmetry between the superconducting islands [47]. We can then distinguish two parameter regimes. If $E_J/E_C < 10$ (e. g., if there is no shunt capacitor), we are in the Cooper-pair box regime, and the qubit is a Cooper-pair box qubit[35]. The energy spectrum will depend strongly on n_g and any charge noise on n_g will lead to a strong dephasing of the Cooper-pair box qubit and a coherence time in the order of $1\,\mu\text{s}$ [20]. By adding the shunt capacitor, we can increase the charge energy E_C to reach the ratio $E_J/E_C > 30$, which is called the transmon regime [20]. The dependence of the energy spectrum on n_g decreases exponentially, with E_J/E_C leading to a spectrum that is independent of n_g. The larger the ratio E_J/E_C is, the wider the decomposition of the transmon eigenstates on the charge basis. As the transmon state is delocalized in the charge basis, it can be viewed as a charge-protected qubit based on a Copper-pair box. At the same time, when E_J/E_C increases, the low-energy eigenstates of the transmon are more localized around the phase $\varphi = 0$, which allows us to separate the linear part from the non-linear cosine part.

$$H_{\text{transmon}} = \underbrace{4E_C(n - n_g)^2 + \frac{E_J}{2}\varphi^2 - E_J}_{\text{linear}} - \underbrace{\left(\cos(\varphi) - E_J + \frac{E_J}{2}\varphi^2\right)}_{\text{non linear}} \tag{2.11}$$

The linear terms can easily be diagonalized using the qubit annihilation operator

$$b = \frac{1}{2}\left(\frac{E_J}{2E_C}\right)^{1/4}\left(\varphi + 2i\sqrt{\frac{2E_C}{E_J}}n\right). \tag{2.12}$$

Thus, the linear part corresponds to an harmonic oscillator with the resonant frequency $\frac{1}{h}\sqrt{8E_JE_C}$. The second term adds non-linearities to the transmon qubit, making it a non-linear harmonic oscillator at low energies. The junction can be viewed as a non-linear inductor $L = L_J/\cos(\varphi)$ with a low-energy inductance $L_J = \dfrac{\varphi_0^2}{E_J} \sim 15\,\text{nH}$. If we only take into account the fourth-order non-linearities, the Hamiltonian of a transmon reads

$$H_{\text{transmon}} = \sqrt{8E_JE_C}b^\dagger b - \frac{E_C}{12}(b^\dagger + b)^4 \approx (\sqrt{8E_JE_C} - E_C)b^\dagger b - \frac{E_C}{2}b^\dagger b^\dagger bb, \tag{2.13}$$

where $f_t = (\sqrt{8E_JE_C} - E_C)/h$, and the last approximation is obtained using a rotating-wave approximation (RWA) that stands as long as $hf_t \gg E_C/4$ (which is the case in the transmon regime). The non-linear term modifies the transmon resonant frequency depending on the transmon state. As shown in Fig. 2.3b, the resonant frequency between levels m and $m+1$ is $f_{m,m+1} = f_t - mE_C$ at the first order in E_C/E_J. The fact that the anharmonicity, defined as $f_{1,2} - f_{0,1}$, is given by E_C sets a limit on the ratio E_J/E_C we can design. Indeed, in order to selectively address the two lowest levels within a time Δt[57] and at a frequency of around 5 GHz, E_C needs to be larger than $1/\Delta t$ and E_J will be fixed by the resonant frequency. In practice, E_C is between 100 MHz and 300 MHz. With this design, the $|0\rangle$ and $|1\rangle$ states (also called the $|g\rangle$ and $|e\rangle$ states) can be isolated (i. e., controlled selectively) and defined the two states of the transmon qubit.

2.2 OPEN QUANTUM SYSTEMS

In the last section, we showed how we can create harmonic oscillators and transmon qubits. We would now like to describe the basic control and measurements we can perform on such a system; however, this is, at this point, impossible. As things stand, we only have the Hamiltonian of those systems, allowing us only to study them as closed quantum systems. Of course, in order to perform measurements and apply controls, we have to interact with the system and, as such, we also need to let the environment interact with it. At this point, the system is no longer a closed system: it is now an open one, and its dynamics need to be described by a new master equation. In the next section, we will investigate how to describe an open quantum system[4].

2.2.1 *The density matrix*

The simplest way to describe a quantum state is to use a vector $|\Psi\rangle$ of the Hilbert space $\mathcal{H}$ associated with the system. However, only a *pure state* can be described in this manner. In order to be able to use a statistical mixture of pure states, also called a *mixed* state, and to study how the system can become entangled with an unknown auxiliary system, we have to use the density-matrix formalism. A density matrix ρ is a representation of the quantum state with the following properties [58]:

- for a pure state, $|\Psi\rangle$, $\rho = |\Psi\rangle\langle\Psi|$
- ρ is hermitian, i. e. $\rho = \rho^\dagger$
- ρ is positive, i. e. $\forall\, |\Psi\rangle \in \mathcal{H},\ \langle\Psi|\,\rho\,|\Psi\rangle \geq 0$
- ρ is normalized, i. e. $\mathrm{Tr}(\rho) = 1$
- The expected mean value of an observable O is given by $\langle O\rangle = \mathrm{Tr}(O\rho)$
- The probability p_μ of finding an outcome m_μ after a measurement is given by $p_\mu = \mathrm{Tr}(\Pi_\mu \rho)$, where Π_μ is the projector on the eigenspace of m_μ
- If the measurement outcome is m_μ, the measurement back-action changes ρ into $\dfrac{\Pi_\mu \rho \Pi_\mu}{p_\mu}$, where the denominator imposes to conserve a trace of 1.

---

[4] It is important to note that even if the quantum system is opened, it is designed to be sufficiently isolated to possess quantum behaviors. More precisely, the time the environment needs to destroy the quantum behavior of the system is longer than the time we need to control and measure its behavior.

As ρ is hermitian and positive, it is diagonalizable only with positive eigenvalues. Thus, we can write

$$\rho = \sum_\mu w_\mu \left|\Psi_\mu\right\rangle \left\langle\Psi_\mu\right| , \tag{2.14}$$

where the normalization of ρ imposes $\sum_\mu w_\mu = 1$. In this case, we can understand ρ as a statistical mixture of the pure states $\{|\Psi_\mu\rangle\}_\mu$, where w_μ is the probability of having the state $|\Psi_\mu\rangle$. From this form, it is a simple matter to use the Schrodinger equation to derive the derivative of ρ

$$\frac{\mathrm{d}\rho}{\mathrm{d}t} = -\frac{i}{\hbar}[H, \rho], , \tag{2.15}$$

with H the Hamiltonian of the system.

We need to highlight the fact that ρ is the best representation we have of the quantum state, based on the information observers currently possess. This observation reveals quantum mechanics as a theory of information [59]: we accumulate in one object (the density matrix) all the information we have about a quantum state[5]. An omniscient observer that knows all the information about a system will be able to write it as a pure state.

That is, if two systems, A and B, are entangled, the quantum state can therefore be described by the density matrix ρ_{AB}. The density matrix ρ_A, which describes the state of A without looking at B, is simply given by the partial trace of ρ_{AB} over B

$$\rho_A = \mathrm{Tr}_B(\rho_{AB}) = \sum_\mu \left\langle\Psi_\mu^B\right| \rho_{AB} \left|\Psi_\mu^B\right\rangle , \tag{2.16}$$

where $\{\left|\Psi_\mu^B\right\rangle\}_\mu$ is a basis of B, and the sandwich of ρ_{AB} produced by the bras and the kets of B acts only on the Hilbert space of B. This way, ρ_A only contains information about the system A; it does not contain any information about the entanglement it has with the system B.

As our systems are open, they exchange energy and information with the environment; thus, the only exact way to describe them is to use the density-matrix formalism. Moreover pure states are non-physical. The quantum version of the third law of thermodynamics says that we can prepare a pure state only by using an infinite amount of resources [60]. Thus, experimentally, there is no such thing as a pure state. However, pure states are a usefull representation which make the description of system easier in many situations.

Before deriving the master equation for our system, let us see how we can be more quantitative about the amount of information contained in the density matrix.

2.2.2 *Von Neumann entropy*

Instead of looking at the amount of information we have about a state, we prefer to look at the amount of information that is unknown (in other words, the amount of

---

[5] If we dare to construct an analogy, this is like asking someone to draw a picture of somebody they have never seen, but only heard about. The drawing will contain all the information the artist has and will not be fully accurate; additionally, parts of the drawing will be blurred when the artist contains only partial information.

information we have to discover if we wish to project the system's current state onto a pure state)[6]. Commonly, this missing information is called *entropy*, as it refers to the same entropy concept found in statistical physics. There are several ways to define the entropy of a quantum state; in this thesis, we will use the von Neumann definition of entropy, which satisfies all the properties an entropy should have [59],

$$S(\rho) = \mathrm{Tr}(\rho \log_2(\rho)) = -\sum_{\mu} w_\mu \log_2(w_\mu), \tag{2.17}$$

where the second equality is easily obtained after the diagonalization of ρ. This shows that the von Neumann entropy of a statistical mixture of pure states is the same as Shannon's entropy[59] of the probability distribution $\{w_\mu\}_\mu$. The $\log_2(x) = \log(x)/\log(2)$ function is the binary logarithm; in this way, the entropy is expressed in units of bits of information.

As an example, let us consider the maximally entropic state of a qubit, $\rho_q = \frac{1}{2}\left|g\right\rangle\left\langle g\right| + \frac{1}{2}\left|e\right\rangle\left\langle e\right|$. We can translate its state as follows: the qubit has 50% chance of being in $\left|g\right\rangle$ and a 50% chance of being in $\left|e\right\rangle$. In this case, the von Neumann entropy gives $S(\rho_q) = 1$, which means we need to measure one bit of information to know the qubit's exact state. This makes sense, as a qubit state is described by one bit of information[7].

The von Neumann entropy will be used in Sec. 8.2.2 to derive the rate at which the measurement extracts information from the system.

2.2.3 *The environment's measurements*

In order to derive the master equation of an open quantum system, we first need to be able to describe the interaction between the system and its environment. To do so, we will derive the *generalized measurement* formalism, and use it to describe the system's interaction with the environment and to derive a differential equation for the system dynamics.

2.2.3.1 *Generalized measurement*

As we will see in Sec. 4.1.2, most measurements are not projective. As such, we need to introduce a formalism that will enable us to deal with all kinds of measurements [7]. First, let us describe how measurements are generally performed. Our system, called system A, interacts with an ancillary system, B, which is used for the purpose of measurement. The measurement scheme is as follows: we let systems A and B interact and become entangled under the unitary evolution U_E, before performing a von Neumann measurement of system B [7]. Let us now consider the effect of this measurement process on system A. As any mixed state is a statistical mixture of pure states, we will, in a first time treat system A as starting in a generic pure state $\left|\Psi^A\right\rangle$. Thus, the full system

---

[6] This is of course impossible, according to the third law of quantum thermodynamics, because of the noise that is always attached to any measurement

[7] This also means that a qubit state cannot encode more than one bit of information.

starts in the state $|\Psi^A\rangle \otimes |0^B\rangle$, where $|0^B\rangle$ is a reference state for B. The entangling operation U_E changes the state of the system in a unitary way, as follows [7]:

$$|\Psi^{AB}\rangle = U_E\,|\Psi^A\rangle \otimes |0^B\rangle = \sum_\mu (M_\mu\,|\Psi^A\rangle) \otimes |\Psi^B_\mu\rangle\,, \tag{2.18}$$

where each $|\Psi^B_\mu\rangle$ corresponds to an eigenvector, associated with the result m_μ of the projective measurement that will be performed on B and M_μ are the *measurement operators* which describes how the state of the system A evolve under the entangling operation U_E for each result m_μ. We have the mathematical relation $M_\mu = \langle\Psi^B_\mu|\, U_E\, |0^B\rangle$. If system A starts in a mixed state, we can write ρ_A, the density matrix of A, as a convex combination of a pure state projectors, applying the same results to each pure state. Thus, the state after the unitary evolution reads

$$\rho_{AB} = U_E(\rho_A \otimes |0^B\rangle\langle 0^B|)U_E^\dagger = \sum_{\mu,\nu} M_\mu \rho_A M_\nu^\dagger \otimes |\Psi^B_\mu\rangle\langle\Psi^B_\nu|\,. \tag{2.19}$$

If the von Neumann measurement of B gives the outcome m_μ, the state of B is projected onto $|\Psi^B_\mu\rangle$ and the state of A becomes $M_\mu\rho_A M_\mu^\dagger/\operatorname{Tr}\left(M_\mu\rho_A M_\mu^\dagger\right)$. By tracing over A, we can show that the probability of measuring the outcome m_μ is given by $p_\mu = \operatorname{Tr}(M_\mu\rho_A M_\mu^\dagger)$. As the size of B is not bounded, the number of outcomes and the number of measurement operators M_μ are not bounded either.

Let us then summarize what we discussed. A measurement scheme can be described using a unitary entanglement with an ancillary system or probe, followed by a projective measurement of the ancillary system. Each measurement outcome m_μ is related to a measurement operator M_μ, which may not be Hermitian. The probability p_μ of obtaining the outcome m_μ is

$$p_\mu = \operatorname{Tr}\left(M_\mu\rho_A M_\mu^\dagger\right), \tag{2.20}$$

and the system state after the measurement becomes

$$\rho_A \to \frac{M_\mu\rho_A M_\mu^\dagger}{p_\mu}. \tag{2.21}$$

As the sum of the probability outcomes has to be equal to 1, the measurement operators must satisfy a normalization equality, as follows

$$\sum_\mu M_\mu^\dagger M_\mu = \mathbb{1}. \tag{2.22}$$

It is easy to confirm that, if the measurement operators are orthogonal projectors, then the Eqs. (2.20) and (2.21) become equivalent to those used by a von Neumann measurement performed on A.

If the measurement is unread, the density matrix ρ_A will be given as a statistical mixture of all possible density matrices after the measurement, weighted by the outcome probabilities [7]

$$\rho_A \to \sum_\mu p_\mu \frac{M_\mu\rho_A M_\mu^\dagger}{p_\mu} = \sum_\mu M_\mu\rho_A M_\mu^\dagger. \tag{2.23}$$

Generalized measurement is a powerful tool. As we will see in the next section, any quantum evolution can be described as an unread generalized measurement; this will allow us to derive the dynamics of an open system.

2.2.3.2 *Quantum maps and Kraus operators*

Any unitary evolution, unread measurement, or interaction by a system with its environment can be described by a linear super-operator[8], $\mathcal{L}$, called a *quantum map* [7]. A quantum map has to be a linear operator that leads to a hermitian, positive, and normalized density matrix. Thus

- $\mathcal{L}(p\rho + q\rho') = p\mathcal{L}(\rho) + q\mathcal{L}(\rho')$ with $p + q = 1$
- $\mathcal{L}^\dagger(\rho) = \mathcal{L}(\rho)$
- $\mathrm{Tr}(\mathcal{L}(\rho)) = 1$
- $\langle\Psi| \mathcal{L}(\rho) |\Psi\rangle \geq 0$ for all $|\Psi\rangle$ in $\mathcal{H}$.

One can show that any quantum map can be written as an unread generalized measurement [7]. In such cases, the measurement operators are also called *Kraus operators*. Thus, any quantum map representing the evolution of the system during the time Δt, including any interaction with an environment, takes the form

$$\rho(t + \Delta t) = \mathcal{L}(\rho(t)) = \sum_\mu M_\mu \rho M_\mu^\dagger. \tag{2.24}$$

There are many possible sets of Kraus operators M_μ for a given map but it is possible to find a set with at most $N_{\mathcal{H}}^2$ Kraus operators, where $N_{\mathcal{H}}$ is the size of the system Hilbert space $\mathcal{H}$, whatever the size of the environment with which the system interacts. These results show that the decoherence process, i. e. the decrease of the coherences due to interaction with an environment, can be seen as a measurement performed by the environment. As an observer of the system, we may not have access to the outcome of this measurement. There is one condition to satisfy to describe the effect of an environment on a system with such a quantum map, the system and the environment have to start in a separable state; i. e. they must not be entangled or classically correlated.

2.2.3.3 *The Lindblad equation*

The quantum map derived in the last section is a time-integrated evolution. When describing our system, we would prefer to use a first-order differential equation to describe the dynamics of ρ as a function of time t. Deriving such a differential equation is not straightforward; the environment has to satisfy certain conditions. For a precise description of the environment, see [61], and for a detailed discussion about the conditions, see [7]. Here, we will only state that the following conditions are enough to derive a first-order differential equation:

- The environment must be a "sink" (e. g. large enough, with many degrees of freedom) whose evolution is not appreciably affected by the system. Thus, we can use a Markov approximation to erase the memory of the environment. The time scale of the correlation and fluctuation of the environment can be denoted by t_c. The Markov approximation involves looking at the system using a time step $\mathrm{d}t$

---

[8] A super-operator acts on operators of the Hilbert space.

larger than t_c, otherwise we need to take into account the memory and fluctuations of the environment to describe the system dynamics. t_c can be viewed as the time the environment needs to reset the modes that are coupled to the system.

- The system dynamics is divided into time slices of duration $\mathrm{d}t$. Mathematically, it means we cannot consider the limit $\mathrm{d}t \to 0$. This "coarse-grained" description erases high-frequency system dynamics, the fluctuations and correlations of the environment, and any entanglement between the system and the environment. In order to capture a dynamics with the typical time scale t_d, the time step $\mathrm{d}t$ has to be smaller than t_d. Thus, we can state the following restriction:

$$t_c \ll \mathrm{d}t \ll t_d. \tag{2.25}$$

- We assume that no measurement has been performed by the observer (or, at least, that only unread measurements have been performed).

Under the above assumptions, at any time t (with time steps $\mathrm{d}t$) the state of the system and the environment can be considered as factorized. This allows us to use a quantum map to compute the system evolution during the next time step $\mathrm{d}t$ with Kraus operators that do not depend on the time t.

We define the derivative of ρ as

$$\frac{\mathrm{d}\rho}{\mathrm{d}t}(t) = \frac{\mathcal{L}_{\mathrm{d}t}(\rho(t)) - \rho(t)}{\mathrm{d}t}, \tag{2.26}$$

where $\mathcal{L}_{\mathrm{d}t}$ is the quantum map describing the evolution of the density matrix during the time $\mathrm{d}t$: $\mathcal{L}_{\mathrm{d}t}(\rho(t)) = \rho(t+\mathrm{d}t)$. As we choose $\mathrm{d}t$ small compared to the typical time scale of the system dynamics, $\rho(t+\mathrm{d}t)$ must be equal to $\rho(t)$ at the first order in $\mathrm{d}t$. This means that at least one of the Kraus operators in $\mathrm{d}t$ is of the order of unity. As the set of Kraus operators is not fixed, we can make it so that only one Kraus operator is of the order of unity. Let us call this Kraus operator M_0, which we can write as

$$M_0 = \mathbb{1} - i\frac{H}{\hbar}\mathrm{d}t - J\mathrm{d}t, \tag{2.27}$$

where we isolate the hermitian $H/\hbar$ and anti-hermitian J parts of the first-order contribution. The decision to call the hermitian part H is not anecdotal: as we will see later, it is in fact the Hamiltonian of the system.

The action of all other Kraus operators, i. e. $M_\mu \rho M_\mu^\dagger$, are of the order of unity in $\mathrm{d}t$. Thus, we write

$$M_\mu = \sqrt{\mathrm{d}t} L_\mu, \tag{2.28}$$

where L_μ is called the jump operator and is independent of t and $\mathrm{d}t$. Using the normalization condition of the Kraus operator set, we can express J as a function of $\{L_\mu\}_\mu$

$$\sum_\mu M_\mu^\dagger M_\mu = \mathbb{1} - 2J\mathrm{d}t + \sum_{\mu\neq 0} \mathrm{d}t L_\mu^\dagger L_\mu = \mathbb{1}, \tag{2.29}$$

obtaining

$$J = \frac{1}{2}\sum_{\mu\neq 0} L_\mu^\dagger L_\mu. \tag{2.30}$$

Note that H does not appear. This make sense, as the normalization condition of the Kraus operator imposes the preservation of the density matrix trace and a Hamiltonian dynamics is unitary and thus does not affect the density matrix trace.

We now know everything we need to write the derivative of the density matrix. Eq. (2.24) reads

$$\frac{\mathrm{d}\rho}{\mathrm{d}t} = -\frac{i}{\hbar}[H,\rho] + \sum_{\mu\neq 0}\mathcal{D}(L_\mu)\rho, \tag{2.31}$$

where $\mathcal{D}$ is the Lindblad super-operator defined as $\mathcal{D}(L)\rho = L\rho L^\dagger - \frac{1}{2}\{L^\dagger L,\rho\}$.

This master equation is in the Lindblad form and, as such, is commonly termed the *Lindblad equation*. In this equation, we retrieve the unitary evolution under the Hamiltonian H as in Eq. (2.15). However, the Hamiltonian is not exactly the same. In the Lindblad equation, H contains all the renormalization effects due to its interaction with the environment, as in, for example, the Lamb shift [61, 7]. When comparing Eqs. (2.15) and (2.31), we can see that the major effect of the environment is adding the Lindblad superoperator terms, which act as the unread measurement of the jump operators. Note also that the Lindblad super-operator form ensures the conservation of the trace of the density matrix.

2.3 DISSIPATION AND CONTROL OF RESONATORS

In this section and the next, we will describe and discuss the Lindblad form of the master equation for resonators (or cavities) and qubits, and the controls and measurements we can perform. As cavities and resonators are equivalent systems, for the rest of this thesis we will always use the word "resonator," except where the system is explicitly a cavity.

2.3.1 *Input–output relation*

In order to apply a control and to probe the resonator, we capacitively couple the resonator to a microwave transmission line (see Fig. 2.5a). In this thesis, all experiments are performed by probing the resonator in reflection; this only needs one transmission line, whereas a measurement in transmission needs two transmission lines. To stay general, we will derive the equations by assuming that the resonator has two ports.

Each transmission line can be described using an infinite number of LC modes in parallel (see Fig. 2.5b); thus, the number of degrees of freedom the transmission line has can be considered as large enough that the transmission line is a "sink." We can then use a master equation with a Lindblad form. The resonator can only lose photons one by one, so the jump operators we have to consider are $\sqrt{\kappa_1}a$, $\sqrt{\kappa_2}a$, and $\sqrt{\kappa_l}a$, where κ_1 (respectively κ_2)) is the coupling rate between the resonator and the first (respectively

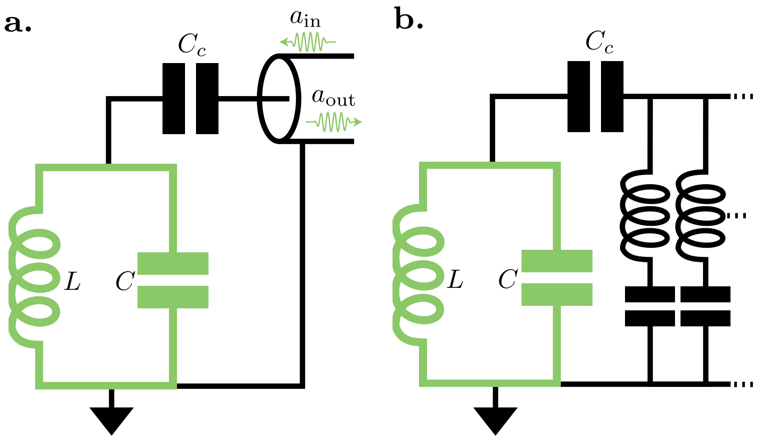

Figure 2.5: **a.** LC mode capacitively coupled to a transmission line. The coupling capacitor C_c depends on the length of the pin in 3D geometry and the capacitor pad size in 2D. **b.** Equivalent descriptions of the transmission line. We replace it with an infinite number of LC modes, corresponding to the line's propagating modes. **c.** A Caldeira–Leggett model of the transmission line. The infinite collection of LC modes is replaced by a linear resistor whose impedance that is equal to that possessed by the line [48]. This representation will be useful in Sec. 3.2.

second) transmission line, κ_l is the rate at which the resonator loses photons due to internal losses, and a is the annihilation operator of the resonator mode. Thus, the master equation is

$$\frac{\mathrm{d}\rho}{\mathrm{d}t} = -\frac{i}{\hbar}[H, \rho] + (\kappa_1 + \kappa_2 + \kappa_l)\mathcal{D}(a)\rho. \tag{2.32}$$

The input and output propagating fields for each transmission line i are linked to the resonator state by the input–output relationship [62], as follows:

$$a_{\mathrm{out},i} - a_{\mathrm{in},i} = -\sqrt{\kappa_i}a, \tag{2.33}$$

where $a_{\mathrm{in},i}$ and $a_{\mathrm{out},i}$ are the annihilation operators of the input and output fields at the end of the transmission line i (i. e. the input and output fields seen by the coupling capacitor C_c).

Using the Heisenberg picture, we can write the quantum Langevin equation within the RWA, followed by the annihilation operator a [48]

$$\frac{\mathrm{d}a}{\mathrm{d}t} = -\frac{i}{\hbar}[H_{\mathrm{bare}}, a] - \frac{\kappa_1 + \kappa_2 + \kappa_l}{2}a + \sqrt{\kappa_1}a_{\mathrm{in},1}(t) + \sqrt{\kappa_2}a_{\mathrm{in},2}(t) + \sqrt{\kappa_l}a_{\mathrm{in},l}(t), \tag{2.34}$$

where H_{bare} is the Hamiltonian of the system under the assumption that no input field was received through the two ports or through internal losses, and $a_{\mathrm{in},l}$ is the annihilation operator representing the input field corresping to the internal losses. Driving port 1 with a coherent field (which is what we have when using a classical microwave source attenuated at low temperature) of complex amplitude α_{in} and angular frequency ω, the mean value of the Langevin equation gives a mean-field equation reading

$$\frac{\mathrm{d}\alpha}{\mathrm{d}t} = -i\omega_r\alpha - \frac{\kappa_{\mathrm{tot}}}{2}\alpha + \sqrt{\kappa_1}\alpha_{\mathrm{in}}, \tag{2.35}$$

where $\kappa_{\text{tot}} = \kappa_1 + \kappa_2 + \kappa_l$, α is the complex amplitude of the resonator coherent field and ω_r is the resonant angular frequency. Employing the Fourier domain to solve this equation and using the input–output relation (see Eq. (2.33)), we can compute the reflected coefficient S_{11} on port 1 and the transmission coefficient S_{21} from ports 1 to 2

$$\begin{cases} S_{11}(\omega) = \dfrac{\alpha_{\text{out},1}(\omega)}{\alpha_{\text{in},1}(\omega)} = -\dfrac{\kappa_1 - \kappa_2 - \kappa_l + 2i(\omega - \omega_r)}{\kappa_{\text{tot}} - 2i(\omega - \omega_r)} \\ S_{21}(\omega) = \dfrac{\alpha_{\text{out},2}(\omega)}{\alpha_{\text{in},1}(\omega)} = \dfrac{-2\sqrt{\kappa_1\kappa_2}}{\kappa_{\text{tot}} - 2i(\omega - \omega_r)} \end{cases} \tag{2.36}$$

These two coefficients are the signal we measure when we perform a spectroscopy of the resonator with an heterodyne detection setup.

2.3.2 *Displacement operator*

In the last section, we described the output field when the resonator is driven by a coherent field. Let us now discuss the effect of this drive on the resonator state. Going back to Eq. (2.34), we see that adding a coherent drive $\alpha_{\text{in}}\mathrm{e}^{-i\omega t}$ through port 1 is equivalent to displacing the state a_{in} by the drive

$$a_{\text{in}} \to a_{\text{in}} + \alpha_{\text{in}}\mathrm{e}^{-i\omega t}. \tag{2.37}$$

Thus, a new term appears in the Langevin equation (2.34) that can be absorbed in the Hamiltonian by adding the drive term H_{drive} [62]:

$$H_{\text{drive}} = i\hbar\sqrt{\kappa_1}(a^\dagger - a)(\alpha_{\text{in}}\mathrm{e}^{-i\omega t} + \alpha_{\text{in}}^*\mathrm{e}^{i\omega t}). \tag{2.38}$$

Using the rotating frame of the resonator and performing RWA, we get

$$H_{\text{RWA}} = i\hbar\sqrt{\kappa_1}(a^\dagger\alpha_{\text{in}}\mathrm{e}^{-i\Delta t} - a\alpha_{\text{in}}^*\mathrm{e}^{i\Delta t}), \tag{2.39}$$

with $\Delta = \omega - \omega_r$ being the detuning of the drive compared to the resonator frequency. This Hamiltonian is equivalent to applying a displacement force in an oscillating direction on the resonator state. If the drive is resonant ($\Delta = 0$), the direction of the force is constant and the state $\rho(t = 0)$ will be transformed after time t in

$$\rho(t) = D(\alpha)\rho(0)D(\alpha)^\dagger, \tag{2.40}$$

where $D(\alpha) = \exp\big(\alpha a^\dagger - \alpha^* a\big)$ is the displacement operator and $\alpha = \sqrt{\kappa}\alpha_{\text{in}}t$. This equation is valid if the dissipation is negligible during the time t (i. e., $t \ll 1/\kappa_{\text{tot}}$). This operator is called "displacement," as it translates the state by α in the phase space. Specifically, if we start in the vacuum $|0\rangle$, the state after a displacement $D(\alpha)$ is the coherent state $|\alpha\rangle = \exp\big(-|\alpha|^2/2\big)\sum_n \dfrac{\alpha^n}{\sqrt{(n!)}}|n\rangle$.

In comparison, if the drive is applied during a time t that is larger than a few $1/\kappa_{\text{tot}}$, the resonator state reaches a steady state due to the competition between the displacement force and the dissipation. The steady state is equal to the coherent state

$|\alpha_{\text{ss}}\rangle$ where α_{ss} is the stationnary solution of the mean-field equation (2.35) in the frame rotating at the drive frequency

$$0 = i\Delta\alpha_{\text{ss}} - \frac{\kappa_{\text{tot}}}{2}\,\alpha_{\text{ss}} + \sqrt{\kappa_1}\alpha_{\text{in}}, \tag{2.41}$$

where the solution is

$$\alpha_{\text{ss}} = \frac{2\sqrt{\kappa_1}\alpha_{\text{in}}}{\kappa_{\text{tot}} - 2i\Delta}, \tag{2.42}$$

2.3.3 *Dissipation and temperature*

We will now describe the resonator's losses in more detail. Here, κ_{tot} is the total loss rate of the resonator (i. e. the rate at which the resonator loses photons). Starting from a coherent field $|\Psi(0)\rangle = |\alpha\rangle$, the state after at time t when no drive is applied is

$$|\Psi(t)\rangle = \left|\alpha \mathrm{e}^{-\kappa_{\text{tot}}t/2}\right\rangle. \tag{2.43}$$

The amplitude of the coherent field decreases at a rate $\kappa_{\text{tot}}/2$, while the mean photon number $\langle a^\dagger a\rangle_{|\Psi(t)\rangle} = |\alpha|^2\mathrm{e}^{-\kappa_{\text{tot}}t}$ decreases exponentially at a rate κ_{tot}. In the same way, the one-photon Fock state $|1\rangle$ decays toward the vacuum at a rate κ_{tot}. Thus, we can define the relaxation time of the cavity as $T_1 = 1/\kappa_{\text{tot}}$.

We usually use two other quantities to quantify the resonator and cavity losses: the quality factor $Q = \omega_r/\kappa_{\text{tot}}$ and the internal quality factor $Q_{\text{i}} = \omega_r/\kappa_l$ [9]. Where a resonator is used as a probe (to read out the state of a qubit, for example—see Sec. 2.5.2), the quality factor has to be limited by the coupling to the transmission line (i. e. $Q \ll Q_{\text{i}}$) so that the information is not lost in the environment due to internal losses. Usually, we use a readout resonator with a quality factor around 10^4 and an internal quality factor around 10^6. When a resonator is used as a storage mode, the coupling to the transmission line is decreased so that the losses are limited only by the internal losses ($Q \sim Q_{\text{i}}$). An internal quality factor of 10^6 has been measured for 2D superconducting resonators [63, 64, 65] and of about $10^7 - 10^9$ for superconducting cavities in circuit QED [46, 66].

What happens if the resonator temperature is not small compared to $\hbar\omega_r/k_B$? In such a situation, the thermal density matrix is

$$\rho = \left(1 - \mathrm{e}^{-\frac{\hbar\omega_r}{k_B T}}\right)\mathrm{e}^{-\frac{\hbar\omega_r}{k_B T}a^\dagger a}, \tag{2.44}$$

with T the effective temperature of the environment. Assuming a single temperature for all the environments, we need to take into account two jump operators, $\sqrt{\kappa_{\text{tot}}(n_{\text{th}}+1)}a$ and $\sqrt{\kappa_{\text{tot}}n_{\text{th}}}a^\dagger$ with n_{th} being the mean photon number of the thermal state. We can define $\kappa_\uparrow = \kappa_{\text{tot}}n_{\text{th}}$ and $\kappa_\downarrow = \kappa_{\text{tot}}(n_{\text{th}}+1)$ as the rate at which the resonator gains a photon from the environment and the rate at which it loses a photon in the environment, respectively. The Lindblad master equation takes the form

$$\frac{\mathrm{d}\rho}{\mathrm{d}t} = -\frac{i}{\hbar}[H,\rho] + \kappa_\downarrow\mathcal{D}(a)\rho + \kappa_\uparrow\mathcal{D}(a^\dagger)\rho \tag{2.45}$$

---

[9] We may also define the external quality factor of each port i as $Q_{\text{ext},i} = \omega_r/\kappa_i$.

and $\kappa_\uparrow$ and $\kappa_\downarrow$ satisfy the detailed balance relation

$$\frac{\kappa_\uparrow}{\kappa_\downarrow} = \mathrm{e}^{-\dfrac{k_B T}{\hbar\omega_r}}, \tag{2.46}$$

and there are related to κ_{tot} through the relation

$$\kappa_{\text{tot}} = \kappa_\downarrow - \kappa_\uparrow \tag{2.47}$$

2.4 DISSIPATION AND CONTROL OF A TRANSMON QUBIT

In this section, we will describe the master equation and the basic controls we can apply to a transmon qubit. We will only consider a single-junction qubit[10].

2.4.1 *Density matrix*

A qubit state can be described using a two-by-two density matrix ρ_q. As the density matrix is hermitian, we can decompose it on a two-by-two hermitian matrix basis, $\{\mathbb{1}\sigma_x, \sigma_y, \sigma_z\}$, with σ_x, σ_y, and σ_z being the Pauli matrices:

$$\rho_q = \frac{1}{2}\begin{pmatrix} 1+z & x-iy \\ x+iy & 1-z \end{pmatrix} = \frac{\mathbb{1} + x\sigma_x + y\sigma_y + z\sigma_z}{2}. \tag{2.48}$$

Thus, any quantum state of the qubit can be given by a 3D vector $\vec{u}(\rho_q) = \{x, y, z\}$. Each of the components x, y, and z correspond to the mean value of the respective Pauli operators: $\langle\sigma_x\rangle = x$, $\langle\sigma_y\rangle = y$, and $\langle\sigma_z\rangle = z$. The so called Bloch vector $\vec{u}(\rho_q)$ has a norm not larger than 1 and the set of vectors, which correspond to all possible qubit states, describe a sphere called the Bloch sphere (see Fig. 2.6). Each point within the sphere is the representation of a qubit state, and the qubit trajectories can be drawn inside. This graphical representation of a qubit state is extremely powerful, as any operation on a qubit state can be translated into a geometrical function applied to the Bloch vector. The pure qubit states correspond to the vector of norm of 1 (see Fig. 2.6a). Thus, the surface of the Bloch sphere corresponds to all pure qubit states, while the inside corresponds to all mixed qubit states (see Fig. 2.6b). The Bloch vector norm and the von Neumann entropy satisfy the relationship $S(\rho_q) = -p\log_2(p) - (1-p)\log_2(1-p)$ with $p = (1 + \|\vec{u}(\rho_q)\|)/2$. Therefore, the closer the Bloch vectors are to the centre of the Bloch sphere, the larger the entropy of the state and the most entropic state is described by the null Bloch vector $\vec{u}(\rho_{\max,S}) = \vec{0}$.

As for the cavity, the qubit has to be coupled to a transmission line in order to apply control[11]. The qubit can lose its excitation by emitting a photon in the transmission line and, more generally, in the environment, and it dephases (i. e. the phase

---

[10] The junction of a transmon qubit can be replaced by a superconducting quantum interferences device (SQUID) in order to obtain a qubit with a tunable resonant frequency that depends on the magnetic flux inside the SQUID loop[20].

[11] This transmission line can be the same transmission line as the one coupled to the resonator. In this case, the qubit is coupled to the transmission line through the resonator thanks to the Purcell effect. We will discuss this more in Sec. 3.3

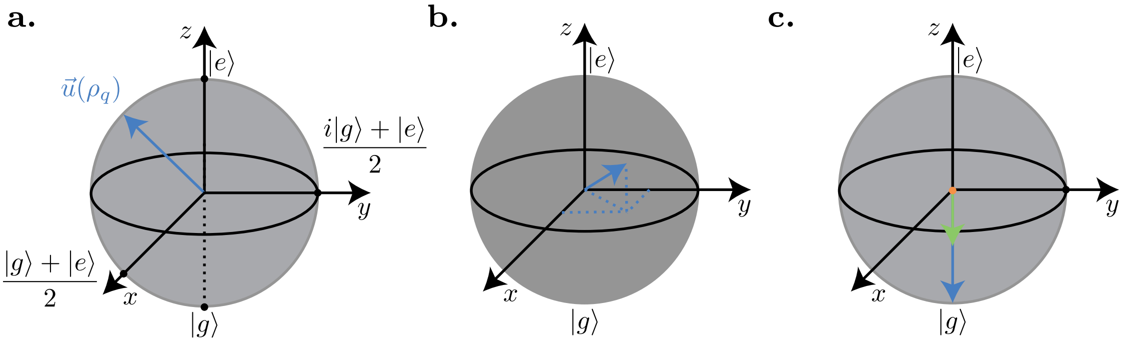

Figure 2.6: Bloch sphere of a qubit for three situations: *a.* a pure state. *b.* a mixed state, and *c.* a thermal state for a temperature below $\hbar\omega/k_B$ (blue), of the order of $\hbar\omega/k_B$ (green), and large compared to $\hbar\omega/k_B$ (orange).

of superposition of $|g\rangle$ and $|e\rangle$ diffuses) due to noise on parameters controlling its frequency and to dispersive coupling with hot modes (see Sec. 2.5.2). An example of noise-producing dephasing is the charge noise from which the transmon is protected exponentially in E_J/E_C (see Sec. 2.1.2). To describe these two effects, we can use two jump operators, $\sqrt{\Gamma_1}\sigma_-$ and $\sqrt{\Gamma_\varphi/2}\sigma_z$, which correspond to relaxation and dephasing, respectively. Here, Γ_1 is the relaxation rate and Γ_φ is the pure dephasing rate[12]. The Lindblad master equation then becomes

$$\frac{\mathrm{d}\rho_q}{\mathrm{d}t} = -\frac{i}{\hbar}[H,\rho_q] + \Gamma_1\mathcal{D}(\sigma_-)\rho_q + \frac{\Gamma_\varphi}{2}\mathcal{D}(\sigma_z)\rho_q. \tag{2.49}$$

From this equation, we can show that the $|e\rangle$ state relaxes toward the $|g\rangle$ state following an exponential decay at a rate Γ_1. We can define the lifetime of the qubit as $T_1 = 1/\Gamma_1$. In the same way, starting from the state $(|g\rangle+|e\rangle)/\sqrt{2}$, the density matrix evolves as

$$\rho_q(t) = \frac{1}{2}\begin{pmatrix} \mathrm{e}^{-\Gamma_1 t} & \mathrm{e}^{-\Gamma_2 t} \\ \mathrm{e}^{-\Gamma_2 t} & 2-\mathrm{e}^{-\Gamma_1 t} \end{pmatrix}, \tag{2.50}$$

with $\Gamma_2 = \Gamma_1/2 + \Gamma_\varphi$ being the decoherence rate. Indeed, the off-diagonal term of the density matrix corresponds to the coherence between the $|g\rangle$ and $|e\rangle$ states. Thus, we can define the coherence time as $T_2 = 1/\Gamma_2$. The life-time T_1 and the coherence time T_2 give the time during which information can be stored in the $|e\rangle$ state or in the phase of a $|g\rangle$ and $|e\rangle$ superposition, respectively. Note that T_2 cannot be greater than $2T_1$; this makes sense as the relaxation of the $|e\rangle$ state affects any superposition of $|g\rangle$ and $|e\rangle$.

In the same way as for a resonator, if the temperature of the qubit T is not negligible compare to $\hbar\omega_q/k_B$, with ω_q being the angular frequency of the qubit, we have to change the relaxation jump operator using $\sqrt{\Gamma_\uparrow}\sigma_+$ and $\sqrt{\Gamma_\downarrow}\sigma_-$, with $\Gamma_\uparrow = p_{\mathrm{th}}\Gamma_1$, and $\Gamma_\downarrow = (1-p_{\mathrm{th}})\Gamma_1$, p_{th} being the mean photon number or the excited state population of the qubit thermal state, and $\sigma_+ = (\sigma_x + i\sigma_y)/2$ and $\sigma_- = (\sigma_x - i\sigma_y)/2$ being

---

[12] We can also define a dephasing rate for a resonator (see Sec. 8.1.1), but it is generally small compared to the relaxation rate κ_{tot}.

the creation and annihilation qubit operators, respectively. Note that $\Gamma_\uparrow$ and $\Gamma_\downarrow$ also satisfy the detailed balance of Eq. (2.46) and that $\Gamma_1 = \Gamma_\downarrow + \Gamma_\uparrow$. The Bloch vector of the thermal state $\rho_{q,\mathrm{th}}$ is given by $\vec{u}(\rho_{q,\mathrm{th}}) = \{0, 0, 2p_{\mathrm{th}} - 1\}$ (see Fig. 2.6c) and the higher the temperature, the closer it is to the Bloch sphere center.

2.4.2 *Bloch dynamics*

When driving the qubit with a coherent field of complex amplitude $\alpha_{\mathrm{in}}(t)\mathrm{e}^{-i\omega_{\mathrm{d}}t}$ with $\alpha_{\mathrm{in}}(t) = |\alpha_{\mathrm{in}}|(t)\mathrm{e}^{-i\phi_d}$ and ϕ_d being the phase of the drive, the Hamiltonian of the qubit becomes[62]

$$H_q = \hbar\omega_q\frac{\sigma_z}{2} - i\hbar\sqrt{\Gamma_c}(\sigma_- - \sigma_+)(\alpha_{\mathrm{in}} + \alpha_{\mathrm{in}}^*), \tag{2.51}$$

with Γ_c being the coupling between the qubit and the port used to drive the qubit. As Γ_1 is the coupling of the qubit to the full environment, we then have $\Gamma_1 \geq \Gamma_c$. In the frame rotating at ω_d, we can perform an RWA to obtain

$$H_{q,\mathrm{RWA}} = -\hbar\delta\frac{\sigma_z}{2} - \hbar\frac{\Omega(t)}{2}(\cos(\phi_d)\sigma_y - \sin(\phi_d)\sigma_x), \tag{2.52}$$

with $\Omega(t) = 2\sqrt{\Gamma_c}|\alpha_{\mathrm{in}}(t)|$ and $\delta = \omega_d - \omega_q$ being the detuning between the drive and the qubit angular frequency, respectively. Let us fix the phase ϕ_d to be equal to 0; then, from Eq. (2.52), we can derive the Bloch equations for a detuned Rabi drive along the σ_y axis, as follows:

$$\begin{cases} \dot{x} = -\Omega z + \delta y - \Gamma_2 x \\ \dot{y} = -\delta x - \Gamma_2 y \\ \dot{z} = \Omega x - \Gamma_1(1 + z) \end{cases}. \tag{2.53}$$

The above equations contain three dynamics: a rotation around the z axis at the angular frequency δ due to the detuning, a rotation around the $-y$ axis at the Rabi angular frequency Ω due to the coherent drive (also called the Rabi drive), and a dissipation at a rate Γ_2 and Γ_1. Due to the dissipation, the state of the qubit will converge toward a steady state that is defined by the Bloch vector coordinates

$$\begin{cases} x_\infty(\Omega, \delta) = \dfrac{\Gamma_1\Gamma_2\Omega}{\Gamma_1(\Gamma_2^2 + \delta^2) + \Gamma_2\Omega^2} \\ y_\infty(\Omega, \delta) = -\dfrac{\Gamma_1\delta\Omega}{\Gamma_1(\Gamma_2^2 + \delta^2) + \Gamma_2\Omega^2} \\ z_\infty(\Omega, \delta) = -1 + \dfrac{\Gamma_2\Omega^2}{\Gamma_1(\Gamma_2^2 + \delta^2) + \Gamma_2\Omega^2} \end{cases}. \tag{2.54}$$

Fig. 2.7 shows the dependence of the steady-state Bloch vector coordinates on the Rabi angular frequency Ω when the drive is resonant $\delta = 0$ and there is no pure dephasing $\Gamma_\varphi = 0$. When the drive strength Ω is small compared to the dissipation rate Γ_1, the qubit relaxes towards $|g\rangle$ faster than it is excited. Thus, the steady state is close to $|g\rangle$. When Ω is of the same order as Γ_1 (i. e. the drive and the dissipation are of the same strength), the qubit steady state is closer to the Bloch sphere center

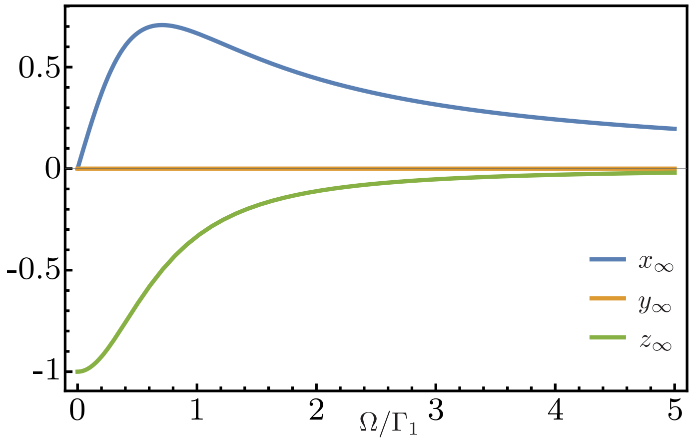

Figure 2.7: Bloch vector coordinates of the qubit steady state a a function of the ratio between the drive strength Ω and the dissipation strength Γ_1. The drive is resonant (i. e. $\delta = 0$) and we assume no pure dephasing (i. e. $\Gamma_\varphi = 0$).

and contains coherences between $|g\rangle$ and $|e\rangle$ (i. e. $x_\infty \neq 0$). This is remarkable, as the stabilization of coherences through the conjugate action of drive and dissipation is not straightforward. The highest coherences are reached for $\Omega = \Gamma_1/\sqrt{2}$ and are equal to $\max(x_\infty) = 1/\sqrt{2}$. When the drive becomes stronger than the dissipation, the qubit state converges towards the center of the Bloch sphere, the most entropic state. In this case, the conjugate action of the drive and the dissipation blurs any information about the qubit state.

If the drive is detuned by δ, the steady state changes; specifically, the qubit gains coherence along the y axis. As the detuning entails a rotation around the z axis of the Bloch vector, we have to compare it to the decay rate in the xy plane, which is given by Γ_2. When the detuning δ is large compared to the decoherence rate Γ_2, the qubit steady state stays close to $|g\rangle$, and the drive has no effect. In this situation, the fast rotation around the z axis due to the detuning δ quickly transforms a Bloch vector with a positive x coordinate into a Bloch vector with a negative x coordinate. The effect of the coherent drive is thus quickly transformed from an excitation into a de-excitation. When the detuning δ is of the same order as Γ_2, the qubit steady state is inside the Bloch sphere (i. e. it is not a pure state) and has some coherence (i. e. $\sqrt{x_\infty^2 + y_\infty^2} \neq 0$). The coherences along the y axis have the same sign as the detuning and, when δ is small enough, they are proportional to δ.

More generally, if the pure dephasing rate Γ_φ is not negligible the coherences of the steady state are smaller. One can show that the maximum coherence is

$$\max\left(\sqrt{x_\infty^2 + y_\infty^2}\ \right) = \frac{1}{2}\sqrt{\frac{\Gamma_1}{\Gamma_2}}; \tag{2.55}$$

which is reachable as long as $\Omega \geq \sqrt{\Gamma_1\Gamma_2}$ with the detuning $\delta_{\max} = \pm\Gamma_2\sqrt{\frac{\Omega^2}{\Gamma_1\Gamma_2} - 1}$.

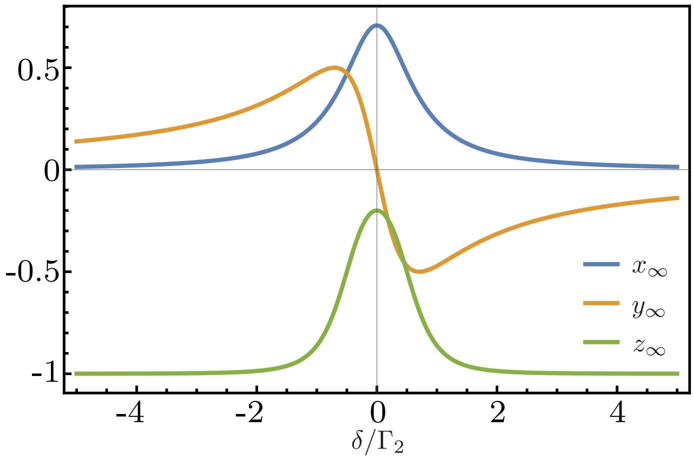

Figure 2.8: Bloch vector coordinates of the qubit steady state driven by a coherent drive as a function of δ/Γ_2 (the ratio between the detuning and the decoherence rate). The drive strength is fixed to $\Gamma_1/\sqrt{2}$, and no pure dephasing is taken into account.

Let us now study the dynamics of the Bloch vector (see Eq. (2.53)). We will assume a resonant drive (i. e. $\delta = 0$) and an initial state described by the Bloch vector $\vec{u}_\rho(t = 0) = \{0, 0, z_0\}$. The solution to the Bloch equations (2.53) is

$$\begin{cases} x(t) = x_\infty(\Omega,0) - \left(\dfrac{\Omega z_0 - \Gamma_R x_\infty(\Omega,0)}{\nu_R} \sin(\nu_R t) + x_\infty(\Omega,0)\cos(\nu_R t) \right) \mathrm{e}^{-\Gamma_R t} \\ y(t) = 0 \\ z(t) = z_\infty(\Omega,0) + \Big((z_0 - z_\infty(\Omega,0))\cos(\nu_R t) \\ \qquad + \dfrac{(\Gamma_R - \Gamma_1) z_0 - \Gamma_R z_\infty(\Omega,0) - \Gamma_1}{\nu_R} \sin(\nu_R t) \Big) \mathrm{e}^{-\Gamma_R t} \end{cases}, \tag{2.56}$$

where $\Gamma_R = \dfrac{\Gamma_1 + \Gamma_2}{2}$ is the Rabi decay rate and $\nu_R = \sqrt{\Omega^2 - \dfrac{(\Gamma_1 - \Gamma_2)^2}{4}}$ is the damped Rabi frequency. Note that these equations are only valid for $\Omega > |\Gamma_1 - \Gamma_2|/2$; i. e. for a strong-enough coherent drive. The system dynamics are not easy to analyze; however, we can observe the cosine and sine evolution at an effective frequency and the exponential decay characteristics of a driven-dissipative system. This becomes easier when the drive is stronger than the dissipation, i. e. $\Omega \gg \Gamma_1,\ \Gamma_2$, as then

$$\begin{cases} x(t) = -z_0 \sin(\Omega t)\mathrm{e}^{-\Gamma_R t} \\ y(t) = 0 \\ z(t) = z_0 \cos(\Omega t)\mathrm{e}^{-\Gamma_R t} \end{cases}. \tag{2.57}$$

The Bloch vector turns around the y axis and the two observables x and z oscillate in phase quadrature. If we apply the coherent drive during a time $t_\pi = \pi/\Omega$ much smaller than $1/\Gamma_R$, then the Bloch vector turns around the y axis at an angle π. This is called a π-pulse; it allows the qubit state to go from $|g\rangle$ to $|e\rangle$ deterministically. In the same way, if the drive is applied during a time $t_{\pi/2} = \pi/(2\Omega)$ (still much smaller than $1/\Gamma_R$),

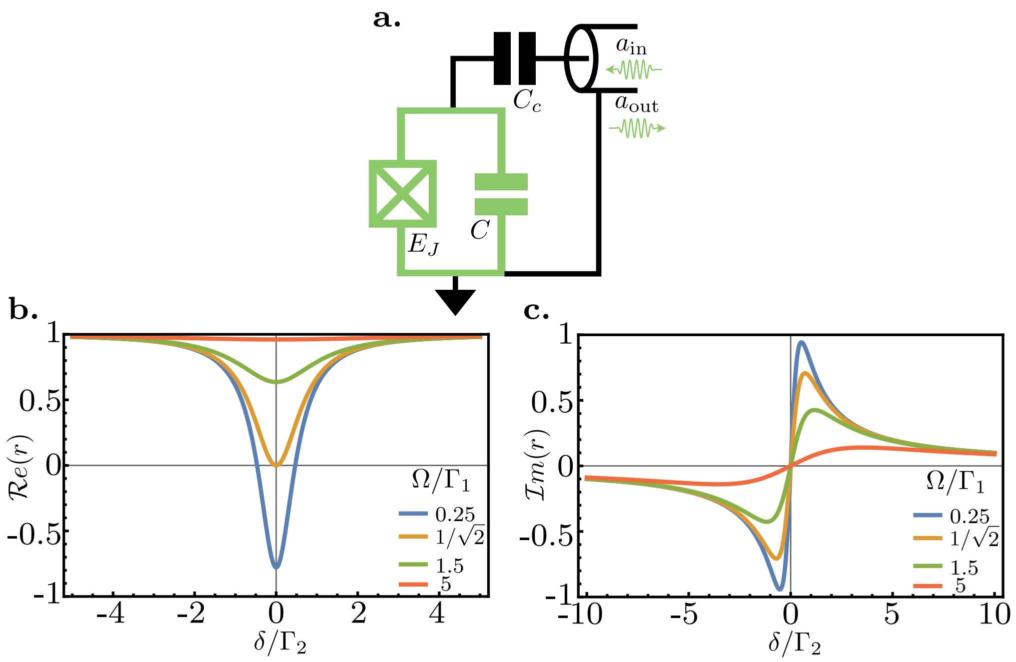

Figure 2.9: **a**. Equivalent electrical circuit of a transmon qubit capacitively coupled to a transmission line. **b and c**. Real and imaginary parts of the reflection coefficient for a strong coupling between the qubit and the transmission line, with no dephasing (i. e., $\Gamma_c = \Gamma_1 = 2\Gamma_2$). The reflection is coefficient depends on the drive strength Ω. Note that the reflection vanishes on resonance for $\Omega = \Gamma_1/\sqrt{2}$ when the steady state coherences are maximal. The imaginary part shows a width broader than the real part (be careful, the x axes are different) as the qubit steady state shows greater coherences for the out-of-phase quadrature when the detuning δ becomes larger.

then we perform a $\pi/2$-pulse, and if the qubit starts at $|g\rangle$, it finishes at $(|g\rangle + |e\rangle)/\sqrt{2}$. More generally, when $\Omega \gg \Gamma_1,\ \Gamma_2$, we can prepare any pure state by starting from $|g\rangle$.

If the strength of the drive is smaller than the dissipation (i. e. $\Omega < |\Gamma_1 - \Gamma_2|/2$) the system shows an over-damped dynamic; that is, there are no oscillations and the state converges exponentially towards the steady state at a rate $\Gamma_R - \sqrt{(\Gamma_1 - \Gamma_2)^2/4 - \Omega^2}$ for $z(t)$ and $\Gamma_R \pm \sqrt{(\Gamma_1 - \Gamma_2)^2/4 - \Omega^2}$ for $x(t)$.

2.4.3 *Fluorescence*

In most cases, a qubit is not driven long enough to reach the steady state; however, this is not the case in this thesis, as we probe the qubit resonant fluorescence (see Chap. 6) [13]. In this case, we will focus on a coupling between the qubit and a transmission line that is so large that the steady state is reached well before the measurement is over (see Fig. 2.9a). The goal of this strong coupling is to ensure that any photons emitted by the qubit will be caught by the measurement transmission line. We can

---

[13] This electromagnetic field is called fluorescence, because it is the same as that emitted by an atom driven by a coherent drive.

write an input–output relationship between the qubit and the propagating mode of the transmission line [62]

$$a_{\text{out}} = a_{\text{in}} - \sqrt{\Gamma_c}\sigma_-, \tag{2.58}$$

where Γ_c is the coupling rate between the qubit and the transmission line[14]. The mean output field depends on the mean value of the annihilation qubit operator $\langle\sigma_-\rangle$. Taking the average value in Eq. (2.58), when we apply a coherent drive detuned by δ, we obtain

$$\alpha_{\text{out}} = \alpha_{\text{in}} - \sqrt{\Gamma_c}\langle\sigma_-\rangle(\alpha_{\text{in}}, \delta) = \alpha_{\text{in}}\left(1 - \frac{2\Gamma_c}{\Omega}\langle\sigma_-\rangle(\Omega, \delta)\mathrm{e}^{i\phi_d}\right), \tag{2.59}$$

where $\langle\sigma_-\rangle$ depends on δ and Ω in a non-linear manner. Let us now consider a drive phase ϕ_d, which is equal to 0 for the coherent drive. Once the steady state is reached, Eq. (2.59) becomes

$$\alpha_{\text{out}} = r(\Omega, \delta)\alpha_{\text{in}}, \tag{2.60}$$

with $r(\Omega, \delta)$ the reflection coefficient

$$r = 1 - \Gamma_c \frac{\Gamma_1(\Gamma_2 - i\delta)}{\Gamma_1(\Gamma_2^2 + \delta^2) + \Gamma_2\Omega^2}. \tag{2.61}$$

The reflected coefficient r shows both a real and an imaginary part; they contribute to the in-phase and out-of-phase quadratures, respectively[15], of the signal α_{out} (see Fig. 2.9b and c). With no detuning, the emission of the qubit is always in an opposite phase compared to α_{in}, leading to a decrease in the in-phase amplitude of α_{out}. When there is a detuning, the qubit emission can also be in phase quadrature with α_{in}, leading to a non-zero out-of-phase amplitude in α_{out}. Note that the reflected coefficient depends on the drive strength Ω; this is a signature of the non-linearity of the qubit. More precisely, r tends towards 1, when Ω increases.

This behavior can be easily understood: the signal emitted by a qubit is always around one photon per $\min(1/\Gamma_1, 1/\Omega)$, as it can only store one photon and needs a time $1/\Gamma_1$ to emit it by spontaneous emission and $1/\Omega$ to emit it by stimulated emission. In comparison, the photon flow of the drive is not bounded, growing as Ω^2/Γ_1. When Ω is large compared to Γ_1, the number of photons per $1/\Omega$ in the drive becomes large compared to 1 and the photon that is absorbed and emitted by the qubit becomes "invisible" in the large flow. At this point, the qubit signal becomes undetectable in the flow of photons and everything happens as if the input drive was completely reflected by the qubit.

The opposite situation occurs when Ω is small compared to Γ_1, in which case the number of photons per unit of $1/\Gamma_1$ in the drive is around or smaller than 1 and the

---

[14] Note that Γ_c is also called the Purcell rate. When the qubit and the transmission line are not directly coupled but the qubit is hybridized with another mode that is coupled to the transmission line, then the coupling rate Γ_c comes from the Purcell effect; we can call this the "Purcell rate." However, this name should not be used if the qubit is directly coupled to the transmission line (see Sec. 3.3 for more details about the Purcell effect).

[15] The expressions "in-phase" and "out-of-phase" refer to the phase of the input drive α_{in}.

photon absorbed and emitted by the qubit is a significant contribution to the signal. This leads to a reflected coefficient that converges towards -1 at resonance when Ω tends towards 0.

The non-linear behavior of a qubit resonant fluorescence does not stop at this dependence on the drive strength Ω. As we will discuss in Sec. 7.3, the qubit resonant fluorescence contains a inelastic part which leads to the well known Mollow triplet [67, 68].

If the qubit temperature is not negligible, then we need to multiply the second term of Eq.(2.61) by p_g the probability to be in the ground state $|g\rangle$. We can write the reflected coefficient as

$$r = 1 - p\frac{\left(1 - i\dfrac{\delta}{\Gamma_2}\right)}{\dfrac{\Gamma_2}{\Gamma_1}\left(1+\left(\dfrac{\delta}{\Gamma_2}\right)^2\right)+\left(\dfrac{\Omega}{\Gamma_1}\right)^2}, \tag{2.62}$$

with $p = p_g\Gamma_c/\Gamma_1$. The following form shows we cannot distinguish the thermal population p_g from the *branching ratio* Γ_c/Γ_1. To measure Γ_c, we either need to measure the thermal population p_g with another experiment, or use two ports and two coherent drives, as detailed in Ref. [38].

Now that we have discussed the open quantum systems that are made up of resonators or qubits, we need to look at the bipartite system, which is made up of a resonator that is capacitively coupled to a transmon qubit.

2.5 DISPERSIVE COUPLING

The coupling between a transmon qubit and a resonator is relatively simple to derive in comparison to other qubits such as the fluxonium [69]. As the phase φ of the transmon qubit is located around 0, the cosine non-linearities can be Taylor expanded (see Eq. (2.11)). As the non-linearities are of the order of E_c, they can be treated as a perturbation. To compare, it is not possible to utilize a perturbative approach in the case of the fluxonium. In such circuits, the full Hamiltonian must be diagonalized in order to ascertain coupling.

2.5.1 *The exchange interaction*

The transmon qubit requires a large capacitor to shunt the JJ and reach the transmon regime. As a consequence coupling the transmon to another resonator presents no major hurdle. The capacitor C_g shown in Fig. 2.10 couples the charge of the transmon mode to the resonator charge. With regard to the transmon, this process is comparable to a charge offset on one of the superconducting islands. The Hamiltonian of the system can then be written as[70]

$$H_{\mathrm{q,r}} = 4E_C(n + \frac{C_g}{2eC_r}Q_r)^2 - E_J\cos(\varphi) + \hbar\omega_r a^\dagger a \tag{2.63}$$

with Q_r as the charge operator of the resonator. Two assumptions must be made to obtain the Hamiltonian. First, it should be assumed that the coupling capacitance C_g

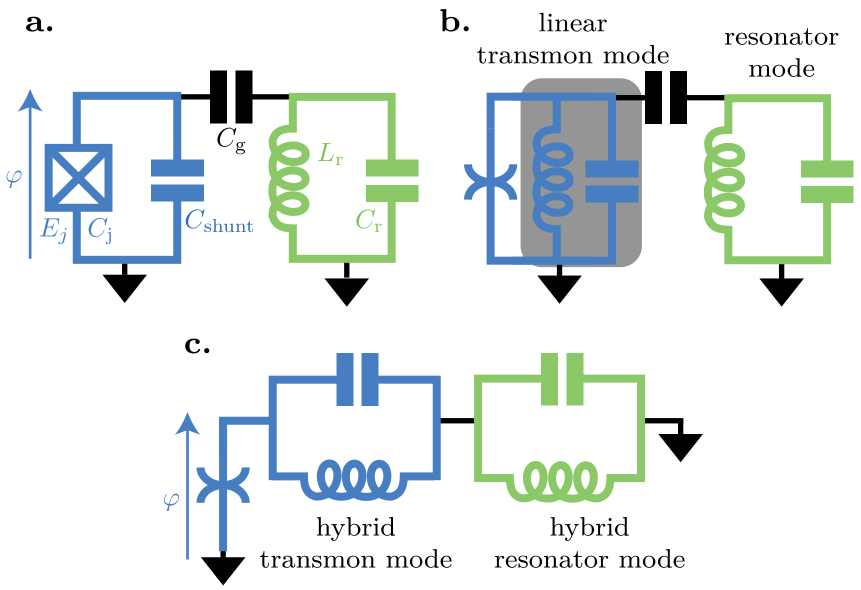

Figure 2.10: Equivalent circuit of a transmon qubit coupled to a resonator. **a**. Capacitive coupling between the transmon and the resonator. C_g is the coupling capacitor. **b**. The non-linear part of the transmon mode can be separated from the linear part. **c**. The mode corresponding to the linear part of the transmon and the resonator hybridize together due to capacitive coupling and form two hybrid modes. Without a non-linear element, the two hybrid modes can be decoupled. As both contribute to the junction phase φ they are dressed by the junction non-linearity. It produces an anharmonic mode, the transmon mode, and an almost linear mode, the resonator, owing to the dispersive coupling.

is smaller than the capacitances of the transmon and resonator, $C_J + C_\mathrm{shunt}$ and C_r, respectively. A derivation beyond this approximation can be found in [62]. Second, as an actual resonator contains an infinite number of modes (see Sec. 2.1.1), it should be assumed that the detuning between the transmon mode and the fundamental mode of the resonator is small compared to the detuning between the transmon mode and all other modes. In this case the transmon is only coupled to the fundamental mode of the resonator. As such, the multimodal nature of the resonator can be disregarded[16]. Since the transmon mode, has a phase φ whose zero-point-fluctuations are much smaller than π, it is, therefore, possible to truncate the cosine to its fourth order expansion and diagonalize its linear part (see Eq. (2.11)). This is equivalent to studying the circuit shown in Fig. 2.10b. The Hamiltonian reads

$$H_{q,r} \approx \hbar\omega_q b^\dagger b + \hbar\omega_r' a^\dagger a - \frac{E_C}{2} b^\dagger b^\dagger b b - \hbar g (b^\dagger - b)(a^\dagger - a), \tag{2.64}$$

where b is the annihilation operator of the transmon mode, ω_r' is the renormalized frequency of the resonator due to the capacitor C_g, and g is the coupling rate between the transmon and the qubit (or between matter and light):

$$g = \frac{\omega_r C_g}{C_\mathrm{shunt} + C_J} \left(\frac{E_J}{E_C}\right)^{\frac{1}{4}} \sqrt{\frac{\pi Z_r}{R_K}}, \tag{2.65}$$

---

[16] The multimodal nature of the resonator cannot always be disregarded. For example, see the Purcell effect, which is described in Sec. 3.3

Here, Z_r is the impedance of the resonator and $R_K = h/e^2 \sim 25.8\,\mathrm{k}\Omega$ is the resistance quantum. The third term of Eq. (2.64) is the non-linear term of the transmon mode. E_C is also referred to as the anharmonicity as it generates it. If the coupling rate is small compared to the resonant angular frequencies, $g \ll \omega_q,\ \omega_r$, an RWA can be used.

$$H_{q,r;\mathrm{RWA}} = \hbar\omega_q b^\dagger b + \hbar\omega_r' a^\dagger a - \frac{E_C}{2} b^\dagger b^\dagger b b + \hbar g (b^\dagger a + b a^\dagger). \tag{2.66}$$

The interaction between the transmon and the qubit is an exchange interaction as it allows excitation to be swapped between the two. Let us analyze the coupling rate g. In order to derive Eq. (2.63), it was assumed that C_g was smaller than $C_J + C_{\mathrm{shunt}}$. As a consequence, the first prefactor in the expression (2.65) of g is small in comparison to ω_r. Even if it assumed that C_g was small compared to $C_J + C_{\mathrm{shunt}}$ to derive Eq. (2.66), we still want to be in the strong coupling regime, meaning $g \gg \Gamma_1,\ \kappa_{\mathrm{tot}}$. This can be achieved as g is proportional to $(E_J/E_C)^{1/4}$ and within the transmon regime that imposes $E_J > 30E_C$. The further into the transmon regime, the larger g becomes. However, the relative anharmonicity of the qubit $E_C/\omega_q = \sqrt{E_C/8E_J}$ decreases with (E_J/E_C). In addition, increasing g occurs at the expense of the qubit anharmonicity. In practice, a coupling rate of a few 100 MHz can be achieved with anharmonicity of a few 100 MHz. It can be observed that g depends on the impedance of the resonator. For example, a large impedance obtained using an array of junctions [71, 72], is an effective way to increase the coupling rate g.

In practice, how does this model apply to a transmon coupled to a 3D cavity (see Fig. 2.4)? With a 3D circuit, the electromagnetic cavity field is diluted in a larger volume and the coupling g is smaller. Despite these constraints, a strong coupling regime is still reachable. The zero-point fluctuation of the charge on the transmon capacitance is $Q_{\mathrm{ZPF}} = 2e(E_J/E_C)^{1/4}$. The transmon can thus be modeled as a dipole with a charge Q_{ZPF} and a length l_q. In addition, the zero-point fluctuation of the cavity's electrical field seen by the transmon dipole is given by $\mathcal{E}_{\mathrm{ZPF}} = \frac{\omega_r}{l_q} \frac{C_g}{C_J + C_{\mathrm{shunt}}} \sqrt{\frac{\hbar Z}{2}}$. The coupling g can, therefore, be viewed as a dipolar interaction $l_q Q_{\mathrm{ZPF}} \mathcal{E}_{\mathrm{ZPF}}$ between the transmon charge and the cavity's electrical field. In the case of a 3D circuit, increasing the length of the superconducting islands of the transmon gives it the shape of an antenna and increases the dipolar interaction and the coupling rate g.

It is interesting to note that if only the first two levels of the transmon mode are considered, the Hamiltonian of Eq. (2.66) becomes the well known Jaynes-Cummings Hamiltonian.

$$H_{\mathrm{JC}} = \hbar\omega_q \frac{\sigma_z}{2} + \hbar\omega_r a^\dagger a + g(a\sigma_+ + a^\dagger \sigma_-). \tag{2.67}$$

Describing the system with Jaynes-Cummings Hamiltonian can, in some cases, be useful (see Sec. 7.3). However, in most cases it is inaccurate. Indeed, to derive the effects of an exchange interaction and the non-linearity of the junction, the multi-level nature of the transmon mode must be taken into account.

2.5.2 *Dispersive regime*

In most cases, circuit QED experiments are designed to operate in the *dispersive* regime. This regime is characterized by a detuning $\Delta = \omega_q - \omega_r$ which is large compared to the coupling rate g (i. e., $g \ll \Delta$). As the charging energy E_C is assumed to be small compared to the angular resonant frequencies ω_q and ω_r, the Hamiltonian of Eq. (2.66) can be split into a linear term H_{L} and a non-linear term H_{NL}

$$\begin{cases} H_{\mathrm{L}} = \hbar\omega_q b^\dagger b + \hbar\omega_r' a^\dagger a + \hbar g(b^\dagger a + b a^\dagger) \\ H_{\mathrm{NL}} = -\dfrac{E_C}{2} b^\dagger b^\dagger b b \end{cases} \tag{2.68}$$

It is then possible to diagonalize the linear term using the dispersive assumption and treat the non-linear term as a perturbation. When the small parameter in the perturbation is defined as $\lambda = g/\Delta \ll 1$, the linear Hamiltonian H_{L} can be diagonalized using a Bogoliubov transformation [62]

$$U_{\mathrm{disp}} = e^{\Lambda(ab^\dagger - a^\dagger b)}, \tag{2.69}$$

where $\Lambda = \arctan(2\lambda)/2$. This is the same unitary evolution as for a beam splitter. This Bogoliubov transformation mixes, or hydridizes, the two linear modes. The linear hydrid modes $\tilde{b}$ of the transmon and $\tilde{a}$ of the resonator obtained after this transformation are

$$\begin{cases} U_{\mathrm{disp}}^\dagger b U_{\mathrm{disp}} = \cos(\Lambda) b - \sin(\Lambda) a \approx b - \lambda a \\ U_{\mathrm{disp}}^\dagger a U_{\mathrm{disp}} = \cos(\Lambda) a + \sin(\Lambda) b \approx a + \lambda b \end{cases}, \tag{2.70}$$

where the approximation is derived using $\lambda \ll 1$. As such, the Hamiltonian of the system transforms into

$$H_{\mathrm{L,disp}} = U_{\mathrm{disp}}^\dagger H_{\mathrm{L}} U_{\mathrm{disp}} = \hbar\tilde{\omega}_q \tilde{b}^\dagger \tilde{b} \ + \hbar\tilde{\omega}_r \tilde{a}^\dagger \tilde{a}, \tag{2.71}$$

with the dressed frequencies

$$\begin{cases} \tilde{\omega}_q = \dfrac{1}{2}\left(\omega_q + \omega_r + \sqrt{\Delta^2 + 4g^2}\ \right) \\ \tilde{\omega}_r = \dfrac{1}{2}\left(\omega_q + \omega_r - \sqrt{\Delta^2 + 4g^2}\ \right) \end{cases}. \tag{2.72}$$

The tilde symbols denote that the annihilation operators $\tilde{a}$ and $\tilde{b}$ now describe hybrid modes given by Eq. (2.70). At this stage, it can be observed that the two hybrid modes are no longer coupled. This result is consistent with any linear Hamiltonian with a linear coupling that can be diagonalized as this leads to uncoupled hybrid modes. The non-linear Hamiltonian part acts on both hybrid modes (see Fig. 2.10c). The full Hamiltonian after the Bogoliubov transformation reads

$$H_{\mathrm{disp}} = \ U_{\mathrm{disp}}^\dagger H_{q,r;\mathrm{RWA}} U_{\mathrm{disp}} \approx \hbar\tilde{\omega}_q \tilde{b}^\dagger \tilde{b} + \hbar\tilde{\omega}_r \tilde{a}^\dagger \tilde{a} - \hbar\frac{\chi_{qq}}{2} \tilde{b}^\dagger \tilde{b}^\dagger \tilde{b}\tilde{b} - \hbar\frac{\chi_{rr}}{2} \tilde{a}^\dagger \tilde{a}^\dagger \tilde{a}\tilde{a} - \hbar\chi_{qr} \tilde{b}^\dagger \tilde{b} \tilde{a}^\dagger \tilde{a}, \tag{2.73}$$

where the last expression is an expansion in orders of λ and only terms conserving the number of excitations in each hybrid mode are kept. The junction non-linearity leads to three non-linear terms: χ_{qq}, χ_{rr} and χ_{qr}

$$\begin{aligned} \chi_{qq} &\approx E_C/\hbar \\ \chi_{rr} &\approx \frac{E_C}{\hbar}\left(\frac{g}{\Delta}\right)^4 \\ \chi_{qr} &\approx \frac{2E_C}{\hbar}\frac{g^2}{\Delta(\Delta - E_C/\hbar)} \end{aligned} . \tag{2.74}$$

The anharmonicity, or *self-Kerr*, of the hybrid transmon mode is given by χ_{qq}. As the hybridization between the bare linear modes is small, the hybrid transmon mode inherits almost all the junction non-linearity. In addition, the anharmonicity of the hybrid transmon mode is almost the same as the bare transmon mode. The two final non-linear terms of Eq. (2.73) appear due to the hybridization that occurs throughout this process. The anharmonicity of the hybrid resonator mode is given by χ_{rr}. It is of the order of λ^4 and can be viewed as a weak non-linearity. Using few photons only, the hybrid resonator mode can still be considered as a linear mode. The final non-linear term represents a coupling between the hybrid transmon and resonator modes. This coupling, known as *dispersive* coupling, shifts the hybrid transmon mode resonant frequency by the cross-Kerr rate χ_{qr} for each photon in the hybrid resonator mode and vice versa. Taking into account the first two states of the hybrid transmon mode, which define the transmon qubit, and small number of photons in the resonator, the Hamiltonian (2.73) becomes

$$H_{\text{disp}} \approx \hbar(\tilde{\omega}_r - \frac{\chi_{qr}}{2})\tilde{a}^\dagger\tilde{a} + \hbar\tilde{\omega}_q\frac{\sigma_z}{2} - \hbar\chi_{qr}\tilde{a}^\dagger\tilde{a}\frac{\sigma_z}{2}. \tag{2.75}$$

Through examining the expression of χ_{qr} in Eqs. (2.74), it is possible to observe a regime defined by $0 < \Delta < E_C/\hbar$. This is known as the straddling regime, in which the cross-Kerr rate sign changes. It is qualitatively different from the usual dispersive regime. In most instances, the straddling regime is avoided and can be better described by an exact diagonalization of the Eq. (2.64) Hamiltonian.

It should be noted that the hybrid modes can be probed using experimental methods. In contrast, bare modes are usually inaccessible, meaning only the parameters of the hybrid modes can be measured. For the remainder of this thesis, and as customary in the literature, the hybrid transmon mode discussed here is simply referred as the transmon mode and the uncoupled mode is referred to as the bare mode.

The dispersive regime is remarkable for two reasons. First, the coupling can be designed to be in the *number-resolved* regime [21] defined by a cross-Kerr rate χ_{qr} bigger than the relaxation and decoherence rate of the modes. This regime enables one to control the qubit conditionally to the resonator state. For example, a π-pulse can be performed on the qubit that is resonant only when there are 0 photons in the resonator. Second, the dispersive coupling enables dispersive readout to be performed on the transmon. Indeed, when a resonator is dispersively coupled to a transmon qubit, probing the resonator with a coherent drive close to resonance leads to a coherent state that depends on the transmon qubit state.

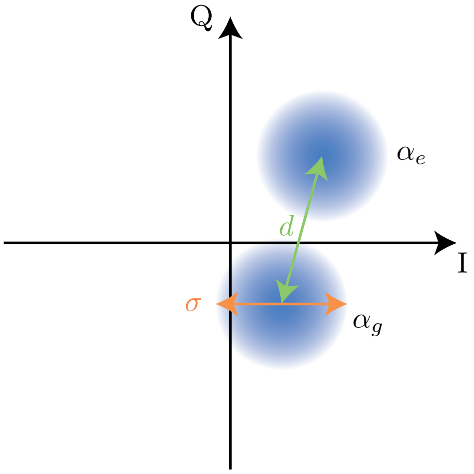

Figure 2.11: Distribution of the heterodyne detection of the $\alpha_{out,1}$ amplitude. The I and Q axes are the real and imaginary parts of $\alpha_{out,1}\sqrt{\kappa_1}$, respectively. For simplicity, we shifted the phase space by $-\alpha_{\rm in}\sqrt{\kappa_1}$.

2.5.3 *Dispersive readout*

We denote $\alpha_g(t)$ and $\alpha_e(t)$ the amplitudes of the driven resonator coherent states for the qubit states $|g\rangle$ and $|e\rangle$, respectively. For a coherent drive $\alpha_{\rm in}$ longer than a few $1/\kappa_{\rm tot}$ but much smaller than $1/\Gamma_1$, the amplitudes $\alpha_g(t)$ and $\alpha_e(t)$ tend towards (see Eq. (2.42)):

$$\begin{cases} \alpha_{g,\rm ss} = \dfrac{2\sqrt{\kappa_1}\alpha_{\rm in}}{\kappa_{\rm tot} - 2i\Delta} \\ \alpha_{e,\rm ss} = \dfrac{2\sqrt{\kappa_1}\alpha_{\rm in}}{\kappa_{\rm tot} - 2i(\Delta + \chi_{qr})} \end{cases}, \tag{2.76}$$

where $\Delta = \omega - \omega_r$ and ω is the frequency of the coherent drive $\alpha_{\rm in}$ and where the relaxation of the qubit was neglected. Thus, the output field of the resonator transmission line depends on the qubit state through the input–output relation in Eqs. (2.33) and (2.76). Using heterodyne or homodyne detection setup (see Sec. 4.3), we can measure the amplitude of the output field[17] $\alpha_{\rm out,1} = \alpha_{\rm in} - \sqrt{\kappa_1}\alpha_{g/e}$ and deduce from the value of the amplitude $\alpha_{\rm out,1}$ the state of the qubit if the noise is small enough (see below).

The dispersive readout (or measurement) of a qubit consists in the heterodyne detection of the output field of a resonator that is coupled dispersively to the qubit. This measurement is intrinsically noisy (see Chap. 4 for a detailed discussion about the noise in quantum measurement), and we denote σ, the standard deviation of the measured amplitude. Fig. 2.11 shows the distribution of the measurements outcomes; it contains two “blobs” of mean value α_g and α_e, and width σ. The distance between the two blobs is denoted as $d = |\alpha_g - \alpha_e|$.

We can define a signal-to-noise ratio (SNR) for the dispersive measurement as

$$\mathrm{SNR} = \frac{d^2}{\sigma^2}, \tag{2.77}$$

---

[17] Here, we consider a measurement of the field reflected by the cavity; the same discussion is valid for the measurement of the transmitted field.

and it has been shown that the SNR of a heterodyne detection can be expressed as [73, 74]

$$\mathrm{SNR} = 4\eta\Gamma_d T_m, \tag{2.78}$$

where η is the quantum efficiency (see Sec. 4.1.2), Γ_d is the *measurement-induced dephasing* rate, and T_m is the measurement integration time. Thus, maximizing the SNR is equivalent to maximizing the measurement-induced dephasing rate Γ_d. The name Γ_d comes from the fact that the qubit pure dephasing increases by Γ_d during the dispersive measurement process. This effect can be viewed as a back-action of the measurement: the dispersive measurement extracts information about the qubit photon number; thus, the conjugate variable, here the phase, must diffuse [8]. This increase of the dephasing also can be viewed as the photon shot noise resulting from the photon distribution of the resonator coherent state during the measurement, which is converted by the dispersive interaction into qubit frequency noise.

The measurement-induced dephasing is not the only effect the dispersive measurement has on the qubit. The average population of the resonator during the measurement shifts the frequency of the qubit; this effect is known as the *AC Stark shift* [75]. These two effects can be derived when eliminating the resonator adiabatically (see Sec. 6.3.4.2 for more information about adiabatic elimination). This leads to an effective Lindblad master equation for the qubit reading [75]:

$$\dot{\rho} = \frac{-i}{\hbar}\left[\hbar(\omega_q - \omega_{AC})\frac{\sigma_z}{2}, \rho\right] + \Gamma_1\mathcal{D}(\sigma_-)\rho + \frac{\Gamma_\varphi + \Gamma_d}{2}\mathcal{D}(\sigma_z)\rho, \tag{2.79}$$

where the AC Stark shift frequency ω_{AC} and the measurement-induced dephasing rate Γ_d read

$$\begin{cases} \Gamma_d = \chi_{qr}\mathcal{I}m(\alpha_g^*\alpha_e) \\ \omega_{AC} = \chi_{qr}\mathcal{R}e(\alpha_g^*\alpha_e) \end{cases}. \tag{2.80}$$

Γ_d and ω_{AC} are proportional to $|\alpha_{\mathrm{in}}|^2$; Fig. 2.12 shows their dependence on κ_{tot}, χ_{qr}, and Δ. They only depend on the ratios $\chi_{qr}/\kappa_{\mathrm{tot}}$ and Δ/χ_{qr}. In order to maximize the measurement SNR, we will opt to design a system in which the ratio $\chi_{qr}/\kappa_{\mathrm{tot}}$ is equal to or above 1. The optimal frequency for the qubit readout is either the medium frequency $\omega = \omega_r - \chi_{qr}/2$, if χ_{qr} is smaller than or equal to κ_{tot}, or the frequencies $\omega = \omega_r$ and $\omega = \omega_r - \chi_{qr}$, which correspond to the resonator frequency when the qubit is in the states $|g\rangle$ or $|e\rangle$, respectively, if χ_{qr} is significantly greater than κ_{tot}. It is important to note that there is no gain to be had (from a measurement perspective) by increasing χ_{qr} above κ_{tot}.

From a generalized measurement formalism perspective, the dispersive readout can be viewed as follows. The resonator is used as an ancillary system or probe, while the dispersive coupling enables the state of the resonator to be entangled with the qubit state. The transmission line's output field state is then entangled with the resonator state and can be measured using either a homodyne or heterodyne detection (see Sec. 4.3 for more detail). As shown in Sec. 4.1.2.2, a measurement is not always projective. The measurement back-action is dependent on the amount of entanglement between the resonator and the qubit states. If the SNR is smaller than 1, the amount

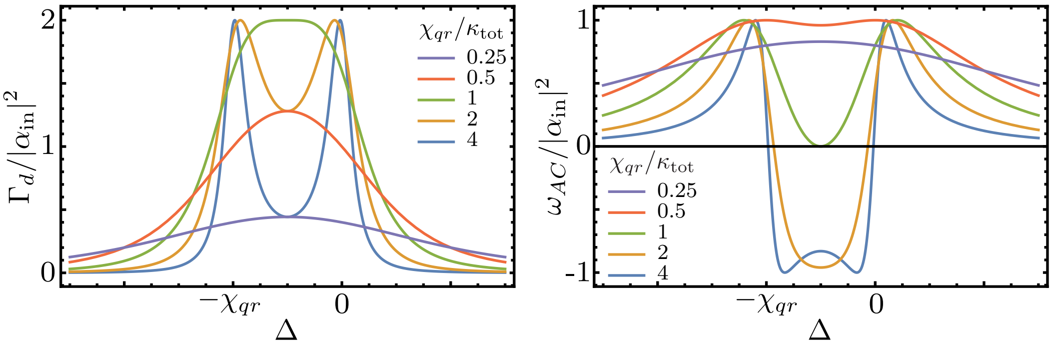

Figure 2.12: Measurement-induced dephasing rate Γ_d and AC Stark shift frequency ω_{AC} divided by the measurement power $|\alpha_{\rm in}|^2$ (in photons per second), as a function of the detuning Δ and various ratios $\chi_{qr}/\kappa_{\rm tot}$. Here, we suppose that the resonator is only coupled to one port and has no losses; i. e. $\kappa_1 = \kappa_{\rm tot}$

of entanglement is much smaller than 1 bit, and the generalized measurement cannot be seen as a projective measurement of the qubit state (Sec. 4.1.2.2 explains the kind of measurement that occurs here). Hopefully, the SNR can be increased by increasing the drive amplitude $\alpha_{\rm in}$. However, the dispersive regime is only valid for photon numbers $|\alpha_g|^2$ and $|\alpha_e|^2$ in the resonator that are smaller than $((\omega_q - \omega_r)/2g)^2$ [70]. Beyond this limit, higher-order non-linear effects appear, such as resonator self-Kerr and qubit ionization [76, 77], and the dispersive readout becomes more complex, with an SNR that could be null.

3

SIMULATION AND FILTERING

A powerful aspect of circuit QED is the wide range of Hamiltonians it is possible to engineer. Theoretical models enable us to make a link between the circuit parameters (e. g. capacitance and inductance) and the Hamiltonian parameters (e. g. coupling rate, frequency, and the Purcell effect); however, we still need a tool with which to simulate the circuit parameters for a particular circuit design. This chapter will discuss simulation based on one of the main finite element simulation software: Ansys high-frequency simulation software (HFSS). It will also describe the energy-participation ratio approach used to compute the Hamiltonian of the system, based on the simulation results. These two tools allow us to "simulate" the design and tune it so that it can reach the targeted Hamiltonian. Specifically, it is possible to simulate both the Purcell effect (a phenomenon that we would usually want to minimize) and the circuit's filters. The first part of this chapter focuses on the simulation and the simulation analysis, while the second part concerns the Purcell effect.

3.1 SIMULATION USING ANSYS HFSS

3.1.1 *Principle*

Ansys HFSS is a piece of software whose purpose is to simulate electromagnetism at high-frequency. It is able to solve Maxwell equations using a finite element method, and allows us to define ports to simulate the system transfer function, thereby giving us access to several electrical engineering tools that characterize the system (such as the S, Z, and ABCD matrices). This is an interesting feature; however, this feature is mostly used to study microwave filters or antenna, not circuits, for which we are more interested in the circuit resonant modes. Ansys HFSS also enables us to directly simulate these modes, allowing access to their frequency and quality factor.

From a circuit QED perspective, the software has several advantages and one significant drawback. The first advantage is that the superconducting layer or bulk does not need to be simulated; we can take this into account just by using a *perfect E* boundary condition[1]. This is a real gain in terms of the speed of the simulation, as it decreases the volume to simulate and removes the difficulty of properly simulating a thin superconducting film. The second advantage is that, once the resonant modes have been simulated, we have access to the electrical and magnetic field in each cell of the mesh, as these have been defined by the system during the simulation process. Thus, we can display the electrical field (as shown in Fig. 3.1), compute the density of the electrical energy, or compute the current in a wire. This information is crucial, as it allows us to tune the coupling rate between two modes, protect a mode from losses, compute

---

[1] This boundary condition mandates that the tangential component of the E field is null on the surface on which the boundary is applied.

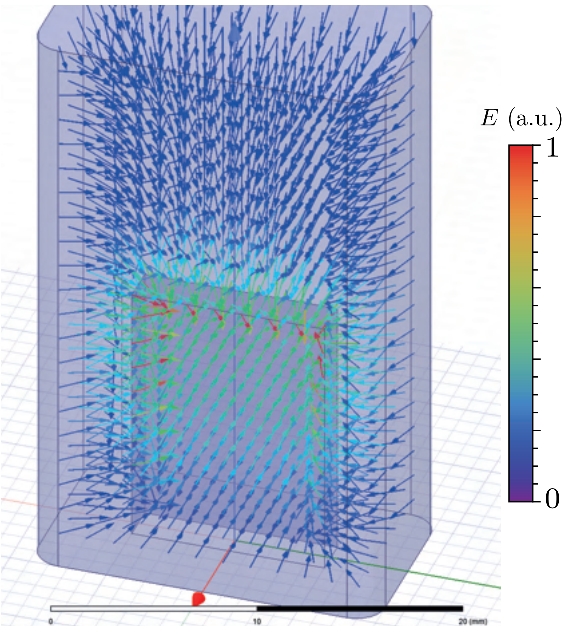

Figure 3.1: The E field belonging to the first mode of a post cavity. Only the vacuum part of the cavity is simulated. The E field vector is pointing towards the summit of the post, where the field norm is maximal. The E field decreases exponentially above the post, which protects the mode against losses located on the top part of the cavity (such as those coming from a seal). In order to couple a transmon qubit to this mode, we have to engineer a dipolar momentum for the transmon going in the same direction as the E field.

which part of the circuit limits the quality factor of a mode, or compute the mutual inductance between a flux line and a SQUID. The disadvantage, however, is that the software only allows us to simulate a linear system, which is not the case of the JJs.

3.1.2 *The black-box quantization approach*

As mentioned above, we cannot simulate a non-linear element using Ansys HFSS software. The solution to this issue that has been found by the circuit QED community is to reproduce the black-box quantization (BBQ) approach used during the simulation. The BBQ approach[78] consists of solving the linear part of the Hamiltonian first, then deriving the effect of the non-linearities (assuming they are small enough to use a perturbation theory). This approach is exactly the same as the one we used to derive the dispersive coupling in Sec. 2.5.2, except that we are now considering a junction in a multi-mode environment. Here, the environment is the cavity or the rest of the circuit.

Let us consider a transmon qubit made of a JJ that is shunted by a capacitor and which has some losses, modeled by a resistance. The transmon is coupled to an arbitrary combination of N distributed linear modes that can be represented by lumped elements (i. e. RLC resonators). We do not need to make any kind of assumptions about the coupling, apart from the fact that it is linear. As the phase Φ and its quantum fluctuation are small compared to π and are centered on 0, the non-linear part of the transmon mode can be isolated. Thus, the non-linearity is coupled to a multi-mode environment

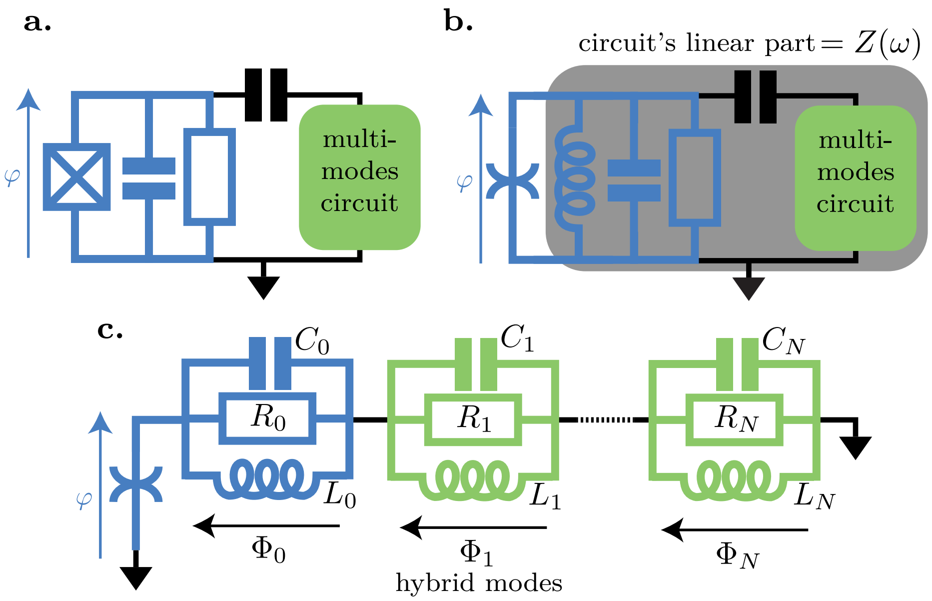

Figure 3.2: **a.** Transmon mode represented by its Josephson junction, the shunting capacitor, and a resistor. The resistor enables to take into account losses. It is coupled to a multi-mode circuit; this can be described as a combination of distributed linear modes, with each of those modes described by a lumped element. **b.** The non-linear part of the transmon mode can be isolated; as such, the non-linearities are coupled to a linear multi-mode environment that is described by the impedance $Z(\omega)$. **c.** The linear part of the circuit can be decomposed using a Foster decomposition of $Z(\omega)$. Thus, the linear part of the circuit is equivalent to $N+1$ hybrid uncoupled linear modes. The phase of the junction $\mathit{\Phi}$ is equal to the sum of all the mode fluxes.

that contains $N+1$ coupled linear modes described by the impedance $Z(\omega)$. Using a Foster decomposition, we can write the impedance as

$$Z(\omega) = \sum_{\mu=0}^{N} \left(-i\omega C_\mu + \frac{1}{-i\omega L_\mu} + \frac{1}{R_\mu} \right)^{-1}. \tag{3.1}$$

Note that more general loss models can be used [79, 80]. We obtain $N+1$ hybrid modes in parallel, where R_μ, C_μ, and L_μ are the resistor, the capacitor, and the inductor of the hybrid mode μ, respectively (see Fig. 3.2b and c). In the regime of weak dissipation (i. e., $R_\mu \gg \sqrt{L_\mu/C_\mu}$), the resonant frequency of the mode μ is given by $\omega_\mu = 1/\sqrt{L_\mu C_\mu}$. The quality factor Q_μ and the impedance Z_μ of each mode can be expressed using the admittance of the linear part $Y(\omega) = 1/Z(\omega)$

$$\begin{aligned} Q_\mu &= \frac{\omega_\mu}{2} \frac{\mathcal{I}m(Y'(\omega_\mu))}{\mathcal{R}e(Y(\omega_\mu))} \\ Z_\mu &= \frac{2}{\omega_\mu \mathcal{I}m(Y'(\omega_\mu)} \end{aligned} . \tag{3.2}$$

These hybrid modes can be described using a quantum annihilation operator a_μ and a flux $\Phi_\mu = \Phi^\mu_{\text{ZPF}}(a_\mu + a^\dagger_\mu)$, with the phase zero-point fluctuation $\Phi^\mu_{\text{ZPF}} = \sqrt{\hbar Z_\mu/2}$. As each hybrid mode is a collective excitation of the circuit, they all participate in the junction phase[2] φ(see Fig. 3.2b). Thus, the effect of the junction's non-linearity can be derived using a perturbation theory and by replacing the phase φ with

$$\varphi = \sum_\mu \frac{\Phi_\mu}{\varphi_0} = \sum_\mu \frac{\Phi^\mu_{\text{ZPF}}}{\varphi_0}(a_\mu + a^\dagger_\mu). \tag{3.3}$$

Taking into account only the fourth-order non-linearity of the junction (i. e. $E_J\varphi^4/24$), as in Sec. 2.5.2, applying a perturbation theory, and keeping only those terms that conserve the number of photons in each mode, the Hamiltonian of the circuit reads as follows:

$$H_{\text{BBQ}} = \sum_\mu \hbar(\omega_\mu + \Delta_\mu)a^\dagger_\mu a_\mu + \frac{1}{2}\sum_{\mu\nu} \chi_{\mu\nu} a^\dagger_\mu a_\mu a^\dagger_\nu a_\nu. \tag{3.4}$$

The frequency Δ_μ is the Lamb-shift effect generated by the non-linearity that occurs due to the interaction between modes; it is equal to $\Delta_\mu = \frac{-e^2}{2L_J}(Z_\mu \sum_\nu Z_\nu - Z^2_\mu/2)$. The rates $\chi_{\mu\mu}$ and $\chi_{\mu\nu}$ are the self-Kerr rate of the mode μ and the cross-Kerr rate between the modes μ and ν, respectively. They read

$$\begin{cases} \chi_{\mu\mu} = -\dfrac{L_\mu}{L_J}\dfrac{C_J + C_{\text{shunt}}}{C_\mu}E_C \\ \chi_{\mu\nu} = -2\sqrt{\chi_{\mu\mu}\chi_{\nu\nu}} \end{cases}. \tag{3.5}$$

A remarkable result emerges from the above equations: the cross-Kerr rate between two modes is given by the geometrical mean of the self-Kerr rate. This implies that, when using only a fourth-order non-linearity, we cannot couple two linear modes in the number-resolved regime. When targeting a given cross-Kerr rate, we have two options. We can have a mode with a strong self-Kerr and another mode with a weak self-Kerr, which is equivalent to a qubit coupled to a linear mode. Alternatively, we can have two modes with two intermediate self-Kerr rates of the order of $\chi_{\mu\nu}/\sqrt{2}$, in which case the self-Kerr rate is of the same order as the relaxation rate. That is, the self-Kerr rate is too large to consider that the mode is linear and too small to use it as a qubit. This is a parameter regime that we usually try to avoid.

It is possible to show [78] that $\frac{L_\mu}{L_J}$ and $\frac{C_J}{C_\mu}$ are always smaller than 1 when the non-linearity comes from a transmon qubit. This leads to the fact that the self-Kerr rates of the modes are always smaller than the anharmonicity of the bare transmon mode.

Before discussing how such an approach can be implemented in a simulation, however, we should note that if we express the self-Kerr and cross-Kerr rates using inductances and capacitances in Eqs. (3.5), the only physical quantity we have to compute is the zero-point fluctuation Φ^μ_{ZPF}, according to Eq. (3.3).

3.1.3 *Energy-participation ratio*

The success of the BBQ approach indicates that we can simulate only the linear part of the circuit in order to obtain the hybrid modes, then measure the zero-point fluctuation

---

[2] In other words, any oscillation of these modes will create an oscillation of the junction phase.

of the phase of each mode to derive the cross-Kerr and self-Kerr rates. The hybrid modes can easily be obtained, as Ansys HFSS can simulate them. In order to simulate only the linear part of the circuit, we replace the junction with an inductor of inductance L_J in the simulation. Then, as described below, the zero-point fluctuation can be computed using the energy-participation ratios [81]. An energy-participation ratio is defined as the percentage of a mode's inductive energy that is stored in the junction

$$p_\mu = \frac{\text{inductive energy stored in the junction by the mode } \mu}{\text{total inductive energy stored in the mode } \mu}. \tag{3.6}$$

The participation ratios can be computed using the simulated modes' electric and magnetic energy. For a resonant mode, the total energy is equally split between inductive E^μ_{ind} and capacitive energy E^μ_{cap}: $E^\mu_{\text{ind}} = E^\mu_{\text{cap}}$. The inductive energy makes two contributions: magnetic energy E^μ_{mag} and kinetic energy E^μ_{kin}. The magnetic energy is stored in the magnetic field, while the kinetic energy is stored in inductive elements such as the inductor of the junction. However, if there are no lumped capacitive elements, the capacitive energy is equal to the electric energy E^μ_{elec}. Thus, we have

$$E^\mu_{\text{elec}} = E^\mu_{\text{cap}} = E^\mu_{\text{ind}} = E^\mu_{\text{mag}} + E^\mu_{\text{kin}}, \tag{3.7}$$

and

$$p_\mu = \frac{E^\mu_{\text{kin}}}{E^\mu_{\text{ind}}} = \frac{E^\mu_{\text{elec}} - E^\mu_{\text{mag}}}{E^\mu_{\text{elec}}}. \tag{3.8}$$

The electric and magnetic energies can both be computed using the complex electric $\underline{\vec{E}}_\nu(\vec{r})$and magnetic $\underline{\vec{B}}(\vec{r})$ fields simulated by Ansys HFSS, as follows:s

$$\begin{aligned} E^\nu_{\text{elec}} &= \frac{1}{4}\mathcal{R}e\left(\int_{\mathcal{V}} \underline{\vec{E}}_\nu(\vec{r})^* \epsilon \underline{\vec{E}}_\nu(\vec{r})\mathrm{d}\vec{r}\right) \\ E^\nu_{\text{mag}} &= \frac{1}{4}\mathcal{R}e\left(\int_{\mathcal{V}} \underline{\vec{B}}_\nu(\vec{r})^* \mu \underline{\vec{B}}_\nu(\vec{r})\mathrm{d}\vec{r}\right) \end{aligned}, \tag{3.9}$$

where ϵ and μ are the electric-permittivity and magnetic-permeability tensors, and $\mathcal{V}$ is the mode volume.

It has been proven that the zero-point fluctuations and energy-participation ratios are linked [81] by

$$(\Phi^\mu_{\text{ZPF}})^2 = p_\mu \frac{\hbar\omega_\mu}{2E_J}. \tag{3.10}$$

Thus, we can replace the zero-point fluctuation with the energy-participation ratio in the BBQ perturbation theory (see Sec. 3.1.2), as follows:

$$\begin{cases} \chi_{\mu\mu} = p_\mu^2 \dfrac{\hbar\omega_\mu^2}{8E_J} \\ \chi_{\mu\nu} = 2\sqrt{\chi_{\mu\mu}\chi_{\nu\nu}} = p_\mu p_\nu \dfrac{\hbar\omega_\mu\omega_\nu}{4E_J} \end{cases}. \tag{3.11}$$

In practice, the participation ratio and the perturbation theory are performed using a Python script called pyEPR, written by Zlatok K. Minev and Zaki Leghtas. This script enables us to deal with more than one junction, to compute the perturbation theory to higher orders, and to apply the same energy-participation ratio approach to losses in order to compute the modes' quality factors (without having to add losses into the simulation). It is necessary to emphasize that this approach is only valid for modes with a quality factor that is much greater than 1, otherwise the electric and magnetic fields are altered too much by the dissipation. Besides, one must avoid lumped capacitors in the simulation otherwise the Eqs.(3.7) and (3.8) are not valid anymore. However, this approach can be applied to any kind of non-linearity, providing a perturbative approach is suitable, and leads to a good agreement between the measured and predicted circuit parameters [81, 82, 83, 84].

The energy-participation ratio approach enables us to compute the quality factor that is due to dielectric losses; however, the coupling to a transmission line is more complex and is therefore trickier to simulate. In such a case, it would be preferable to add the dissipation to the Ansys HFSS simulation and let the software simulate the modes' quality factors.

3.2 COUPLING TO A TRANSMISSION LINE

The coupling to a transmission line is an important feature as it defines the minimum relaxation rate (and thus the maximum relaxation time T_1) and the speed at which a gate can be applied on qubit modes. This section will discuss three different ways to simulate these couplings for 3D and 2D circuits. Each following section will start by presenting the model of transmission line used (the geometry and materials) in order to explain how we can simulate it and with which boundary condition.

3.2.1 *3D circuits*

In 3D geometries, the three different ways to simulate the coupling all need to first add a part of the transmission lines to the simulation (see Fig. 3.3). Many different kinds of transmission line exist. In terms of circuit QED applications, we are interested in a transmission line that is suitable for radio frequency signals, such as a coaxial cable [43]. In this scenario, we prefer to use a transmission line instead of a wave-guide, as the transmission line supports transverse electromagnetic (TEM) or quasi-TEM propagation modes, which have low frequency cut-off and no dispersion for TEM modes and a small one for quasi-TEM modes. In addition, the power of the signal is low enough that we do not need a wave-guide. It is worth noting that a wave-guide's frequency cut-off can be useful, as a filter [85]. The transmission line used, which is a coaxial cable, finishes by a launcher with a microwave pin entering inside the cavity. The capacitive coupling between the pin the cavity modes depends on the pin penetration length.

Before saying how to simulate a coaxial cable, let us recall what it is. A coaxial cable is made of a cylindrical inner conductor surrounded by a dielectric and an outer conductor[3]. The radius and nature of the inner conductor and dielectric are chosen

---

[3] Because the dielectric is *non simply connected*, the coaxial cable enables the propagation of a TEM mode [43].

according to the type of microwave pin and launcher used. In this thesis, the launcher are made of a copper inner conductor (diameter 1.3 mm) and Teflon dielectric (diameter 4.1 mm), leading to an impedance of 50 Ω.

As shown in Fig. 3.3, the pin and a part of the launcher are added in the simulation, the pin diameter is chosen equal to the inner conductor diameter and the beginning of the simulated coaxial cable and the cavity are separate by the thickness of the wall cavity (see Fig. 3.3). To reduce the complexity of the simulation, the outer conductor can be replaced by a perfect E boundary condition on the outer surface of the dielectric. This is equivalent to assuming that the outer conductor is a superconductor. As is shown in Fig. 3.3, the pin goes trough a vacuum cylinder before entering in the cavity. This is used to take into account the thickness of the cavity's superconducting bulk (which is not simulated). This vacuum cylinder represents the hole that is made through the cavity wall in order to insert the pin, thus the boundary condition applied to its outer surface is a perfect E boundary. The diameter of the hole is equal to 3 mm in order to obtain an impedance of 50 Ω when considering the pin and the hole as an a coaxial cable. As the diameter of the hole is smaller than the dielectric diameter, there is a "ring" of dielectric to which we have to apply a boundary condition. This ring is the part of the dielectric that is in contact with the cavity wall; as such, the boundary condition is again a perfect E boundary.

At this point, only one surface in this design has no boundary condition: the ring at the end of the transmission line (see Fig. 3.3). This ring is called the "dissipative surface", and it is on this surface that we will apply a specific boundary condition that will simulate the semi- infinite transmission line. The Caldeira–Leggett model (see Fig. 2.5) shows that it is possible to replace a semi-infinite transmission line with a dissipative element that has the same impedance. A non-dissipative element (the transmission line) can be modeled as a dissipative element as any signals emitted in the transmission line never come back. However, even with this simplification, we still need to simulate a finite extent of the transmission line in such a way that the geometry of the mode fields is well established before reaching the dissipative element. Thus, the length of the transmission line in the simulation has to be at least the size of the mode's wavelength.

The parameter we tune in order to reach the targeted coupling rate between the mode and the transmission line is the length of the pin. As long as the pin sticks inside of the hole, there is an exponential increase of the coupling rate as a function of the pin length. The following "rule of thumbs" applies: the coupling increases by a factor of 10 every millimeter.

This thesis uses three different dissipative boundary conditions. First is the perfectly matched layer (PML) boundary, which adds a fictitious material that can absorb any electromagnetic field that impinges on it. As such, we only need to simulate the eigenmodes of the system and their quality factors. The PML boundary is recommended for use with free-space and guided-wave termination. It has the advantage of being able to absorb waves in any direction and at any frequency; therefore, in order to reduce the simulated volume, it is recommended that the PML boundary be situated a quarter of a wavelength away from the mode (it can even be brought closer, coming down to 1/10 of a wavelength). The PML boundary has drawbacks; namely, it results in a slower

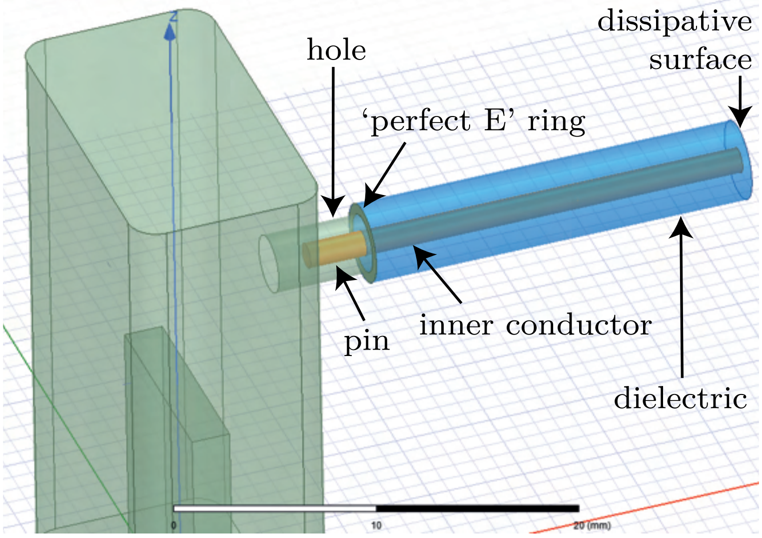

Figure 3.3: Ansys HFSS simulation of a post cavity coupled to a transmission line. Only the inner conductor (in orange) and the dielectric (in blue) are simulated. The outer conductor is replaced by a perfect E boundary condition on the surface of the dielectric. The inner conductor is made of copper and the dielectric is made of Teflon. The length of the vacuum cylinder around the pin is set by the thickness of the superconducting cavity.

simulation convergence and a has a larger RAM use, which could be compensated for by the reduced volume.

The second type of boundary is the wave-port boundary. We can define the dissipative surface as a wave port and use it to measure the reflection coefficient. In this case, we use a driven modal simulation, which takes longer as we have to simulate the reflection coefficient for various frequencies. The reflection coefficient shows a resonance at the mode frequency from which we can extract the coupling to the transmission line using Eq. (2.36). It has the advantage of being able to show the frequency dependence of the reflection coefficient; this dependence is not trivial if the mode is protected by filters (see Sec. 3.3). We can detect an impedance mismatch either by looking at the impedance matrix or by looking for wiggles or parasitic resonances in the reflection coefficient.

The last boundary is the lumped RLC boundary, which can only be applied to the dielectric section of the dissipative surface. It consists of a parallel combination of a lumped resistor, inductor, and/or capacitor applied to the dissipative surface, while an eigenmode simulation gives the quality factor of the dissipation. For our purposes, we use only a resistor, while the resistance is set to the impedance transmission-line value (i. e. $50\,\Omega$). When applying this boundary, the software requires a "current flow" line to be defined. The line does not define the direction of an RLC dipole; rather, the simulation uses it as a region of space where the calculation must converge in the simulation. Thus, it is recommended that the current flow line be drawn from the dielectric inner circle to the outer circle. This boundary works as follows: the software computes a surface impedance Z_s ohms/square from the resistance, inductance, and capacitance values. Then, on the surface, the electric and magnetic fields' tangential components, $\vec{E}_{\tan}$ and $\vec{H}_{\tan}$, follow the boundary condition

$$\vec{E}_{\tan} = Z_s(\vec{n} \wedge \vec{H}_{\tan}), \tag{3.12}$$

where $\vec{n}$ is the surface's unit normal vector. As expected, this boundary condition does not rely on a specific direction given by a current flow line, is easy to use, and does not increase the amount of RAM needed; however, it is not recommended for use with a non-rectangular surface as HFSS assume that the surface is always rectangular. With non-rectangular surface it may lead to a less accurate representation of the lumped RLC element.

All these three boundary conditions have been used in this thesis; we have checked that they all generate the same value for the coupling between the modes and the transmission line. The PML boundary is the most accurate, but it needs a larger amount of memory and a longer simulation time. The RLC boundary is a good compromise between speed, accuracy, and memory requirement, while the wave-port boundary offers interesting results when filters are used between the mode and the transmission line. Experimentally, we can (during the first cool down of the experiment) obtain a coupling rate of the same order as the one targeted. This allows us to refine the pin length over the course of cool downs and thereby get closer to the targeted value. Of course, when the coupling rate is large enough, it is even possible to measure it at room temperature.

3.2.2 *2D circuits*

The geometry we often used with 2D circuits is the coplanar waveguide (CPW) geometry, which is based on a dielectric substrate on top of which is located a center strip conductor, surrounded by two semi-infinite ground planes, on top (see Fig. 3.4a). The CPW architecture offers several advantages [86]. It supports a quasi-TEM propagation mode[4], it is easier to fabricate as there is no need for a ground plane on the bottom of the dielectric and it does not need any via holes nor a wraparound. In addition (from a design and performance point of view) shunts are easy to fabricate, radiation losses are small as there is no dipolar momentum, and the cross-talk between adjacent lines is weak. The drawbacks of CPW come from the existence of the two ground planes; that is, two modes exist—an even one where the two ground planes always have the same potential, and an odd one, where the two ground planes have opposite potentials. In the case of circuit QED, the odd mode is a parasitic one that is removed by connecting the two ground planes using an air bridge above the center track (see Fig.3.4b and c).

In 2D geometries, coupling between a transmission line and a mode is achieved by sharing a capacitor (see Fig.3.4b), while the capacitance determines the coupling rate. This coupling rate can be simulated in the same way as in the third 3D-geometry method (RLC boundary method). The transmission line's track is connected to the ground through two rectangles with lumped RLC boundaries. A resistance R is at-

---

[4] Due to the fact that there are two different dielectrics in a CPW geometry—the substrate dielectric and the air/vacuum—there are two different propagation speeds and, therefore, a TEM mode cannot exist. However, modes do exist that are nearly TEM and with a low dispersion; these are called quasi-TEM modes

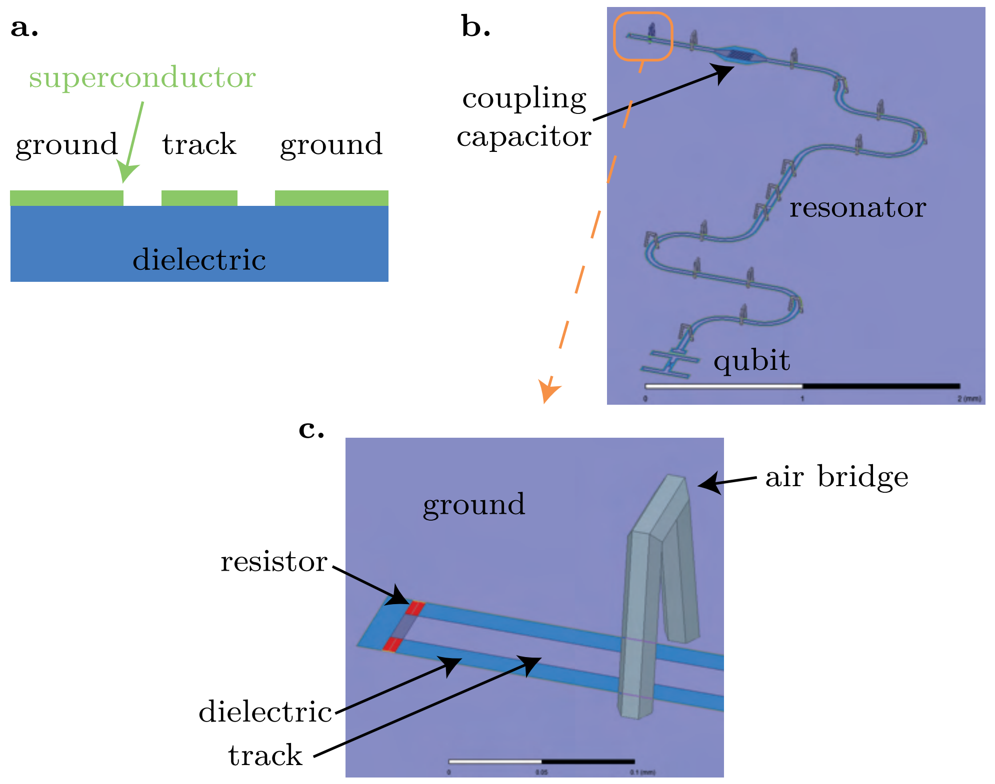

Figure 3.4: **a.** A vertical cut-through of the CPW architecture. On the top of a dielectric, a center strip conductor (also called a track) is surrounded by two ground planes. In circuit QED, the conductors are replaced by superconductors. **b.** An Ansys HFSS simulation of a qubit coupled to a readout resonator, which is then coupled to a CPW transmission line through a coupling capacitor. The dielectric is shown in blue and the superconductor in grey, and air bridges can be seen connecting the ground planes to each side of the track. **c.** Close-up of the CPW transmission line. In the simulation, the track of the transmission line is shorted to the ground by two lumped resistors (shown in red) in order to mimick the infinite length of the transmission line and its equivalent dissipation.

tributed to the two rectangles, which is equivalent to adding two parallel resistors of resistance R at the end of the transmission line. If each resistance R is equal to twice the impedance of the transmission line, the two resistors are equivalent to an infinite transmission line. An eigenmode simulation gives access to the mode quality factor, from which we can derive the coupling rate. We could use only one resistor with a resistance equal to the transmission-line impedance, but the convergence of the simulation would be slower if we did so. Thus, as the transmission-line mode is symmetric with respect to the track, it is better to use a dissipation that has the same symmetry. As the current in the resistors goes from the track to the ground, it is recommended that we define a current flow line going from the track to the ground.

In the simulation shown in Fig. 3.4b, only the bare resonator mode is capacitively coupled to the transmission line. However, due to the hybridization, both the resonator and qubit hybrid modes are coupled to the transmission line. The fact that the qubit mode is coupled to the transmission line is called the Purcell effect; this effect is interesting because it enables us to drive the resonator and the qubit through the same transmission line. However, it can be too strong and, in which case, can limit the lifetime T_1 of the qubit.

3.3 THE PURCELL EFFECT

3.3.1 *History*

The Purcell effect is an enhancement of the spontaneous emission of a quantum system by its environment. It was discovered in the 1940s by Edwards Mills Purcell when he was studying the enhancement of the spontaneous emission of an atom in a resonant cavity [87]. By changing the environment from the vacuum to a resonant cavity, the density of state at the atom's resonant frequency changes and, according to Fermi's golden rule, the spontaneous emission rate changes as well. Purcell concluded that the higher the quality factor of the cavity is, the higher the spontaneous emission rate is, which is a non-straightforward result. We can, however, understand it easily as follows: the density of states D_c of a cavity at its fundamental resonant frequency is (see Eq. 3.19)

$$D_c = \frac{2}{\pi \kappa_{\text{tot}}}. \tag{3.13}$$

This result comes from the fact that we have only one mode with a linewidth of κ_{tot}. Thus, at a fixed frequency, increasing the quality factor is equivalent to decreasing κ_{tot}, leading to an increase in the density of states.

3.3.2 *Bad cavity limit*

Let us derive the Purcell relaxation rate of a transmon qubit coupled to a resonator[5]. In this example, only the resonator is coupled to a transmission line, with a rate κ that is assumed to be larger than the coupling rate g between qubit and resonators (i. e. we are in the weak coupling regime). Starting from the linear part of the exchange's Hamiltonian (see Eq. (2.66)), we can move in the frame rotating at the transmon frequency for both modes. The Hamiltonian reads

$$\tilde{H}_{q,r;\text{RWA}} = -\Delta a^\dagger a + g(ba^\dagger + b^\dagger a), \tag{3.14}$$

with $\Delta = \omega_q - \omega_r$ being the detuning between the two modes. In the rotating frame, the quantum Langevin equations of the field amplitudes become

$$\begin{cases} \langle \dot{a} \rangle = \dfrac{-i}{\hbar}\langle [\tilde{H}_{q,r;\text{RWA}}, a] \rangle - \dfrac{\kappa}{2}\langle a \rangle = i\Delta \langle a \rangle - ig\langle b \rangle - \dfrac{\kappa}{2}\langle a \rangle \\ \langle \dot{b} \rangle = \dfrac{-i}{\hbar}\langle [\tilde{H}_{q,r;\text{RWA}}, b] \rangle = -ig\langle a \rangle \end{cases}. \tag{3.15}$$

---

[5] This derivation is based on that by Marius Villier, given in the lecture notes from the Ecole de Physique des Houches 2021 cQED OXY-Jeunes sessions but it can be done differently [7, 88]. This approach is valid when applied to any system that contains two coupled linear modes.

Due to the weak coupling assumption and in absence of drive, we can assume that the resonator mode is always in its steady state, i. e. $\langle \dot{a} \rangle = 0$. This assumption is valid, whatever the value of the detuning Δ. The steady state $\langle a \rangle_{\mathrm{ss}}$ reads

$$\langle a \rangle_{\mathrm{ss}} = \frac{ig\langle b \rangle}{i\Delta - \kappa/2}, \tag{3.16}$$

and by replacing the mean value of a by its steady state value in the mean-field equation for mode b, we get

$$\langle \dot{b} \rangle = \frac{-g^2}{\Delta^2 + \kappa^2/4}(-i\Delta + \kappa/2)\langle b \rangle. \tag{3.17}$$

In this way, we obtain two results: first, the frequency of the transmon mode is shifted by $g^2\Delta/(\Delta^2 + \kappa^2/4)$ (this is the Lamb shift of the transmon mode induced by the resonator mode due to the exchange coupling being corrected by the resonator losses); and second, the transmon state decays spontaneously at a rate of

$$\Gamma_p = \frac{g^2\kappa}{\Delta^2 + \kappa^2/4}, \tag{3.18}$$

which is called the Purcell rate. The Purcell rate is given by a Lorentzian function of Δ that has the width κ. This can be explained easily, as the density of state $D_c(\omega)$ of the resonator reads

$$D_c(\omega) = \frac{1}{2\pi} \frac{\kappa}{(\omega - \omega_r)^2 + \kappa^2/4}. \tag{3.19}$$

Thus, the Purcell rate is, as expected, proportional to the resonator density of state at the transmon frequency $D_c(\omega_q)$. If the detuning Δ is small compared to the resonator losses κ, we retrieve the same expression and conclusion as Purcell: that the Purcell effect increases with the resonator quality factor. In the circuit QED field, this regime of parameters is rare, as a strong regime coupling can easily be achieved, but this is not the case for some hybrid systems, such as the spin-resonator system in electron spin resonance experiments, with which the resonant Purcell effect is often used [89].

3.3.3 *Strong and dispersive regime*

As has been said in Sec. 2.5, most circuit QED experiments are conducted using the strong and dispersive regime, i. e. $\Delta \gg g \gg \kappa$. In such cases, the exchange interaction allows the excitation between the transmon and the resonator to be coherently swapped; this phenomenon is called the vacuum Rabi oscillation [19]. As the resonator is lossy, there is a finite probability of losing the excitation in the resonator before it is swapped again in the transmon. In the former section, we assumed that the resonator is always in its steady state; however, this assumption can no longer be made as the exchange rate is bigger than the loss rate. In the strong and dispersive regime, the Purcell rate is derived as [70]

$$\Gamma_p = \frac{g^2\kappa}{\Delta^2}. \tag{3.20}$$

These results can easily be understood: the ratio g/Δ is the amount of hybridization between the transmon and the resonator mode. Thus, g^2/Δ^2 is the probability that an excitation of the hybrid transmon mode occurs in the bare resonator mode. Thus, this excitation has a probability $\kappa \mathrm{d}t$ to be lost during the next time step $\mathrm{d}t$, leading to the Purcell rate seen in Eq. (3.20). This formula can easily be retrieved by applying the Bogoliubov transformation to the Lindblad dissipation term; however, as we will discuss below, this is not the proper way to derive it.

If either the strong or the dispersive assumptions are not satisfied, we can derive the Purcell rate of the transmon mode using the weaker assumption $\kappa \ll \sqrt{\Delta^2 + 4g^2}$[88], in which case the Purcell rate reads

$$\Gamma_p = \frac{\kappa}{2}\left(1 - \frac{\Delta}{\sqrt{\Delta^2 + 4g^2}}\right). \tag{3.21}$$

We can easily check whether the three Purcell rates from Eqs.(3.18), (3.20) and (3.21) give the same results $\kappa g^2/\Delta^2$ under the dispersive approximation, whatever the ratio g/κ. However, these expressions are only valid for an inverted situation; that is, where the Purcell rate is induced by a lossy transmon qubit on a resonator. As has been shown in [90], for a lossy resonator, we need to take the multi-mode nature of the resonator into account. Additionally, we did not take into account the dependence of κ on the angular frequency ω. We did the approximation that $\kappa(\omega)$ is flat; however, this is only true around the resonator frequency and $\kappa(\omega_q)$ can differ from $\kappa(\omega_r)$. In the next two sections, we will discuss the multi-mode nature of the resonator, the convergence problem, and the dependence of κ on the angular frequency ω.

3.3.4 *The multi-mode Purcell effect*

The transmon mode is coupled to not one but an infinity of lossy modes[6]. First, we study a lumped circuit where the resonator is replaced by a finite-length transmission line[90]. The Purcell rate becomes asymmetric with respect to the detuning Δ and is smaller for negative detuning $\delta < 0$ (i. e., when the transmon frequency is below the cavity frequency) than for positive detuning $\delta > 0$ (i. e., when the transmon frequency is above the resonator frequency). This is one of the explanation about why the circuit QED community designs readout resonators to work at frequencies above qubits resonant frequencies. The reason for this can easily be understood if we take into account the resonator's second mode.

This multi-mode behavior is already taken into account by the Ansys HFSS simulation. Another way to study this concept is to look at the admittance $Y_0(\omega)$ seen by the transmon (see Fig. 3.5). By studying this classical circuit [91, 90], we can see that the Purcell rate is given by

$$\Gamma_p = \frac{\mathcal{R}e(Y_0(\omega_q))}{C_J + C_{\text{shunt}}}. \tag{3.22}$$

---

[6] As a transmon contains only one mode, the Purcell effect due to a lossy qubit on a resonator is given by the Eqs.(3.18), (3.20) and (3.21).

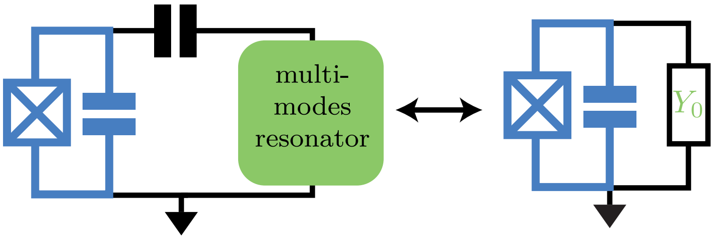

Figure 3.5: Transmon qubit capacitively coupled to a multi-mode resonator. We can replace the multi-mode resonator and the coupling capacitor with an equivalent admittance $Y_0(\omega)$. The Purcell rate of the transmon mode, due to the resonator losses, is given by the real part of the admittance Y_0 at the transmon's resonant frequency.

Even if all the above simulating approaches work and show a good agreement with the experiment [90], we still have to be careful if we want to generalize the theory to a multi-mode system. We can show that assuming the resonant frequency of the n-th resonator mode is $(n+1)\omega_r$ and its impedance $Z/(n+1)$, its losses κ_n and its coupling rate g_n with the transmon are given by $g_n = g\sqrt{n+1}$ and equate to $\kappa_n = \kappa(n+1)^2$ [90]. Taking into account the fact that the detuning Δ_n between the transmon and the n-th resonator mode is linear with n, we can easily show that the series $\sum_n \Gamma_{p,n}$, where $\Gamma_{p,n}$ is the Purcell rate due to the mode n, diverges.

This divergence can be solved by more precise studies that take into account the spatial extent of modes. We can study the system with a transmission line (the resonator) of length l and a spatial zero dimensional transmon. It has been shown in [92] that the coupling and transmon capacitors become shorter at high frequency, acting as a low-pass filter. Thus, the amplitude of the n-th resonator mode at the qubit position is suppressed for large n. This effectively causes a powerlaw with a low exponant of g_n and decreases the scaling of the loss rate κ_n. Although this model has already solved the divergence problem, it still views the transmon as a dot in space, which is an approximation. Indeed, if we want to derive the coupling g_n, we always have to use the dipolar approximation, which assumes that the transmon length is small compared to the wavelength of the resonator mode. While this approximation is valid for low-frequency modes, it is not valid for high-frequency modes as the wavelength decreases as $1/n$. It has been shown [93] that the effective coupling capacitance between a transmon of length $2l_q$ and the n-th mode of the resonator is proportional to $\mathrm{sinc}(2\pi l_q/\lambda_n) \sim 1/n$. This is due to the fact that the coupling is given by the overlap of the transmon and the n-th mode's resonator electrical field. We have to integrate this coupling over the full extent of the transmon, taking into account the spatial dependence of the electrical field phase. For high-frequency modes, the phase changes too quickly, leading to a loss of coherence and a decrease in the coupling rate. We can view the transmon as a collection of zero extension antennas; if they are not oscillating in phase, there will be no excitation of the transmon mode.

3.3.5 *Purcell filters*

We have not yet discussed the dependence of the loss rate κ on the angular frequency ω. The loss rate κ is obtained when the Markov approximation is performed on the environment. When doing so, it is shown that the loss rate reads [94]

$$\kappa(\omega) = 2\pi D_e(\omega)|g_e(\omega)|^2, \tag{3.23}$$

with $D_e(\omega)$ being the density of state of the environment at angular frequency ω and $g_e(\omega)$ being the coupling rate of the environment mode to the resonator, at angular frequency ω. Now Eq. (3.18) can be seen from a new perspective—the transmon mode perspective. The resonator is the transmon environment and the density of state of this effective environment is equal to $D_c(\omega)$.

Eq. (3.23) shows that we have two ways to tune the loss rate and suppress the Purcell rate. That is, we can either design a coupling g_e or a density of state D_e that is small at the transmon frequency, while keeping the loss rate κ at the value needed for the resonator. In our experiment, g_e is already set by the choice of the capacitive coupling. Thus, a convenient way to protect a mode from the Purcell effect is to design an environment density of state that is small at the mode frequency. An easy way to do this is to use *Purcell filters* [95] placed between the system (which, here, is formed by the transmon and the resonator) and the transmission line. It must show a close-to-1 reflection amplitude $|r|$ at the transmon frequency (or at the frequency of the mode we have to protect) and a close-to-1 transmission amplitude $|t|$ at the resonator frequency (or at the lossy mode's frequency). If the filter has no loss, the Purcell rate becomes

$$\Gamma_P(\omega) \rightarrow \Gamma_P(\omega)|t(\omega)|^2. \tag{3.24}$$

Various types of Purcell filter exist; the most commonly used are the stub filter [95] (or $\lambda/4$ filter) and the band-pass filter [96]. The stub filter is designed to have destructive interference at the transmon frequency, leading to a high reflection coefficient. The stub filter imposes a good frequency matching as the destructive interference phenomenon happens only at specific frequencies. The band-pass filter is an added resonator. It has to be close to the resonator mode in terms of frequency. Usually, we can simply choose a band-pass filter that is resonant with the resonator mode. However, as the resonator is coupled to the transmission line through the band-pass filter, the Purcell filter has a higher loss rate than the resonator does. Thus, we have to be careful that the exchange coupling rate between the transmon and the Purcell filter is small, otherwise it will add a non-negligible Purcell effect.

Some Purcell filters are incorporated inside the transmission line (see Sec. 9.2.1), in which case the impedance of the filter must be matched to that of the transmission line. If there is an impedance mismatch (which there always is due to the SMA connectors or the line filtering) we can create a standing wave (i. e. a resonant mode, as in a Fabry–Perot cavity) that can change in response to the transmission line's density of modes and thus strongly enhance the transmon's relaxation rate.

As we will see, this filtering concept is crucially important, as it is not only used to protect a mode from the Purcell effect but, more generally, to protect a quantum state from decoherence.

3.4 FILTERING, NOISE, AND DECOHERENCE

The filtering of a superconducting circuit is essential, as the noise seen by the system and its relaxation are related through the fluctuation dissipation theorem. Let us assume that an harmonic mode is coupled to a noise source, described by the quantum operator $\hat{F}$, with the following coupling Hamiltonian:

$$V = A\hat{\phi}\hat{F} = A\phi_{\text{ZPF}}(\hat{a} + \hat{a}^\dagger)\hat{F}. \tag{3.25}$$

Thus, using Fermi's golden rule, the probabilities $\kappa_\downarrow$ and $\kappa_\uparrow$ (of losing and gaining a photon, respectively) are [8]

$$\begin{cases} \kappa_\downarrow = \dfrac{A^2\phi^2_{\text{ZPF}}}{\hbar^2} S_{FF}(+\omega_r) \\ \kappa_\uparrow = \dfrac{A^2\phi^2_{\text{ZPF}}}{\hbar^2} S_{FF}(-\omega_r) \end{cases}, \tag{3.26}$$

where ω_r is the resonant angular frequency of the mode and S_{FF} is the quantum noise spectral density. Thus, from the system's perspective, the noise in the environment generates dissipation. As the noise is quantum, the spectral density is not an even function of ω, leading to a relaxation rate that is higher than the excitation rate. Filtering the environment becomes essential, as it allows us to decrease the spectral density amplitude and to reach a dissipation rate that is low enough to allow coherent control of the system. Thus, the cavity QED architecture makes sense, as it uses the cavity to filter the noise from the environment.

In Eq. (3.23), we related the total loss rate κ to the environment density of state D_e, whereas, in Eq. (3.26), the total loss rate $\kappa = \kappa_\downarrow - \kappa_\uparrow$ is related to the quantum noise spectral density. We can easily check whether these two expressions are compatible. Assuming the mode is coupled to the transmission line capacitively, we can derive the charge noise spectral density of one harmonic oscillator using the resonant frequency ω_o [8], as follows:

$$S_{QQ}(\omega) = 2\pi Q^2_{\text{ZPF}}(n_b(\omega_o)\delta(\omega_o + \omega) + (n_b(\omega_o) + 1)\delta(\omega_o - \omega)), \tag{3.27}$$

with $n_b(\omega)$ being the Bose–Einstein occupation factor at energy $\hbar\omega$. As the Kronecker functions that appear are simply the density of state $D_{ho}(\omega)$ and $D_{ho}(-\omega)$ of the harmonic oscillator, we can easily derive the charge noise spectral density for a transmission line, which is a collection of harmonic oscillators with a density of state $D_e(\omega)$. This leads to the spectral density

$$S_{QQ}(\omega) = 2\pi Q^2_{\text{ZPF}}(|\omega|)(n_b(\omega)D_e(\omega) + (n_b(-\omega) + 1)D_e(-\omega)), \tag{3.28}$$

where $D_e(\omega < 0) = 0$. We can also easily check that the relaxation rate $\kappa(\omega_r) = \kappa_\downarrow(\omega_r) - \kappa_\uparrow(\omega_r)$ is indeed proportional to the density of state $D_e(\omega_r)$. Thus, the Purcell effect and the Purcell filter can be viewed as an enhancement or a filtering of the noise perceived by a mode. The effect of a Purcell filter can be viewed as a filtering of the environment noise. This noise is decreased by the transmission coefficient t, leading to the spectral density $|t(\omega)|^2 S_{QQ}(\omega)$.

In the last paragraph, we discussed relaxation only; however, a quantum system is also sensitive to dephasing. If a parameter F of a mode's Hamiltonian shows quantum fluctuations, then the frequency of the mode can fluctuate as well. This leads to the dephasing rate [20]

$$\Gamma_\varphi = \frac{1}{2}\left(\frac{\partial \omega_r}{\partial F}\right)^2 S_{FF}(\omega \to 0). \tag{3.29}$$

As such, the dephasing rate is related to the quantum noise spectral density at low frequency.

Similarly to the Purcell effect, if the transmon mode has a dephasing rate Γ_φ, given by Eq. (3.29), the exchange interaction between the transmon mode and the resonator mode leads to two new dissipation terms (commonly known as dressed dephasing [94]): $\Gamma_\Delta \mathcal{D}(a^\dagger b)$ and $\Gamma_{-\Delta}\mathcal{D}(ab^\dagger)$ with $\Gamma_{\pm\Delta} = \left(\frac{\partial \omega_r}{\partial F}\right)^2 \frac{g^2}{\Delta^2} S_{FF}(\pm\Delta)$. These two terms relate to the excitation and decay of the transmon state at the rate $\overline{n}\Gamma_{\pm\Delta}$, with $\overline{n}$ being the average number of photons in the resonator. Thus, this term leads to the spurious transition of the transmon, either during readout or if the resonator mode is hot. This term can be viewed as either an up- or down-conversion of the photon noise at frequency Δ by the resonator photons, indicating the importance of filtering the system, not only at low and resonant frequencies, but also at those frequencies that correspond to the detuning between the modes.

4

QUANTUM MEASUREMENT

We usually learn from quantum physics textbooks that a measurement is an instantaneous collapse of the quantum state. The word "collapse" refers to a situation where the coherence between measurement eigenvectors is erased and the system state is projected randomly onto one of those eigenvectors; this is the so-called von Neumann measurement. This measurement raises many issues. First is that it is difficult to describe all measurements using this formalism. For example, if a photodetector measures the excitation of a qubit and goes "click" (i. e., detects a photon), we know before the measurement occurs that there was a non-null probability that the qubit was in the excited state. However, after the measurement, the qubit is in its ground state, as its excitation has been absorbed by the photodetector. Such a measurement is described using the measurement operator $|e\rangle\langle g|$, which is not a von Neumann measurement (see Sec. 2.2.3.1). Second, not all the measurements are projectives; some of them leave the quantum state with coherences in the measurement eigenvectors' basis. These measurements are called *weak* measurements. To reconcile those two cases with von Neumann measurement we need to take into account a *probe* mode. Third, a measurement is never instantaneous; we can always define a measurement bandwidth that is related to the minimal amount of time needed to perform a projective (or *strong*) measurement.

In this chapter, we discuss the different types of generalized measurements that can be performed and define the relevant quantities used to characterize them. Specifically, we will focus on the heterodyne and homodyne measurements and on the photodetector, all of which are at the center of this thesis. To finish, we will discuss the idea of a quantum-limited amplifier and describe the amplifier that is used in the thesis: a Josephson traveling-wave parametric amplifier (TWPA).

4.1 STERN AND GERLACH EXPERIMENT

This section discusses the different types of measurements and defines the relevant parameters, using a idealized Stern and Gerlach experiment as an example. Although the historical experiment was initially used to prove the quantum nature of spins[1], its idealized version is a perfect and easily studied example of generalized measurement.

4.1.1 *Measurement scheme*

The Stern and Gerlach experiment was imagined by Otto Stern in 1921 and conducted by Walther Gerlach in 1922 [97]. In this experiment, a silver atom beam is sent into an inhomogeneous magnetic field. As silver atoms can be seen as spin-1/2 particles,

---

[1] Let's remark that the initial experiment was performed to test the Bohr-Sommerfeld hypothesis entailing that the atom angular momentum is quantized. It was only several years later that the spin existence was postulate.

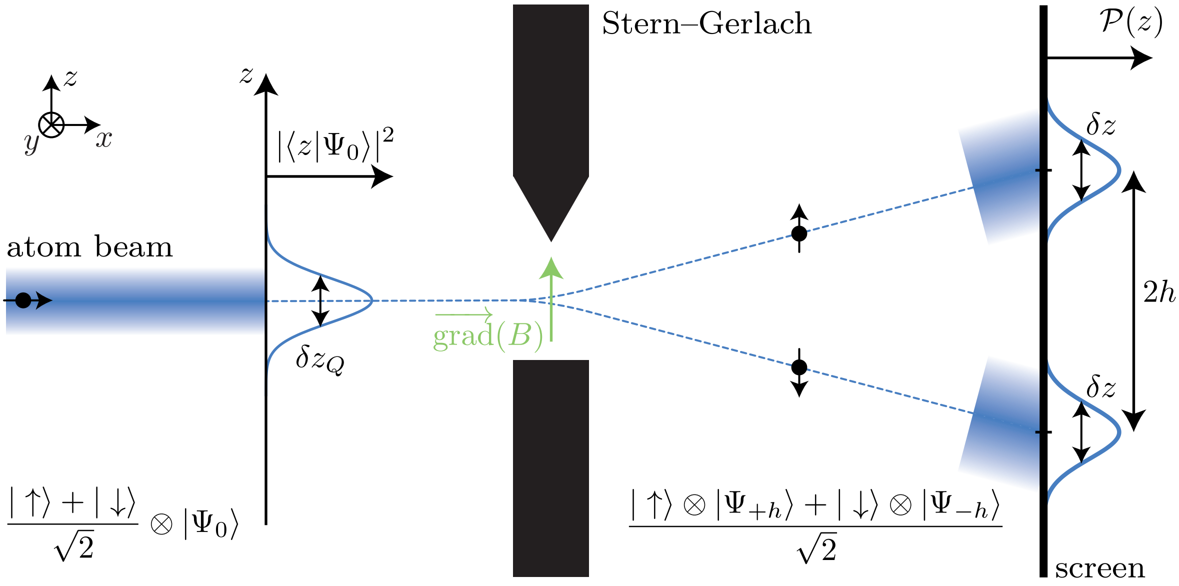

Figure 4.1: The Stern and Gerlach experiment. An atom beam, polarized along the x direction, goes through a magnetic field gradient. Due to the spin and the magnetic field interaction, the beam is deviated depending on the z component of the spin. This interaction is a unitary evolution that entangles the atom spin and the position's degree of freedom. The beam arrives on a screen that performs a von Neumann measurement of the atom's z coordinate. Depending on the distance h between the two beam spots on the screen, the initial quantum noise δz_Q, and the final total noise δz, various types of quantum measurements can be achieved.

the magnetic field gradient in the z direction deviates the beam according to the spin z-component (see Fig. 4.1). A screen enables us to measure the position of atoms after the deflection occurs.

The quantum states of the beam's atoms have two parts: one describing the spin degree of freedom, the other the z position degree of freedom. Thus, the quantum state can be written as $|\Psi\rangle = |\Psi_s\rangle \otimes |\Psi_z\rangle$, where $|\Psi_s\rangle$ and $|\Psi_z\rangle$ are the quantum states of the spin and the position, respectively. In this idealized version of the experiment, we assume that the atom spin state is prepared in $|+x\rangle = (|\uparrow\rangle + |\downarrow\rangle)/\sqrt{2}$, where $|\uparrow\rangle$ and $|\downarrow\rangle$ are the two eigenvectors of the σ_z operator. As there is no environment, no unknown auxiliary system, and no uncertainty in the initial state, we can use the Hilbert space vectors instead of the density matrix. After the beam's focusing process, there will always be a non-null beam width, which is given by the quantum standard deviation δz_Q of the position z. For example, if the beam is focused using an optical trap, δz_Q will be the zero-point fluctuation[2]. Thus, the position's quantum state is described by the vector $|\Psi_0\rangle$, leading to a probability density of $|\Psi_0(z)|^2$, which is centered on zero with the width δz_Q (see Fig. 4.1).

After the magnetic field, the atom state reads

$$|\Psi\rangle = (|\uparrow\rangle \otimes |\Psi_{+h}\rangle + |\downarrow\rangle \otimes |\Psi_{-h}\rangle\ )/\sqrt{2}, \tag{4.1}$$

---

[2] Here we assume that the thermal fluctuation does not affect the beam preparation which was the case in the historical experiment.

and the spin degree of freedom is entangled with the position degree of freedom. The measurement of the atom position on the screen can be modeled as a von Neumann measurement and leads to the projection of the $|\Psi_{+h}\rangle$ and $|\Psi_{-h}\rangle$ states on the position eigenvector $|z\rangle$. The spin state reads

$$|\Psi_s\rangle = \frac{\langle z|\Psi_{+h}\rangle\,|\uparrow\rangle + \langle z|\Psi_{-h}\rangle\,|\downarrow\rangle}{\sqrt{|\,\langle z|\Psi_{+h}\rangle\,|^2 + |\,\langle z|\Psi_{-h}\rangle\,|^2}}. \tag{4.2}$$

This is the protocol for a generalized measurement (see Sec. 2.2.3.1), with the measurement operator $M(z)$ being associated with the measurement outcome z, as follows:

$$M(z) = \begin{pmatrix} \langle z|\Psi_{+h}\rangle & 0 \\ 0 & \langle z|\Psi_{-h}\rangle \end{pmatrix}. \tag{4.3}$$

When looking at the probability density of atom detections, we can see that the width of the density is equal to δz and is larger than δz_Q (see Fig. 4.1). This occurs because the measurement setup adds noise; for example, the noise of the magnetic field gradient or the noise of atom detection by the screen. As such, the total noise δz of the atom position is made of two contributions: a quantum part δz_Q, which cannot be removed and is contained in $|\Psi_{\pm h}\rangle$, and a classical part δz_c, which is added by the measurement scheme. The total noise reads as $\delta z = \sqrt{\delta z_Q^2 + \delta z_c^2}$. The measurement operator of Eq. (4.3) takes only the quantum noise into account. When adding the classical noise, after the measurement the density matrix ρ_{s} of the spin state becomes

$$\rho_{\mathrm{s}} \rightarrow \frac{\int p_c(z')M(z-z')\rho_{\mathrm{s}}M^\dagger(z-z')\mathrm{d}z'}{\mathrm{Tr}\left(\int p_c(z')M(z-z')\rho_{\mathrm{s}}M^\dagger(z-z')\mathrm{d}z'\right)}, \tag{4.4}$$

where $p_c(z')$ is the probability density of the classical noise. Based on the respective values of $2h$, δz_Q, and δz_c, we can identify a fourth case.

4.1.2 *Measurement regimes*

4.1.2.1 *Strong measurements*

If the difference $2h$ between the mean signals for spin up and down is large compared to the total noise δz (see Fig. 4.2a), there is no ambiguity in the state of the system after the atom detection has taken place. From the point of view of the quantum state, if there is no classical noise δz_c, the states $|\Psi_{+h}\rangle$ and $|\Psi_{-h}\rangle$ are orthogonal ($\langle\Psi_{+h}|\Psi_{-h}\rangle = 0$) and there is a high entanglement of one bit between the spin and the position. With a non negligeable classical noise, the state must be described with a density matrix and the entanglement is erase by the classical noise. However the classical noise is not large enough to blur the measurement result as $2h$ is larger than δz_c. If the measurement outcome's z is positive (negative), the spin state is projected on $|\uparrow\rangle$ ($|\downarrow\rangle$) as $\langle z|\Psi_{-h}\rangle = 0$ ($\langle z|\Psi_{+h}\rangle = 0$). This measurement is projective and is called a *strong* measurement or *single-shot* measurement; it is usually the qubit-state readout regime we would want to reach [98].

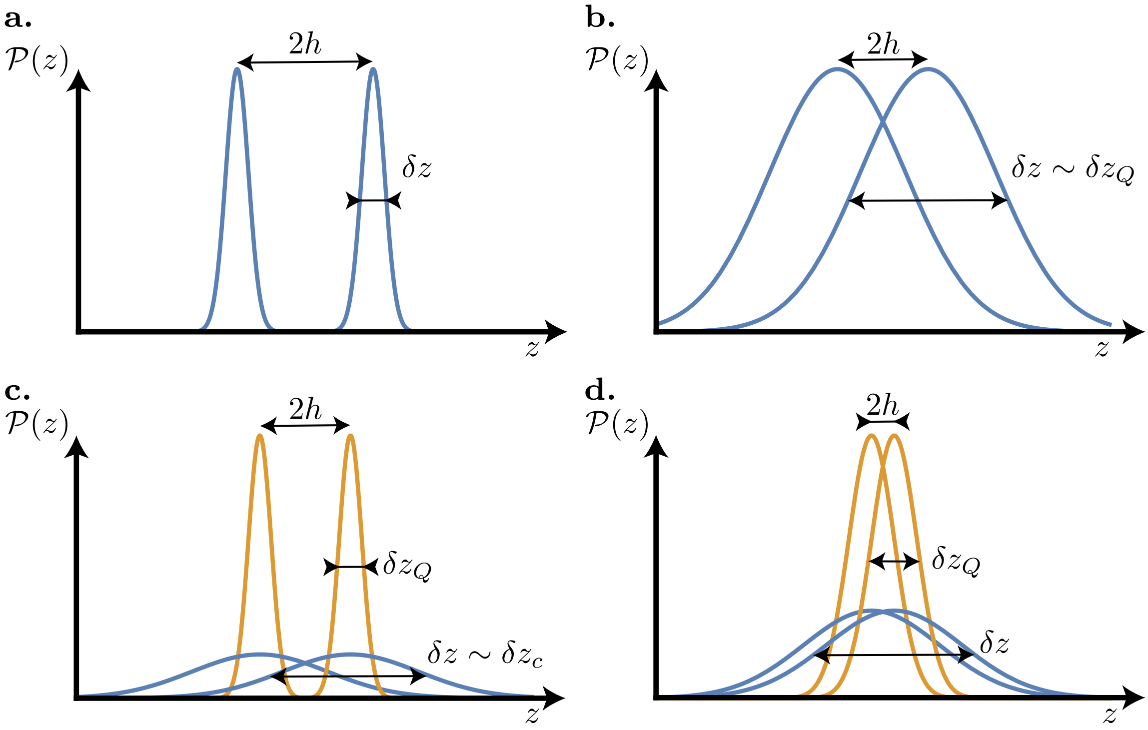

Figure 4.2: Density probability $\mathcal{P}(z)$ of the atom detection with the classical noise added by the measurement scheme (blue) and with only the quantum noise (orange). **a.** Strong measurement. The signal $2h$ is bigger than the noise δ_z **b.** Weak measurement. The signal $2h$ is of the same order as the quantum noise δz_Q, and the classical noise is negligible **c.** Unread strong measurement. The signal $2h$ is greater than the quantum noise δz_Q, but is of the same order or smaller than the classical noise δz_c. **d.** Unread weak measurement. The signal $2h$ is of the same order as the quantum noise δz_Q, but is smaller than the classical noise δz_c.

4.1.2.2 *Weak measurement*

When the classical noise is small compared to the signal and the signal is smaller than the quantum noise (i. e. $\delta z_c \ll 2h$ and $2h \leq \delta z_Q$) the amount of entanglement (much less than one bit) between the position and spin degree of freedom is not large enough to achieve a strong measurement. There is an overlap between the two states $|\Psi_{+h}\rangle$ and $|\Psi_{-h}\rangle$ ($\langle\Psi_{+h}|\Psi_{-h}\rangle \neq 0$). When measuring the position of the atom, we cannot deduce the spin state without ambiguity (see Fig. 4.2b); this ambiguity comes from the quantum fluctuation. The atom spin state after the position measurement is a coherent superposition of $|\uparrow\rangle$ and $|\downarrow\rangle$, which is given by Eq. (4.2). This measurement is called a *weak* measurement, which can be used to measure quantum trajectories [74].

4.1.2.3 *Partially read strong measurement*

In the two last cases, the classical noise was negligible compared to the quantum noise and/or the signal. We will now study a case wherein the classical noise δz_c is of the same order or larger than the signal $2h$ and is much larger than the quantum noise δz_Q; i. e. $\delta z_c \sim 2h \gg \delta z_Q$. Here, the amount of entanglement we would have between the position and spin degree of freedom whitout classical noise is large enough to result in a strong measurement (the yellow curve in Fig. 4.2c), but the classical noise erases the entanglement and blurs the results of the position measurement (the blue curve in Fig. 4.2c). As the measurement is strong from the point of view of the quantum noise (i. e. $2h \gg \delta z_Q$), the final spin state has no coherence. The classical noise transforms the pure spin state into a statistical mixture of $|\uparrow\rangle$ and $|\downarrow\rangle$, while the density matrix reads

$$\rho_{\mathrm{s}} = p(z)\left|\uparrow\right\rangle\left\langle\uparrow\right| + (1 - p(z))\left|\uparrow\right\rangle\left\langle\uparrow\right|, \tag{4.5}$$

where $p(z)$ is the probability of detecting a spin $|\uparrow\rangle$ at the position z and is mostly given by the classical noise. The measurement is strong; however, only a part of the information is recovered, being equivalent to reading only a part of the measurement. If the classical noise becomes much larger than the signal, then we cannot recover the measurement information; as such, the measurement becomes an unread measurement that is equivalent to a decoherence process.

4.1.2.4 *Partially read weak measurement*

The last case is defined as a classical noise, a quantum noise, and a signal of the same order; i. e. $2h \sim \delta z_c \sim \delta z_Q$. In this case, the measurement is a weak measurement that is blurred by the classical noise. The final spin state is a statistical mixture of the coherent superposition of $|\uparrow\rangle$ and $|\downarrow\rangle$. This is usually a regime of parameters that we try to avoid for a qubit-state readout. In circuit QED, as the classical noise is rarely negligible, quantum trajectory experiments are usually performed in a partially read weak measurement regime, rather than in a pure weak measurement regime.

4.2 MEASUREMENT CHARACTERISTICS

In the last section we discussed the various strengths of a quantum measurement, which can be quantified using various parameters such as the signal-to-noise ratio (SNR). In this section we will introduce the main characteristics and parameters of quantum measurements, such as continuous and quantum non-demolition (QND) measurements.

4.2.1 *SNR and quantum efficiency*

From the study of the Stern and Gerlach experiment (see the previous section), we can see that the measurement is characterized by two parameters: the SNR and the quantum efficiency η.

$$\begin{cases} \mathrm{SNR} = \dfrac{(2h)^2}{\delta z^2} \\ \eta = \dfrac{\delta z_Q^2}{\delta z^2} \end{cases}. \tag{4.6}$$

The quantum efficiency compares the classical noise to the quantum noise and, more generally, the minimal amount of noise imposed by quantum mechanics to the total amount of noise. It gives the percentage of the measurement information recovered, which is equivalent to saying that it quantifies the amount of information that is preserved from the classical noise. The SNR quantifies whether the amount of information recovered is enough to determine the state of the system without any ambiguity. For a qubit-state readout, we would want a high SNR (larger than 10) and a quantum efficiency close to 1.

For a dispersive qubit readout and qubit fluorescence measurement, the signal amplitude is limited either by the higher-order non-linearities effect (see Sec. 2.5.3) or by the fact that a qubit can only store one photon (see Sec. 2.4.3). To reach the fastest strong measurement, it becomes essential to reach a close-to-1 quantum efficiency. The signal power being only a few photons, measuring the signal without amplification will not work because of the microwave room-temperature noise which is about thousands of photons and the acquisition card sensitivity which is too low. Noise is always added during an amplification process; a good amplification scheme is composed of an amplifier that adds a noise that is negligible compared to that of the signal. In a circuit QED experiment, the first amplifier is usually a quantum-limited amplifier such as the Josephson parametric converter (JPC) [99], Josephson parametric amplifier (JPA) [100], or a TWPA [30]. These amplifiers add a noise that is close to the minimal one imposed by quantum mechanics. The gain of about +20 dB from these amplifiers is large enough so that the noise added by the rest of the amplification scheme is almost negligible; thus, the efficiency of the amplification scheme is mainly dominated by the quantum efficiency of the first quantum-limited amplifier.

4.2.2 *QND measurements*

One of the most important features of a quantum measurement is whether or not it demolishes the system's quantum state. Here the word "demolition" does not refer to a collapse nor to a projection of the quantum state; rather, it refers to the fact that a measurement can get the system out of the Hilbert space thus making it impossible to measure it again, or leads to a measurement outcome in a following measurement that is not correlated to the first one. As an example, let us describe two types of demolition measurements. First of these is the Stern and Gerlach experiment, in which the atom detection by the screen leads to the absorption of the atom; therefore, performing a second measurement is impossible.

The second example is the measurement of a qubit by a photodetector. The photodetector is able to detect any photon emitted by the qubit. If the photodetector "clicks", this means the qubit was in the excited state. We use the past tense as the qubit emitted the photon stored in the excited state and so it is now in the ground state. Thus, while the "click" is a measurement of the qubit's excited state, the qubit state after the measurement is $|g\rangle$. The measurement operator is $|g\rangle\langle e|$. If we perform a second measurement, the result will be "no click".

In comparison, the dispersive readout of a qubit is a QND measurement when driving the resonator such that the photon number remains low [70]. For a large drive, leading to a large number of photons in the resonator, the resonator photons can induce a qubit transition during the measurement, leading to a non-QND measurement (or "demolition measurement") [101].

4.2.3 *Continuous vs discrete measurements*

As described in Sec. 2.2.3.1, a quantum measurement consists of two steps: an entanglement process between the system and the probe and a von Neumann measurement of the probe. In practice, the von Neumann measurement can be a continuous process such as a voltage measurement, which needs to be integrated over time in order to suppress the noise. Depending on the characteristics of the two processes, a quantum measurement can be viewed as either a discrete or a continuous time process.

4.2.3.1 *Continuous case*

If the two processes are continuous and occur simultaneously, then we can divide the measurement in time steps that are as small as the time step $\mathrm{d}t$ used to study the system dynamics (see Sec. 2.2.3.3). This is the case of the dispersive readout of a qubit. The entanglement between the cavity and the qubit and the homodyne/heterodyne measurement of the outgoing field occur approximately at the same time. This kind of measurement allows us to consider the measurement as continuous in time. When dividing a measurement with duration T into N shorter measurements of duration T/N, the noise of shorter measurements is integrated over a smaller time, leading to a smaller SNR. It has been shown that the SNR is proportional to the integration time[3] T. For a measurement made with a phase-sensitive amplifier (see Sec. 4.3.3.2 for the definition of a phase-sensitive amplifier), the relationship reads [74]

$$\mathrm{SNR} = 8\Gamma_m T, \tag{4.7}$$

where Γ_m is the measurement rate[4] (i. e. the speed at which the information is recovered by the observer). The measurement rate is related to the quantum efficiency η and the dephasing rate Γ_d by the relationship [8]

$$\Gamma_m = \eta\Gamma_d. \tag{4.8}$$

The dephasing rate is the rate at which coherences between the measurement eigenvectors decrease, which implies that we cannot measure faster than the speed at which the state dephases. These fundamental results come from the measurement back-action. Every time information is extracted from the system, the back-action of the measurement dephases the quantum state, leading to its collapse. We can see the dephasing rate as the rate at which information is acquired by the environment, only a part of which η is recovered by the observer.

As the SNR depends linearly on the integration time T, we can continuously change the measurement strength: from a weak measurement to a strong measurement. Thus,

---

[3] To be more precise, the SNR is proportional to the inverse measurement bandwidth (see supplementary information in [102]). If the measurement time (which is equal to the integration time) is longer than the inverse bandwidth of the resonator, amplifiers, or filters, etc., the inverse measurement bandwidth is equal to the integration time.

[4] The definition of the SNR is not universal. Using the notation from the Stern and Gerlach experiment, we can find the following definitions: $\mathrm{SNR} = h^2/\delta z^2$ [8] and $\mathrm{SNR} = (2h)^2/(2\delta z)^2$ [62]. These definitions do not change the definition of the measurement rate Γ_m in Eq. (4.7); only the prefactor (here 8) changes.

a strong measurement can be viewed as the averaging of a series of weak measurements [103].

If back-action of a weak measurement is a continuous process, it is not always the case for a strong measurement. If the inverse of the measurement rate is much smaller than that of the system dynamics and the time step $\mathrm{d}t$ of the Lindblad equation, this means a strong measurement is performed at every time step $\mathrm{d}t$. One can apply a threshold to the continuous measurement record to discretize it and the back-action may be discret. During this discret back-action processes, the quantum state occurs *quantum jumps*.

This is the case for a qubit probed by a photodetector with a photon loss rate much smaller than the photodetector detection rate. In such a case, the measurement value is either “click” or “no click” and when a “click” is recorded, the qubit quantum state is projected in $|g\rangle$ and the qubit dynamics is discret.

When a measurement can be considered as continuous, we can define a jump operator L in the same way we define it when deriving the Lindblad master equation (see Sec. 2.2.3.3). The jump operator defines the measured observable and the back-action of the measurement. Under the Markov approximation (see Sec. 2.2.3.3), the jump operator is independent of t. We can take the continuous measurement record and its stochastic nature in the master equation into account, leading to a stochastic master equation that enables us to derive the density matrix at any time t, based on the measurement records [74]. If the measurement rate is large enough to discretize the measurement record, one can replace the stochastic continuous record by a stochastic discrete record [102].

4.2.3.2 *Discrete case*

An example of discrete measurement in time is the measurement of a resonator’s photon number (see Chap. 5.3.1 for more details about photon-number measurement protocols). To obtain such a measurement, we first have to entangle the qubit and the resonator in such a way that the qubit state encodes information about the photon number. Here the qubit is a probe, and a dispersive readout of its state enables us to read out the information about the photon number. We usually need a series of measurements to recover enough information to make conclusions about the photon number. As the entanglement operation takes a fixed time and we need to perform measurements after various entanglement operations, we cannot divide the measurement into smaller photon-number measurements. Thus, the photon-number measurement is a discrete measurement in time, and we cannot derive a jump operator for such a measurement. One of the goals of this thesis was to use a new approach to perform a photon-number measurement that is continuous in time (see Chap. 7). As such, for the rest of this chapter, we will focus on measurements that are continuous in time, as this is the type of measurement used in this thesis. We will pay particular attention to the homodyne and heterodyne measurement of an electromagnetic field, as they are used for dispersive qubit readouts and for the multiplexed photon-number measurements performed during this thesis.

4.3 HOMODYNE AND HETERODYNE MEASUREMENTS

4.3.1 *Principles*

Homodyne and heterodyne measurements are methods used to recover information encoded in the phase or quadrature of a radio frequency (RF) or an optical electromagnetic radiation. The homodyne (heterodyne) measurement is the measurement of one quadrature (two quadratures) of the radiation. Detection of a homodyne or heterodyne measurement is based on the down-conversion of the oscillating signal by a local oscillator (LO) oscillating at the same frequency ω as the signal; this is equivalent to performing a demodulation. The general form of a classical signal s is $s(t) = I(t)\cos(\omega t) + Q(t)\sin(\omega t)$, with $I(t)$ and $Q(t)$ being the two slowly varying quadratures. The down-converting signal takes the form $s_d(t) = I(t)\cos(\phi) + Q(t)\sin(\phi)$, with ϕ being the LO phase. By changing the phase ϕ, we can select the quadratures I or Q, which are measured by the homodyne detection. For a heterodyne measurement, the oscillating signal first has to be split into two; the first part of the signal is down-converted by the LO, while the other part is down-converted by the same LO but phase shifted by $\pi/2$. This enables us to have two down-converted signals, each of which encodes a different quadrature but with an SNR that is twice as small as the one of the homodyne detection. The splitting of the signal is mandatory, as the Heisenberg principle forbids us to measure the two quadratures (I and Q) at the same time. This process comes from quantum optics [61], and there are several ways to implement it in the microwave domain. Here we will focus on the detection scheme used in this thesis, demonstrating that we cannot focus only on the detection part but have to take into account the generation of the oscillating signal and the amplification process as well.

4.3.2 *Use of an intermediate frequency*

The generation/detection setup used in this thesis is based on four elements: the use of an intermediate frequency; the generation of a signal; the noise detection; and the amplification process. The first three will be discussed here, with the last one discussed in the following section.

The heterodyne measurement scheme used in this thesis is shown in Fig. 4.3. In order to simplify the quadrature measurement, the RF signal $s_{\mathrm{RF}}(t) = I(t)\cos(2\pi f_{\mathrm{RF}} t) + Q(t)\sin(2\pi f_{\mathrm{RF}} t)$, which oscillates at a frequency of f_{RF}, is down-converted by a detuned LO at the frequency $f_{\mathrm{LO}} = f_{\mathrm{RF}} + f_{\mathrm{IF}}$. A low-pass filter leads to an intermediate frequency (IF) signal, $s_{\mathrm{IF}}(t) = I(t)\cos(2\pi\ f_{\mathrm{IF}} t) - Q(t)\sin(2\pi f_{\mathrm{IF}} t)$, at the frequency $-f_{\mathrm{IF}}$. This signal is digitized by an analog-to-digital converter (ADC), and a numerical demodulation enables us to measure both I and Q quadratures. Because of the heterodyne detection noise (classical and quantum), I and Q are stochastic processes.

The numerical demodulation enables us to go over the cost of splitting the signal into two in order to perform a heterodyne detection. It does not break the Heisenberg principle, as the I and Q oscillate in phase quadrature and then, when the I quadrature is maximal, the Q quadrature is null and so effectively can never measure the two quadratures at the same time. This is obvious when considering a sampling frequency equal to $f_{\mathrm{IF}}/4$, wherein the digitized signal reads $[I(t_0), -Q(t_1), -I(t_2), Q(t_3), I(t_4), ...]$.

If we are to probe the system with the RF signal, we have to generate it first. As there is no arbitrary waveform generator with a sampling frequency that is high enough to generate an RF signal[5], we generate an IF signal in the 10-100 MHz range first and up-convert it into a RF signal at a few GHz. For phase-locking reasons, the up-conversion is achieved with the same LO oscillator as the down-conversion. If this up-conversion step is performed with a single IF signal and a regular mixer, it generates two RF signals at the frequencies $f_{\mathrm{LO}} \pm f_{\mathrm{IF}}$. Only one of these signals is resonant with the system and can acquire information about the system state. In this thesis, the relevant RF signal is always the lower side band: $f_{\mathrm{LO}} - f_{\mathrm{IF}}$. During the down-conversion process, the relevant RF signal is down-converted to the frequency $-f_{\mathrm{IF}}$, while the parasitic RF signal oscillating at frequency $f_{\mathrm{LO}} + f_{\mathrm{IF}}$ is down-converted to the frequency f_{IF}. The numerical demodulation of the digitized signal cannot then distinguish between these two signals, while the information contained in the relevant signal is blurred by the parasitic one. To avoid this, we generate two IF signals in phase quadrature and combine them both with the LO. This enables us to suppress the upper side band during the up-conversion process and generate only one RF signal oscillating at the frequency[6] f_{RF}. This single sideband up-conversion can also be performed using a single sideband mixer with only one IF signal.

If the amplification scheme has a bandwidth larger than $2f_{\mathrm{IF}}$, a similar problem to the one described in the previous paragraph raises the noise. After the amplification scheme, the noise at the frequencies $f_{\mathrm{LO}} \pm f_{\mathrm{IF}}$ are equivalent. The down-conversion process brings these noise to the frequency $\pm f_{\mathrm{IF}}$, and both are numerically demodulated. Thus, the relevant signal at the frequency $-f_{\mathrm{IF}}$ is attached to two noises at the frequencies $\pm f_{\mathrm{IF}}$ and leads to a reduction of the SNR by a factor two. To avoid this, we have to down-convert only those frequencies that fall below f_{LO}. This can be done either by using an image-reject (or image-rejection) mixer or by performing a numerical demodulation of the two IF signals generated by the down-conversion. The down-conversion leads to two spatially separated IF signals, the first of which reads [62]

$$\begin{aligned} s_{\mathrm{IF}}(t) =& \overline{I}(t)\cos(2\pi\ f_{\mathrm{IF}}t) - \overline{Q}(t)\sin(2\pi f_{\mathrm{IF}}t) \\ &+ \mathcal{R}e(\xi^*_{-\mathrm{IF}}(t)\mathrm{e}^{-i\omega_{\mathrm{IF}}t}) + \mathcal{R}e(\xi^*_{+\mathrm{IF}}(t)\mathrm{e}^{i\omega_{\mathrm{IF}}t}), \end{aligned} \tag{4.9}$$

with $\overline{I}$ and $\overline{Q}$ the mean value of the I and Q quadratures and $\xi_{\pm\mathrm{IF}}(t)$ being the complex noise amplitude at frequency $\pm f_{\mathrm{IF}}$. The second reads

$$\begin{aligned} s'_{\mathrm{IF}}(t) =& -\overline{I}(t)\sin(2\pi f_{\mathrm{IF}}t) - \overline{Q}(t)\cos(2\pi f_{\mathrm{IF}}t) \\ &+ \mathcal{R}e(\xi^*_{-\mathrm{IF}}(t)\mathrm{e}^{-i\omega_{\mathrm{IF}}t-i\pi/2}) + \mathcal{R}e(\xi^*_{+\mathrm{IF}}(t)\mathrm{e}^{i\omega_{\mathrm{IF}}t-i\pi/2}). \end{aligned} \tag{4.10}$$

Thus, after a numerical demodulation of $s_{\mathrm{IF}}(t)$ and $s'_{\mathrm{IF}}(t)$ at the frequency $-f_{\mathrm{IF}}$, we obtain two complex envelops $s_0(t)$ and $s'_0(t)$, respectively. They reads

$$\begin{aligned} s_0(t) &= \overline{I}(t) + i\overline{Q}(t) + \tilde{\xi}_{-\mathrm{IF}}(t) + \tilde{\xi}^*_{+\mathrm{IF}}(t) = I(t) + iQ(t) + \tilde{\xi}^*_{+\mathrm{IF}}(t), \\ s'_0(t) &= i(\overline{I}(t) + i\overline{Q}(t)) + i\tilde{\xi}_{-\mathrm{IF}}(t) - i\tilde{\xi}^*_{+\mathrm{IF}}(t) = i(I(t) + iQ(t)) - i\tilde{\xi}^*_{+\mathrm{IF}}(t), \end{aligned} \tag{4.11}$$

---

[5] Actually there are but their price tag is prohibitive

[6] There are two phase-quadrature configurations: one suppresses the lower side band, the other the upper one

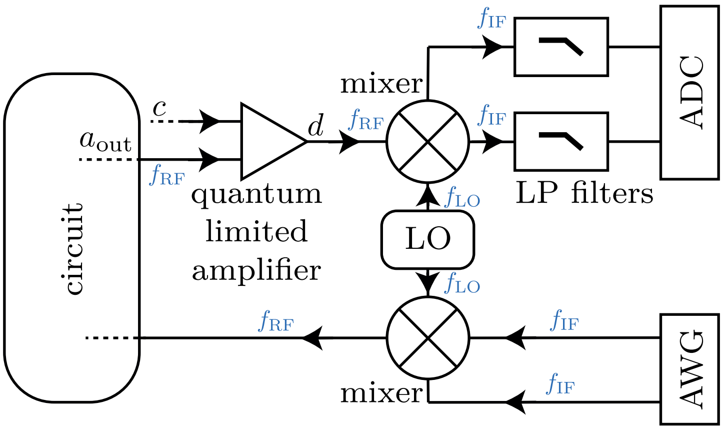

Figure 4.3: Scheme of a heterodyne measurement. An arbitrary waveform generator (AWG) emits an IF signal f_{IF}. The signal is up-converted using a mixer and an LO, generating a carrier at the frequency f_{LO}. The RF signal going out of the mixer is at the frequency $f_{\text{RF}} = f_{\text{LO}} - f_{\text{IF}}$. The RF signal is used to probe the circuit and the outgoing RF signal is amplified using a quantum-limited amplifier. The amplifier mixes and amplifies the mode a_{out}, which contains information about the circuit state with an idler mode b. The mode d going out of the amplifier is at the frequency f_{RF}. The signal is down-converted using the same LO and sent trough low pass (LP) filters. The down-converted signal oscillating at the frequency f_{IF} is then digitized using an ADC. A final demodulation at the frequency f_{IF} is numerically performed.

where $\tilde{\xi}_{\pm\text{IF}}$ are the complex noise $\xi_{\pm\text{IF}}$ filtered by the demodulation process. From Eq. (4.11), it is easy to obtain that adding $-is_0'(t)$ to $s_0(t)$ enables to suppress the noise at frequency $+f_{\text{IF}}$.

If the amplification scheme has a narrow bandwidth smaller than f_{IF} centered on the RF frequency f_{RF}, after the down-conversion the noise at the frequency f_{IF} will be negligible compared to the noise at the frequency $-f_{\text{IF}}$; thus, we can disregard it.

4.3.3 *Quantum-limited amplifiers*

Up to now, it seems one can perform a heterodyne measurement without dividing the SNR by two as is commonly the case in the optical community. This is due to the fact we have treated the ADC and the numerical demodulation as classical; we can do so as the RF signal has been amplified enough to be treated classically. In fact, we pay the same price as the optical physicists at the level of the amplification process. Let us now focus on the quantum-limited amplifier as, at this stage, the RF signal is quantum and so we have to treat the amplification as a quantum process. The outgoing mode d of the amplifier cannot simply be equal to $d = \sqrt{G}a_{\text{out}}$ with G being the gain of the amplifier, as the mode d will not satisfy the canonical commutation relationship $[d, d^\dagger] = G \neq 1$[7]. Two strategies, corresponding to two types of amplifiers, can be used to amplify.

---

[7] Except if the gain G is equal to 1, but this is not a relevant regime for an amplifier.

4.3.3.1 *Phase-preserving amplifiers*

The first strategy consists of mixing the signal mode a_out with an idler mode c. The outgoing mode d then reads

$$d = \sqrt{G} a_\text{out} - \sqrt{G-1} c^\dagger. \tag{4.12}$$

In this type of amplification process, the outgoing mode d satisfies the canonical commutation relationship $[d, d^\dagger] = 1$. Such amplifiers are called *phase-preserving* amplifiers as they amplify both quadratures of the signal. However, whatever the value of the gain G is, this amplification process divide the SNR by two. As the mode a_out is mixed with the idler, the mode d contains, at best, twice the noise of the initial signal mode a_out. This is easy to show by deriving the variance of the $d + d^\dagger$ quadrature for the mode a_out in a coherent state and the idler c in the vacuum. We find that the variance is amplified by $2G - 1 \sim 2G$ instead of only G (see Fig. 4.4).

When talking about a coherent state, we can say that the phase-preserving amplification adds half a photon of noise. As the noise added is quantum (i. e. the amount of entanglement between the system and the mode d is the same than that between the system and the mode a_out) there is no decrease in the quantum efficiency. The Eq. (4.7) is simply modified, reading [73]

$$\text{SNR} = 4\Gamma_m T. \tag{4.13}$$

If there is no decrease in the quantum efficiency, we still double the quantum noise and thus have divided the SNR by two.

Phase-preserving amplifier are well suited for heterodyne measurement but nothing forbids “discarding” one of the quadrature after the numerical demodulation to perform a homodyne measurement. However this homodyne measurement will be done with the intrinsic noise of a heterodyne measurement. We can cite the JPC and the Josephson TWPA as examples of a phase-preserving amplifier [30, 104, 99].

4.3.3.2 *Phase-sensitive amplifiers*

The second type of amplification process is called *phase sensitive*. In this case there is no need for an idler mode, as the output mode d of the amplifier is related to the signal mode a_out by

$$d = \sqrt{G} a_\text{out} + \mathrm{e}^{i\theta} \sqrt{G-1} a_\text{out}^\dagger. \tag{4.14}$$

Such an amplification process amplifies only one quadrature of the signal, de-amplifying the opposite quadrature. Thus, the amplified signal is squeezed along a direction given by the angle θ (see Fig. 4.4 with $\theta = 0$). No noise is added in this process, and Eq. (4.7) stays valid. We can still perform a heterodyne measurement using the ADC; this is because, as one quadrature was de-amplified, that quadrature contains only noise. Thus, we measure only the quadrature of a_out along the θ direction, and the measurement is equivalent to a homodyne one. This amplification process can be achieved using a JPA, for example [100].

If we measure two quadratures with the ADC, whether they encode one or both quadratures of the RF signal mode a_out depends only on the type of quantum-limited

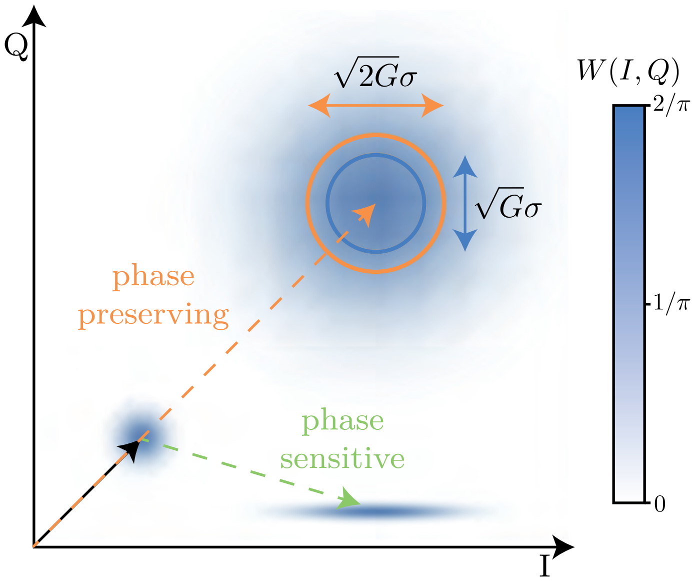

Figure 4.4: Drawing of the amplification of a coherent state in the quadrature space. The Wigner function of the original coherent state (dark arrow) is amplified with a gain $G = 10$, either in a phase-sensitive (green) or phase-preserving (orange) way $\theta = 0$ (see App. c for the definition of a Wigner function). The phase-preserving process adds half photon of noise. The blue circle (no photon of noise added) and the orange circle (half photon of noise added) represent the width of the coherent state Wigner function in the IQ space.

amplifier used: a phase-sensitive amplifier allows ideal homodyne measurement, while a phase-preserving amplifier allows ideal heterodyne and inefficient homodyne measurements. In this thesis, the quantum-limited amplifier we used was a TWPA (phase-preserving amplifier); the next section will present its characterization.

4.4 AN EXAMPLE OF A PHASE-PRESERVING AMPLIFIER: THE JOSEPHSON TRAVELLING-WAVE PARAMETRIC AMPLIFIER

4.4.1 *Principle*

The parametric amplification process is based on the interaction of a signal with a non-linearity, thereby enabling the wave-mixing process. The non-linearity has to be excited by a source of energy, a large electromagnetic field called a pump for a superconducting quantum-limited amplifier. The pump oscillates at the frequency f_p in order to amplify the signal at the frequency f_s and an idler mode at the frequency f_i. Two types of mixing processes are used for parametric amplification: three-wave mixing, where $f_\mathrm{p} = f_\mathrm{s} + f_\mathrm{i}$, and four-wave mixing, where $2f_\mathrm{p} = f_\mathrm{s} + f_\mathrm{i}$. The parametric amplification gain depends on the interaction time between the signal and the non-linear medium. There are two approaches that can be used to increase this interaction time: embed the non-linearity in a resonator [98, 105, 106, 107], or propagate the signal in a non-linear transmission line [30, 108, 109]. The Josephson travelling-wave parametric amplifier

(TWPA) uses the second approach, using the microwave analogue of a non-linear optical fiber. The transmission line is made using the JJ as the source of the non-linearities [109]. The main issue with such an amplifier is the phase mismatch, also called momentum conservation. During the propagation, the signal, idler, and pump phases all change differently, leading to a decrease in the gain. The phase mismatch of a Josephson TWPA, based on a four-wave mixing non-linearity, reads

$$\Delta k = \Delta k_{\mathrm{disp}} + \Delta k_{\mathrm{Kerr}}, \tag{4.15}$$

where Δk_{disp} is the phase mismatch caused by the dispersion relationship of the transmission line [110] and Δk_{Kerr} is the phase mismatch due to the third-order phase modulation process which depends on the pump power [111, 112]. If the phase mismatch is null, the gain increases exponentially with the transmission line length. On the contrary, if the phase mismatch is non-zero, the gain increases only quadratically with the transmission line length [112].

There are two approaches to cancelling the phase mismatch. We can engineer the dispersion relation, changing Δk_{disp} either by using a spatial impedance modulation (which opens a gap in the dispersion relation [108, 113, 114, 115, 116, 117, 118, 119, 120]) or by introducing resonant elements in the transmission [30, 121, 116], thereby creating a stop-band gap. Alternatively, we could engineer Δk_{Kerr}, the third-order phase modulation process, by reversing the sign of the non-linearity [122].

Various types of superconducting TWPAs exist; these differ according to the type of non-linearity, the phase mismatch solution and the meta-material used (i. e. the source of the non-linearity). The meta-materials used are either based on JJ or on non-linear kinetic inductance [108, 113, 114, 115, 117, 118, 119, 116]. Superconducting TWPAs are amplifiers with numerous aspects that could still be improved (e. g., by improving noise, saturation power, or reciprocity). The review [123] discusses state-of-the-art TWPAs and the open challenges for the future in this regard.

4.4.2 *First characterization*

The Jospehson TWPA used in this thesis was made by the Lincoln Labs. It is based on a four-wave mixing process and the phase mismatch is canceled using resonant elements. Thus, the dispersion relation shows a gap and the phase mismatch is canceled when pumping the amplifier at a frequency close from the gap. We first characterized the TWPA using the overlap between the $|e\rangle$ and $|g\rangle$ state measurement quadrature distributions of a qubit. This approach does not need any calibration but is not quantitative. Then we calibrated the measurement-induced dephasing of a qubit in order to measure the quantum efficiency of the TWPA (see section 4.4.3). To confirm the measured quantum efficiency, we check its value using the correlations between weak and strong measurements of the qubits (see section 4.4.4).

In order to characterize the TWPA's quantum efficiency, we used a circuit with a transmon qubit and a resonator, the whole setup is detailed in Fig. b.1 in App. b. The cavity allows us to read the state of the qubit by dispersive measurement. The resonator frequency is $\omega_r/2\pi = 7.13766$ GHz and the qubit frequency $\omega_q/2\pi = 4.18337$ GHz. We measured an anharmonicity for the qubit of $\alpha/2\pi = 160$ MHz, a cross-Kerr rate

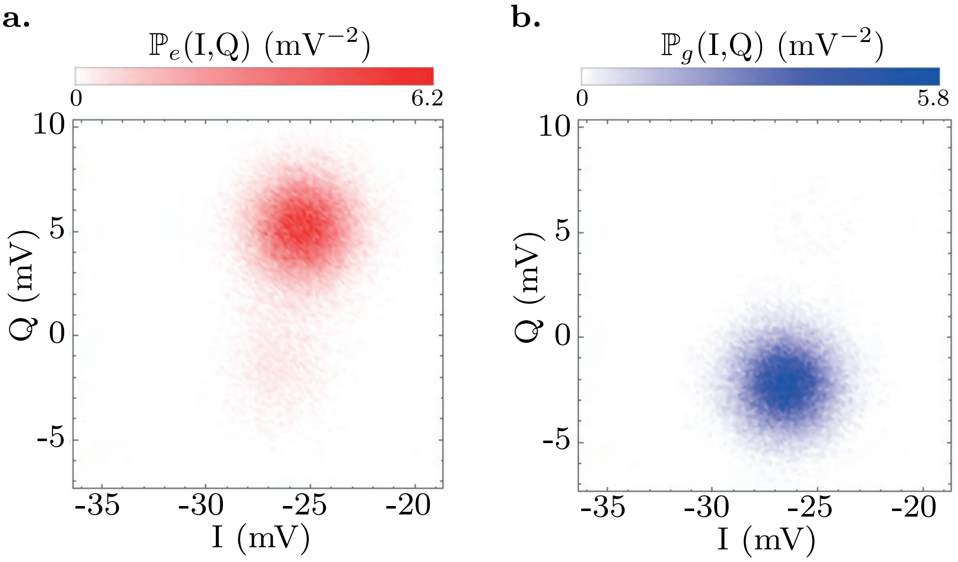

Figure 4.5: Heterodyne measurement probability distribution for **a.** $|e\rangle$ and **b.** $|g\rangle$ states. The distribution corresponding to the e state is deformed because of decoherence ($T_1 = 12\ \mu s$) during the measurement duration 1.8 μs. The TWPA is pumped at 6.0035 GHz and with 9.8 dBm power referred to the room temperature stage.

between the qubit and the resonator $\chi/2\pi = 0.58$ MHz and a coupling rate for the resonator $\kappa/2\pi = 3.91$ MHz. We used the TWPA to amplify the transmitted signal at the resonator frequency. We performed heterodyne measurement of that signal (see Sec. 4.3), which gave us the probability densities (or probability distributions) of the quadratures in the (I,Q) space for each qubit state. We denote these distributions by $\mathbb{P}_g$(I,Q) for $|g\rangle$ state and $\mathbb{P}_e$(I,Q) for $|e\rangle$ state. Fig. 4.5 shows these distributions for a pump frequency of 6.035 GHz and a pump power of 9.8 dBm.

For several sets of frequencies and powers of the TWPA pump, we measured the overlap between $|e\rangle$ and $|g\rangle$ probability distributions of the qubit. We define the overlap $\mathcal{O}_{eg}$ as

$$\mathcal{O}_{eg} = \frac{\int\int \mathrm{dIdQ}\mathbb{P}_g(\mathrm{I,Q})\mathbb{P}_e(\mathrm{I,Q})}{\sqrt{\int\int \mathrm{dIdQ}\mathbb{P}_g(\mathrm{I,Q})^2 \int\int \mathrm{dIdQ}\mathbb{P}_e(\mathrm{I,Q})^2}}. \tag{4.16}$$

The Fig. 4.6 shows the dependence of the overlap with the TWPA pump parameters. The gap opened in the dispersion relation due to added resonant elements correspond to the yellow band between 6.1 GHz and 6.6 GHz. As expected, the minimum of overlap is obtain when pumping close to the gap. We decided to zoom in on the area around 6 GHz and pump power of 10 dBm referred to the room temperature stage (red box on the Fig. 4.6a), which seems to have the best discrimination between $|e\rangle$ and $|g\rangle$ states (see Fig. 4.6b). This first characterization enables to choose a first TWPA working point before going into more quantitative analyses.

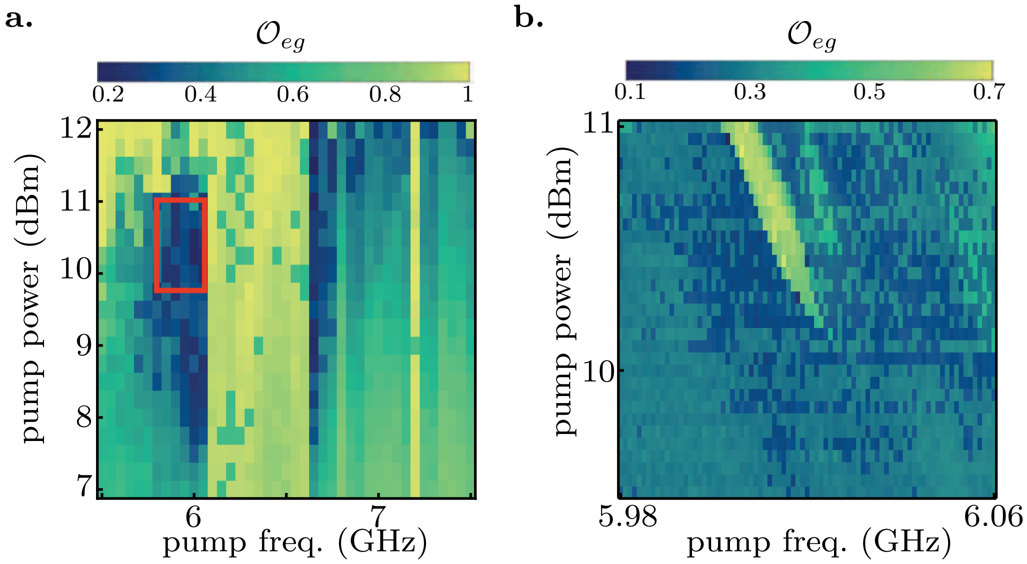

Figure 4.6: Overlap between the probability distributions of $|e\rangle$ and $|g\rangle$ states. We first sweep the pump frequency and then sweep the pump power for each frequency. We see the gap of the dispersion relation between 6.1 GHz et 6.7 GHz. **a.** Large scan of the TWPA pump parameter. The red square defines the area studied with a refined mesh. **b.** Refined scan of the area showing the best overlap.

4.4.3 *Quantum efficiency map*

The relevant quantities one wants to measure for a quantum-limited amplifier are the gain, the quantum efficiency or the noise rise of the amplification scheme as a function of the pump parameters. One can derive those quantities from the $|e\rangle$ and $|g\rangle$ probability distributions.

The quantum efficiency can be derived using Eq. (4.13), the SNR is derived from the probability distributions and the dephasing rate can be calibrated using Ramsey oscillations. The pulse sequence to probe the measurement-induced dephasing rate is represented on Fig. 4.7. This sequence is equivalent to Ramsey oscillations obtained with the cavity driven in a steady state during the whole time. To reach the steady

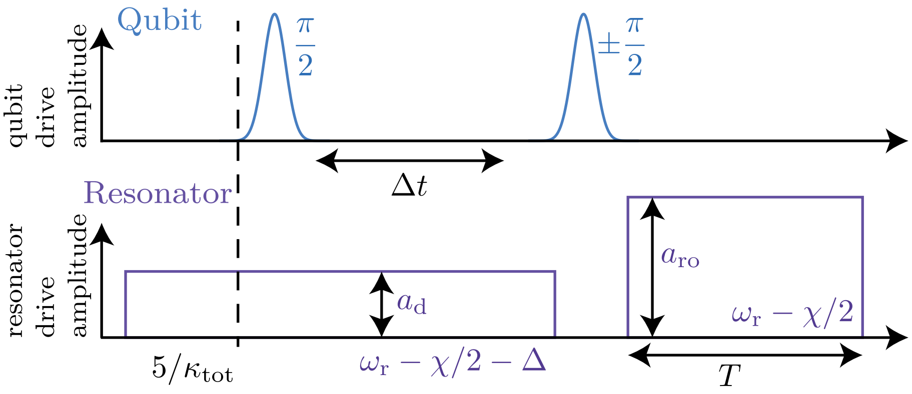

Figure 4.7: Ramsey pulse sequence used to measure the measurement-induced dephasing rate.

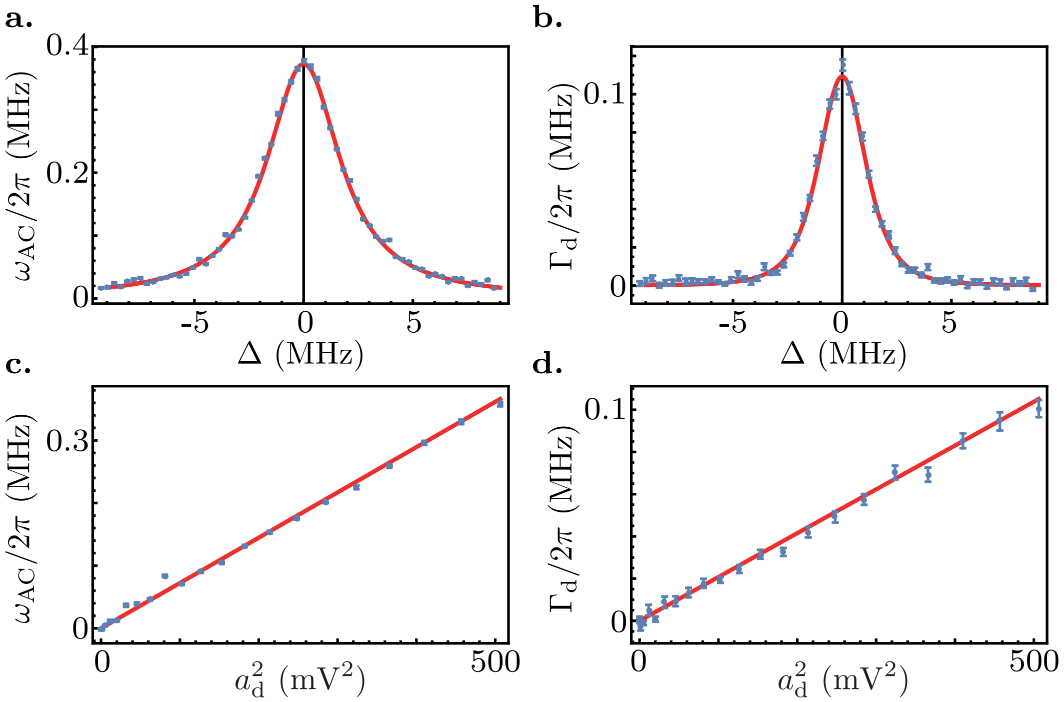

Figure 4.8: AC Stark shift ω_{AC} and measurement-induced dephasing rate Γ_d as a function of the resonator drive detuning Δ and amplitude a_{d}. **a.** and **b.** AC Stak shift and measurement-induced dephasing rate as a function of detuning at fixed amplitude a_{d}. **c.** and **d.** AC Stak shift and measurement-induced dephasing rate as a function of amplitude for $\Delta = 0$.

state of the cavity, we wait a few $1/\kappa$ before the first $\pi/2$ pulse. For each set of parameters (detuning Δ and drive amplitde a_{d}), we repeated the sequence, which contains measurement for several values of Δt, twice. Once with a $\pi/2$ pulse before the qubit readout and once with a $-\pi/2$ pulse in order to create a reference that supresses low frequency noise. We swept the time Δt between the two qubit pulses to measure Ramsey oscillations. By fitting them, we access the AC Stark shift and the measurement-induced dephasing rate for different detuning Δ and amplitude a_d. In order to determine the measurement-induced dephasing rate at the readout amplitude a_{ro}, one has to calibrate the dependency of the AC Stark shift and the measurement-induced dephasing rate with the amplitude a_{d} and the detuning Δ (see Fig. 4.8). As explain in Sec. 2.5.3, the measurement-induced dephasing rate and the AC Stark shift read

$$\begin{cases} \Gamma_d(t) = \chi\mathcal{I}m(\alpha_{\mathrm{g}}(t)^*\alpha_{\mathrm{e}}(t)) \\ \omega_{AC}(t) = \chi\mathcal{R}e(\alpha_{\mathrm{g}}(t)^*\alpha_{\mathrm{e}}(t)) \end{cases}, \tag{4.17}$$

with α_{g} and α_{e} the complex amplitudes of the resonator field.

The signal to noise ratio can be measured from the distance ΔV between the mean of $|e\rangle$ and $|g\rangle$ distributions and the standard deviation σ of the $|g\rangle$ distribution (assuming it is the same as the $|e\rangle$ distribution). The SNR reads $SNR = \Delta V^2/\sigma^2$. Thus, the quantum efficiency reads

$$\eta = \frac{\Delta V^2}{\sigma^2} \times \frac{1}{4\int_0^T \Gamma_d(t, a_{\mathrm{ro}})\mathrm{d}t}, \tag{4.18}$$

with T the integration time of the heterodyne measurement and where the time integral takes into account the transient regime of the resonator during the read out[8].

With a TWPA pump set at frequency 6.035 GHz and power 9.8 dBm (referred to the room temperature stage), we have $\Delta V = 7.5$ mV and $\sigma = 1.442$ mV for $\Gamma_{\mathrm{d}} = 31.8\,\mathrm{rad\,\mu s^{-1}}$ and $T = 1.8\,\mathrm{\mu s}$. This leads to a quantum efficiency of the full amplification scheme of

$$\eta = 0.118. \tag{4.19}$$

One has to emphasize that the setup contained a beam splitter between the TWPA and the resonator, leading to the decrease of the quantum efficiency by at least a factor two. The microwave setup was designed in order to perform photocounting experiment (see Chaps. 5, 6 and 7) and two signals had to be mixed before being amplifier with the TWPA. For the TWPA characterization, only one of the two signals was used.

The $|e\rangle$ and $|g\rangle$ probabilty distributions are measured for various powers and frequencies of the TWPA pump (we first sweep the power and then sweep the frequency for each pump power) and the quantum efficiency is computed for each pump parameter set. In order to measure also the TWPA gain, we measured the distance ΔV between the two distribution with the TWPA pump off and defined the TWPA gain as

$$G_{\mathrm{TWPA}} = 20\log_{10}(\frac{\Delta V_{\mathrm{TWPA\ on}}}{\Delta V_{\mathrm{TWPA\ off}}})\ \mathrm{dB}. \tag{4.20}$$

In the same way, to measure the TWPA noise rise, we chose a arbitrary pixel as reference and define the noise rise as

$$P_{nr} = 20\log_{10}(\frac{\sigma}{\sigma_{ref}})\ \mathrm{dB}. \tag{4.21}$$

Thus, the noise rise is the amount by which the noise increases or decreases compare to the reference.

Figs. 4.9 show maps of the quantum efficiency, gain of the TWPA, and noise rise. One can see the there is a specific area, close to the gap for which the highest quantum efficiency is reached at medium pump power. If the gain continues to increase when increasing the pump power, the noise rise increases faster leading to a decrease of the quantum efficiency. One can look at the correlation between the gain and the quantum efficiency (see Fig. 4.10). The quantum efficiency saturates at large gain and there are no clear correlations between the two.

4.4.4 *Weak and stong measurement correlations*

Another way to compute the quantum efficiency is to measure the correlations between a weak and a strong measurement of the qubit state. The weak measurement backaction can be derived from the weak measurement record and a prediction of the strong

---

[8] If we assume the resonator in its steady state, the measurement-induced dephasing does not depend on the time t and we recover the expression of Eq. (4.13).

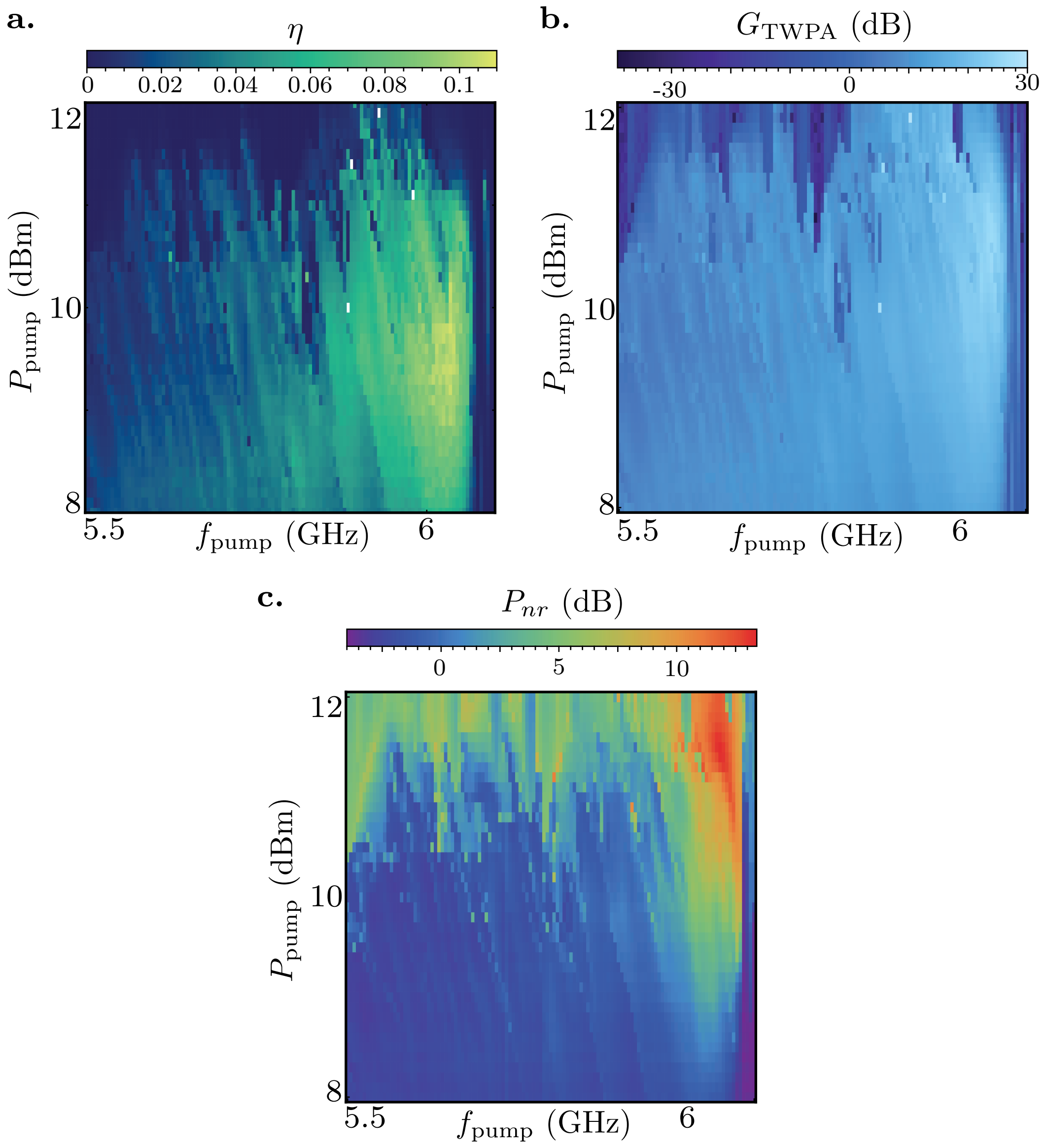

Figure 4.9: **a.** Quantum efficiency η, **b.** gain G_{TWPA} and **c.** power noise rise P_{nr} as a function of the TWPA pump frequency and power. White squares correspond to data impossible to analyze.

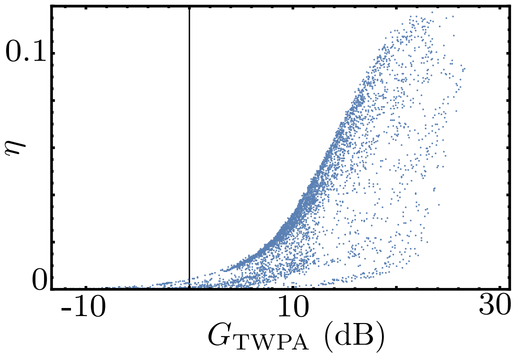

Figure 4.10: quantum efficiency as a function of the gain of the TWPA.

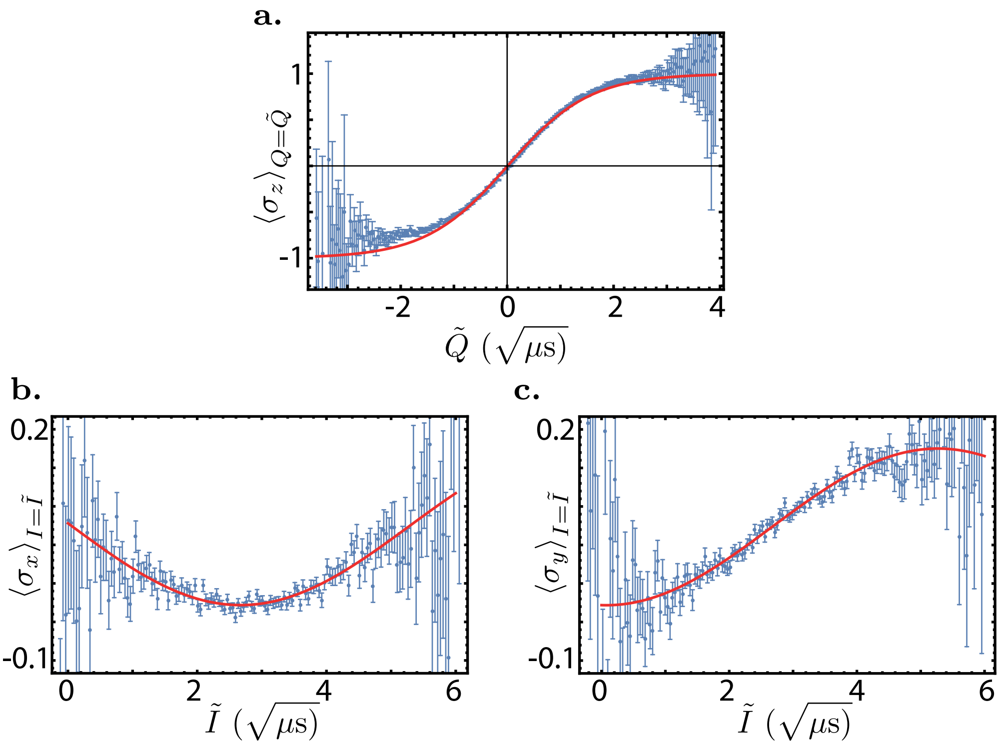

Figure 4.11: Correlations between weak and strong measurements of the qubit state **a.** σ_z and Q, **b.** σ_x and I, and **c.** σ_y and I. Red lines are obtained using Eq. (4.22)

measurement mean value can be done based on the weak measurement record. To carry on this experiment, we start from an equal superposition of $|e\rangle$ and $|g\rangle$ qubit states. We then let the qubit interact with a weak drive at the frequency of the readout resonator. The drive amplitude is ten times smaller than the one of a strong measurement. After 600 ns of interaction, we perform a tomography of the qubit. Two traces are acquired. First we record the reflected weak drive amplitude. The homodyne measurement of this signal gives us a weak measurement of σ_z when measuring the Q quadrature or $i\sigma_z$[9] when measuring the I quadrature [74]. The second measurement is a full qubit state tomography. This measurement either gives us the value of σ_x, σ_y or σ_z. For every realization we have therefore a couple $[\tilde{Q}/\tilde{I}\ ;\ \sigma_x/\sigma_y/\sigma_z]$.

With the two records we can post-select on the weak measurement values of Q or I to compute the mean value of the tomography. It means that for every possible value $\tilde{Q}$ (or $\tilde{I}$) of the weak measurement, we select all the realizations with $Q = \tilde{Q}$ (or $I = \tilde{I}$) and we compute the mean value of σ_x, σ_y or σ_z for those realizations. This allows us to have access to the correlations between weak and strong measurements. We expect the following behaviors for the correlations [74]

$$\begin{aligned}\langle\sigma_z\rangle_{Q=\tilde{Q}} &= \tanh(\mathrm{artanh}(z_0) + \sqrt{\eta\Gamma_d}\tilde{Q})\\ \langle\sigma_x\rangle_{I=\tilde{I}} &= \cos(\sqrt{\eta\Gamma_d}\tilde{I})e^{(1-\eta)\Gamma_d t} \qquad ,\\ \langle\sigma_y\rangle_{I=\tilde{I}} &= \sin(\sqrt{\eta\Gamma_d}\tilde{I})e^{(1-\eta)\Gamma_d t}\end{aligned} \tag{4.22}$$

---

[9] The measurement of $i\sigma_z$ give access to the evolution of the phase between $|e\rangle$ and $|g\rangle$ states.

with z_0 the mean value of σ_z after the $\pi/2$ preparation pulse and Q and I the weak measurement records normalized with respect to the noise. The normalization of the weak measurement records is such that the variance of the two records Q and I is equal to the weak measurement time[10]. Fig. 4.11 shows measured and predicted correlations for $t = 600$ ns, and $\Gamma_d = 31.8$ rad.MHz. We extract from the data the following value for the quantum efficiency

$$\begin{cases} \eta = 0.14 \text{ for } \sigma_z \\ \eta = 0.12 \text{ for } \sigma_x \text{ and } \sigma_y \end{cases} . \tag{4.23}$$

These results concur with the former determination of the quantum efficiency in the last section.

---

[10] There are two ways to normalize the records in the stochastic master equation. Here we decided to normalize it by the diffusion coefficient of the noise. In this case, the unit of the record is in unit of square root of second [8].

Part II

PHOTOCOUNTING

5

PHOTOCOUNTERS

A photocounter is a key element for any quantum microwave toolbox. Photocounters are needed in numerous situations such as quantum key distribution [124, 125, 126, 127], quantum computing [128, 129], quantum communication [130, 131, 132, 133, 134, 135, 136, 137], quantum simulations [138, 139, 140, 141], and boson sampling [140, 142, 143, 144, 145]. However, counting microwave photons is a harder challenge than counting optical photons. In optics, it is solved thanks to single-photon avalanche photodiodes and superconducting nanowire single-photon detectors [146]. However this component is still an open research field for the microwave domain. The major difference between the two (microwave and optical photons) comes from the energy scale. If an optical photon has an energy of about 10^{15} Hz, a microwave photon has an energy up to 10^6 times smaller. An optical photon has an energy that is bigger than the room-temperature photon noise and so can be detected at room temperature. In comparison, a microwave photon is negligible compare to the room-temperature photon noise. So a probe working at low temperatures that is sensitive to a small energy scale (small compared to optical energy) is required.

The variety of counting modes in circuit and cavity QED is rather large. First, we can consider situations in which we only try to detect whether there is more than zero photons. In such cases, we will talk about photodetectors, not photocounters. There exist already a large range of such devices and protocols [76, 147, 148, 149, 150, 151, 29, 27], which are starting to be used in order to improve measurements in situations such as electron spin resonance experiments [152]. We can classify superconducting photocounter protocols into two types: those for propagating photons [27, 153]; and those for stationary photons (i. e. photons stored in a stationary mode) [22, 23, 21, 26, 24, 25, 28]. In this thesis, we will focus on stationary photocounters; however, any stationary photocounter can become a propagative photocounter using a catch-and-release protocol [27]. At the beginning of this thesis, all the known superconducting photocounters used a qubit as a probe in order to measure the number of photons. A series of binary questions were then asked iteratively in order to refine our knowledge about the system state, with each answer providing, at most, one bit of information about the system state. All these measurements were discrete in time, and the information was extracted piece by piece. The goal of this thesis is to build to a photocounter that is continuous in time, that can extract all the information at the same time, and that offers a performance that is better compare to that offered by a state-of-the-art photocounter. This type of photon counter is missing in the quantum engineering tool box as, at the beginning of this thesis, there was no continuous photon counter and all of the former photon counter was measuring the number of photon using decimation, i. e. extracting the photon number information piece by piece. This is an interesting challenge, as it is not possible to encode more than one bit of information in a qubit state and it would enable one to perform adaptative measurements or feedbacks based on continuous record and to coutinuously monitor the photon number which may encode the syndrome of a quantum error correction code [154].

After a description of the circuit used, this chapter will focus on the usual way in which photocounting is achieved; this was first introduced in relation to Rydberg atoms [22, 23], before being implemented in circuit QED [21, 26]. We will also discuss the numerous protocols involved. This chapter will finish with a discussion regarding the limitations of the usual approach and how to overcome these limitations. The main experiments will then be presented in the two chapters that follow.

Remarks: Most of the results shown in this chapter are published in Ref. [155]

5.1 CIRCUIT

5.1.1 *Design*

The circuit is composed of 4 electromagnetic modes whose parameters can be found in Sec. 5.1.2. A high-Q harmonic oscillator, called *storage mode*, is composed of a $\lambda/2$ coplanar waveguide (CPW) resonator (green in Fig. 5.1). The storage resonator is capacitively coupled to two transmon qubits. The *multiplexing qubit* (orange) has a spontaneous photon emission rate $\Gamma_{1,\mathrm{mp}} = (44\ \mathrm{ns})^{-1}$ into a transmission line that is high compared to other modes. In contrast, the *yes-no qubit* (blue) is capacitively coupled to a low-Q *readout resonator* (purple) and has a long coherence time $T_{2,\mathrm{yn}} = 27\ \mu\mathrm{s}$. The circuit enables the implementation of the standard approach to count the number of photons in the storage mode, which resonates at $f_\mathrm{s} = \omega_\mathrm{s}/2\pi = 4.558$ GHz. The yes-no qubit with a frequency $f_\mathrm{yn} = \omega_\mathrm{yn}/2\pi = 3.848$ GHz is used to perform the standard photocounting approach or storage mode tomography; while the multiplexing qubit with a frequency $f_\mathrm{mp} = \omega_\mathrm{mp}/2\pi = 4.238$ GHz is used to perform continuous photocounting (see Chaps. 6 and 7). Both qubits are dispersively coupled to the resonator so that their frequency respectively redshifts by $\chi_{\mathrm{s,yn}}/2\pi = 1.4$ MHz and $\chi_{\mathrm{s,mp}}/2\pi = 4.9$ MHz per additional photon in the storage mode. The measurement setup is described in App. b.

5.1.2 *Parameters*

All parameters of the 4 modes can be measured using standard circuit-QED techniques (see Table 5.1). Frequencies of the readout mode and multiplexing qubit are measured by spectroscopy. Frequencies of storage mode and yes-no qubit are measured using two-tone spectroscopy with the readout mode. Yes-no qubit decay and decoherence rate are measured with the time evolution of the probability to find the qubit excited after a π pulse and using Ramsey oscillations. Readout mode decay rate and cross-Kerr rate between readout mode and yes-no qubit are measured using the measurement-induced dephasing rate by the readout mode on the yes-no qubit. Cross-Kerr rate between the storage mode and the two qubits are measured using qubit spectroscopy with the storage state initialized in various coherent states. Anharmonicities are measured using spectroscopy of the qubit excited state. Decay and decoherence rates of the storage mode are measured with the time evolution of the probability to have 0 photon in the storage mode after a displacement and storage Ramsey interferometry experiment.

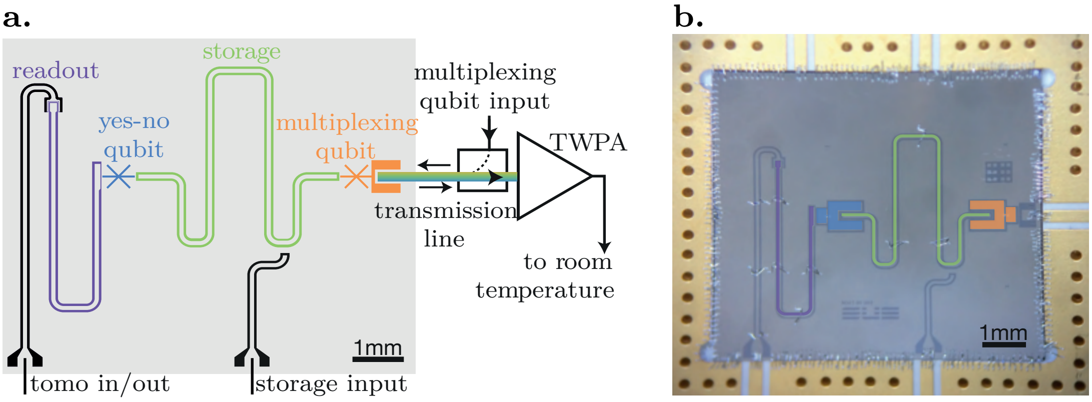

Figure 5.1: **a.** Scheme of the device in coplanar waveguide architecture. The storage mode (green) is coupled to a transmon multiplexing qubit (orange), which is directly coupled to a transmission line (rainbow). A directional coupler and broadband Josephson TWPA allow us to probe the qubit in reflection. An additional transmon yes-no qubit (blue) and its readout resonator (purple) are used as a reference photon counter and storage tomography. **b.** Optical picture of the circuit. The readout resonator is colored in purple, storage mode in green, yes-no qubit in blue and multiplexing qubit in orange. All dark grey areas are silicon, grey areas are niobium on silicon and Josephson junctions are made of Al/AlOx/Al.

Multiplexing qubit decay and decoherence rates are measured by fitting the qubit spectroscopy for various drive amplitudes. All those parameters enable us to write a master equation model based on the Lindblad equation with the Hamiltonian

$$\begin{aligned}\hat{H} \;=\;& \hbar\omega_{\mathrm{ro}}\hat{n}_{\mathrm{ro}}+\hbar\omega_{\mathrm{s}}\hat{n}_{\mathrm{s}}+\hbar\omega_{\mathrm{yn}}\hat{n}_{\mathrm{yn}}+\hbar\omega_{\mathrm{mp}}\hat{n}_{\mathrm{mp}}\\ &-\hbar\chi_{\mathrm{ro,yn}}\hat{n}_{\mathrm{ro}}\hat{n}_{\mathrm{yn}}-\hbar\chi_{\mathrm{s,yn}}\hat{n}_{\mathrm{s}}\hat{n}_{\mathrm{yn}}-\hbar\chi_{\mathrm{s,mp}}\hat{n}_{\mathrm{s}}\hat{n}_{\mathrm{mp}}\\ &-\hbar\chi_{\mathrm{yn,yn}}\hat{n}_{\mathrm{yn}}(\hat{n}_{\mathrm{yn}}-1)-\hbar\chi_{\mathrm{mp,mp}}\hat{n}_{\mathrm{mp}}(\hat{n}_{\mathrm{mp}}-1),\end{aligned} \tag{5.1}$$

where $\hat{n}_{\mathrm{ro}}$, $\hat{n}_{\mathrm{s}}$, $\hat{n}_{\mathrm{yn}}$, and $\hat{n}_{\mathrm{mp}}$ are the photon number operators respectively for the readout, storage, yes-no qubit and multiplexing qubit. $\chi_{a,b}$ is the cross-Kerr rate between modes a and b. $\chi_{a,a}$ is the self-Kerr rate of the mode a. The master equation on the system density matrix ρ reads

$$\begin{aligned}\dot{\rho} \;=\;& -\frac{i}{\hbar}[\hat{H},\rho]+\Gamma_{\mathrm{ro}}\mathcal{D}(\hat{a}_{\mathrm{ro}})\rho+2\Gamma_{\phi,\mathrm{s}}\mathcal{D}(\hat{n}_{\mathrm{s}})\rho+\Gamma_{1,\mathrm{s}}\mathcal{D}(\hat{a}_{\mathrm{s}})\rho\\ &+2\Gamma_{\phi,\mathrm{yn}}\mathcal{D}(\hat{n}_{\mathrm{yn}})\rho+\Gamma_{1,\mathrm{yn}}\mathcal{D}(\hat{a}_{\mathrm{yn}})\rho+2\Gamma_{\phi,\mathrm{mp}}\mathcal{D}(\hat{n}_{\mathrm{mp}})\rho\\ &+\Gamma_{1,\mathrm{mp}}\mathcal{D}(\hat{a}_{\mathrm{mp}})\rho,\end{aligned} \tag{5.2}$$

where $\hat{a}_b$ is the annihilation operator of mode b. For a qubit mode b, the dephasing rate $\Gamma_{\phi,\mathrm{b}}$ is linked to the decoherence rate by $\Gamma_{2,\mathrm{b}}=\Gamma_{1,\mathrm{b}}/2+\Gamma_{\phi,\mathrm{b}}$.

5.2 STANDARD PHOTOCOUNTING

5.2.1 *Principle*

In the standard approach [21, 26], which probes whether there are k photons, the probability to have k photons is encoded as the probability $\mathbb{P}_{\mathrm{e}}$ to excite the yes-no

circuit parameters	symbol	Hamiltonian term	value
readout resonator frequency	$\omega_{\mathrm{ro}}/2\pi$	$\hbar\omega_{\mathrm{ro}}\hat{n}_{\mathrm{ro}}$	7.138 GHz
storage mode frequency	$\omega_{\mathrm{s}}/2\pi$	$\hbar\omega_{\mathrm{s}}\hat{n}_{\mathrm{s}}$	4.558 GHz
yes-no qubit frequency	$\omega_{\mathrm{yn}}/2\pi$	$\hbar\omega_{\mathrm{yn}}\hat{n}_{\mathrm{yn}}$	3.848 GHz
multiplexing qubit frequency	$\omega_{\mathrm{mp}}/2\pi$	$\hbar\omega_{\mathrm{mp}}\hat{n}_{\mathrm{mp}}$	4.238 GHz
readout/yes-no qubit cross-Kerr rate	$\chi_{\mathrm{ro,yn}}$	$-\hbar\chi_{\mathrm{ro,yn}}\hat{n}_{\mathrm{ro}}\hat{n}_{\mathrm{yn}}$	$2\pi \times 0.4$ MHz
storage/yes-no qubit cross-Kerr rate	$\chi_{\mathrm{s,yn}}$	$-\hbar\chi_{\mathrm{s,yn}}\hat{n}_{\mathrm{s}}\hat{n}_{\mathrm{yn}}$	$2\pi \times 1.4$ MHz
storage/multiplexing qubit cross-Kerr rate	$\chi_{\mathrm{s,mp}}$	$-\hbar\chi_{\mathrm{s,mp}}\hat{n}_{\mathrm{s}}\hat{n}_{\mathrm{mp}}$	$2\pi \times 4.9$ MHz
yes-no qubit self-Kerr rate	$\chi_{\mathrm{yn,yn}}$	$-\hbar\chi_{\mathrm{yn,yn}}\hat{n}_{\mathrm{yn}}(\hat{n}_{\mathrm{yn}}-1)$	$2\pi \times 160$ MHz
multiplexing qubit self-Kerr rate	$\chi_{\mathrm{mp,mp}}$	$-\hbar\chi_{\mathrm{mp,mp}}\hat{n}_{\mathrm{mp}}(\hat{n}_{\mathrm{mp}}-1)$	$2\pi \times 116$ MHz

circuit parameters	symbol	jump operator	value
readout decay rate	Γ_{ro}	$\Gamma_{\mathrm{ro}}\mathcal{L}(\hat{a}_{\mathrm{ro}})\rho$	$(40\ \mathrm{ns})^{-1}$
storage decay rate	$\Gamma_{1,\mathrm{s}}$	$\Gamma_{1,\mathrm{s}}\mathcal{L}(\hat{a}_{\mathrm{s}})\rho$	$(3.8\ \mu\mathrm{s})^{-1}$
storage decoherence rate	$\Gamma_{2,\mathrm{s}}$	$2\Gamma_{\phi,\mathrm{s}}\mathcal{L}(\hat{n}_{\mathrm{ro}})\rho$	$(2\ \mu\mathrm{s})^{-1}$
yes-no decay rate	$\Gamma_{1,\mathrm{yn}}$	$\Gamma_{1,\mathrm{yn}}\mathcal{L}(\hat{a}_{\mathrm{yn}})\rho$	$(20\ \mu\mathrm{s})^{-1}$
yes-no decoherence rate	$\Gamma_{2,\mathrm{yn}}$	$2\Gamma_{\phi,\mathrm{yn}}\mathcal{L}(\hat{n}_{\mathrm{yn}})\rho$	$(27\ \mu\mathrm{s})^{-1}$
multiplexing decay rate	$\Gamma_{1,\mathrm{mp}}$	$\Gamma_{1,\mathrm{mp}}\mathcal{L}(\hat{a}_{\mathrm{mp}})\rho$	$(42\ \mathrm{ns})^{-1}$
multiplexing decoherence rate	$\Gamma_{2,\mathrm{mp}}$	$2\Gamma_{\phi,\mathrm{mp}}\mathcal{L}(\hat{n}_{\mathrm{mp}})\rho$	$(84\ \mathrm{ns})^{-1}$

Table 5.1: Table of circuit parameters.

qubit by driving it with a π-pulse at $f_{\mathrm{drive}} = f_{\mathrm{yn}} - k\chi_{\mathrm{s,yn}}$. The state of the yes-no qubit is read out using the dedicated resonator. As we used the qubit as a probe, one cannot measure more than 1 bit of information at each readout. To demonstrate this photon-counting ability, we use a microwave tone at f_{s} to prepare the storage mode in a coherent state $|\beta\rangle = e^{-|\beta|^2/2}\sum_{n=0}^{+\infty}\frac{\beta^n}{\sqrt{n!}}|n\rangle$, which is a superposition of all Fock states with mean photon number $\bar{n} = |\beta|^2$. The probability $\mathbb{P}_{\mathrm{e}}$ is then measured and shows resolved peaks as a function of f_{drive} for every photon number up to about 7 (Fig. 5.2). One can notice a decrease of the signal amplitude for high photon number compare to the master equation model. This decrease has two origins. First, there exists a parasitic cross-Kerr between the readout resonator mode and the storage mode. Thus, for large photon number in the storage, the resonator frequency shifts and the qubit calibration is not anymore valid. One can erase this effect by calibrating this frequency shift and change the readout pulse frequency accordingly. Second, because the displacement pulse envelop is a troncated Gaussian function, it starts and finishes with a step with a high of about 13% of the pulse amplitude. This leads to high frequency components which can ionize the qubit for large displacement [76] leading to a decrease of the signal amplitude. This effect can be decreased with better pulse shaping.

This experiment shows the simpler photocounting protocols based on the standard approach. We will discuss the other protocols in Sec. 5.3.1. Yet, using this experiment one can calibrate the number of photons in the storage mode.

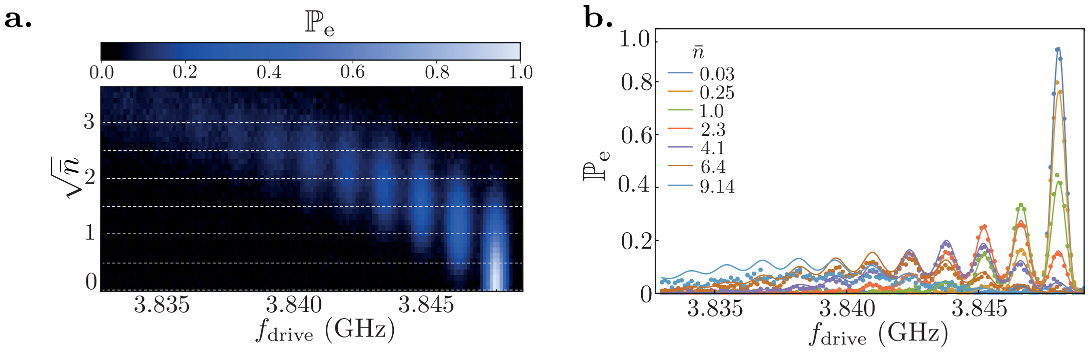

Figure 5.2: Standard photon-counting. The storage mode is prepared in a coherent state with an average photon number $\bar{n}$ using a microwave pulse at storage frequency and amplitude V_s. **a, b,** Measured probability $\mathbb{P}_\mathrm{e}$ that the yes-no qubit gets excited by a π-pulse at a frequency f_drive. Peaks appear at $f_\mathrm{yn} - k\chi_\mathrm{s,yn}$ and indicate the probability to store k photons. The dots in **b** are cuts along the dashed lines in **a** and match the master equation model (solid lines), hence providing a calibration of $\bar{n}$ as a function of the drive amplitude V_s.

5.2.2 *Photon number calibration*

In this experiment, we use the standard photocounting measurement as a calibration of the photon number in the storage mode. The linear relation between β and the amplitude V_s of the tone at ω_s is extracted using a master-equation based model reproducing the measured $\mathbb{P}_\mathrm{e}$ (solid lines in Fig. 5.2b). The storage mode can be displaced by driving it on resonance with a voltage $V_\mathrm{s}(t)\cos(\omega_\mathrm{s} t + \phi_\mathrm{s})$, where $V_\mathrm{s}(t)$ is the pulse envelope. The driving Hamiltonian of the storage mode reads

$$i\hbar(\epsilon_\mathrm{s}(t)\hat{a}_\mathrm{s}^\dagger - \epsilon_\mathrm{s}^*(t)\hat{a}_\mathrm{s}) \text{ where } \epsilon_\mathrm{s}(t) = \mu V_\mathrm{s}(t)e^{i\phi_\mathrm{s}}. \tag{5.3}$$

The scaling factor $\mu = 1.45\ (\mathrm{mV}.\mu\mathrm{s})^{-1}$ is calibrated by fitting the photocounting measurement results obtained using the yes-no qubit with the master equation simulation (see App. d). Fig. 5.3a shows the evolution of ϵ_s with V_s. For every experiment, the storage mode displacements are realized using a Gaussian pulse shape $\epsilon_\mathrm{s}(t) = \lambda(t)\epsilon_\mathrm{max}$ with a maximum amplitude ϵ_max, a width 25 ns and a duration 100 ns. We simulated the dynamics of the storage mode under this Gaussian displacement taking into account the couplings, relaxation and decoherence rates (see App. d) for various amplitudes ϵ_max. We then computed the expectation value of the photon number operator $\langle\hat{n}_\mathrm{s}\rangle$ at the end of the pulse. Fig. 5.3b shows the square root of $\langle\hat{n}_\mathrm{s}\rangle$ as a function of ϵ_max. Fitting with a linear function, we find that $\sqrt{\langle\hat{n}_\mathrm{s}\rangle} = 59.1\epsilon_\mathrm{max}$. As ϵ_s increases linearly with V_s, ϵ_max increases linearly with the maximum voltage amplitude $V_\mathrm{max,s}$ of the Gaussian pulse $V_\mathrm{s}(t) = \lambda(t)V_\mathrm{max,s}$. Using the two linear regressions, we can express the photon number of the storage mode as $\sqrt{\langle n_\mathrm{s}\rangle} = (85.9\ \mathrm{V}^{-1})\, V_\mathrm{max,s}$.

5.3 MEASUREMENT TIME

In this section we compare the following various photon number measurement schemes using a qubit of frequency f_q that is dispersively coupled to a storage mode of frequency

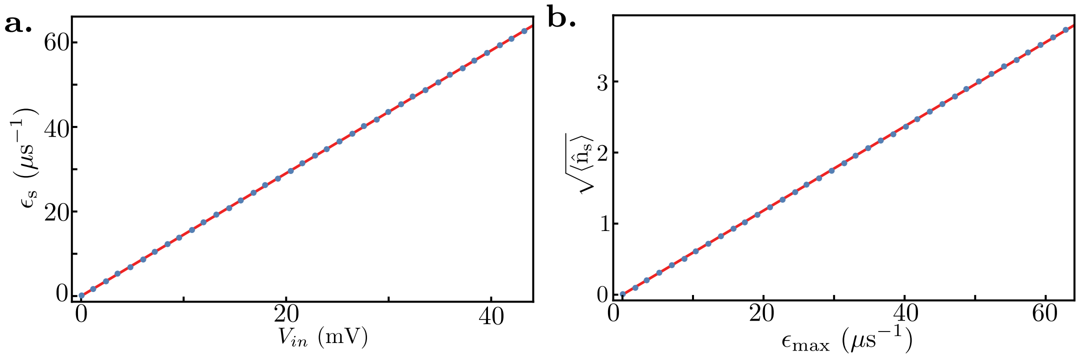

Figure 5.3: Calibration of the average number of photons $\langle n_\mathrm{s} \rangle$ in the storage mode as a function of the displacement amplitude. **a.** Evolution of the displacement amplitude ϵ_s with the pulse envelope V_s. **b.** Square root of the average photon number $\langle n_\mathrm{s} \rangle$ in the storage mode as a function of the drive amplitude. The storage is displaced by 100 ns long Gaussian pulse with a width of 25 ns. The same pulse shape is used in the simulation. From the two linear fits we extract the evolution of the mean number of photons with the amplitude of the pulse $\sqrt{\langle n_\mathrm{s} \rangle} = \left(85.9\ \mathrm{V}^{-1}\right)\ V_{\max,\mathrm{s}}$.

f_s. We assume the cross Kerr rate χ between the storage mode and the qubit to be greater than the decoherence rate of the qubit Γ_2. The goal is to measure the photon number N assuming it is smaller than $N_{\max}$.

5.3.1 *Comparison between protocols*

5.3.1.1 *Sequential brute force*

The brute force approach consists in measuring whether or not there are k photons in the storage mode for all possible values of k from 0 to $N_{\max}$ [26]. For each $k = 0, 1, 2, 3, ...$, we apply a photon number conditional π pulse to the qubit at frequency $\omega_q - k\chi$ so that the qubit is excited only if there are k photons in the storage mode. Reading out the qubit state gives the answer to the question ‘Are there k photons?’. The full measurement stops as soon as this binary answer is positive so that it takes $N+1$ consecutive measurements and a time given by $(T_\pi + T_\mathrm{ro})(N+1)$. The time T_π is the time of a conditional π pulse, hence it is at least about[1] $2\pi/\chi$, while the qubit readout time T_ro is limited by other parameters in order to get a single-shot readout. This approach is highly sensitive to measurement errors as an error at a step $k < N$ will stop the measurement, leading to a false photon number, before the step N and an error at the step N will entail continuing the measurement up to the step $N_{\max}$ without finding the photon number.

5.3.1.2 *Passive photon number decimation using weak measurement*

This approach, which was implemented with Rydberg atoms in cavity [23], consists in encoding the photon number in the phase of the qubit by waiting a time $2\pi/(N_{\max}\chi)$

---

[1] The conditional π pulse must be long enough to ensure there is no frequency components detuned by $\pm\chi$. This contition depends on the pulse waveform but the properties of the Fourier transform impose that a wavepacket with a frequency width about χ must have a temporal width about at least $2\pi/\chi$.

after the qubit has been prepared in state $(|g\rangle + |e\rangle)/\sqrt{2}$. The protocol is composed of a series of p sequences, where each sequence encodes the photon number into the phase of the qubit and realizes a $\pi/2$ pulse on the qubit with a phase $2\pi p/N_{\max}$ followed by a qubit readout. Using generalized measurement theory, one infers the probability that the cavity is in a given Fock state.

After the p sequences the variance of the photon number is $\sigma = N_{\max}/(\sqrt{p}\pi)$ (see appendix A in Ref. [25]). Therefore, the required number of repetitions k to get a fixed error probability on the photon number scales as $k \propto N_{\max}^2$. Since each measurement takes at least $2\pi/(N_{\max}\chi)$, the total measurement time scales at least as $2\pi N_{\max}/\chi$. This approach is quite insensitive to measurement errors as any error will be suppressed by the other measurements during the averaging step.

5.3.1.3 *Active photon number decimation*

The previous protocol can be improved by optimizing the phase of the final $\pi/2$ pulse to maximize the amount of information extracted on the cavity photon number. It was realized in Ref. [24] using Rydberg atoms in cavity. Because of the use of feedback on a weak measurement, we could not find a closed form for the measurement time in this case [25]. However it was shown that the total time is larger than the total time taken by a binary decimation with feedback (see below).

5.3.1.4 *Binary decimation with feedback*

This method was shown to provide the least number of steps for sequential photocounting [22]. Each step consists in applying an unconditional $\pi/2$ pulse to the qubit, wait a time $\pi/2^k\chi$, apply a new unconditional $\pi/2$ pulse with a phase ϕ_k that encodes the least significant[2] k^{th} bit b_k of the photon number $N = \sum_k b_k 2^k$ into the qubit state. Importantly, the phase ϕ_k depends on the results of the $k-1$ former measurements. The sequence needs to be repeated $p = \log_2(N_{\max}+1)$ times with k going from 0 to $p-1$. This procedure was recently implemented in Ref. [27].

The measurement time is at least given by the sum of the total interaction time between qubit and cavity and of the total feedback latency. The total interaction time is bounded by $\sum_p \pi/(2^p\chi) = 2\pi/\chi$. However the feedback latency scales as p and can be written as $T_{\text{fb}} \log_2(N_{\max}+1)$.

From the point of view of measurement error, this approach is higly sensitive to error due to the feedback. A measurement error at step $k-1$ leads to a wrong phase ϕ_k and an error at step k. The measurement error at the step $k-1$ propagates to all the following measurements.

5.3.1.5 *Binary decimation with optimal pulse control*

An optimal binary decimation can also be implemented without using a feedback loop by measuring a series of generalized parity operators which yields the bit values of the binary decomposition of the photon number in the storage mode. The k^{th} generalized

---

[2] here least significant is to be understood as the last bit in the binary decomposition, and not in terms of amount of information

Protocol	$t_{\text{meas}} \propto$	complexity	error propagation
Sequential brute force	$2\pi(N+1)/\chi$	$N+1$ gates	yes
Passive decimation	$2\pi N_{\text{max}}/\chi$	N_{max}^2 gates and complex analysis	no
Binary code feedback	$T_{\text{fb}} \log_2(N_{\text{max}}+1)$	feedback	yes
Binary code optimal control	$(T_{\text{reset}} + 2\pi/\chi) \log_2(N_{\text{max}}+1)$	optimal control	no

Table 5.2: Protocols for photocounting using a qubit

parity measurement consists in an optimal pulse that excites the qubit conditioned on the value of the k^{th} bit. The $p = \log_2(N_{\text{max}}+1)$ parity measurements are performed in a time sequence. A subsequent measurement and dynamic reset of the qubit state completes the sequence [156, 28]. Such an optimal pulse can only be performed in a time of the order of the dispersive interaction time $2\pi/\chi$. It leads to a total measurement time scaling as $(2\pi/\chi + T_{\text{reset}}) \log_2(N_{\text{max}}+1)$ where T_{reset} is the duration of the active reset protocol.

From the point of view of error propagation, this approach is more robust than the binary decimation by feedback as all measurements are independent. A measurement error at step k will not affect the following steps.

5.3.1.6 *Summary*

In the table, we provide a summary of the various advantages and drawbacks of the photocounting methods (see Tab. 5.2). No time sequence measurement is able to provide a measurement time that does not depend on the photon number. As all approaches use the qubit state to encode the answer to a binary question, all these photon number measurements are discrete in time. Moreover, none of these measurements implement a measurement of the observable n_s as they extract information bit by bit. For example, the binary decimation implements measurements of the photon-number-bit observables.

How to improve these approaches ? Making them continuous in time is not simple as the entanglement gate between the storage and the qubit and the measurement of the qubit state cannot be done simultaneously. Besides, making the full sequence in a time that is short compared to the storage relaxation time and the other gate time is difficult as the duration of the sequence time increase with the maximum photon number. Furthermore, one cannot perform multiple steps of the photon-counting protocol at the same time as a qubit cannot encode more than 1 bit.

One can improve the measurement protocols by changing 2 ingredients. First, although the entangling gate is performed such that a binary question is encoded in the qubit state, the frequency of the qubit is already encoding the storage photon number thanks to the dispersive interaction. Thus, measuring the qubit frequency is equivalent to measuring the storage photon number. This can be done easily by probing the qubit in reflection and measuring its fluorescence field. Second, all the former approaches use a sequence of questions in time, but with the recent improvement in wide band quantum-limited amplifiers [30], one can now use the spectral domain to multiplex measurements [157, 158, 159]. Using those two tools, one can create a multiplexed photocounter, thus enabling a new measurement scheme with completely different characteristics and a better upper bound for the measurement time.

5.3.2 *Gedanken multiplexed photocounter*

In this section, we show how, despite using a single qubit as well, multiplexed measurements are able to determine the photon number in a constant time (independent of the number of photons) in contrast with the standard approach. We consider an ideal detector for the propagating modes in order to better illustrate the interest of multiplexing. The ideal detector is made of a frequency multiplexer followed by a perfect photodetector on each of its outputs (Fig. 5.4). The multiplexer is made of a parallel ensemble of bandpass filters that are each centered on the frequency $f_{\mathrm{mp}} - k\chi_{\mathrm{s,mp}}/2\pi$ with a bandwidth $\chi_{\mathrm{s,mp}}/2\pi$. The protocol proceeds in three steps to count the number of photons in the storage mode starting in state $|\psi\rangle_{\mathrm{s}}$, as detailed in Fig. 5.4.

- First, the multiplexing qubit is excited with a π-pulse that is short enough so that it prepares the qubit in the excited state irrespective on the number of photons.
- Second, the qubit decays in the transmission line converting its excitation into a single photon contained in a propagating wavepacket whose envelope decays at a rate $\Gamma_{1,\mathrm{mp}}$. In the limit where $\Gamma_{1,\mathrm{mp}} \ll \chi_{\mathrm{s,mp}}$, and without pure dephasing of the qubit, the photon emission produces an entangled state between the storage mode and the propagating modes of the line. Here the qubit is not a probe, it is used to generate frequency entanglement between the propagating wavepacket photon and the storage mode. The system state reads

  $$\sum_k \langle k|\psi\rangle_{\mathrm{s}} \bigotimes_j |\delta_{k,j}\rangle_j \otimes |k\rangle_{\mathrm{s}},$$

  where $|\cdot\rangle_j$ represents the quantum state of the propagating mode going through the multiplexer on branch j corresponding to frequencies in the band (see Fig. 5.4c)

  $$[f_{\mathrm{mp}} - (j+1/2)\chi_{\mathrm{s,mp}}/2\pi, f_{\mathrm{mp}} - (j-1/2)\chi_{\mathrm{s,mp}}/2\pi[.$$

  Matching the temporal envelope of the modes to the exponential decay at a rate Γ_1 [150], the mode is occupied by either $|0\rangle_j$ or $|1\rangle_j$ depending on the storage photon number, hence the notation $|\delta_{k,j}\rangle_j$.
- Finally, a single photodetector clicks and reveals the number of photons k with probability $|\langle k|\psi\rangle|^2$ (Fig. 5.4d). In case of ideal detectors with zero false positives, the click detects the associated propagating mode in $|1\rangle_k$, and therefore, as the line is entangled with the storage mode, the measurement back-action projects the storage mode in Fock state $|k\rangle$.

The total measurement time, a few $1/\Gamma_{1,\mathrm{mp}}$, corresponds to the time it takes for one photodetector to click. The time is thus *independent on the number of photons* stored

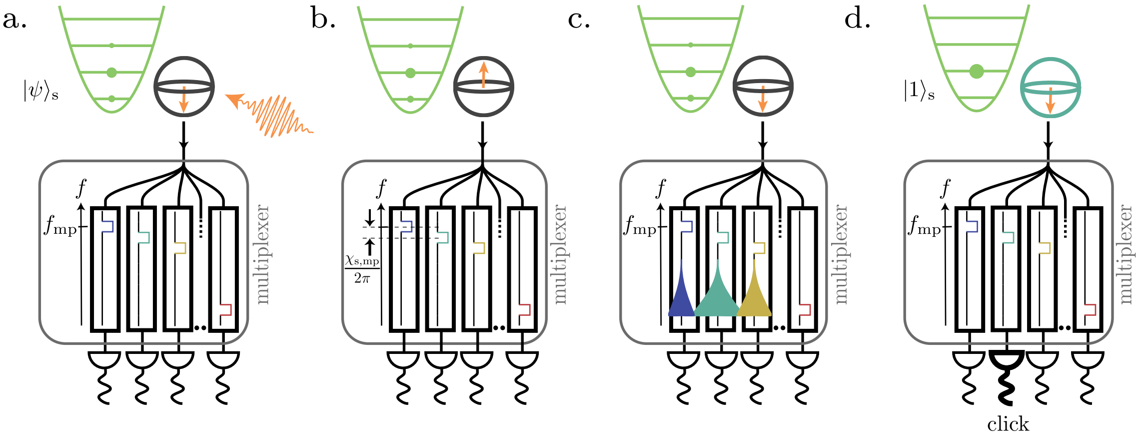

Figure 5.4: Gedanken multiplexing experiment. **a.** An unconditional π pulse is applied to the multiplexing qubit while the cavity is prepared in state $|\psi\rangle_s$. **b.** The qubit is prepared in the excited state. **c.** The qubit spontaneously emits a photon into the transmission line, where a multiplexer sorts the emitted radiation according to its frequency. Each port k of the multiplexer is bandpass filtered around frequency $f_{\mathrm{mp}} - k\chi_{\mathrm{s,mp}}$ by a rectangular component displaying the frequency band. **d.** Eventually a single photodetector (detector $k = 1$ in the figure) clicks with probability $|\langle k|\psi\rangle|^2$, allowing us to deduce the photon number. The storage mode is projected on the corresponding Fock state (here $|1\rangle_{\mathrm{s}}$) in a typical time $T_{1,\mathrm{mp}}$ that does not depend on the average number of photons in the storage mode.

in the storage mode. Note that in order to avoid spectral leakage into other ports, $\Gamma_{1,\mathrm{mp}}$ is limited by $\chi_{\mathrm{s,mp}}$ so that the shortest measurement time is limited to a few $1/\chi_{\mathrm{s,mp}}$.

In contrast to sequential measurements for which increasing the maximal number of photons that can be detected requires additional temporal resources (of the order of $\log_2(N_{\max})$), this gedanken experiment shows that the multiplexed measurement is able to operate in a constant time at the expense of additional spectral resources. Besides, the unconditional π pulse can be performed in a time much smaller than the relaxation time of the cavity. With a qubit relaxation time and a photodetector measurement time much smaller than the storage one, one obtains a measurement that can be considered as continuous in time when it is repeated.

In practice, building such an array of frequency sensitive photodetectors remains an open challenge in the microwave domain, despite encouraging recent progress towards this goal [147, 148, 149, 150, 151, 76, 27]. One can identify the two main ingredients to build a simpler version of such a multiplexed photocounter. The first is the ability to photocount by measuring the fluorescence of the qubit. The second is the ability to multiplex this fluorescence measurement. Based on these two ingredients, we performed an experiment where the unconditional qubit π-pulse is replaced by a continuous frequency comb containing all the possible resonant frequencies of the qubit and the perfect array of photodetectors is replaced by a multiplexed heterodyne measurement of all the frequencies of the frequency comb reflected by the qubit. As we will see, the frequency comb can be understood as a series of unconditional pulses. With the right comb amplitude, it is equivalent to applying periodically an unconditional qubit π-pulse. The next chapter will present the calibration of the qubit used to perform this multiplexed photocounting protocol and will discuss the implementation of the first ingredient: the fluorescent photocounting. The multiplexed photocounting will be discuss in the Chap. 7.

CONCLUSION

Here are the main conclusions of this chapter:

- The standard photocounting approach uses the dispersive interaction to entangle the qubit state and the resonator state. The type of entanglement gate used defines the binary question asked to the system.
- The readout of the qubit state gives at most one bit of information. It recovers the answer of a binary question.
- The standard photocounting approach recovers information bit by bit with the best protocols (the binary decimation). Thus, it is discrete in time.
- The optimal protocol (the binary decimation) needs a measurement time scaling with the maximum photon number N_{max} as $\log_2(N_{\mathrm{max}})$.
- Using frequency resources instead, one can reach a measurement time independent of N_{max}.

6

FLUORESCENCE BASED PHOTON NUMBER MEASUREMENT

Fluorescence measurements correspond to the detection of photons or electromagnetic fields emitted by a quantum system. They are routinely performed in experiments on atoms, ions and nitrogen-vacancy centers in diamond. In circuit QED, fluorescence measurements can realize qubit readouts [85, 160, 161], probe quantum trajectories [162, 163, 164, 165, 166, 167, 168, 169], explore quantum thermodynamics [38, 170], access the light-matter interaction [171, 172, 173, 174, 175, 176, 68], cooling processes [29], and demonstrate the generation of single photons [177]. Although a large range of experiments can be performed using superconducting qubit fluorescence, it is very rarely used in quantum measurement. As the signal of qubit fluorescence measurement saturates and even decreases at large probe power (see Sec. 2.4.3), resonator fluorescence measurements are preferred. In this thesis, we use the fluorescence of a transmon qubit to read out the number of photons stored in a resonator. This was possible thanks to the dispersive coupling between these two modes. Interestingly, this is the reverse of the usual situation in which resonator fluorescence is used to read out a qubit photon number [20]. This chapter will discuss the characterization of the qubit used to perform the fluorescent photocounting, the photocounting ability, and the measurement back-action of the fluorescence photocounting. From this point onwards, we will use the word “fluorescence” to talk about the fluorescence of the multiplexing qubit (in contrast to the fluorescence of the readout resonator).

Remarks: Most of the results shown in this chapter are published in Ref. [155, 178]

6.1 QUBIT CHARACTERIZATION

6.1.1 *Rabi oscillations*

The multiplexing qubit of the circuit (see Fig. 5.1) is intended to be used with fluorescence measurement. The multiplexing qubit is characterized using reflection spectroscopy; once we know its frequency, we can measure Rabi oscillations in order to calibrate the linear relationship between the drive amplitude and the Rabi oscillation angular frequency Ω. As the qubit is probed in fluorescence, the Rabi pulse also acts as a readout pulse. The average fluorescence record (i. e., the reflected pulse) reads (see Sec. 2.4.3 and Eq. (2.58)):

$$\langle a_{\mathrm{out}}\rangle(t) = \langle a_{\mathrm{in}}\rangle(t) - \sqrt{\Gamma_c}\langle\sigma_{-,\mathrm{mp}}\rangle(t), \tag{6.1}$$

where $\langle a_{\mathrm{in}}\rangle(t)$ is the input pulse complex amplitude and $\sigma_{-,\mathrm{mp}}$ the qubit lowering operator. Thus, one can observe Rabi oscillations of the multiplexing qubit by applying a 1 μs-long square pulse at f_{mp} with a varying amplitude V_{mp} referred to the IF signal (see Sec. 4.3). The reflected signal, which is demodulated by time steps of 10 ns,

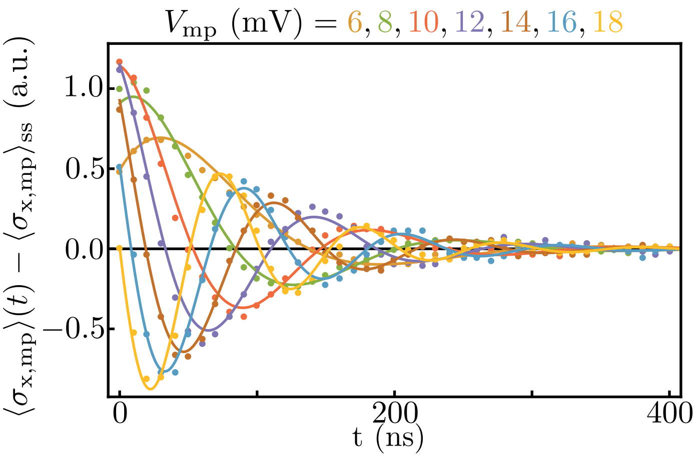

Figure 6.1: Multiplexing qubit Rabi oscillations for various driving amplitudes.The measured Rabi oscillations observed in the reflection coefficient at qubit frequency (dots) are reproduced by Eq. (6.2 (solid line). The vertical axis represents the deviation of the qubit in phase coherence $\langle\sigma_{\mathrm{x,mp}}\rangle$ to its steady-state value. This calibration allows us to extract the scaling parameter ξ, relates the drive amplitude voltage amplitude V_{mp} to the Rabi frequency a $\Omega = 2\pi\xi V_{\mathrm{mp}} = 2\pi(0.543 \pm 0.002\ \mathrm{GHz.V^{-1}}\ )V_{\mathrm{mp}}$.

displays damped oscillations given by Eq. (2.56). When subtracting the steady-state signal reached at the end of the pulse, the real part of the signal reads as follows:

$$\begin{aligned}&\sqrt{\Gamma_{1,\mathrm{mp}}}\langle\sigma_{\mathrm{x,mp}}\rangle(t) - \sqrt{\Gamma_{1,\mathrm{mp}}}\langle\sigma_{\mathrm{x,mp}}\rangle_{\mathrm{ss}} \simeq \\ &A\cos\left[\sqrt{(2\pi\xi V_{\mathrm{mp}})^2 - \left(\frac{\Gamma_{1,\mathrm{mp}} - 2\Gamma_{\phi,\mathrm{mp}}}{16}\right)^2}(t-t_0) + \phi\right] \times e^{-(t-t_0)/T},\end{aligned} \tag{6.2}$$

where $\langle\sigma_{\mathrm{x,mp}}\rangle_{\mathrm{ss}}$ is the value of the mean value of the $\sigma_{\mathrm{x,mp}}$ operator in the steady state. We obtain $\xi = 0.543 \pm 0.002\ \mathrm{GHz.V^{-1}}$, meaning that the Rabi frequency is calibrated as $\Omega = 2\pi\xi V_{\mathrm{mp}} = (0.543\ \mathrm{GHz.V^{-1}})V_{\mathrm{mp}}$ (see Fig. 6.1).

Once the Rabi angular frequency is calibrated, we can use it to measure the relaxation rate and the decoherence rate of the multiplexing qubit.

6.1.2 *Spectroscopy*

Based on Eq. (2.61), measuring the reflection coefficient for various Rabi angular frequencies Ω and probe frequencies f_{probe} enables a precise measurement of the relaxation and the decoherence rates. With the heterodyne measurement of the fluorescence field, we measure the qubit reflection coefficient, the transmission line spectrum, and the Jospehson TWPA gain that depends on the frequency. When conducting a spectroscopy of the multiplexing qubit, the heterodyne record reads

$$\begin{aligned}\overline{I}(f_{\mathrm{probe}},\Omega) + i\overline{Q}(f_{\mathrm{probe}},\Omega) &= \underline{G}(f_{\mathrm{probe}})\langle a_{\mathrm{out}}\rangle(f_{\mathrm{probe}},\Omega) \\ &= \underline{G}(f_{\mathrm{probe}})r(f_{\mathrm{probe}},\Omega)\langle a_{\mathrm{in}}\rangle(\Omega),\end{aligned} \tag{6.3}$$

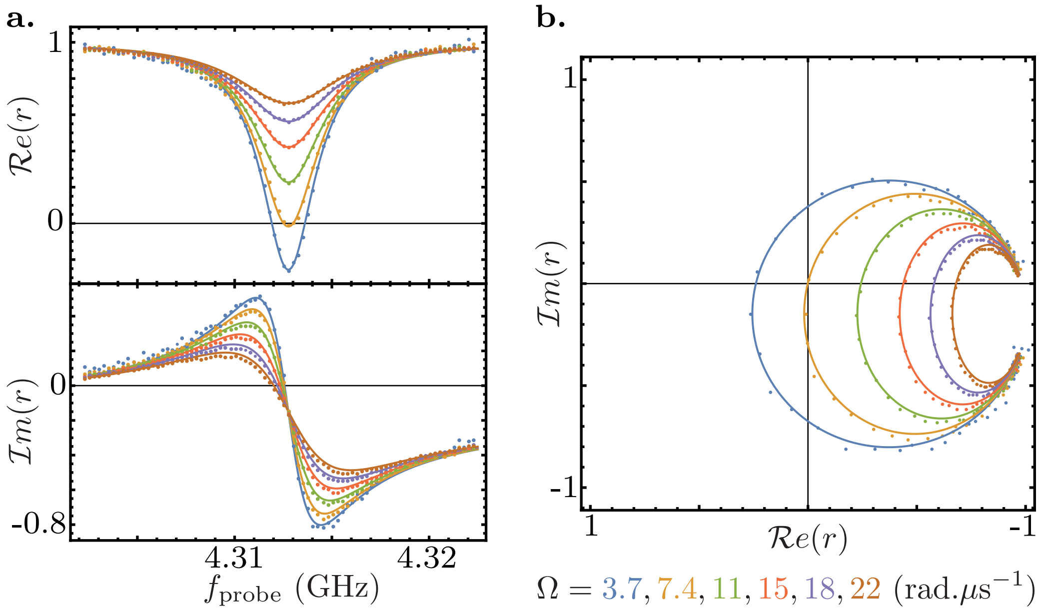

Figure 6.2: Reflection coefficient of the multiplexing qubit as a function of probe frequency for various probe amplitudes, expressed in units of the Rabi angular frequency Ω. The measured reflection coefficient (dots) are reproduced by the Eq (2.36). **a.** Real and imaginary parts of the reflected coefficiention as a function of probe frequency. **b.** Reflection coefficient in the complex plane for varying frequencies.

with $\underline{G}(f_\text{probe})$ being a complex factor that takes into account the total gain and phase shift of the setup at the frequency f_probe[1]. In this thesis, we were able to calibrate $\underline{G}(f_\text{probe})$ by displacing the storage mode with a large coherent-state amplitude (about a hundred photons). Thanks to the dispersive coupling, the multiplexing qubit resonance frequency is then shifted enough that the reflection coefficient can be considered as equal to 1. The heterodyne records for this reference spectroscopy read

$$\overline{I}_\text{ref}(f_\text{probe},\Omega) + i\overline{Q}_\text{ref}(f_\text{probe},\Omega) = \underline{G}(f_\text{probe})\langle a_\text{out}\rangle(\Omega) = \underline{G}(f_\text{probe})\langle a_\text{in}\rangle(\Omega). \quad (6.4)$$

Dividing the record of the first spectroscopy by the record of the reference spectroscopy gives access to the multiplexing qubit reflection coefficient. This reads (see Eqs. (6.3) and (6.4)),

$$r(f_\text{probe},\Omega) = \frac{\overline{I}(f_\text{probe},\Omega) + i\overline{Q}(f_\text{probe},\Omega)}{\overline{I}_\text{ref}(f_\text{probe},\Omega) + i\overline{Q}_\text{ref}(f_\text{probe},\Omega)}. \quad (6.5)$$

The measured reflection coefficient is shown in Fig. 6.2 as a function of the probe frequency and the Rabi angular frequency. The imaginary part is shifted by 0.15 due to a parasitic reflection in the setup. We can fit it with Eq. (2.36); this gives access to the relaxation rate $\Gamma_{1,mp}$ and the decoherence rate $\Gamma_{2,mp}$.

---

[1] We assume that all amplifiers work in the linear regime, meaning that the gain does not depends on the input field amplitude.

6.2 FLUORESCENCE PHOTOCOUNTING

6.2.1 *Photocounting a coherent state*

The intrinsic limitation of the standard approach (see Sec. 5.3.1) is that measuring the qubit state can at most reveal one bit of information per step. It is possible to avoid this constraint by observing the qubit frequency directly instead of measuring its state. The multiplexing qubit is coupled to the transmission line so that when there are k photons in the storage mode, the qubit emits a fluorescence signal into the mode of the transmission line that is centered around the qubit frequency $f_{\mathrm{mp}} - k\chi_{\mathrm{s,mp}}/2\pi$. Of course, the qubit needs to be excited for the emission occurs. This encoding ability can thus be observed by driving the multiplexing qubit with a single microwave drive through the transmission line (see Fig. 5.1) [177, 68, 161, 164]. The measured real part $\mathcal{R}e(r)$ of the reflection coefficient at frequency f_{probe} is reduced when the probe resonates with the qubit, hence revealing the photon number k [29]. This reduction arises from the coherent emission by the qubit in phase opposition with the reflected drive [179] (see Eq. (2.58)). Therefore, on average, the distribution of photon numbers in the storage mode can be deduced from the relative amplitudes of the reduction of $\mathcal{R}e(r)$ at each frequency $f_{\mathrm{mp}} - k\chi_{\mathrm{s,mp}}/2\pi$. The reflected coefficient reads

$$r(f_{\mathrm{probe}}) = 1 - \sum_k p_s(k)\frac{2\Gamma_c}{\Omega}\langle\sigma_{-,\mathrm{mp}}\rangle(\delta = f_{\mathrm{probe}} - f_{\mathrm{mp}} + k\frac{\chi_{\mathrm{s,mp}}}{2\pi}), \tag{6.6}$$

where $p_s(k)$ is the probability that the storage contains k photons and $\langle\sigma_{-,\mathrm{mp}}\rangle(\delta)$ is the mean value of the lowering operator when the qubit is driven by a coherent tone detuned by δ.

In Figs. 6.3 a,b, we show the measured qubit *emission coefficient* $1 - \mathcal{R}e(r)$ as a function of a single probe frequency f_{probe} and of the initial amplitude of the storage mode coherent state $\sqrt{\bar{n}}$. The measurement is performed using a drive strength $\Omega = \chi_{\mathrm{s,mp}}/4$ (expressed as the corresponding Rabi angular frequency), a pulse duration of 2 μs, which is smaller than the storage lifetime of 3.8 μs, and the reference technique describes in Sec. 6.1.2. Resolved peaks develop for every photon number up to at least 9. Using the former calibration of $\bar{n}$ (see Sec. 5.2.2), a master-equation based model enables us to reproduce the measurement results (see Appendix d).

The observation of resolved peaks is due to our choice of parameters. We designed the relaxation rate of the multiplexing qubit $\Gamma_{1,\mathrm{mp}} = (42\ \mathrm{ns})^{-1}$ so that the decoherence rate $\Gamma_{2,\mathrm{mp}} = \Gamma_{1,\mathrm{mp}}/2$ is smaller than the dispersive shift $\chi_{\mathrm{s,mp}}$. When peaks are separated, probing the qubit at one of its resonance frequencies $f_{\mathrm{mp}} - k\chi_{\mathrm{s,mp}}/2\pi$ opens a communication channel with a maximal bandwidth $\Gamma_{2,\mathrm{mp}}/2\pi$ carrying information only about Fock state $|k\rangle$. We maximize the bandwidth of each channel by designing $\Gamma_{1,\mathrm{mp}}$ as large as possible by adjusting the direct coupling to the transmission line, under the constraint of keeping the peaks resolved (see Sec. 5.1.2).

This fluorescence photon-counting ability was demonstrated earlier in Ref. [29] using a continuous drive to cool down a hot radio-frequency mode. Here, this fluorescence photon-counting ability is used with pulsed drive and we will focus on its back-action.

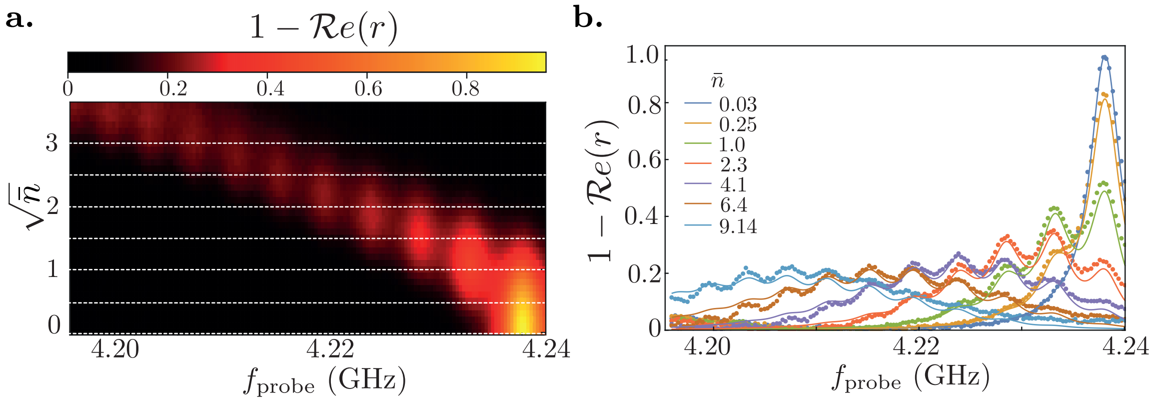

Figure 6.3: Fluorescence photon-counting **a, b,** Measured emission coefficient $1-\mathcal{R}e(r)$ as a function of the probe frequency $f_{\rm probe}$ and the mean photon number $\bar{n}$ in the storage mode. The emission coefficient exhibits a resolved peak for each photon number. The dots in **b** are cuts along the dashed lines in **a** and are captured by a master equation model described in App. d (solid lines).

As we will see, one can improve this measurement using a multiplexing approach (see Chap. 7).

6.2.2 *Comparison with the standard photocounting approach*

We have shown that both fluorescence photon-counting and standard photon-counting (Figs. 6.3 and 5.2) allow us to ask questions along the lines of “are there k photons?” We can already see that the fluorescence photon-counting measurement is continuous both in time and in strength, whereas the standard measurement is only continuous in strength. The important difference between both techniques is that only the fluorescence photon-counting process can be multiplexed. Indeed, when using the standard technique, we need to read out and reset the qubit at the end of each step. The readout step cannot be multiplexed, as it always occurs at the readout mode frequency. In contrast, with the fluorescence readout, information about a given photon number k is constantly extracted through the frequency mode $f_{\rm mp}-k\chi_{\rm s,mp}/2\pi$ of the transmission line. The key ingredient to our approach is thereby enabled; that is, the multiplexing measurement of the reflection coefficient at every frequency $f_{\rm mp}-k\chi_{\rm s,mp}/2\pi$.

Naively, we could view the fluorescence photon-counting approach as an encoding of the photon number into the qubit state. Indeed the record depends on the mean expected value of the multiplexing qubit lowering operator. If this were to be true, even by multiplexing the measurement we would not be able to extract more than 1 bit of information at a time. This is not the case; the multiplexing qubit works as an “encoder”, exactly in the same way as a readout resonator used to measure a dispersively coupled qubit does. In order to understand the role of encoder, let us go back to the basis of heterodyne detection, which measures the output field $a_{\rm out}(f_{\rm RF})$ at the frequency $f_{\rm RF}$ (see Sec. 4.3). The multiplexing qubit or the readout resonator are used as entangling devices between the rest of the system and the many modes $\{a_{\rm out}(f)\}_f$ of the transmission line. Each of the transmission-line modes can contain an infinite amount of information, and the number of transmission-line modes that could be entangled with the system is only bounded by the bandwidth of the line. Thus, the amount of information we can extract using heterodyne detection is not bounded; rather, it is the entangling process that bounds the amount of information we can extract.

In the standard approach, the storage is first entangled with a dispersively coupled qubit (the yes–no qubit in the Sec. 5.2.1), following which this qubit is entangled with the transmission-line modes thanks to the presence of the readout resonator. As the entanglement between the storage mode and the transmission-line modes is generated through the qubit, the amount of information we can extract from this entanglement process is limited by the amount of information a qubit can store: 1 bit. In addition, the system can only be entangled with one transmission-line mode $a_{\mathrm{out}}(f_{\mathrm{pulse}})$, which oscillates at the frequencies of the readout pulse f_{pulse}. Thus, it is impossible to multiplex the standard approach, as the entangled transmission-line mode is always the same.

In the fluorescent approach, the storage mode is directly entangled with the many transmission-line modes thanks to the multiplexing qubit. Each Fock state $|n\rangle$ of the storage resonator may be entangled with one transmission line mode $a_{\mathrm{out}}(f_{\mathrm{mp}} - n\chi_{\mathrm{s,mp}}/2\pi)$ oscillating at the frequency $f_{\mathrm{mp}} - n\chi_{\mathrm{s,mp}}/2\pi$. Thus, the amount of information we can extract through this entanglement process is only bounded by the line bandwidth, as, using a multiplexing approach, we can read out, at the same time, all the transmission line mode states which can collectively host much more than a single bit of information.

Before discussing the multiplexing fluorescence photon-counting process, we will discuss the measurement back-action of the fluorescence based photon number measurement. Indeed, here the probed system is a harmonic oscillator (a multi-level system) and the probe/encoder used is a non-linear element (the multiplexing qubit); thus, we can expect a measurement back-action that is more complex than the one resulting from a dispersive qubit readout.

6.3 FLUORESCENCE BACK-ACTION

6.3.1 *Modeling of the measurement operator*

We introduce here a simple model to characterize the measurement and its back-action on the resonator. The measurement uses a phase preserving amplifier in order to amplify the signal at a frequency $f_{\mathrm{mp}} - k\chi_{\mathrm{s,mp}}/2\pi$ when probing Fock state k and records a complex amplitude $I^{(k)} + iQ^{(k)}$. Here, we assume that the measurement record only extracts the information on the occupation of the Fock state $|k\rangle$, which is experimentally valid in the limit $\chi_{\mathrm{s,mp}} \gg \Gamma_{2,\mathrm{mp}}$. Without decoherence and in the limit of long measurement time, its back-action on the storage mode would project the storage state either on Fock state $|k\rangle$ or on the complementary subspace $\Pi_{\perp}^{(k)}\mathcal{H}_s$, where $\Pi_{\perp}^{(k)} = \mathbf{1} - |k\rangle\langle k|$ and $\mathcal{H}_s$ is the Hilbert space of the storage resonator.

In practice, the measurement proceeds by first entangling the resonator, which is in a state $|\psi_s\rangle$, and the signal mode of the phase preserving amplifier (i. e. the output field of the multiplexing qubit). When probing Fock state $|k\rangle$, the entangled state reads $|\alpha, 0\rangle \otimes \Pi^{(k)}|\psi_s\rangle + |\alpha_\perp, 0\rangle \otimes \Pi_\perp^{(k)}|\psi_s\rangle$, where $\Pi^{(k)} = |k\rangle\langle k|$, and states denoted as $|\alpha, \beta\rangle$ are the state of the amplified field denoted by the coherent states amplitude of the signal and the idler modes at the input of the amplifier (see Sec. 4.3.3.1). As discuss in Sec. 7.3, describing the output field of the qubit as a coherent state is an approximation as we don't capture the incoherent emission of the qubit.

We distinguish two cases: the case where the probe is resonant with the multiplexing qubit, leading to a reflected amplitude α, and the case where it is off resonant leading to a reflected amplitude $\alpha_\perp$. The resonance frequency of the qubit depends on the number of photons in the resonator so that the reflected amplitude α indicates k photons while $\alpha_\perp$ indicates that there are not k photons. For an incoming amplitude α_{in} onto the multiplexing qubit, we get (see Eq.(2.59))

$$\begin{cases} \alpha_\perp = \alpha_{\text{in}} \\ \alpha = \alpha_{\text{in}} \left(1 - \dfrac{2\Gamma_{1,\text{mp}}}{\Omega} \langle \sigma_{-,\text{mp}} \rangle_{\text{ss}} \mathrm{e}^{i\phi_d}\right) \end{cases}, \tag{6.7}$$

where $\langle \sigma_{-,\text{mp}} \rangle_{\text{ss}}$ is the steady state mean value of the multiplexing qubit lowering operator. If the qubit is driven by a single tone, the maximum of $|\langle \sigma_{-,\text{mp}} \rangle_{\text{ss}}|$ is reached for $\Omega = \Gamma_{1,\text{mp}}/\sqrt{2}$.

The measurement operator (Kraus operator) corresponding to the heterodyne detection of a propagating field encoding the information on the $|k\rangle$ state thus reads

$$M^{(k)}(I^{(k)}, Q^{(k)}) = \langle \Psi_{\text{I}^{(\text{k})},\text{Q}^{(\text{k})}} | \alpha, 0\rangle \Pi^{(k)} + \langle \Psi_{\text{I}^{(\text{k})},\text{Q}^{(\text{k})}} | \alpha_\perp, 0\rangle \Pi_\perp^{(k)}, \tag{6.8}$$

where $|\Psi_{\text{I}^{(\text{k})},\text{Q}^{(\text{k})}}\rangle$ is the state on which the amplified field (i. e. the signal and the idler mixed field) is projected after the heterodyne measurement performed by the phase preserving amplifier followed by a heterodyne detection setup (see Secs. 4.3 and 4.3.3.1).

Following the supplementary information of Ref. [103], in the case of a phase preserving amplifier the inner product $\xi(\beta, I, Q) = \langle \Psi_{\text{I},\text{Q}} | \beta, 0\rangle$ is given up to a global phase factor (independent on β, I and Q) by

$$\xi(\beta, I, Q) = \frac{1}{\sqrt{\pi}2\sigma_0} e^{-\dfrac{|\beta|^2}{2(2\sigma_0)^2}} e^{-\dfrac{(I-\beta)^2}{2(2\sigma_0)^2}} e^{-\dfrac{(Q+i\beta)^2}{2(2\sigma_0)^2}} \tag{6.9}$$

where σ_0 is the amplitude of the zero-point fluctuations (the variance of the measured I is $2\sigma_0^2$ in the quantum limit of phase preserving amplification).

Therefore, we finally get the following analytical expression of the measurement operators when probing Fock state $|k\rangle$, in the case of $\Gamma_{2,\text{mp}} \ll \chi_{\text{s,mp}}$

$$\begin{aligned} M^{(k)}(I^{(k)}, Q^{(k)}) \quad = \quad & \tfrac{1}{\sqrt{\pi}2\sigma_0} e^{-\dfrac{|\alpha_\perp|^2}{2(2\sigma_0)^2}} e^{-\dfrac{(I^{(k)}-\alpha_\perp)^2}{2(2\sigma_0)^2}} e^{-\dfrac{(Q^{(k)}+i\alpha_\perp)^2}{2(2\sigma_0)^2}} \Pi_\perp^{(k)} \\ & + \tfrac{1}{\sqrt{\pi}2\sigma_0} e^{-\dfrac{|\alpha|^2}{2(2\sigma_0)^2}} e^{-\dfrac{(I^{(k)}-\alpha)^2}{2(2\sigma_0)^2}} e^{-\dfrac{(Q^{(k)}+i\alpha)^2}{2(2\sigma_0)^2}} \Pi^{(k)}. \end{aligned} \tag{6.10}$$

The same approach enables to derive the measurement operator for a homodyne detection made with a phase-preserving amplifier. The measurement operator reads

$$M^{(k)}(I^{(k)}) = \langle \Psi_{\text{I}^{(\text{k})}} | \alpha, 0\rangle \otimes \Pi^{(k)} + \langle \Psi_{\text{I}^{(\text{k})}} | \alpha_\perp, 0\rangle \otimes \Pi_\perp^{(k)}. \tag{6.11}$$

The product $\xi(\beta, Q) = \langle \Psi_{\mathrm{I}} | \beta, 0 \rangle$ is given up to a global phase factor (independent on β and I) by

$$\xi(\beta, I) = \frac{1}{(4\pi\sigma_0^2)^{1/4}} e^{-\frac{\mathcal{I}m(\beta)^2}{2(2\sigma_0)^2}} e^{-\frac{(I-\beta)^2}{2(2\sigma_0)^2}}. \tag{6.12}$$

Therefore, the measurement operators for the homodyne detection when probing Fock state $|k\rangle$, in the case of $\Gamma_{2,\mathrm{mp}} \ll \chi_{\mathrm{s,mp}}$, reads

$$\begin{aligned} M^{(k)}(I^{(k)}) \quad = \quad & \tfrac{1}{(4\pi\sigma_0^2)^{1/4}} e^{-\frac{\mathcal{I}m(\alpha_\perp)^2}{2(2\sigma_0)^2}} e^{-\frac{(I^{(k)}-\alpha_\perp)^2}{2(2\sigma_0)^2}} \Pi_\perp^{(k)} \\ & + \tfrac{1}{(4\pi\sigma_0^2)^{1/4}} e^{-\frac{\mathcal{I}m(\alpha)^2}{2(2\sigma_0)^2}} e^{-\frac{(I^{(k)}-\alpha)^2}{2(2\sigma_0)^2}} \Pi^{(k)}. \end{aligned} \tag{6.13}$$

Assuming the multiplexing qubit is in its steady state (see Sec. 2.4.2), one can inject the expression of α and $\alpha_\perp$ in the heterodyne and homodyne measurement operators. One obtains that the photon number information is encoded in the in-phase record $I^{(k)}$.

6.3.2 *Post-selection and correlation*

The back-action of the fluorescence photon-counting measurement can be studied by performing a tomography of the storage mode at the end of the fluorescence measurement process. The storage tomography is a direct Wigner tomography [32, 180, 181] performed thanks to the yes–no qubit (see App. c for details about Wigner tomography and Sec. 5.1 for details about the yes-no qubit).

6.3.2.1 *The basics of the Wigner function*

A Wigner tomography performed by measuring the displaced parity operator. The measured Wigner function $W(\alpha)$ reads

$$W(\alpha) = \frac{2}{\pi} \mathrm{Tr}(D^\dagger(\alpha) \rho D(\alpha) \mathcal{P}), \tag{6.14}$$

where $D(\alpha)$ is the displacement operator of the storage mode by a coherent state $|\alpha\rangle$, and $\mathcal{P} = e^{i\pi \hat{a}_{\mathrm{s}}^\dagger \hat{a}_{\mathrm{s}}}$ is the photon number parity operator.

The Wigner tomography is a complete tomography of the storage state, meaning that all the information in the storage density matrix is contained in the Wigner function, and that we can reconstruct the density matrix from the Wigner function. As an example, the Wigner function $W(\alpha)_{|\beta\rangle}$ of a coherent state $|\beta\rangle$ is a Gaussian function centered on β with a width of 1/2, where

$$W(\alpha)_{|\beta\rangle} = \frac{2}{\pi} \mathrm{e}^{2|\alpha-\beta|^2}. \tag{6.15}$$

6.3.2.2 *Post-selection*

Remark: The post-selection experiment described in this section was performed during a different run to that of most of the results of this thesis. The storage and the

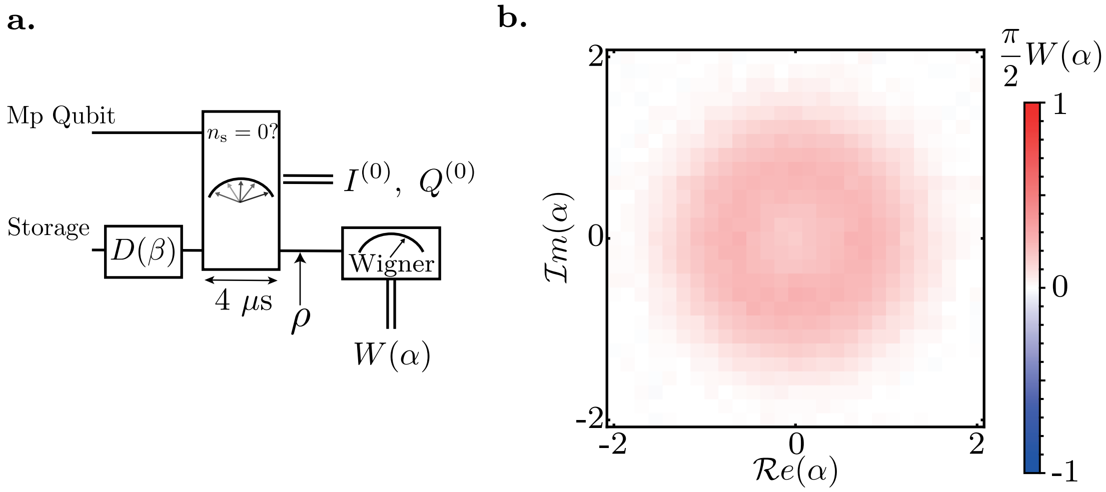

Figure 6.4: **a.** Circuit diagram of the post-selection experiment protocol. The Wigner tomography is represented by the Wigner measurement box (see Appendix c for more details). The initial coherent state amplitude is $\beta = 1.4$. **b.** The Wigner function of a coherent state $|\beta = \sqrt{1.4}\rangle$ after 4 µs of unread fluorescence measurement asking the question "Are there 0 photons?" The donut's shape is characteristic of a statistical mixture of Fock states.

multiplexing qubit lifetimes were 7.1 µs and 30 ns, respectively. The high relaxation rate of the multiplexing qubit leads to a higher SNR for the fluorescence measurement; however, the storage–multiplexing qubit dispersive interaction was not in the photon number-resolved regime.

Let us now characterize the photon-counting abilities of the fluorescence measurement. We initialize the storage mode in a coherent state $|\beta = \sqrt{1.4}\rangle$, then probe, with the multiplexing qubit, whether there are 0 photons, using a microwave pulse at the frequency f_{mp}, before measuring the Wigner function of the storage mode (see Fig. 6.4a). The fluorescent readout gives two records, $I^{(0)}$ and $Q^{(0)}$, for each realization of the experiment. When averaging over all realizations, the Wigner function measured takes the shape of a donut (see Fig6.4b) that corresponds to a statistical mixture of Fock states. As the mean photon number of the initial coherent state is small, measuring whether there are 0 photons is almost the same as measuring the photon number. Thus, the storage state after this unread fluorescence photon measurement contains no coherences in the Fock basis. This loss of coherences makes sense, as the phase and photon number are conjugate variables; thus, measuring the photon number will diffuse the phase of the storage state.

Looking at the histograms of the $I^{(0)}$ and $Q^{(0)}$ fluorescence records, we can see that the $Q^{(0)}$ histogram is simply a Gaussian distribution, whereas the $I^{(0)}$ histogram is the sum of two Gaussian distributions (see Fig.6.5a and b), as predicted by the measurement operators (see Sec. 6.3.1). We can identify the distribution with the smallest mean value (the green distribution in Fig.6.5) as the "0-photon" distribution (i. e., the distribution we would have if the storage was in the vacuum). In the same way, the distribution with the highest mean value (the yellow distribution in Fig.6.5) can be identified as the distribution of experiments with "not 0 photons". The SNR of the

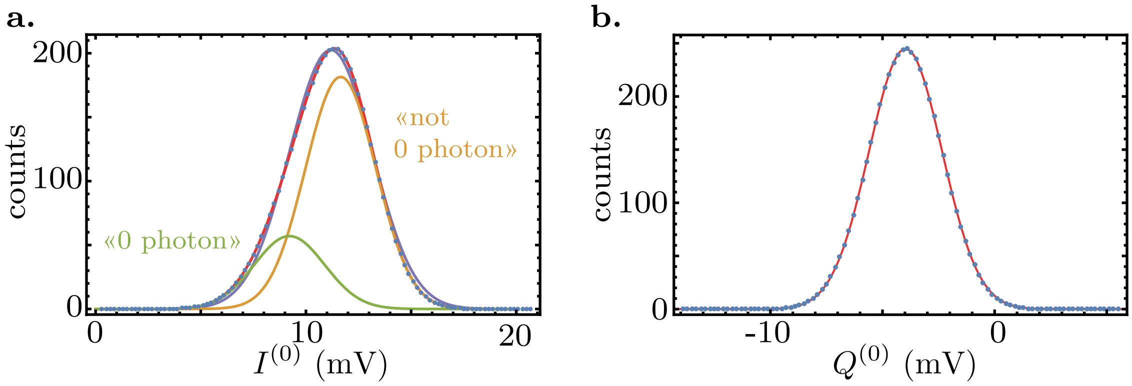

Figure 6.5: Histograms of the $I^{(0)}$ and $Q^{(0)}$ fluorescence records when measuring whether there are 0 photons when the storage mode is prepared in $|\beta\rangle = |\sqrt{1.4}\rangle$. **a.** The $I^{(0)}$ histogram is composed of two Gaussian distributions corresponding to the "0 photon" (green line) and "not 0 photon" (yellow line) results. The red line is the sum of the two distributions. The purple line is a fit using only one Gaussian distribution. This single Gaussian distribution fit is not able to reproduce the shape of the distribution. Thus we reject the hypothesis that the $I^{(0)}$ histogram is composed of a single Gaussian distribution. **b.** The $Q^{(0)}$ histogram contains no information. It corresponds to a single Gaussian distribution (red line).

fluorescence measurement is about 2; it was possible to reach this number thanks to the higher relaxation rate of the multiplexing qubit. Even if the SNR is too small to be in the strong measurement regime, we can still highlight the back-action of the fluorescence measurement using post-selection. We can first post-select all the experiment's realizations for which the fluorescence record $I^{(0)}$ is smaller than 7 mV. Based on the $I^{(0)}$ histogram, these experiments are mainly experiments with 0 photons. The Wigner function measured for this ensemble of realizations is shown in Fig. 6.6a. We can reproduce this tomography using the Wigner function of a thermal state [7]:

$$W_{\rho(n_{\text{th}})}(\alpha = x + ip) = \frac{2}{\pi}\frac{1}{2n_{\text{th}}+1}e^{-2|\alpha|^2/(2n_{\text{th}}+1)}, \tag{6.16}$$

where n_{th} is the thermal photon number. Fig. 6.6b shows the agreement between the measured Wigner function along the $X = \mathcal{R}e(\alpha)$ and $P = \mathcal{I}m(\alpha)$ axes and the theory. Only the thermal photon number is used as a fitting parameter. We can determine that the post-selected Wigner function is the one for a thermal state with the thermal photon number $n_{\text{th}} = 0.01 \pm 0.006$, that is in good agreement with an independent measurement[2] of the thermal photon number, giving $n_{\text{th}} < 0.009$.

In the same way, we can post-select all realizations that have a fluorescence record $I^{(0)}$ that is higher than 13 mV. The Wigner function of this ensemble is shown in Fig. 6.7a; here, we can see the appearance of negativity at the center of the quadrature phase space, which is in agreement with the Wigner function of a Fock state $|1\rangle$. The negativity is smaller than that of a Fock state $|1\rangle$ as we are post-selecting based on the fact there is not 0 photon, which means we can have 2 photons as well. The Wigner function is well reproduced using a statistical mixture of Fock states from 0 to 3 photons.

---

[2] This independent measurement was the same as the one in Sec. 5.2.1. However the storage thermal photon number measured was different as the two measurement carried out during different cool downs.

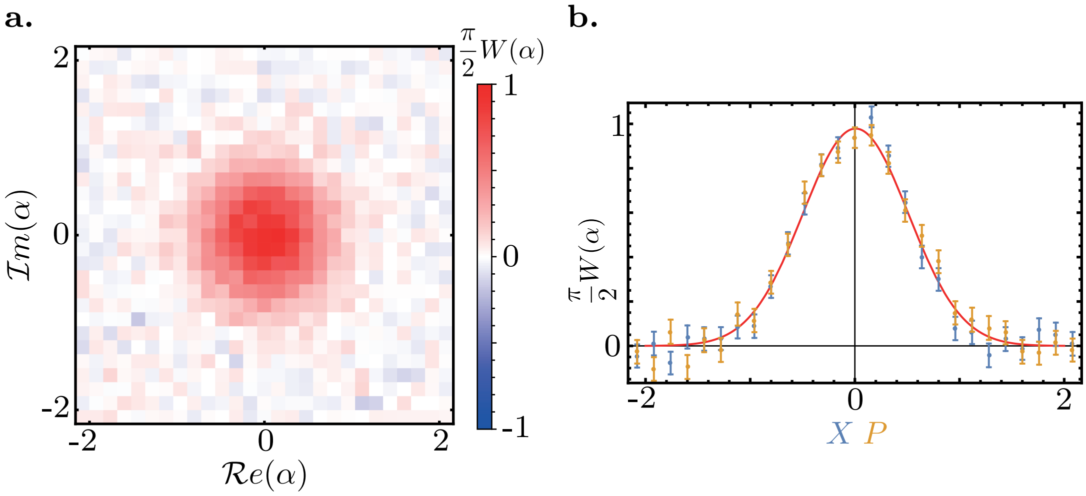

Figure 6.6: **a.** The measured storage mode Wigner function when post-selecting on fluorescence records $I^{(0)} \geq 7\,\mathrm{mV}$ corresponding to "0 photons". **b.** A comparison between a thermal-state Wigner function, with 0.01 thermal photons, and the post-selected measured Wigner function along the $X = \mathcal{R}e(\alpha)$ and $P = \mathcal{I}m(\alpha)$ axes.

The Wigner function used to reproduce the post-selected measured Wigner function is as follows

$$W(\alpha)_{\text{"not0photon"}} = p_0 W(\alpha)_{|0\rangle} + p_1 W(\alpha)_{|1\rangle} + p_2 W(\alpha)_{|2\rangle} + (1 - p_0 - p_1 - p_2) W(\alpha)_{|3\rangle}, \quad (6.17)$$

where p_0, p_1, and p_2 are fitting parameters corresponding to the probabilities of having, respectively, 0, 1 and 2 photons in the post-selected storage state. We obtain a good agreement between the model and the measured Wigner function (see Fig. 6.7b) with $p_0 = 0.18$, $p_1 = 0.49$ and $p_2 = 0.26$. Compared to the initial photon distribution ($p_0 = 0.23$, $p_1 = 0.34$, $p_2 = 0.24$ after the initialization and $p_0 = 0.44$, $p_1 = 0.36$, $p_2 = 0.15$ after the $4\,\mu\mathrm{s}$ fluorescence measurement) we can see that the post-selection has the effect of decreasing the probability of having 0 photons and to increase the probability of having more than 0 photons.

Based on the two post-selected Wigner functions studied, we can conclude that the fluorescence measurements do encode information about the question "Are there 0 photons?".

6.3.3 *Back-action dynamics*

The back-action dynamics, which is the dynamics of the storage mode due to the fluorescence measurement, can be studied by measuring the Wigner function of the storage mode after fluorescence measurements of various durations t and frequencies f_{probe}. This experiment uses the same sequence as the post-selection experiment (see the previous section and Fig. 6.4a) but we vary the fluorescence measurement durations and frequencies. In comparison to the post-selection measurement, here we dismiss the fluorescence record; the only record entering in the analysis is the Wigner function $W(\alpha, t, f_{\text{probe}})$, which depends on the time t and frequency f_{probe}. For each repetition

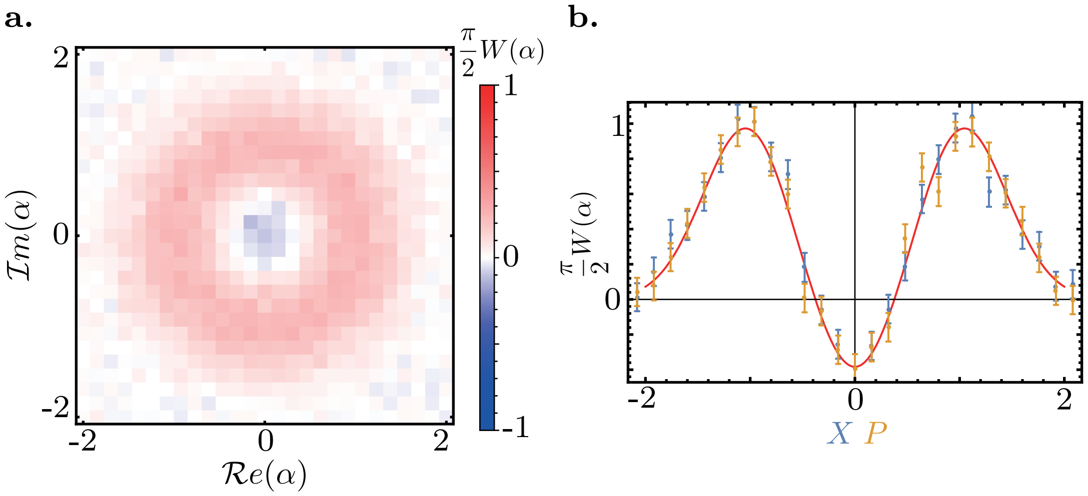

Figure 6.7: **a.** The measured storage mode Wigner function when post-selecting on fluorescence $I^{(0)} \geq 13\,\mathrm{mV}$ corresponding to "not 0 photons". **b.** A comparison between the Wigner function of a statistical mixture of Fock states and the post-selected measured Wigner function along the $X = \mathcal{R}e(\alpha)$ and $P = \mathcal{I}m(\alpha)$ axes.

of the experiment, we initialize the storage mode in a coherent state $|\beta = 1.75\rangle$ and use a fluorescence measurement amplitude $\Omega = \Gamma_{1,\mathrm{mp}}/\sqrt{2}$.

6.3.3.1 *Density matrix coherences*

As noted in Sec. 6.3.2.1 and Appendix c, the Wigner function is in one to one correspondence with the density matrix, so that we can reconstruct the density matrix from the Wigner function (see App. c for the reconstruction process). Using the evolution of the density matrix, we probe the dynamics of coherences between Fock states in order to extract the measurement-induced dephasing rate of the fluorescence measurement for each pair of Fock states. This measurement-induced dephasing will naturally depend on the frequency f_{probe} of the fluorescence measurement. However, the coherences are also affected by the relaxation rate of the storage mode; thus, we decided to normalize the off-diagonal density-matrix elements in order to remove the trivial effects of the storage-mode relaxation. Let us now show that, in the absence of Hamiltonian evolution and measurement back-action, the quantity $|\rho_{\mathrm{nm}}|/\sqrt{\rho_{\mathrm{nn}}\rho_{\mathrm{mm}}}$ indeed evolves only because of dephasing and that its dynamics are not affected by relaxation. We will now consider the storage mode alone, under the influence of its relaxation and dephasing channels in a frame rotating at f_{s}:

$$\dot{\rho} = \Gamma_{1,s}\mathcal{D}(\hat{a}_{\mathrm{s}})\rho + 2\Gamma_{\phi,s}\mathcal{D}(\hat{a}_{\mathrm{s}}^{\dagger}\hat{a}_{\mathrm{s}})\rho. \tag{6.18}$$

From this equation, we can compute the time derivative of the density-matrix elements

$$\begin{aligned}\dot{\rho}_{\mathrm{nm}} =& \Gamma_{1,\mathrm{s}}\left(\rho_{\mathrm{n+1m+1}}\sqrt{(n+1)(m+1)} - \frac{n+m}{2}\rho_{\mathrm{nm}}\right) \\ & - \Gamma_{\phi,\mathrm{s}}\rho_{\mathrm{nm}}(n-m)^2.\end{aligned} \tag{6.19}$$

If the storage mode is initialized in a coherent state $|\alpha_o\rangle$, the solution to the equation is

$$\rho_{\mathrm{nm}}(t) = e^{-|\alpha_o|^2 e^{-\Gamma_{1,s}t}} \frac{\alpha_o^m e^{-m\Gamma_{1,s}t/2} (\alpha_o^*)^n e^{-n\Gamma_{1,s}t/2}}{\sqrt{n!m!}} e^{-\Gamma_{\phi,\mathrm{s}}(n-m)^2 t}, \tag{6.20}$$

and we get

$$\tilde{\rho}_{\mathrm{nm}} = \frac{|\rho_{\mathrm{nm}}|}{\sqrt{\rho_{\mathrm{nn}}\rho_{\mathrm{mm}}}}(t) = e^{-\Gamma_{\phi,\mathrm{s}}(n-m)^2 t}. \tag{6.21}$$

Thus, the normalization does in fact remove the effect of the relaxation rate $\Gamma_{1,s}$ and only characterizes the dephasing rate. In addition, the normalized coherences are independent of the initial coherent state amplitude.

Here, the dephasing rate $\Gamma_{\phi,\mathrm{s}}$ will contain the intrinsic dephasing rate of the storage mode and the measurement-induced dephasing rate due to the fluorescence measurement, which will depend on the measurement frequency and strength. Even if it is a strong (or even wrong) assumption that the fluorescence measurement has a back-action of the form $\mathcal{D}(\hat{a}_\mathrm{s}^\dagger \hat{a}_\mathrm{s})\rho$, we will see that we can still obtain a good agreement between theory and measurement by only assuming that the Eq. (6.21) is valid for a measurement-induced dephasing rate depending on n and m.

6.3.3.2 *Coherence dynamics*

Using each of the Wigner functions $W(\alpha, t, f_{\mathrm{probe}})$, we can reconstruct the density matrix $\rho(t, f_{\mathrm{probe}})$ for each time t and frequency f_{probe}. Before going further into this analysis, we have to check that the reconstructed density matrix is a physical state (meaning that its trace is equal to 1 and the matrix is positive). Here, the density matrix is truncated to 4 photons, due to the size and mesh of the Wigner function and the amplitude of the initial coherent state $\beta = 1.75$. We determine that the trace of the truncated density matrix is smaller than 1 (0.93 on average, with a standard deviation of 0.03 over the whole density matrix). In order to know whether this difference comes from the truncation, we can still check whether the measured Wigner function may corresponds to a physical state by computing its integral over the phase space $\iint \mathrm{d}\alpha W(\alpha)$. The normalization condition of the density matrix $\mathrm{Tr}(\rho) = 1$ is equivalent to the Wigner function normalization $\iint \mathrm{d}\alpha W(\alpha) = 1$. Over the 441 Wigner functions measured for this experiment, the integral over the phase space is equal to 0.99 ± 0.03. The positivity is a property more difficult to check as it do not correspond to some properties of the Wigner function and the density matrix being truncated, it may be non-positive. Thus, we can conclude that the density matrix extracted from the Wigner function is indeed physical up to the truncation. This truncation is not a problem, as long as we only work with the density matrix elements and do not compute any expected mean values for the operators from the truncated density matrix.

The next step before looking at the coherences is to check that the dynamics of the diagonal elements of the density matrix does not depend on the fluorescence measurement (as expected from a QND photon number measurement and as predicted by the simple model of Eq. (6.20)). Fig. 6.8a,b,c,d, and e show the value of the diagonal density matrix element as a function of the measurement time t and normalized detuning $\Delta_{\mathrm{mp}}/\chi_{\mathrm{s,mp}} = 2\pi(f_{\mathrm{mp}} - f_{\mathrm{probe}})/\chi_{\mathrm{s,mp}}$. Up to the precision of the experiment, we

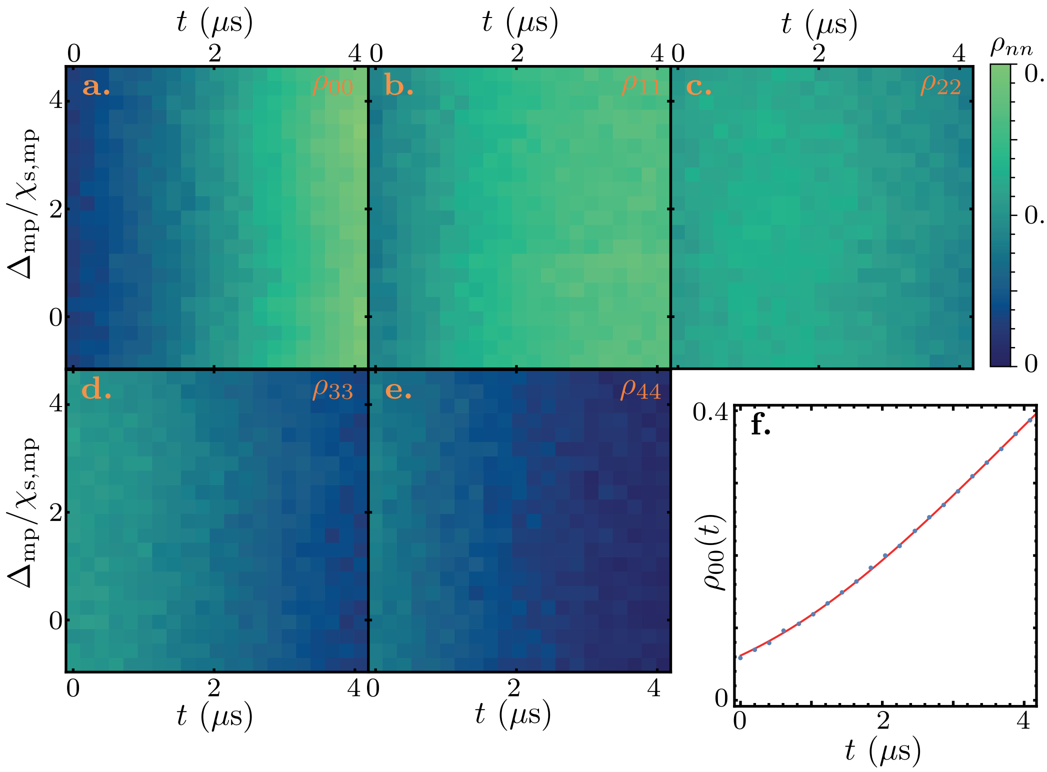

Figure 6.8: **a., b., c., d. et e.** Diagonal element ρ_{nn} of the storage mode density matrix as a function of time t and detuning $\Delta_{\rm mp}$. We check that the dynamics of the diagonal elements does not depend on $\Delta_{\rm mp}$. **f.** The measured (dots) and fitted (line) probability of having 0 photons as a function of time t.

do not see any dependence of diagonal elements $\rho_{\rm nn}$ on the fluorescence measurement frequency $f_{\rm probe}$. We do, however, observe a dependence on the measurement time t, which is attributed to the storage relaxation (as predicted by Eq. (6.20)). We check this assumption by extracting the storage relaxation rate $\Gamma_{\rm 1,s}$ of the $\rho_{00}(t)$ dynamics (see Fig. 6.8) using the fitting function

$$\rho_{00}(t) = \exp\left(-n_0 \mathrm{e}^{-t\Gamma_{\rm 1,s}}\right), \tag{6.22}$$

where n_0 is the initial photon number. We determine that $\Gamma_{\rm 1,s} = (3.79(2)\,\mu\mathrm{s})^{-1}$ is in agreement with the former calibration of the storage lifetime (see Sec. 5.1.2). The initial photon number, measured as $n_0 = 2.78 \pm 0.01$, is below the theoretical value $1.75^2 = 3.06$. We can attribute this difference to the 370 ns duration needed to measure the Wigner function, during which the storage mode unavoidably relaxes.

Following these two sanity checks, we can look at the dynamics of the normalized coherences $\tilde{\rho}_{\rm nm}$. Fig. 6.10 shows the normalized coherences as a function of fluorescence measurement time t and re-scaled detuning $\Delta'_{\rm mp}$ in units of $\chi_{\rm s,mp}$. The difference between the multiplexing qubit resonance frequencies corresponding to two successive photon numbers is not constant owing to higher order effects[3]. Therefore, for an easier interpretation of the figures, we rescale the detuning $\Delta_{\rm mp}$ into a new detuning $\Delta'_{\rm mp}$ in

---

[3] Because of higher order cross-Kerr terms, the cross-Kerr rate depends on the storage mode Fock state. This effect was not taken into account before as it entails only small effects. Here, we take it into

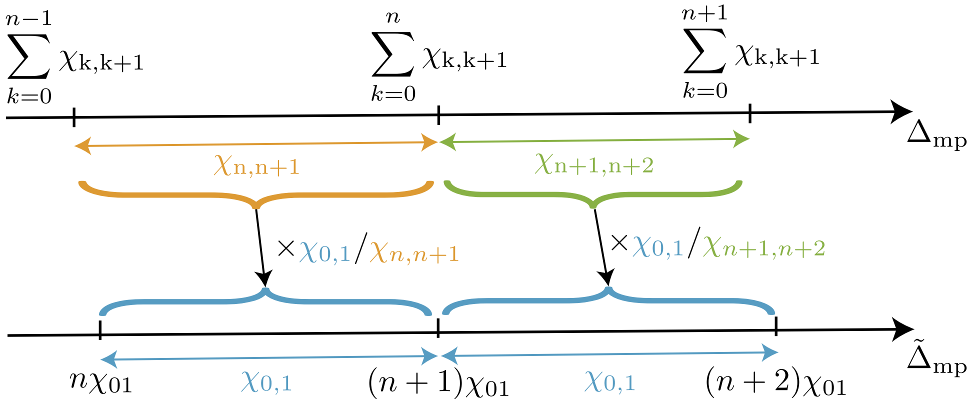

Figure 6.9: Scheme about how the detuning $\Delta_{\rm mp}$ is rescaled in $\Delta'_{\rm mp}$. Each slice of $\Delta_{\rm mp}$ of length $\chi_{n,n+1}$, starting at the detuning corresponding to n photons in the storage mode to the detuning correponding to $n+1$ photons, are multiplied by $\chi_{0,1}/\chi_{n,n+1}$ such that the corresponding slice of $\Delta'_{\rm mp}$ has a length of $\chi_{0,1} = \chi_{\rm s,mp}$.

such a way that the detuning $\Delta'_{\rm mp}$ is exactly given by $n\chi_{\rm s,mp}$ when there are n photons. Here is how this rescaling is realized. We denote $\chi_{n,n+1}$ the differences between the multiplexing qubit resonant frequencies corresponding to n and $n+1$ photons in the storage mode. We have that $\chi_{0,1} = \chi_{\rm s,mp}$, $\chi_{n-1,n} \geq \chi_{n,n+1}$ and the resonant frequency of the multiplexing qubit when the storage mode host n photons is $\omega_{\rm mp} - \sum_{k=0}^{n-1}\chi_{k,k+1}$. The detuning axis is re-scale by slices: the slice $\left[\sum_{k=0}^{n-1}\chi_{k,k+1}, \sum_{k=0}^{n-1}\chi_{k,k+1} + \chi_{n,n+1}\right]$ is multiplied by $\chi_{0,1}/\chi_{n,n+1}$ (see Fig. 6.9). The mathematical formula is

$$\Delta'_{\rm mp} = \begin{cases} \Delta_{\rm mp} & \text{if } \Delta_{\rm mp} < \chi_{0,1} \\ (\Delta_{\rm mp}-\chi_{0,1})\dfrac{\chi_{0,1}}{\chi_{1,2}} + \chi_{0,1} & \text{if } \Delta_{\rm mp} < \chi_{0,1}+\chi_{1,2} \\ \left((\Delta_{\rm mp}-\chi_{0,1})\dfrac{\chi_{0,1}}{\chi_{1,2}} - \chi_{0,1}\right)\dfrac{\chi_{1,2}}{\chi_{2,3}} + 2\chi_{0,1} & \text{if } \Delta_{\rm mp} < \sum_{k=0}^{2}\chi_{k,k+1} \\ \vdots & \vdots \\ \left(\left((\Delta_{\rm mp}-\chi_{0,1})\frac{\chi_{0,1}}{\chi_{1,2}}-\chi_{0,1}\right)\ldots-(n-1)\chi_{0,1}\right)\frac{\chi_{n-1,n}}{\chi_{n,n+1}}+n\chi_{0,1} & \text{if } \Delta_{\rm mp} < \sum_{k=0}^{n}\chi_{k,k+1} \end{cases}. \tag{6.23}$$

When the re-scaled detuning $\Delta'_{\rm mp}$ is equal to $n\chi_{\rm s,mp}$, this implies that the drive is resonant with the multiplexing qubit only if the storage mode contains n photons.

We can see the strong dependence of the normalized coherences $\tilde{\rho}_{nm}$ dynamics on the re-scaled detuning $\Delta'_{\rm mp}$. First, when looking at the dynamics of the coherences between the Fock states $|n\rangle$ and $|m\rangle$, the dephasing is strong when the fluorescence measurement probes around the re-scaled detunings $\Delta'_{\rm mp} = n\chi_{\rm s,mp}$ and $\Delta'_{\rm mp} = m\chi_{\rm s,mp}$. This makes sense as, for these detunings, the fluorescence measurement is asking questions along the lines of "Are there n/m photons?" Thus, we are expecting that the phase between the Fock state $|n\rangle$ (or $|m\rangle$) and the other Fock states diffuses, leading to a decrease in coherence. An interesting behavior is that the strongest dephasing does not happen

---

account to know precisely when the drive is resonant with the multiplexing qubit and for how many photons in the storage.

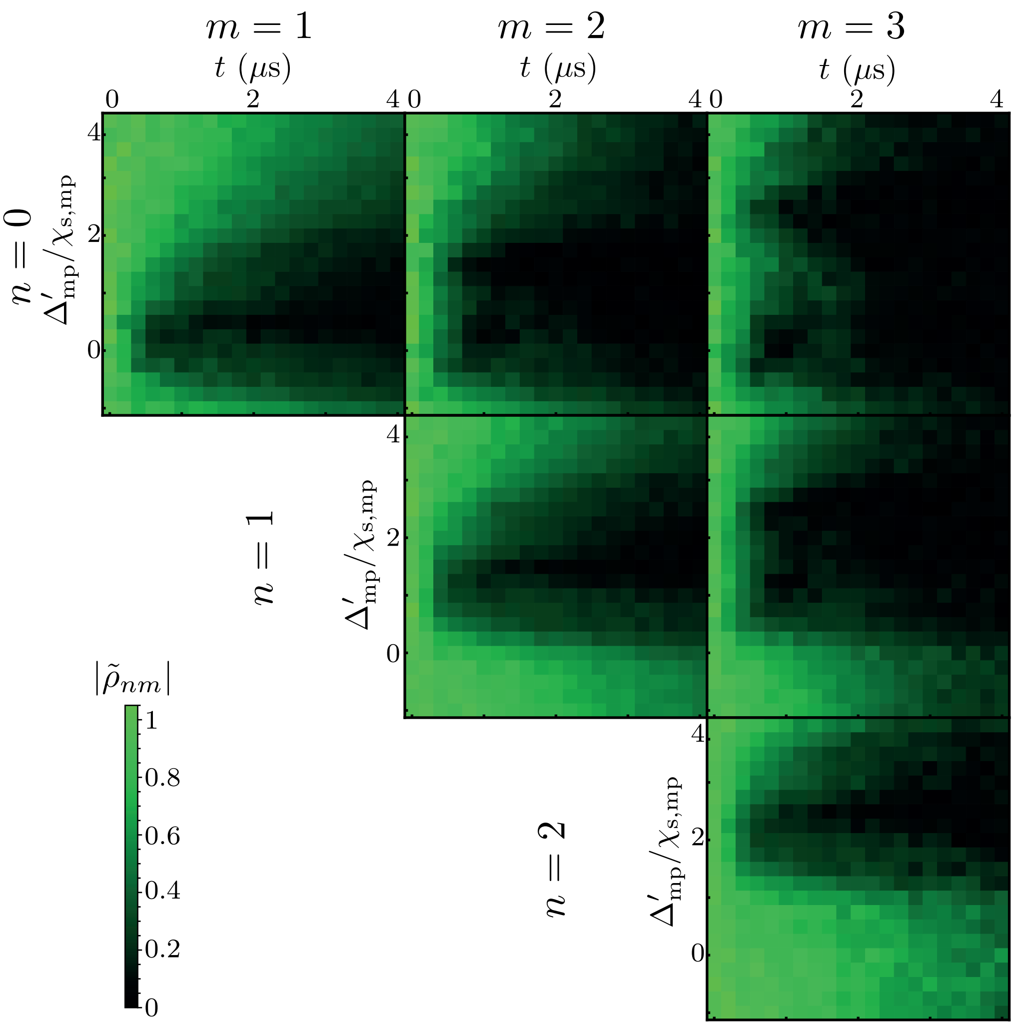

Figure 6.10: Normalized off-diagonal elements $\tilde{\rho}_{\mathrm{nm}}$ as a function of the measurement time t and re-scale detuning Δ'_{mp}. We can see the strong dependence of the $\tilde{\rho}_{\mathrm{nm}}$ dynamics on Δ'_{mp}.

for the re-scaled detuning $\Delta'_{\mathrm{mp}} = n\chi_{\mathrm{s,mp}}$ or $\Delta'_{\mathrm{mp}} = m\chi_{\mathrm{s,mp}}$, but for the detunings that are above and below, respectively. This behavior is not surprising, as we can observe the same in the dispersive readout of a qubit. When the total loss rate of the readout resonator is of the same order as the cross-Kerr rate χ_{qr} between the qubit and the resonator, the optimal readout angular frequency is not $\omega_r - \chi_{\mathrm{qr}}$, $\omega_r - \chi_{\mathrm{qr}}/2$ or ω_r but an intermediate frequency (see Sec. 2.5.3). This is exactly the same situation as the fluorescence measurement has a cross-Kerr rate $\chi_{\mathrm{s,mp}}$ only 1.25 times bigger than the relaxation rate $\Gamma_{1,mp}$.

In order to be more quantitative, we can extract (for each frequency $f_{\mathrm{probe}} = f_{\mathrm{mp}} - \Delta_{\mathrm{mp}}/2\pi$) the rate $\Gamma^{nm}_{\mathrm{d,s}}(\Delta_{\mathrm{mp}})$ at which the normalized coherence $\tilde{\rho}_{\mathrm{nm}}$ dephases. According to Eq. (6.20), this dephasing rate contains both the intrinsic dephasing rate of the storage mode and the measurement-induced dephasing rate of the fluorescence measurement. The next section will discuss this measurement-induced dephasing and introduce a theory that reproduces our observations.

6.3.4 *Measurement-induced dephasing*

In order to explain our measurements, we have to study the bipartite storage/multiplexing qubit system and derive an effective master equation for the storage mode only. This effective master equation will contain the measurement-induced dephasing.

6.3.4.1 *The bipartite system*

The bipartite master equation in the interaction frame reads

$$\begin{cases} H_{\mathrm{s,mp}}/\hbar = -\chi_{\mathrm{s,mp}} n_{\mathrm{s}} \dfrac{\sigma_{\mathrm{z,mp}}}{2} + \Delta_{\mathrm{mp}} \dfrac{\sigma_{\mathrm{z,mp}}}{2} + \dfrac{\Omega}{2} \sigma_{\mathrm{x,mp}} \\ \dot{\rho}_{\mathrm{s,mp}} = \dfrac{-i}{\hbar} [H_{\mathrm{s,mp}}, \rho_{\mathrm{s,mp}}] + \Gamma_{1,\mathrm{mp}} \mathcal{D}(\sigma_{-,\mathrm{mp}}) \rho_{\mathrm{s,mp}} \end{cases}, \tag{6.24}$$

where $\Delta_{\mathrm{mp}} = 2\pi(f_{\mathrm{mp}} - f_{\mathrm{probe}})$, and we neglect the relaxation of the storage mode and the dephasing of the multiplexing qubit. There is two regimes of parameters which are easy to study.

The first regime corresponds to $\chi_{\mathrm{s,mp}} \gg \Gamma_{1,\mathrm{mp}}$, which corresponds to the photon number-resolved regime. In this case, the drive Ω affects the qubit only if it is resonant (i. e. only if $\Delta_{\mathrm{mp}} - k\chi_{\mathrm{s,mp}} = 0$, with k an integer) and the master equation can be simplified using an RWA. This is not the best regime from a fluorescence measurement perspective, as the rate $\Gamma_{1,\mathrm{mp}}$ at which information is extracted is small.

The second regime corresponds to $\chi_{\mathrm{s,mp}} \ll \Gamma_{1,\mathrm{mp}}$. In this case, the dynamic of the multiplexing qubit is faster than the entangling rate, and the system is essentially dissipative. We can perform an adiabatic elimination of the multiplexing qubit in order to obtain an effective master equation for the storage mode. However, this regime is not the best for fluorescence measurement, as the coupling between the storage and the multiplexing qubit is, compared to the qubit relaxation, a perturbation.

Here, the experiment regime is defined by $\chi_{\mathrm{s,mp}} \sim \Gamma_{1,\mathrm{mp}}$ ($\chi_{\mathrm{s,mp}} = 1.25\Gamma_{1,\mathrm{mp}}$ in this experiment). Thus, we cannot use a RWA or a simple adiabatic elimination. The solution, found by A. Sarlette, is to derive an adiabatic elimination at any order in $\chi_{\mathrm{s,mp}}/\Gamma_{1,\mathrm{mp}}$ [178]. Thus, the effective master equation of the storage mode is valid whatever the value of the ratio $\epsilon = \chi_{\mathrm{s,mp}}/\Gamma_{1,\mathrm{mp}}$. We will not derive the demonstration of this adiabatic elimination here (in can be found in our article [178]); however, we will introduce the starting point and the main conclusion.

6.3.4.2 *Adiabatic elimination*

The master equation of the bipartite system can be written using two quantum maps: $\mathcal{L}_0$ and $\mathcal{L}_1$ (see Sec. 2.2.3.2 for the definition of a quantum map). The dynamics of the system follow the master equation

$$\dot{\rho}_{\mathrm{s,mp}} = (\mathcal{L}_0(\rho_{\mathrm{s,mp}}) + \epsilon \mathcal{L}_1(\rho_{\mathrm{s,mp}})), \tag{6.25}$$

where $\mathcal{L}_0$ contains the dissipative driven dynamics of the multiplexing qubit, and $\mathcal{L}_1$ the coupling between the storage mode and the multiplexing qubit. The goal of the adiabatic elimination is to write an effective quantum map $\mathcal{L}_{\mathrm{eff}}$ for the storage-mode density matrix ρ. To do so, we introduce a Kraus map or completely positive trace-preserving map $\mathcal{K}$ to move from the density matrix ρ to the bipartite one $\rho_{\mathrm{s,mp}}$:

$$\rho_{\mathrm{s,mp}} = \mathcal{K}(\rho) = \sum_k M_k \rho M_k^\dagger, \tag{6.26}$$

where $\sum_k M_k^\dagger M_k = \mathbb{1}$

As the time derivative and the Kraus map $\mathcal{K}$ commute, starting from Eq. (6.25), the problem boils down to how to find $\mathcal{L}_{\mathrm{eff}}$ and $\mathcal{K}$, such that

$$\mathcal{K}(\mathcal{L}_{\mathrm{eff}}(\rho)) = (\mathcal{L}_0 + \epsilon \mathcal{L}_1)(\mathcal{K}(\rho)). \tag{6.27}$$

Solving this equation exactly, can be difficult. This is why we used to express $\mathcal{L}_{\mathrm{eff}}$ and $\mathcal{K}$ as a series expansion in ϵ, solve each order separately to improve the accuracy of the solution [182]. Existing work on a different system stopped the series expansion to the second order [183, 184, 185]. In Ref. [178], we derive the analytic solution at an arbitrary order for any subspace of the Hilbert storage space generated by the Fock states $\{|n\rangle, |m\rangle\}$. The effective quantum map $\mathcal{L}_{\mathrm{eff}}$ reads as

$$\begin{aligned}\dot{\rho}_{\{n,m\}} =& \mathcal{L}_{\mathrm{eff}}(\rho) = -i\delta\omega(n,m)\left[|n\rangle\langle n| - |m\rangle\langle m|, \rho_{\{n,m\}}\right] \\ &+ \frac{\Gamma_{\mathrm{MID}}(n,m)}{2}\mathcal{D}(|n\rangle\langle n| - |m\rangle\langle m|)\rho_{\{n,m\}},\end{aligned} \tag{6.28}$$

where $\rho_{\{n,m\}}$ is the storage density matrix restricted to the subspace $\{|n\rangle, |m\rangle\}$ and $\delta\omega$ and Γ_{MID} are the "AC Stark shift" and the measurement-induced dephasing rates between the Fock states $|n\rangle$ and $|m\rangle$, respectively. These quantities read

$$\begin{cases} \delta\omega(n,m) = \dfrac{\lambda - \lambda^*}{4i} \\ \Gamma_{\mathrm{MID}}(n,m) = -\dfrac{\lambda + \lambda^*}{2} \end{cases}, \tag{6.29}$$

where λ is the eigenvalue with the highest real part of the matrix

$$\begin{pmatrix} -\Gamma_{1,\mathrm{mp}}/2 & -\tilde{\Delta}_{\mathrm{mp}} & 0 & 0 \\ \tilde{\Delta}_{\mathrm{mp}} & -\Gamma_{1,\mathrm{mp}}/2 & -\Omega & 0 \\ 0 & \Omega & -\Gamma_{1,\mathrm{mp}} & -\Gamma_{1,\mathrm{mp}} - i2\tilde{\chi}_{\mathrm{s,mp}} \\ 0 & 0 & -i2\tilde{\chi}_{\mathrm{s,mp}} & 0 \end{pmatrix}, \tag{6.30}$$

where $\tilde{\chi}_{\mathrm{s,mp}} = (n-m)\chi_{\mathrm{s,mp}}$ is an effective cross-Kerr rate and $\tilde{\Delta}_{\mathrm{mp}} = \Delta_{\mathrm{mp}} - \dfrac{n+m}{2}\chi_{\mathrm{s,mp}}$ an effective probe detuning.

6.3.4.3 *Comparing theory and experiment*

Now that we are able to predict the measurement-induced dephasing rate of the fluorescence measurement, we can compare the theory to the experiment. Fig. 6.11 shows a comparison between the dephasing rate $\Gamma_{\mathrm{d,s}}^{nm}(\Delta'_{\mathrm{mp}})$ extracted from the normalized coherence dynamics and the theoretical dephasing rate $\Gamma_{\varphi,\mathrm{s}}(n-m)^2 + \Gamma_{\mathrm{MID}}(n,m)$ for

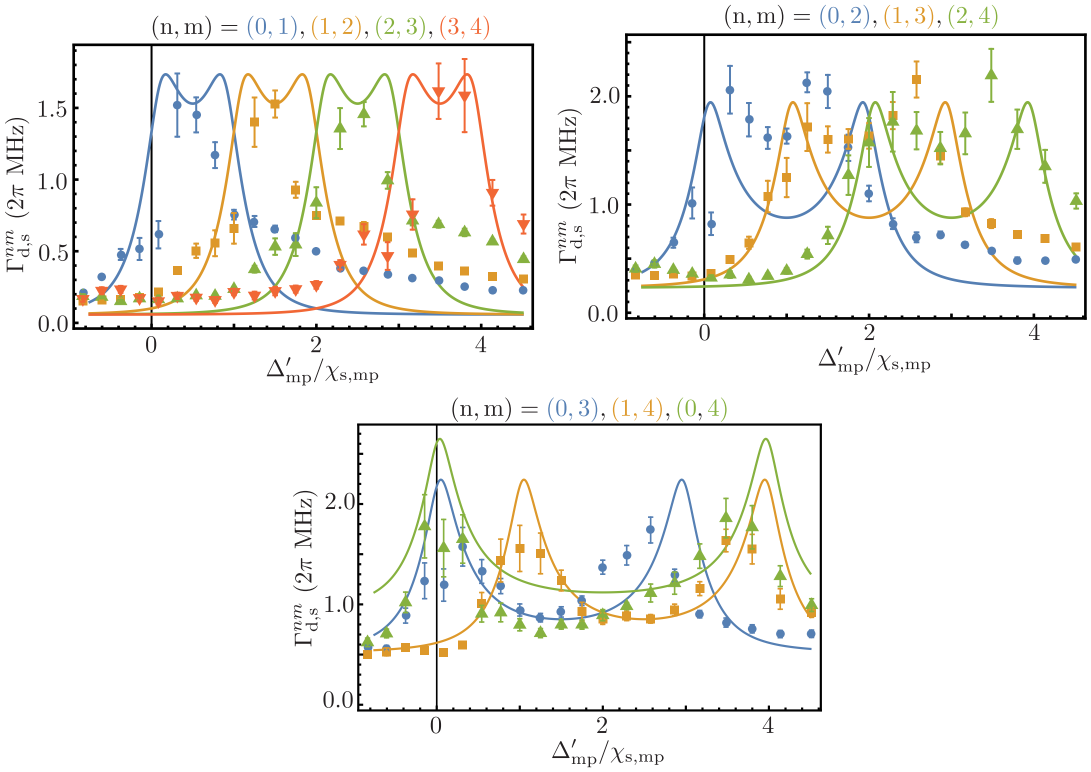

Figure 6.11: Decoherence rate of superpositions between Fock states induced by a fluorescence photon measurement. In each panel, dots show the measured dephasing rate of the normalized coherences $\tilde{\rho}_{\mathrm{nm}}$ using Fig. 6.8. The lines represent the highest eigenvalue of (6.30), without any free parameters. An offset equal to $\Gamma_{\phi,\mathrm{s}}(n-m)^2$, which is the intrinsic dephasing rate of the storage mode, is added to obtain the total dephasing rate.

n and m going from 0 to 4. The rate $\Gamma_{\varphi,\mathrm{s}}$ is the intrinsic dephasing rate of the storage mode (see Sec. 5.1.2) and is equivalent to an offset, as it does not depend on the frequency f_{probe}.

Without any free parameters, we can obtain a good agreement between the measured dephasing rate and the predicted one. The small discrepancy between the theory and the experiment (particularly the asymmetry as a function of n and m) may be explained by the photon loss rate of the storage mode and the higher-order cross-Kerr rate between the storage mode and the multiplexing qubit, which is not captured in the simplified theoretical model and force to use the re-scaled detuning Δ'_{mp} to compare the measurements and the theory. As expected (and in agreement with the dispersive qubit readout) in a regime with resolved resonance peaks ($|\tilde{\chi}_{\mathrm{s,mp}}| > \Gamma_{2,\mathrm{mp}}$), the decoherence rate $\Gamma^{nm}_{\mathrm{d,s}}$ is larger when the single drive probes whether there are n photons or m photons with a moderate drive amplitude Ω. In comparison, in a regime with poorly resolved resonances (that is, where ($|\tilde{\chi}_{\mathrm{s,mp}}| < \Gamma_{2,\mathrm{mp}}$)) the decoherence rate is larger when probing at the middle frequency $\tilde{\Delta}_{\mathrm{mp}} = 0$. The premises of this effect are visible in Fig. 6.11, as the maximal decoherence rate occurs at a re-scaled detuning that is slightly closer to $(n+m)\chi_{\mathrm{s,mp}}/2$, with a stronger effect for small $|m-n|$, both in the theory and in the experimental observations.

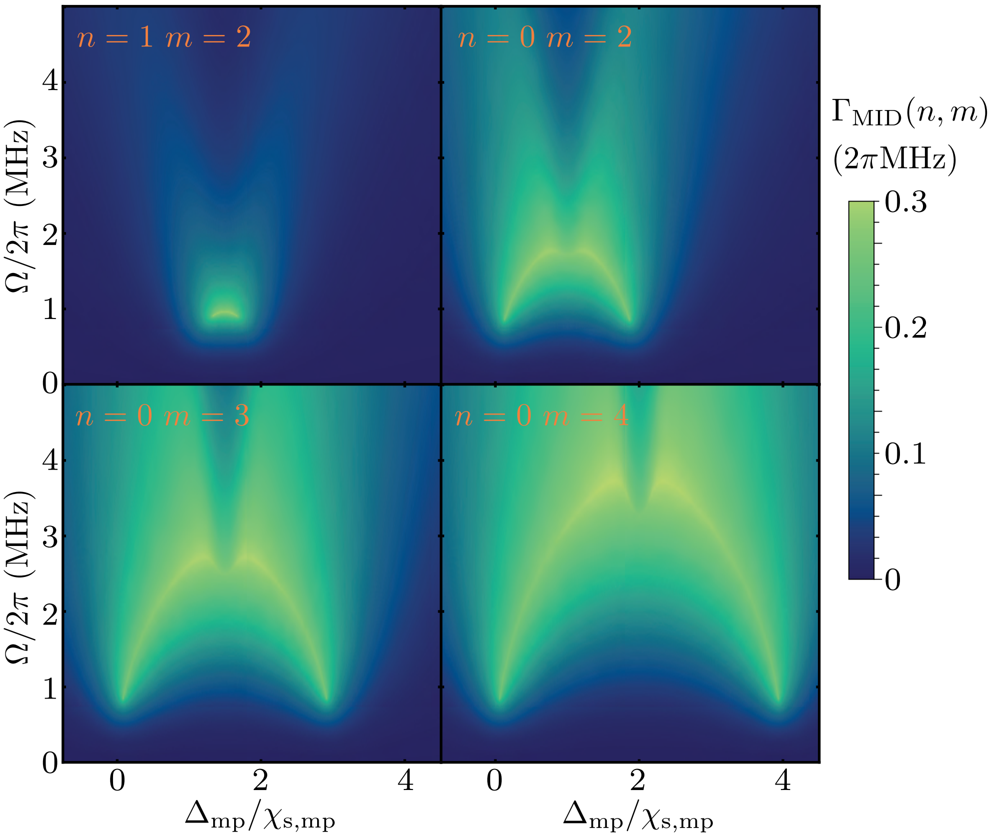

Figure 6.12: Predicted measurement-induced dephasing rate between the Fock states $|n\rangle$ and $|m\rangle$ using Eq.(6.29) as a function of the fluorescence measurement amplitude Ω and the detuning Δ_{mp}. We can see a strong non-linear behavior as a function of Ω. For this graph, we set $\Gamma_{1,\mathrm{mp}} = \chi_{\mathrm{s,mp}} = 1$ (rad.MHz).

The main difference between photon number fluorescence measurement and a qubit dispersive readout is the dependence on the drive strength Ω, which we can study thanks to the theoretical model. In the case of the qubit dispersive readout (see Sec. 2.5.3), the measurement-induced dephasing Γ_{MID} scales linearly with the square of the drive amplitude α_{in}, and the ratio $\Gamma_{\mathrm{MID}}/\alpha_{\mathrm{in}}^2$ is independent of α_{in}. However, Fig. 6.12 shows that the measurement-induced dephasing rate of the fluorescence measurement does not scale linearly with $\Omega^2 = 4\Gamma_{1,\mathrm{mp}}\alpha_{\mathrm{in}}^2$, and that the shape of the function $\Gamma_{\mathrm{MID}}(\Delta_{\mathrm{mp}})$ depends strongly on Ω. We were expecting such a behavior, as the theory predicts that the measurement-induced dephasing rate Γ_{MID} of the fluorescence measurement cannot be greater than $\Gamma_{1,\mathrm{mp}}/2$. This bound makes sense, as the fluorescence emission has a rate limited by $\Gamma_{1,\mathrm{mp}}$, and the number of excitations stored by the multiplexing qubit is limited to 1.

The evolution of the measurement-induced dephasing rate with the drive strength Ω can be understood by looking at the qubit steady state. The linewidth[4] $\delta\omega$ of x_∞ and z_∞ (see Sec. 2.4.2 for a definition) is equal to

$$\delta\omega = 2\Gamma_2\sqrt{1+\frac{\Omega^2}{\Gamma_2\Gamma_1}}. \tag{6.31}$$

In the same way, the width of the y_∞ maxima scales as $\Omega^2/\Gamma_{1,\mathrm{mp}}$ when Ω is much larger than Γ_1 and Γ_2. This shows that the "linewidth" of a qubit increases with the drive strength Ω. Thus, the interesting quantity to look at for the fluorescence measurement is the ratio[5] $\tilde{\chi}_{\mathrm{s,mp}}/\delta\omega$ and, by increasing the drive strength, we can decrease the value of the ratio, bringing the optimal probe frequency closer to $\tilde{\Delta}_{\mathrm{mp}} = 0$. For large Ω, the linewidth $\delta\omega$ of the qubit becomes much larger than the effective cross-Kerr rate $\tilde{\chi}_{\mathrm{s,mp}}$ and the measurement-induced dephasing rate decreases. This non-trivial behavior does not exist in the qubit dispersive readout and is a consequence of the non-linearity of the probe (which, here, is the multiplexing qubit).

CONCLUSIONS

Here are this chapter's main conclusions:

- The fluorescence of a qubit can be used to count the number of photons in a dispersively coupled resonator.
- The fluorescence photon measurement is continuous in time and strength.
- The fluorescence measurement can be multiplexed, whereas the standard approach cannot.
- The multiplexing qubit is used as an entangling device between the storage mode and the many modes of the transmission line. Information is not stored in the multiplexing qubit but, rather, in the state of the many transmission-line modes.
- The correlations between the fluorescence measurement and the Wigner tomography prove that the fluorescence record encodes information about the storage mode photon number.
- The dephasing rate induced by the fluorescence measurement can be measured and predicted by adiabatically eliminating the multiplexing qubit.
- The dephasing rate induced by the fluorescence measurement is expected to show a non-linear behavior as a function of the drive strength Ω. This is a key difference between the photon number fluorescence measurement and the qubit dispersive readout.

---

[4] This is defined here as the frequency band where x_∞ and z_∞ are above half of their maximum for a fixed value of Ω.

[5] As a comparison, the measurement-induced dephasing rate of the qubit dispersive readout is controlled by the ratio $\chi_{qr}/\kappa_{\mathrm{tot}}$, see Sec. 2.5.3. This ratio is independent of the drive amplitude α_{in}.

7

MULTI-FREQUENCY RESONANCE FLUORESCENCE

Frequency multiplexed measurements in circuit QED consist of the simultaneous detection of several signals propagating in the same transmission line but at different frequencies. The detection can be a heterodyne/homodyne detection or a photon detection, as in the gedanken experiment proposed in Sec. 5.3.2. Frequency multiplexing has already been used to read out as many as six qubits coupled to a single feed line [158, 159, 157, 53].

In terms of photon number measurement, the standard approach consists of a time domain-division multiplexing measurement (see Fig. 7.1) during which questions about the storage photon number are asked one after the other, each time using all of the measurement bandwidth. As we discuss in Sec. 5.3.2, by using the frequency domain, we can improve the measurement time of photon number measurements. This new approach is based on two ingredients: first, the fact that we can photocount using the fluorescence of a dispersively coupled qubit, which we explained in Chap. 6; and second, the fact that we can multiplex this fluorescence measurement. In this chapter, we will prove that it is possible to perform the fluorescence photon number measurement using a frequency domain-division multiplexing approach (see Fig. 7.1), in which questions about storage photon numbers are asked simultaneously and the measurement bandwidth is shared between all the questions.

By studying the multiplexing qubit dynamics when the qubit is probed by a frequency comb, we will be able to show that the multiplexed fluorescence photon number measurement is continuous in time. This will lead us to define an infinite frequency comb approximation, permitting us, in the next chapter, to derive a back-action theory for the multiplexed photon number measurement.

This multiplexed fluorescence measurement is only one part of a more complex phenomenon: the resonance fluorescence of a qubit simultaneously driven by multiple frequencies. We call this phenomenon "multi-frequency resonance fluorescence". Actually, the multiplexed fluorescence measurement is simply the multiplexed measurement of the *coherent* emission of a qubit. A qubit can also emit photons incoherently, thanks to spontaneous emission, and as it is a non-linear system, the qubit's scattering can be inelastic. In this chapter, we will define the idea of coherent and incoherent emissions, examining how the qubit scattering can be characterized by its spectral density and how this density can be measured using a heterodyne detection setup. We will see that the multi-resonance fluorescence can be qualitatively explained using the infinite frequency comb approximation. This will lead us to a discussion concerning the following question: "Are we recovering all the available information about the photon number when we measure only the coherent qubit emission?"

Remarks: In this thesis, the word "multiplexing"will always refer to "frequency multiplexing". **Remarks**: Most of the results shown in this chapter are published in Ref. [155]

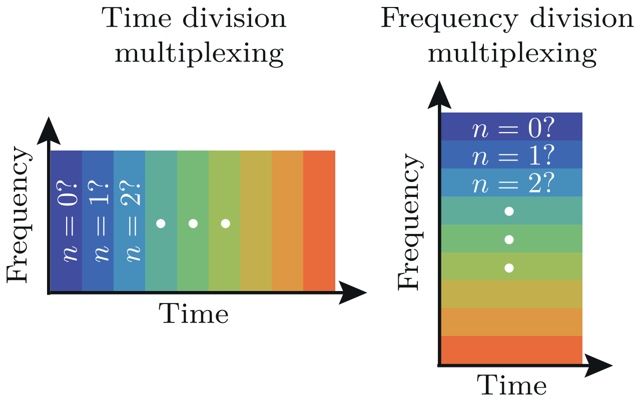

Figure 7.1: Time–division multiplexing takes place one question at a time, while frequency-division multiplexing simultaneously retrieves multiple answers.

7.1 MULTIPLEXED PHOTON NUMBER MEASUREMENT

7.1.1 *Principle*

As explained in Sec. 6.2.2, the fluorescence photon number measurement can be multiplexed. This is achieved by probing the multiplexing qubit at all the angular frequencies $\{\omega_{\mathrm{mp}} - k\chi_{\mathrm{s,mp}}\}_{0\leq k\leq 8}$ simultaneously. In this thesis, we have chosen to restrict the counting to nine frequencies, and thus will probe the photon numbers from 0 to 8. As shown in Fig. 7.2, if the storage mode is in a Fock state, only one frequency will be resonant with the multiplexing qubit, as we are in the number-resolved regime. In a simplified model, the reflected frequency comb will be unchanged; that is, except for the resonant frequency, in which the in-phase amplitude is decreased (see Sec. 2.4.3). Thus, the multiplexed heterodyne detection of the frequency comb reveals the storage photon number[1]. Using the photon number-resolved regime is not mandatory when performing this experiment; however, doing so makes it easier to decode the information stored in each comb's frequency.

The heterodyne detection setup does not need any major changes to be made in order to perform this multiplexed detection. A scheme showing the generation and detection of the comb is shown in Fig. 7.3 (for more details about heterodyne detection, see Sec. 4.3). An intermediate frequency (IF) comb can be generated using an arbitrary waveform generator (AWG) $\{\omega_{\mathrm{IF}} + k\chi_{\mathrm{s,mp}}\}_{0\leq k\leq 8}$, where $\omega_{\mathrm{IF}}/2\pi = 75\,\mathrm{MHz}$. To do so, we need an AWG with a bandwidth greater than $(\omega_{\mathrm{IF}} + 8\chi_{\mathrm{s,mp}})/2\pi$. In our case, the AWG has a bandwidth of 500 MHz, and the maximal comb frequency we used is 115 MHz (see App. b). A Gaussian envelope is chosen as the comb's time envelope in order to decrease the spectral broadening that occurs due to the finite duration of the comb pulse. This IF comb is mixed with a local oscillator (LO) using a lower single-side band mixer in order to generate the radio frequency (RF) comb $\{\omega_{\mathrm{mp}} - k\chi_{\mathrm{s,mp}}\}_{0\leq k\leq 8}$. The reflected RF comb is then amplified using a broadband amplifier—here a Josephson TWPA (see Sec. 4.4)—before being down-converted by the LO, which uses a lower image reject mixer. The IF comb is digitized and a numerical demodulation is performed at

---

[1] We will see, in Secs. 7.2.2.2 and 8.3.1, that the situation is more complex than this.

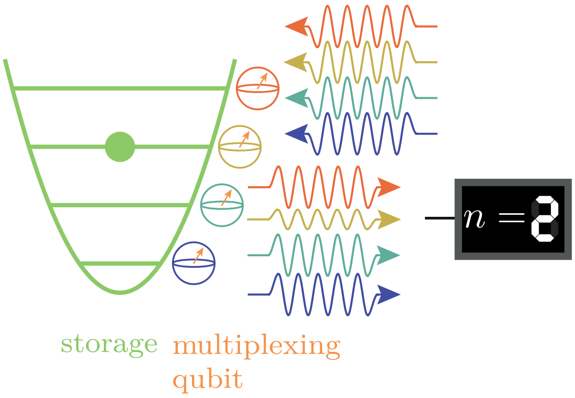

Figure 7.2: The frequency (color) of the multiplexing qubit encodes the storage photon number. The reduction in the reflection amplitude of the qubit at one of the frequencies reveals the number of photons in the storage mode; for example, here there are two photons.

the frequency $\{f_{\mathrm{IF}} + k\chi_{\mathrm{s,mp}}/2\pi\}_{0\leq k\leq 8}$. Each demodulation leads to a record $I^{(k)}(t) + iQ^{(k)}(t)$, which encodes the probability that k photons are stored in the storage mode.

7.1.2 *Demultiplexing*

We have to be careful when demodulating the signal at all the comb frequencies, as a demodulation process requires certain constraints that are easy to satisfy for a single frequency but difficult to satisfy for multiple frequencies. The signal $s(t)$ that we want to demultiplex is of the form[2]

$$s(t) = \sum_{k=0}^{8} I_0^{(k)} \cos(2\pi f_{\mathrm{IF},k} t), \tag{7.1}$$

where $f_{\mathrm{IF},k} = f_{\mathrm{IF}} + k\chi_{\mathrm{s,mp}}/2\pi$ is the intermediate frequency of the record k, and $I_0^{(k)}$ is its amplitude.

In order to demultiplex the IF comb, the sampling frequency of the digitization process must be larger than $2f_{\mathrm{IF},8}$, which is usually easily achieved. Additionally, the duration of the measurement T_{m}, which is usually equal to the length of demodulation window, must be greater than the inverse of the frequency step of the comb $T_{\mathrm{m}} > 2\pi/\chi_{\mathrm{s,mp}} \simeq 200\,\mathrm{ns}$, otherwise the numerical demodulation would not be able to distinguish the comb's two adjacent frequencies. If we want to achieve a perfectly uncorrelated demodulation process, it would be preferable to have a measurement time that is divisible by the period of each frequency of the comb. This means that

$$\forall k \in [\![0, 8]\!],\ \exists n \text{ such that } T_{\mathrm{m}} = \frac{n}{f_{\mathrm{IF},k}}, \tag{7.2}$$

which will ensure that the signal at frequency $f_{\mathrm{IF},k}$ averages to zero when demodulating the frequency $f_{\mathrm{IF},k'}$. This is impossible to do in practice, because the cross-Kerr rate

---

[2] Here, we only focus on the in-phase quadrature, but the whole discussion is valid when adding an out-of-phase quadrature.

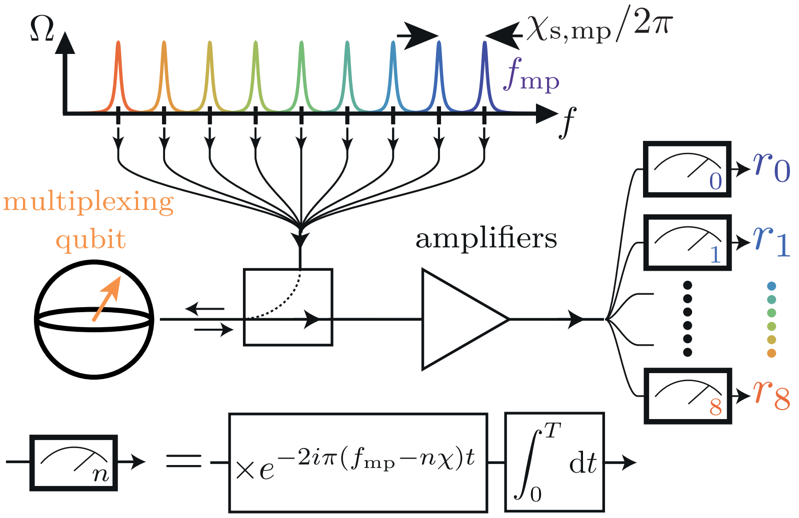

Figure 7.3: The qubit is probed by a frequency comb of amplitude Ω, which is generated using an arbitrary waveform generator. The reflected pulse is amplified and digitized before numerical demodulation occurs at every frequency $f_{\mathrm{mp}} - k\chi_{\mathrm{s,mp}}/2\pi$. This multiplexing–demultiplexing process leads to the reflection coefficients r_k that each encodes the probability that k photons are stored.

$\chi_{\mathrm{s,mp}}$ depends on the storage photon number (due to the higher-order Kerr effect); thus, the comb's frequency steps are not constant. However, the longer the measurement, the smaller the leakage of the $f_{\mathrm{IF},k}$ is when demodulating at $f_{\mathrm{IF},k'}$. Let us consider only the case where $k \in \{0,1\}$ (2 tones only), as doing so will allow us to offer a simpler example. The demodulation at the frequency $f_{\mathrm{IF},0}$ reads

$$I^{(0)} = \frac{2}{T_{\mathrm{m}}}\int_0^{T_{\mathrm{m}}} \mathrm{d}t I_0^{(0)}\frac{1+\cos(4\pi f_{\mathrm{IF},0}t)}{2} + I_0^{(1)}\frac{\cos(\chi_{\mathrm{s,mp}}t)+\cos(2\pi(f_{\mathrm{IF},0}+f_{\mathrm{IF},1})t)}{2}. \tag{7.3}$$

Let us assume that T_{m} is chosen such that it is divisible by $1/f_{\mathrm{IF},0}$. The record $I^{(0)}$ takes the form

$$I^{(0)} = I_0^{(0)} + \frac{2}{T_{\mathrm{m}}}\int_0^{T_{\mathrm{m}}} \mathrm{d}t I_0^{(1)}\frac{\cos(\chi_{\mathrm{s,mp}}t)+\cos(2\pi(f_{\mathrm{IF},0}+f_{\mathrm{IF},1})t)}{2}. \tag{7.4}$$

The last term, which is the demodulation of the record $k=1$ at the frequency $f_{\mathrm{IF},0}$, is not necessarily equal to zero, as T_{m} is not necessarily divisible by $1/f_{\mathrm{IF},1}$. Thus, if T_{m} and f_{IF} are not carefully chosen, the record $I^{(0)}$ reads

$$I^{(0)} = I_0^{(0)} + p_{\mathrm{leak}} I_0^{(1)}, \tag{7.5}$$

where $|p_{\mathrm{leak}}|$ is the fraction of information from the record $k=1$ that leaks into $I^{(0)}$ during the demodulation process. This percentage is bounded by

$$|p_{\mathrm{leak}}| < \frac{2}{T_{\mathrm{m}}\chi_{\mathrm{s,mp}}} + \frac{1}{T_{\mathrm{m}}\pi(f_{\mathrm{IF},0}+f_{\mathrm{IF},1})} \simeq \frac{2}{T_{\mathrm{m}}\chi_{\mathrm{s,mp}}}, \tag{7.6}$$

where the last equality comes from our choice of parameters $f_{\mathrm{IF}} \gg \chi_{\mathrm{s,mp}}/2\pi$. Within this thesis's circuit parameters (see Sec. 5.1.2), the maximum leakage percentage for a measurement of 2 µs is about 3.2%.

As the measurement time cannot be divisible by the periods of all the comb frequencies, we use a demodulation code, choosing a different demodulation window length $T_{\mathrm{d},k}$ for the demodulation of each record k. The demodulation length $T_{\mathrm{d},k}$ is chosen to be the closest to T_m, such that $T_{\mathrm{d},k}/f_{\mathrm{IF},k}$ is an integer.

The demodulation window $T_{\mathrm{d},k}$ needs to be as close as possible to T_m for all k, which means that the relation in Eq. (7.2) is almost verified. Here, we have chosen an intermediate frequency f_IF of 75 MHz, as this offers several advantages. First is that, for a measurement time of 2 µs—which is what is used in multiplexed photon number measurement (see Sec. 7.1.3)—the measurement time is divisible by $1/f_\mathrm{IF}$. Second, this frequency is much larger than $\chi_{\mathrm{s,mp}}/2\pi$ or $1/T_\mathrm{m}$, leading to only a small variation in $T_{\mathrm{d},k}$ (for example, $T_{\mathrm{d},8} = 1.998\,\mu\mathrm{s}$); thus, there is only a small amount of information leakage. Indeed, in this parametric regime, the fraction of information p_leak leaking from the frequency $f_{\mathrm{IF},1}$ when it is demodulated at the frequency $f_{\mathrm{IF},0}$ reads

$$p_\mathrm{leak} = \frac{1}{T_{\mathrm{d},0}} \int_{T_{\mathrm{d},1}}^{T_{\mathrm{d},0}} \cos(\chi_{\mathrm{s,mp}} t)\mathrm{d}t \Rightarrow |p_\mathrm{leak}| < \frac{T_{\mathrm{d},0} - T_{\mathrm{d},1}}{T_{\mathrm{d},0}} \sim 0.001. \tag{7.7}$$

Thus, for this choice of intermediate frequency and measurement time, we can approximate that the record $I^{(k)}$ is only equal to $I_0^{(k)}$. From each record, we can then define a reflected coefficient r_k using the same reference technique as that used in Sec. 6.1.2.

7.1.3 *Photon-counting a coherent state*

To demonstrate the multiplexed photon-counting abilities of our circuit, we perform the following experiment. We initialize the storage mode in a coherent state with mean photon number $\bar{n}$ and measure simultaneously the *emission coefficients* $1 - \mathcal{R}e(r_k)$ at all frequencies $\{f_\mathrm{mp} - k\chi_{\mathrm{s,mp}}/2\pi\}_{0\leq k\leq 8}$. This multiplexed approach is of course much faster than measuring the reflection coefficient at every frequencies one at a time. Fig. 7.4 shows these emission coefficients as a function of the average initial photon number $\overline{n}$ for a drive strength $\Omega = \chi_{\mathrm{s,mp}}/2$ and a measurement duration of 2 µs. For a given $\bar{n}$, every measurement channel k gives an average signal that is a linear combination of the photon number distribution. This linear combination is such that the average signal of channel k is mainly a linear function of the probability to have k photons (see Sec. 8.3.1). As $\bar{n}$ is varied, the shape of the average signal of channel k reproduces a Poisson distribution distorted by relaxation processes, channel cross-talk that increases with driving strength (see Sec. 6.3.4) and demodulation cross-talk (see Secs. 7.2.2.2 and 8.3.1). This multiplexed photon-counting signal can be reproduced using a master equation approach (solid lines in Fig. 7.4) using the photon number calibration of the standard photon-counting approach (see Sec. 5.2.2 for the photon number calibration and appendix d for the master equation approach). This result thus demonstrates the applicability of our multiplexing approach to photon-counting by simultaneously probing information about the presence of 9 possible photon numbers in the resonator. Besides, we demonstrate that the two ingredients, fluorescence and multiplexing, of the gedanken photon-counting approach (see Sec. 5.3.2) are indeed feasible.

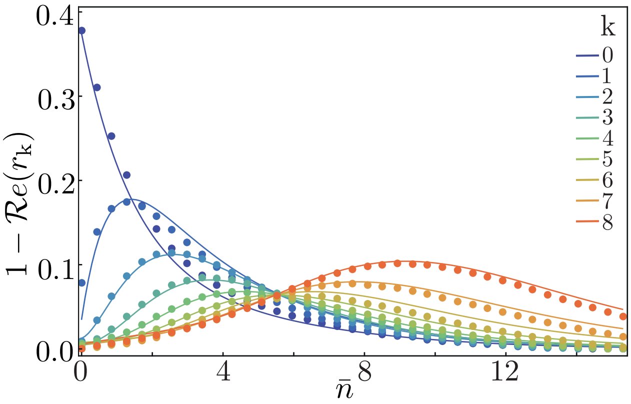

Figure 7.4: Multiplexed photon-counting. Dots: simultaneously measured average emission coefficients corresponding to every photon number k from 0 to 8 as a function of the initial mean photon number $\bar{n}$ in the storage mode. r_k is here the reflection coefficient at $f_{\mathrm{mp}} - k\chi_{\mathrm{s,mp}}/2\pi$. Solid lines: prediction based on a master equation without free parameters (see appendix d).

So how does this proof-of-principle experiment compare with standard photocounting? Each method has its own advantages and drawbacks. The multiplexed photon-counting scheme trades off the temporal constraint and complexity of optimal control of the standard approach for the need of an efficient quantum measurement on a large frequency bandwidth. The efficient measurement of the reflected pulse requires the use of a near quantum-limited amplifier with a dynamical bandwidth of at least a dozen of $\chi_{\mathrm{s,mp}}$ which is now possible using a TWPA [30]. However, in this experiment we didn't succeed to reach the single-shot regime due to the too short lifetime of the storage mode. Thus, one measurement extracts only a part of the 3 bits of photon number information and one can recover all the information only by averaging repeated measurements. The relevant parameter to characterize the strength of our measurement is the parameter $\eta\Gamma_{1,\mathrm{mp}}/\Gamma_{1,\mathrm{s}}$ which is equal to 17 in this experiment. This ratio can be viewed as the number of photons emitted by the multiplexing qubit and which could be detected by the heterodyne detection setup during the lifetime of the storage mode. Increasing it by an order of magnitude would make single-shot measurements possible.

Now we have demonstrated that multiplexed photon number measurement can be performed, let us discuss about some characteristics of this measurement.

7.2 CHARACTERISTICS OF THE MULTIPLEXED FLUORESCENCE MEASUREMENT

In order to compare the multiplexed approach to the standard one, we would like to characterize the multiplexing photon number measurement. The main characteristics we are interested in are the scaling of measurement time with the photon number and the dynamic of the measurement: is it continuous in time ?

The first part of this section will focus on the measurement time and how it depends on the number of frequencies demultiplexed. As the dynamics of the multiplexing measurement is given by the dynamics of the multiplexing qubit, the second part of this section will be dedicated to the study of the dynamic of a qubit driven by a frequency comb.

7.2.1 *Measurement time*

It is out of scope of this thesis work to derive an exact expression of the photon number measurement time for the multiplexed photon number measurement. However, we can determine wether the measurement time depends on the maximum photon number $N_{\max}$ one wants to measure. In contrast with the gedanken experiment which uses photodetectors, multiplexed heterodyne measurements are inherently noisy. This noise comes from the Heisenberg uncertainty principle. For standard photocounting which also uses heterodyne measurement, this noise is usually neglected as the signal amplitude of dispersive qubit readout is not bounded and increase linearly with the drive power[3]. On the contrary, qubit fluorescence measurement will always have a signal amplitude bounded by $\Gamma_c/\sqrt{2}$ (where Γ_c is the coupling rate between the multiplexing qubit and the transmission line, see Sec. 2.4.3).

Identifying the photon number in the storage mode consists in determining which channel contains an amplitude α while all the others contain an amplitude $\alpha_\perp$ (see Sec. 6.3.1 and Sec. 8.3.1). The measurement records $\{I^{(k)}, Q^{(k)}\}_k$ are stochastic processes centered on $\alpha_\perp$ (except for one value of k, where it is centered on α). Determining the photon number comes down to discriminating which record is centered on α only using the ensemble of noisy records $\{I^{(k)}, Q^{(k)}\}_k$.

For a measurement time t, the measurement records $\{I^{(k)}, Q^{(k)}\}_k$ are averaged over that duration, t. Thus the time-averaged intrinsic noise contained in the measurement records scales as $1/\sqrt{t}$ and the time averaged mean value is independent on t. The problem can be mapped onto the following game. $N_{\max}$ stochastic variables $\{u_i\}_{1\leq i\leq N_{\max}}$ are each randomly chosen using a Gaussian distribution centered on 0 with a width $1/\sqrt{t}$. Another stochastic variable u_0 is randomly chosen using a Gaussian distribution[4] centered on 1 with a width $1/\sqrt{t}$. The list $\{u_i\}_{0\leq i\leq N_{\max}}$ is scrambled randomly into a list l and the goal consists in identifying the variable u_0 using only the list l. The optimal strategy is to pick the highest element of the list l. The probability to make an error and lose the game is then given by the probability that the maximum of the $\{u_i\}_{1\leq i\leq N_{\max}}$ are higher than u_0

$$\mathcal{P}_{\text{error}} = \mathcal{P}\left(\max_{N_{\max}\geq i\geq 1}(u_i) > u_0\right). \tag{7.8}$$

We can rescale all the distribution by $\sqrt{t}$, thus u_0 are chosen randomly using a Gaussian distribution centered on $\sqrt{t}$ with a width of 1 and each of the $\{u_i\}_{1\leq i\leq N_{\max}}$ using a Gaussian distribution centered on 0 with a width of 1. One can show that the mean of the maximum of $\{u_i\}_{1\leq i\leq N_{\max}}$ tends towards $\sqrt{2\ln(N_{\max})}$ as $N_{\max}$ tends towards infinity [186].

$$\text{mean}\left[\max_{N_{\max}\geq i\geq 1}(u_i)\right] \sim \sqrt{2\ln(N_{\max})} \tag{7.9}$$

---

[3] This is true as long we stay in the dispersive regime, see Sec. 2.5.3

[4] Here we again approximate the output field of the multiplexing qubit as a coherent state (see Sec. 7.3).

Besides, the median of the max of $\{u_i\}_{1\leq i\leq N_{\mathrm{max}}}$ is equal to the mean value within an error scaling as $1/\sqrt{N_{\mathrm{max}}}$:

$$\begin{aligned}\mathrm{median}\left[\max\nolimits_{N_{\mathrm{max}}\geq i\geq 1}(u_i)\right] &= \mathrm{mean}\left[\max\nolimits_{N_{\mathrm{max}}\geq i\geq 1}(u_i)\right]\\ &\quad +O\left(1/\sqrt{N_{\mathrm{max}}}\right).\end{aligned} \tag{7.10}$$

Since the error probability is between 1/4 and 3/4 if the median of u_0 is equal to the median of the maximum of $\{u_i\}_{1\leq i\leq N_{\mathrm{max}}}$, this leads to

$$\begin{aligned}1/4 < \mathcal{P}_{\mathrm{error}} < 3/4 &\Rightarrow \sqrt{t} \sim \sqrt{2\log N_{\mathrm{max}}}\\ &\Rightarrow t \sim \log(N_{\mathrm{max}})\end{aligned} \tag{7.11}$$

From this expression, we understand that the measurement time for a fixed error probability scales as $\log(N_{\mathrm{max}})$. Thus, the multiplexed measurement shows a measurement scaling similarly to the state-of-the-art standard approach (the binary decimation, see Sec. 5.3.1). The main differences between the binary decimation and the multiplexed measurement scaling is that the scaling of the binary decimation comes from the entangling process between the storage and the yes-no qubit, whereas the multiplexed measurement scaling comes from the noise of the heterodyne measurement. Using a detection setup without noise, such as the photodetectors of the gedanken approach, one can reach a better scaling. Indeed, in Sec. 8.2.2 we will derive that the best scaling one can reach[5] with the multiplexing approach based on the frequency comb, is a measurement time independent of N_{max}.

We demonstrate that the multiplexed measurement and the binary decimation scale similarly. However, the multiplexed measurement is not based on a decimation of the photon number information as former protocols, it recovers all the information at the same time. Moreover, by describing its dynamics, one can show that the multiplexed photon number measurement is a continuous measurement which is not the case for the binary decimation.

7.2.2 *Dynamics of a qubit driven by a comb*

In this section, we will focus on the dynamics of the multiplexing qubit when it is probed by a frequency comb. The goal is to study its emission rate as every time it emits a photon, the storage and the transmission line many modes are entangled and information about the storage photon number is extracted out of the system. We will not take into account the dispersive coupling of the multiplexing qubit with the storage mode. It will be added later in Sec. 8.2. Removing the dispersive coupling is not an issue as we are going to study the multiplexing qubit dynamics under the approximation that the frequency comb is infinite. In this case, the qubit dynamics stays the same when its resonant frequency is shifted by $\chi_{\mathrm{s,mp}}$, thus the qubit dynamics is independent on the storage state.

---

[5] Here we are talking about the smallest measurement time one can have when using a detection setup recovering all the information without noise.

7.2.2.1 *Hamiltonian evolution*

We consider a single qubit driven by a frequency comb with $2p+1$ frequency peaks at every $f_{\mathrm{mp}} + k\chi_{\mathrm{s,mp}}/2\pi$ for $-p \leq k \leq p$. Thus, the frequency comb is centered on the qubit frequency f_{mp}. In the frame rotating at the qubit frequency, the Hamiltonian reads

$$H(t) = \frac{\Omega}{2}\left(\sum_{k=-p}^{p} \cos(k\chi_{\mathrm{s,mp}}t)\right)\sigma_{\mathrm{x,mp}}. \tag{7.12}$$

Surprisingly, there is no term in $\sigma_{\mathrm{y,mp}}$ even if the qubit is driven by $2p$ detuned tones. This is due to the symmetry of the comb with respect to the qubit frequency. The term in $\sigma_{\mathrm{y,mp}}$ is anti-symmetric in k and its sum over all the value of k vanishes and the qubit dynamic will only be in the yz-plane of the Bloch sphere. After a time t, the qubit state will thus be rotated around the x-axis of the Bloch sphere by an angle $f(t)$ with

$$f(t) = \Omega t \sum_{k=-p}^{p} \mathrm{sinc}(k\chi_{\mathrm{s,mp}}t), \tag{7.13}$$

where $\mathrm{sinc}(x) = \sin(x)/x$. For large integers p, we can approximate the sum as

$$\sum_{k=-\infty}^{+\infty} \mathrm{sinc}(\pi k T) = \frac{1}{T}, \tag{7.14}$$

which is valid for $0 < T < 2$. Note that for a small number of peaks $2p+1$, this approximation is invalid close to $T=0$ or 2. The expression allows us to approximate $f(t)$ for $0 < \chi_{\mathrm{s,mp}}t/2\pi < 1$. It is then simple to derive $f(t)$ at any time t since it is periodic up to the term in $k=0$. With this we get

$$f(t) \approx \pi\frac{\Omega}{\chi_{\mathrm{s,mp}}} + 2\pi\frac{\Omega}{\chi_{\mathrm{s,mp}}}\left\lfloor \frac{t\chi_{\mathrm{s,mp}}}{2\pi}\right\rfloor =: \bar{f}(t), \tag{7.15}$$

where $\lfloor x \rfloor$ is the integer part of x. Therefore the rotation angle $f(t)$ evolves by steps. A comparison of the actual $f(t)$ and of the staircase approximation for a comb with 21 frequencies ($p=10$) is shown in Figure 7.5. To put it simply, the action of the comb consists in performing a Rabi rotation on the qubit by discrete steps instead of a continuous evolution as is the case for a single driving frequency. At each period $2\pi/\chi_{\mathrm{s,mp}}$, the qubit rotates almost instantaneously by an angle $2\pi\frac{\Omega}{\chi_{\mathrm{s,mp}}}$. This results can be understood as a consequence of Fourier transform properties. The Fourier transform of a comb being a comb, the frequency comb pulse is in fact a time comb of period $2\pi/\chi_{\mathrm{s,mp}}$.

Without decoherence, if the qubit starts in state $|g\rangle$ at time t_0, the qubit state after a time t reads

$$\begin{aligned}|\psi(t)\rangle &= \cos\left(\tfrac{f(t)-f(t_0)}{2}\right)|g\rangle + i\sin\left(\tfrac{f(t)-f(t_0)}{2}\right)|e\rangle \\ &\approx \cos\left(\tfrac{\Omega\pi}{\chi_{\mathrm{s,mp}}}\left\lfloor\frac{(t-t_0)\chi_{\mathrm{s,mp}}}{2\pi}\right\rfloor\right)|g\rangle + i\sin\left(\tfrac{\Omega\pi}{\chi_{\mathrm{s,mp}}}\left\lfloor\frac{(t-t_0)\chi_{\mathrm{s,mp}}}{2\pi}\right\rfloor\right)|e\rangle\,.\end{aligned} \tag{7.16}$$

Let us focus on some particular values of $\frac{\Omega}{\chi_{\mathrm{s,mp}}}$.

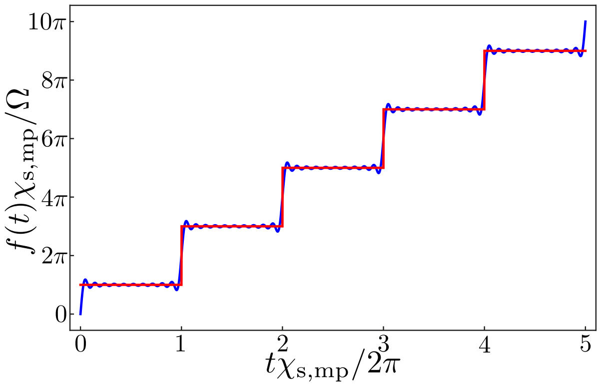

Figure 7.5: Exact rotation angle $f(t)$ in blue and its staircase approximation $\bar{f}(t)$ in red. The duration of each step is equal to $2\pi/\chi_{\mathrm{s,mp}}$ and its height to $\frac{2\pi\Omega}{\chi_{\mathrm{s,mp}}}$. The quality of the approximation improves as the number of peaks $2p+1$ in the comb gets larger. The fact that the trajectory starts with a half-jump is a particularity of having assumed that all comb components have the same phase at $t=0$. Random initial phases of the signals (e.g. due to initializing the qubit after its photon emission into the measuring transmission line at a random time) would most often position $t=0$ on a flat portion of the staircase.

- If $\frac{\Omega}{\chi_{\mathrm{s,mp}}}$ is integer, the staircase approximation with $\bar{f}(t)$ keeps the qubit in $|g\rangle$ at all times, just performing a full rotation on the Bloch sphere at each Rabi pulse. In presence of relaxation, a photon loss can only happen during the short duration of the Rabi pulse, which decreases as $1/(p+1)$. One can say that the frequency comb has barely no effect on the qubit.
- If $\frac{\Omega}{\chi_{\mathrm{s,mp}}}$ is half-integer, the staircase approximation with $f=\bar{f}$ makes the qubit state jump periodically between $|g\rangle$ and $|e\rangle$. Intuitively, one can expect that this maximal extent of the evolution on the Bloch sphere entails a maximal qubit emission. This will be confirmed in Sec. 7.3.3.2.

Now we describe the Hamiltonian dynamics of the multiplexing qubit, one need to add the relaxation in order to understand multiplexing qubit emission and the entangling process between the storage and the transmission line.

7.2.2.2 *Integrated qubit dynamics in the presence of relaxation*

In the following, we use the infinite comb approximation $f(t)\approx\bar{f}(t)$. This allows us to integrate the qubit dynamics exactly. The continuous photon decay at rate $\Gamma_{1,\mathrm{mp}}$ is interrupted by discrete Rabi rotations at discrete times. The qubit state is confined in the $y-z$ plane of the Bloch sphere. Under this approximation, after the Rabi pulse number $k+1$, the qubit state is given by

$$\begin{pmatrix} y(kT+T) \\ z(kT+T) \end{pmatrix} = \begin{pmatrix} \cos\theta & -\sin\theta \\ \sin\theta & \cos\theta \end{pmatrix} \begin{pmatrix} e^{-\Gamma_{1,\mathrm{mp}}T/2}\,y(kT) \\ e^{-\Gamma_{1,\mathrm{mp}}T}z(kT)+(e^{-\Gamma_{1,\mathrm{mp}}T}-1) \end{pmatrix} \quad (7.17)$$

where $T=2\pi/\chi_{\mathrm{s,mp}}$ is the period, $\theta=\frac{2\pi\Omega}{\chi_{\mathrm{s,mp}}}$ is the angle spanned in the Bloch sphere during a discrete jump. The origin of time $t=0$ is chosen to start just after a Rabi jump.

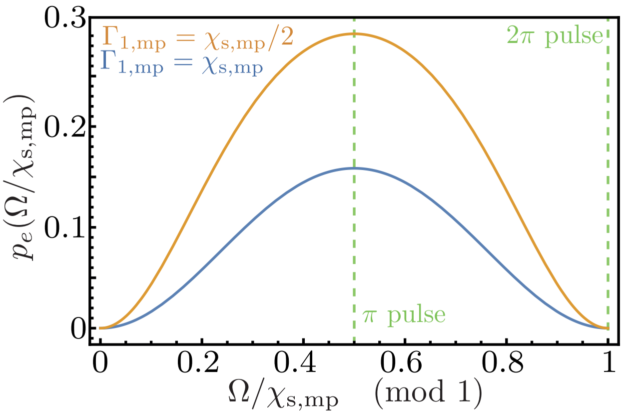

Figure 7.6: Average qubit excited state population when the qubit is probed by an infinite frequency comb. The green dashed line give the ratio $\Omega/\chi_{\mathrm{s,mp}}$ for which the Rabi pulses are either π-pulses or 2π-pulses.

The permanent solution of this discrete-time map right after a step is

$$\begin{aligned}\bar{y}(kT) &= \frac{e^{\Gamma_{1,\mathrm{mp}}T/4}\sinh(\Gamma_{1,\mathrm{mp}}T/2)\sin\theta}{\cosh(3\Gamma_{1,\mathrm{mp}}T/4)-\cos\theta\cosh(\Gamma_{1,\mathrm{mp}}T/4)}\,,\\ \bar{z}(kT) &= \frac{\sinh(\Gamma_{1,\mathrm{mp}}T/2)(e^{-\Gamma_{1,\mathrm{mp}}T/4}-e^{\Gamma_{1,\mathrm{mp}}T/4}\cos\theta)}{\cosh(3\Gamma_{1,\mathrm{mp}}T/4)-\cos\theta\cosh(\Gamma_{1,\mathrm{mp}}T/4)}\,.\end{aligned} \tag{7.18}$$

The average qubit excited state population over one period in the permanent regime reads

$$p_e(\Omega/\chi_{\mathrm{s,mp}}) := \frac{1}{T}\int_0^T \langle e|\rho(t)\,|e\rangle = \frac{1-e^{-\Gamma_1 T}}{\Gamma_1 T}\,\frac{(1+\bar{z}(kT))}{2}\,. \tag{7.19}$$

When using the parametrization $c \equiv \cos(\theta)$, one easily checks that p_e is a strictly decreasing function of $c \in [-1,1]$. As a function of θ, it has maxima for $\theta = (2k+1)\pi$ (i. e. $\Omega/\chi_{\mathrm{s,mp}}$ half integer) and minima for $\theta = 2k\pi$ (i. e. $\Omega/\chi_{\mathrm{s,mp}}$ integer). The latter are no surprise and give $p_e = 0$ as the Rabi pulse is a 2π-pulse and takes the state from $|g\rangle$ back to $|g\rangle$ (see Fig. 7.6); for finite number of peaks in the comb $2p+1$, the Rabi pulse is not instantaneous and $p_e > 0$ at these minima. The maximum is reached when the Rabi pulse is a π-pulse and its value would be $p_e = \frac{\tanh(\Gamma_{1,\mathrm{mp}}T/2)}{\Gamma_{1,\mathrm{mp}}T}$ with the infinite-comb approximation (see Fig. 7.6).

According to this approximation, the average rate of photon emission, which is linked to the measurement strength (each photon reveals information about the qubit frequency and hence the photon number), is thus $p_e\Gamma_{1,\mathrm{mp}} = \tanh(\Gamma_{1,\mathrm{mp}}T/2)/T$ with the optimal choice of $\Omega = \chi_{\mathrm{s,mp}}/2 + k\chi_{\mathrm{s,mp}}$, where k is integer.

- At fixed $T = 2\pi/\chi_{\mathrm{s,mp}}$, the emission rate increases with $\Gamma_{1,\mathrm{mp}}$ and converges towards $\chi_{\mathrm{s,mp}}$. For $\Gamma_{1,\mathrm{mp}} \gg \chi_{\mathrm{s,mp}}$, the qubit has the time to fully relax during one period. Therefore, in simple terms, at each period in the stepwise evolution, the qubit is excited and then releases deterministically a single photon into the output transmission line.

- Likewise, for a fixed $\Gamma_{1,\mathrm{mp}}/\chi_{\mathrm{s,mp}}$ (thus fixed probability p_e to emit a photon during a period), the average emission rate increases when T decreases. Therefore the average emission rate increases as $\chi_{\mathrm{s,mp}}$.
- For a fixed $\Gamma_{1,\mathrm{mp}}$, the largest average emission rate is obtained for $\chi_{\mathrm{s,mp}}$ as large as possible, but it saturates at $P\Gamma_{1,\mathrm{mp}} = \Gamma_{1,\mathrm{mp}}/2$. This is consistent with the fact that $\Gamma_{1,\mathrm{mp}}$ is a hard limit on the photon emission rate.

Surprisingly, we have found that the entanglement dynamics here is the same as that in the gedanken experiment. Here, the frequency comb is equivalent to a π pulse when $\Omega/\chi_{\mathrm{s,mp}} = 1/2$, and the entanglement between the storage and the transmission line is simply due to the spontaneous emission of the multiplexing qubit. The only difference is that the gedanken experiment contains only one π pulse, whereas the multiplexed measurement is a time series of multiple π pulses. Thus, the multiplexed measurement can be seen as the gedanken experiment repeated every time T with a heterodyne detection setup.

Based on these entanglement dynamics, we can conclude that the multiplexed measurement is continuous in time, that the ratio $\Omega/\chi_{\mathrm{s,mp}}$ enables us to continuously tune the multiplexing qubit emission rate, and that the measurement rate is not constant. Indeed, as the emission rate is periodic at the frequency $\chi_{\mathrm{s,mp}}/2\pi$, we might expect that the measurement rate does the same. This raises a cross-talk issue that becomes evident at the numerical demodulation step of the heterodyne detection. As mentioned in Sec. 7.1.3, there is cross-talk between the records $\{r_k\}_k$ (and even between the records $\{I^{(k)} + iQ^{(k)}\}_k$) "due" to the numerical demodulation. During the excitation of the frequency comb, the expected value of the qubit lowering operator $\langle\sigma_{-,\mathrm{mp}}\rangle(t)$ oscillates at the frequency $\chi_{\mathrm{s,mp}}/2\pi$. This means that the Fourier transform of $\langle\sigma_{-,\mathrm{mp}}\rangle(t)$ contains peaks that can be detuned by multiples of $\chi_{\mathrm{s,mp}}/2\pi$. We will confirm these peaks when measuring the spectral density in Sec. 7.3.3.2. Thus, even if the storage mode state is a Fock state, we will obtain a non-null averaged signal for all the records r_k. This cross-talk can be suppressed using an advanced demodulation waveform instead of the cosine and sine functions of constant amplitude [187, 188].

This qubit dynamics raises another question; that is, what is the link between the measurement rate and the measurement-induced dephasing. Indeed, we expect to extract information about the storage photon number every time the multiplexing qubit emits a photon. This means that we want to maximize the probability that the multiplexing qubit is exited in order to maximize the measurement-induced dephasing. However, our detection setup is based on heterodyne detection; its purpose, therefore, is to measure the coherence of the qubit. We would prefer to maximize the coherence of the multiplexing qubit, as this will allow us to maximize the measurement rate. Based on these considerations, it seems that the measurement rate will not be proportional to the measurement-induced dephasing rate. We will examine this point in more detail in Sec. 7.4.

Here, the study of the measurement dynamics allows us to conclude that the multiplexed measurement is a continuous measurement in terms of both time and strength. In fact, we have obtained an even more interesting result; that is, the multiplexed measurement shows how a frequency comb has enabled a new dynamics (compared to the

Bloch dynamics) and, thereby, a new entangling process, which may open the door to new experiments. Another use of microwave combs can be seen in the work of Gertler et al.; they use two frequency combs to engineer an autonomous stabilization of a cavity photon parity [189].

The infinite frequency comb approximation will be used in the next chapter to derive the measurement-induced dephasing rate of the multiplexed photon number measurement. It is worth noting, however, that this approximation has already been useful, as it has enabled us to qualitatively describe the multi-frequency resonance fluorescence of the multiplexing qubit.

7.3 RESONANCE FLUORESCENCE OF A QUBIT WITH A FREQUENCY COMB

In the first chapter of this thesis, we discussed the fluorescence of a qubit (see 2.4.3). At that point, however, we only addressed the coherent elastic scattering of the qubit. In this section, we will study the resonance fluorescence of the multiplexing qubit, defining the concepts of coherent and incoherent emission and elastic and inelastic scattering. All these concepts are connected to spectral density of the qubit emitted field, which has already been studied for a qubit probed at a single frequency [67, 68, 190, 171, 191]. One of the most famous manifestations of the spectral density is the Mollow triplet [67]. Here, we will look at the qubit emitted field spectral density as it applies to a multi-resonance fluorescence; this is when a multiplexing has multiple resonance frequencies, each of which is probed by a frequency comb.

After a theoretical section to define and derive the relations between the relevant quantities (emission rate, auto-correlation functions, spectral densities,...), the spectral density of the output field will be studied through four experiments which differs either by the drive (single frequency or frequency comb), by the state of the storage (vacuum or coherent state $|\alpha\rangle$), by the physical parameters sweep along the experiment (drive amplitude Ω or coherent state amplitude α) or by the normalization used (normalization by the noise, by the reflected comb when the storage contains about 100 photons or both). The Tab. 7.1 summarizes the parameters of each experiments and their goals.

7.3.1 *Qubit scattering*

Remark: For the sake of simplicity, in this section we will use the same notation as that used in Sec. 2.4.3 for the qubit fluorescence.

7.3.1.1 *Coherent and incoherent emissions*

The fluorescence field amplitude $\langle a_{\text{out}}\rangle$ studied in Sec. 2.4.3 is defined as the coherent part of the qubit field [61]. We can define a coherent emission I_{coh} as

$$I_{\text{coh}}(t) = |\langle a_{\text{out}}(t)\rangle|^2 = \alpha_{\text{in}}^2(t) - \sqrt{\Gamma_c}\alpha_{in}(t)\langle\sigma_x\rangle(t) + \Gamma_c\frac{\langle\sigma_x\rangle^2(t)}{4}, \tag{7.20}$$

where Γ_c is the coupling rate between the qubit and the transmission line used to record the fluorescence field (see Sec. 2.4.3) and the last equality is obtained for a coherent input drive α_{in} with a phase $\phi_d = 0$. Interestingly, the coherent emission contains the

Sec.	drive freq.	storage state	sweep	normalization	goal
7.3.2.2	single	vacuum	Ω	noise	Mollow triplet observation, test of the measurement setup
7.3.3.1	comb	vacuum	Ω	noise and 100 photons	Spectrum when qubit frequency is on the border of the comb
7.3.3.2	comb	$\|\alpha = 3\rangle$	Ω	100 photons	Comb centered Compare to infinite comb approximation
7.3.3.3	comb	$\|\alpha\rangle$	α	100 photons	Shift the qubit frequency from the border to the center of the comb

Table 7.1: Parameters and goal of experiments measuring the reflected drive spectral density. From left to right the columns gives: the section in which the experiments is described and discussed, if the drive used to probe the multiplexing qubit is monochromatic or if it is a comb, the initial storage state, the parameters sweep during the experiment (either the drive amplitude Ω, either the storage coherent state amplitude α), the method used to normalized the spectrum (see each section for more details) and the goal of each experiments

stimulated emission of the qubit $\sqrt{\Gamma_c}\alpha_{\text{in}}\langle\sigma_x\rangle$ and the coherent part of the spontaneous emission of the qubit $\Gamma_c\frac{\langle\sigma_x\rangle^2}{4}$. Indeed, even if the spontaneous emission is a stochastic process, it still contains a coherent part as it is proportional to the qubit's excited-state population, which depends on the drive strength. This coherent emission (expressed in photon/Hz) can be compared to the total emission I_{tot} or photon rate $\langle a_{\text{out}}^\dagger(t)a_{\text{out}}(t)\rangle$, which reads

$$I_{\text{tot}}(t) = \langle a_{\text{out}}^\dagger(t)a_{\text{out}}(t)\rangle = |\alpha_{\text{in}}|^2(t) - \frac{\Omega(t)}{2}\langle\sigma_x\rangle(t) + \Gamma_c\frac{1+\langle\sigma_z\rangle(t)}{2}. \tag{7.21}$$

The first term is the photon flow of the input drive, reflected off the qubit. The second term corresponds to the absorption and stimulated emission of photons by the qubit due to the input drive. As expected, this term's weight increases with the amplitude of the drive $\alpha_{\text{in}} = \Omega/(2\sqrt{\Gamma_c})$. The last term is the spontaneous emission of the qubit, which is given by the product of the qubit excitation probability and of the spontaneous relaxation rate in the transmission line Γ_c. When looking at the time dependence of the photon rate I_{tot}, we can see that it oscillates when the qubit undergoes Rabi oscillations. This makes sense, as the qubit acts as a "single photon reservoir" for the drive. The qubit absorbs and emits photons, following the oscillation pattern of the Rabi oscillations. When averaged over time, the photon rate is equal to $|\alpha_{\text{in}}|^2$, which is the photon rate of the input drive. For a long drive, the phase of the Rabi oscillations becomes random, due to the stochastic spontaneous emission, and the qubit state converges towards its steady state. The photon rate stops oscillating and converges towards the steady-state value

$$I_{\text{tot}}(t \to +\infty) = |\alpha_{\text{in}}|^2 - \frac{\Omega}{2}x_\infty + \Gamma_c \frac{1+z_\infty}{2} = |\alpha_{\text{in}}|^2, \tag{7.22}$$

where x_∞ and z_∞ are the qubit steady-state Bloch coordinates (see Eq. (2.54)) and we assume that $\Gamma_c = \Gamma_1$. In this steady state, the total photon rate of the reflected drive is always equal to that of the input drive.

However, when looking at the coherent emission I_{coh}, we can see that it is in fact not equal to the photon rate I_{tot}; specifically, the steady-state value of the coherent emission is smaller than $|\alpha_{\text{in}}|^2$. The difference between the two is defined as the incoherent emission of the qubit I_{inc}:

$$I_{\text{inc}}(t) = I_{\text{tot}}(t) - I_{\text{coh}}(t) = \Gamma_c \left(\frac{1+\langle\sigma_z\rangle(t)}{2} - \frac{\langle\sigma_x\rangle^2(t)}{4} \right). \tag{7.23}$$

The existence of an incoherent emission by the qubit was expected, as the amplitude of the reflected coefficient of the qubit is smaller than 1 at resonance, even if no transmitted signal was considered. The energy missing in the coherent emission is emitted incoherently by the qubit.

It is interesting to note that both the coherent and incoherent emissions can be measured and related to work and heat transfers in quantum thermodynamics [169].

In this thesis, we will focus on the spectral density of the output field (see below for the definition), which can be split into the elastic and inelastic scattering of the qubit.

7.3.1.2 *Elastic and inelastic scattering*

The coherent and incoherent emissions and the photon rate defined in the last section (see Eqs. (7.20), (7.23), and (7.21)) do not take into account the frequency of the photons. In the lab frame, the mode a_{out} is defined as [62, 48]

$$a_{\text{out}}(t) = \frac{-i}{\sqrt{2\pi}} \int_{-\infty}^{+\infty} \mathrm{d}\omega a_{\rightarrow}(\omega) \mathrm{e}^{-i\omega t}, \tag{7.24}$$

where $a_{\rightarrow}(\omega)$ is the propagating mode of the transmission line oscillating at the frequency ω and moving away from the multiplexing qubit[6]. The time evolution of $a_{\text{out}}(t)$ gives the decomposition over the modes $a_{\rightarrow}(\omega)$ and, thus, gives the frequency of the $a_{\text{out}}(t)$ photons.

As the qubit is a non-linear system, the photon can be inelastically scattered. This means that the photon emitted by the qubit has a frequency different from the one belonging to the drive. The photon rate can be characterized by its spectral density $S_{\text{out}}(\omega)$. For the rest of the section, we consider that the drive amplitude α_{in} is real and constant and that the system state is in a stationary regime. Thus, the spectral density is defined as [67]

$$S_{\text{out}}(\omega) = \frac{1}{2\pi} \int g_{\text{out}}(\tau) \mathrm{e}^{-i\omega\tau} \mathrm{d}\tau, \tag{7.25}$$

---

[6] This equation is only valid if we assume that the system only responds to frequencies close to ω_{mp} [62].

where $g_{\text{out}}(\tau)$ is the field correlation function defined as [8]

$$g_{\text{out}}(\tau) = \langle a_{\text{out}}^\dagger(t+\tau)a_{\text{out}}(t)\rangle, \tag{7.26}$$

which does not depend on the time t for a stationary process. The relation between the spectral density and the correlation function in Eq. (7.25) comes from the Wiener–Khinchin theorem [67, 8][7]. In the lab frame, the correlation functions read

$$g_{\text{out}}(\tau) = |\alpha_{\text{in}}|^2 \mathrm{e}^{i\omega_d\tau} - \sqrt{\Gamma_c}(\langle a_{\text{in}}^\dagger(t+\tau)\sigma_-(t)\rangle + \langle\sigma_+(t+\tau)a_{\text{in}}(t)\rangle) + \Gamma_c\langle\sigma_+(t+\tau)\sigma_-(t)\rangle. \tag{7.27}$$

The correlation function $g_{\text{out}}(\tau)$ contains three terms. The first one is the correlation function of the input drive, and the second one is the cross-correlation between the input drive and the qubit. As we are in the stationary regime (meaning that the qubit has reached its steady state), the stochastic spontaneous emission of the qubit has randomized the phase of the Rabi oscillation. Thus, the σ_- and a_{in} operators are uncorrelated. The correlation function $g(\tau)$ becomes

$$g_{\text{out}}(\tau) = |\alpha_{in}|^2 \mathrm{e}^{i\omega_d\tau} - \frac{\Omega}{2}\langle\sigma_x\rangle \mathrm{e}^{i\omega_d\tau} + \Gamma_c\langle\sigma_+(t+\tau)\sigma_-(t)\rangle. \tag{7.28}$$

The last term of the correlation function $g_{\text{out}}(\tau)$ is more difficult to compute. The only stochastic event that can make the operators σ_- and σ_+ uncorrelated is a spontaneous emission, which happens at the rate Γ_1. Thus, we expect to have correlations between σ_- and σ_+ for times τ that are smaller than Γ_1. The expression of the correlation $\langle\sigma_+(t+\tau)\sigma_-(t)\rangle$ can be found in Ref. [67]; here, we will use its Fourier transform, which is derived in the same reference, to obtain the spectral densities:

$$\begin{aligned} S_{\text{out}}(\omega) =& |\alpha_{in}|^2\delta(\omega-\omega_d) - \frac{\Omega}{2}x_\infty\delta(\omega-\omega_d) \\ &+ \Gamma_c\left[\frac{x_\infty^2+y_\infty^2}{4}\delta(\omega-\omega_d) + \frac{\Gamma_1\Omega^2}{2\pi}\frac{1+z_\infty}{2}\frac{(\omega-\omega_d)^2+\Omega^2/2+\Gamma_1^2}{|d(i(\omega-\omega_d))|^2}\right], \end{aligned} \tag{7.29}$$

where $d(s) = (s+\Gamma_1)((s+\Gamma_2)^2-(\omega_q-\omega_d)^2) + \Omega^2(s+\Gamma_2)$.

The first term of the spectral density is the spectral density of the reflected input drive, which only contributes to the angular frequency ω_d. The second term $-\frac{\Omega}{2}x_\infty\delta(\omega-\omega_d)$ is the combination of two phenomena: the absorption by the qubit, which is negative, and the stimulated emission of the qubit, which is positive. As expected, the qubit only absorbs and emits photons by stimulation, at the drive angular frequency ω_d. Due to the spontaneous emission, the absorbed photon rate is higher than the rate of photons emitted by stimulation; thus, this second term is, overall, negative. The last term, which is the spectral density of the spontaneous qubit emission, is the sum of two sub-terms. The first of these sub-terms, which contributes only to elastic scattering, is the coherent scattering of the qubit. The second sub-term, which contributes to both elastic and inelastic scattering, is the incoherent scattering of the qubit [67]. The expression of the coherent scattering is easy to understand, as it is simply the coupling

---

[7] The Wiener–Khinchin theorem is valid for any stationary and **stochastic** process. Thus, it allows us to derive the spectral density of both the coherent and incoherent emissions.

rate times the qubit coherence. The expression of the second sub-term is more difficult to explain; we first notice the factor $(1+z_\infty)/2$, which is the qubit excited population. As expected, the incoherent emission must be proportional to both the coupling rate and the qubit excited population. The rest of the term depends strongly on the value of Ω compared to Γ_1, Γ_2 and to the detuning $(\omega_q-\omega_d)^2$. One interesting regime is defined as $\Omega \gg \Gamma_1, \Gamma_2, |\omega_q-\omega_d|$; this leads to the so-called Mollow triplet.

7.3.1.3 *Mollow triplet*

The spectral density can be simplified in the regime $\Omega \gg \Gamma_1, \Gamma_2, |\omega_q-\omega_d|$. Here, z_∞ tends towards $1/2$, x_∞ and y_∞ tend towards 0, and Ωx_∞ tends towards Γ_1. Moreover, the incoherent scattering of the qubit takes the form derived in Ref. [67], such that the spectral density reads

$$\begin{aligned} S_{\text{out}}(\omega) =& |\alpha_{in}|^2\delta(\omega-\omega_d) - \frac{\Gamma_1}{2}\delta(\omega-\omega_d) \\ &+ \frac{\Gamma_c}{2}\left[\frac{(\Gamma_1+\Gamma_2)/4}{(\omega-\omega_d-\Omega)^2+\left(\dfrac{\Gamma_1+\Gamma_2}{2}\right)^2} + \frac{\Gamma_2}{(\omega-\omega_d)^2+\Gamma_2^2}\right. \\ &\left. + \frac{(\Gamma_1+\Gamma_2)/4}{(\omega-\omega_d+\Omega)^2+\left(\dfrac{\Gamma_1+\Gamma_2}{2}\right)^2}\right], \end{aligned} \tag{7.30}$$

where the last term, which is the spectral density of the incoherent qubit scattering, is the sum of three Lorentzian functions, known as the Mollow triplet [67, 68, 190, 171, 191]. This means that the qubit emits incoherent photons at the angular frequencies $\omega_d+\Omega$ and $\omega_d-\Omega$. This frequency conversion does not break the energy conservation. The mean energy flow of the Mollow triplet is equal to $\Gamma_c\hbar\omega_d$, while the energy flow coming from the drive and absorbed by the qubit is equal to $\Gamma_1\hbar\omega_d$. If the qubit is strongly coupled to the transmission line, these two energy flows are equal. If another decay channel exists for the qubit, a part of the absorbed energy is lost into this channel. The energy is still conserved, but the energy flow emitted by the qubit in the transmission line is smaller than the one that is absorbed.

This frequency conversion can easily be explained by using a dressed model to describe the qubit-drive system [61]. In this model, the drive is described as a lossy harmonic mode a that is resonant with the qubit; this mode interacts with the qubit through an exchange interaction $\hbar g(a\sigma_+ + a^\dagger\sigma_-)$. We note $|g,N\rangle$ and $|e,N\rangle$, the system states corresponding to the qubit in its ground and excited states, respectively, with N photons in the drive. As the drive is resonant with the qubit, the states $|e,N\rangle$ and $|g,N+1\rangle$ have the same energy. The exchange interaction lifts the degeneracy, and the new eigenstates are $|+,N+1\rangle = (|e,N\rangle + |g,N+1\rangle)\sqrt{2}$ and $|-,N+1\rangle = (|e,N\rangle - |g,N+1\rangle)\sqrt{2}$. The eigenvector's energies are $(N+1)\hbar\omega_q + \hbar\Omega/2$ and $(N+1)\hbar\omega_q - \hbar\Omega/2$ (see Fig. 7.7) with $\Omega = \hbar g\sqrt{\langle N\rangle}$ being the Rabi angular frequency and $\langle N\rangle$ being the mean photon number of the drive [61]. When the system decays from the sub-space $\{|+,N+1\rangle, |-,N+1\rangle\}$ to the subspace $\{|+,N\rangle, |-,N\rangle\}$,

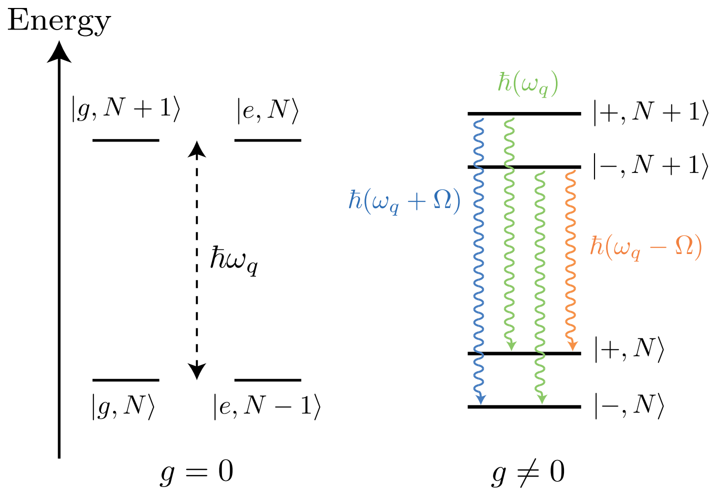

Figure 7.7: Energy diagram of the qubit dressed state. When the coupling rate g is equal to zero, the states $|g, N\rangle$ and $|e, N\rangle$ are degenerate. When $g \neq 0$, the degeneracy is lifted, and the qubit's states are dressed by the drive. New transition frequencies then appear.

photons with three different frequencies can be emitted: ω_q, $\omega_q + \Omega$, and $\omega_q - \Omega$. Here, we retrieve the same frequencies as the Mollow triplet. On average, there is twice the number of decay channels emitting a photon with the frequency ω_q than there is emitting a photon with the frequency $\omega_q \pm \Omega$ (see the number of arrows in Fig. 7.7). We also see this result when looking at the amplitude of each Lorentzian function of the Mollow triplet. In Eq. (7.30), the Lorentzian function centered on ω_d is twice taller than Lorentzian functions that are centered on $\omega_d \pm \Omega$, while half of the incoherent scattering is around the frequency ω_d.

We will now describe the spectral density of the reflected field and explain how we are able to measure it.

7.3.2 *Resonance fluorescence measurement*

7.3.2.1 *Principle*

In practice, we cannot measure the correlation function $g(\tau)$ directly; instead, the output field a_{out} is first amplified and mixed with an idler mode by a phase-sensitive amplifier (see Sec. 4.3.3.2) and, after a frequency down-conversion, the intermediate frequency (IF) $s_{\text{IF}}(t)$ signal is digitized (see Sec. 4.3). The $s_{\text{IF}}(t)$ signal is a stochastic signal, a part of which oscillates at the angular frequency ω_{IF}, with a complex stochastic envelope $s_0(t) = I(t) + iQ(t)$. The goal of the numerical demodulation when performing a heterodyne detection is to recover the best estimation of this complex envelope. It has been shown in Ref. [192] that the correlation function of the complex record $s_0(t)$ is related to $g_{\text{out}}(\tau)$ through the following relationship:

$$\langle s_0^*(t+\tau) s_0(t) \rangle = \frac{\hbar\omega_{\text{mp}} Z_0}{2} (G g_{\text{out}}(\tau) + N_{\text{n}} \delta(\tau)) \mathrm{e}^{-i\omega_d \tau}, \tag{7.31}$$

where G is the gain of the phase-sensitive amplifier, N_n is the noise added by the amplification process, and Z_0 is the transmission line impedance. Similarly to Eq. (7.24), Eq. (7.31) is only valid when we assume that the system responds around the frequency ω_mp.

In this thesis, we have decided to use the stochastic IF signal $s_\mathrm{IF}(t)$ to measure the correlation function. The complex envelope $s_0(t)$ is obtained by demodulating the RF signal at the frequency $-f_\mathrm{IF}$[8] (or the angular frequency $-\omega_\mathrm{IF}$) at the point at which f_IF tends towards infinity[9]. The demodulation has to be achieved in a time window that is equal to k/f_IF, where k is an integer. Let us choose the smallest window, with a length of $1/f_\mathrm{IF}$. Thus, the complex envelope $s_0(t)$ and the IF signal $s_\mathrm{IF}(t)$ are related through the equation

$$s_0(t) = \lim_{f_\mathrm{IF}\to+\infty} 2f_\mathrm{IF} \int_{t-1/(2f_\mathrm{IF})}^{t+1/(2f_\mathrm{IF})} \mathrm{d}t' s_\mathrm{IF}(t')\mathrm{e}^{-i\omega_\mathrm{IF}t'}. \tag{7.32}$$

In App. e, we show that the Fourier transform $\tilde{g}_{s_0}(\omega)$ of the complex envelope correlation function $g_{s_0}(\tau) = \langle s_0^*(t+\tau)s_0(t)\rangle$ is related to the Fourier transform $\tilde{g}_{s_\mathrm{IF}}(\omega)$ of the IF signal correlation function $g_{s_\mathrm{IF}}(\tau) = \langle s_\mathrm{IF}(t+\tau)s_\mathrm{IF}(t)\rangle$ by

$$\tilde{g}_{s_0}(\omega) = \frac{1}{\pi^2}\tilde{g}_{s_\mathrm{IF}}(\omega - \omega_\mathrm{IF}) \tag{7.33}$$

As the IF signal is a stochastic and stationary process, we can use the Wiener–Khinchin theorem to express the Fourier transform $\tilde{g}_{s_\mathrm{IF}}$ as its average power spectral density $\langle|\tilde{s}_\mathrm{IF}(\omega)|^2\rangle$, where $\tilde{s}_\mathrm{IF}$ is the Fourier transform of s_IF. Using this relation and Eqs. (7.33) and (7.31), we can obtain the following relation between the spectral density and the Fourier transform of the IF signal:

$$\frac{\hbar\omega_\mathrm{mp}Z_0}{2}(GS_\mathrm{out}(\omega+\omega_d)+N_\mathrm{n}) = \langle|\tilde{s}_\mathrm{IF}(\omega-\omega_\mathrm{IF})|^2\rangle. \tag{7.34}$$

This can be rewritten using the fact that the power spectral density $\langle|\tilde{s}_\mathrm{IF}(\omega)|^2\rangle$ is an even function and the condition $\omega_d = \omega_\mathrm{mp} = \omega_{RF} = \omega_{LO} - \omega_{IF}$ of a resonant drive, as

$$\langle|\tilde{s}_\mathrm{IF}(\omega)|^2\rangle = \frac{\hbar\omega_\mathrm{mp}Z_0}{2}(GS_\mathrm{out}(\omega_\mathrm{LO}-\omega)+N_\mathrm{n}). \tag{7.35}$$

In practice, the IF signal is digitized; thus, we have to ensure that the discrete Fourier transform of the sampled IF signal is equal to the Fourier transform of the continuous IF signal. The Nyquist-Shannon theorem states that this is the case if the IF signal does not contain a frequency that is above half of the analog-to-digital converter (ADC) sampling frequency; i. e. meaning there is no spectral aliasing. This is ensured by the low-pass filter used after the down-conversion (see Sec. 4.3), which has a frequency cut-off, equal to 200 MHz, that is below half of the ADC sampling frequency (equal to 250 MHz). This also means that only a spectrum in the range of 200 MHz around the multiplexing qubit frequency can be probed using our heterodyne detection setup.

---

[8] We are using the lower side band for our heterodyne detection setup; thus, $\omega_d = \omega_{RF} = \omega_{LO} - \omega_{IF}$ and the IF signal oscillate at $-\omega_\mathrm{IF}$. See Sec. 4.3

[9] If f_IF stays finite, as it would in a real demodulation process, we do not obtain $s_0(t)$ but an estimation of $s_0(t)$, which is filtered by the demodulation process.

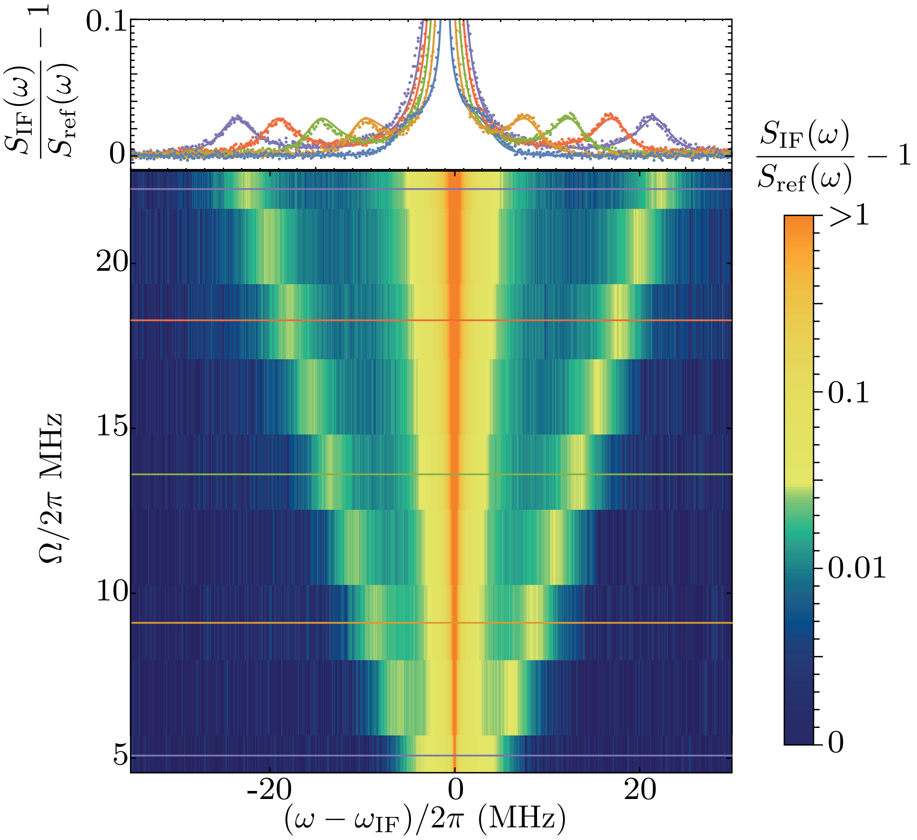

Figure 7.8: Measured normalized spectral density as a function of frequency ω and drive strength Ω. The Mollow triplet, which is characterized by resonances detuned by $\pm\Omega$, is visible. Upper insert: Cuts of the 2D map for values of Ω, indicated by colored lines. The measured spectrum (dots) are compared to the theory (line) using Eq. (7.29).

7.3.2.2 *Measurement*

In order to probe the Mollow triplet, we probe the multiplexing qubit and record, during $T_m = 8.192\,\mu\mathrm{s}$, the IF signal that has been digitized following the down-conversion of the multiplexing qubit fluorescence field. The discrete Fourier transform of the digitized IF signal is computed using the fast Fourier transform algorithm. The absolute value of the measured spectrum is raised to the power 2, before averaging over 450,000 repetitions of the experiment. Due to the finite measurement time T_m, the average power spectral density $S_{\mathrm{IF}}(\omega)$ measured is

$$S_{\mathrm{IF}}(\omega, T_m) = \langle|\tilde{s}_{\mathrm{IF}(T_m)}(\omega)|^2\rangle = \frac{T_m}{2\pi}\langle|\tilde{s}_{\mathrm{IF}} * \mathrm{sinc}(\omega \mathrm{T_m}/2)|^2\rangle, \tag{7.36}$$

in which the symbol $*$ denotes the convolution product. For larger measurement times, we have the relationship [8]

$$\lim_{T_m \to \infty} S_{\mathrm{IF}}(\omega, T_m) = \langle|\tilde{s}_{\mathrm{IF}}|^2\rangle. \tag{7.37}$$

The experiment is then repeated, this time without using a probe as a reference. This second measurement enables us to measure the noise coming from the amplification process and to calibrate the dependence of the amplifier gain on the frequency. We denote this reference spectrum as $S_{\mathrm{ref}}(\omega)$. As T_m is much larger than both the typical auto-correlation time and $2\pi/\chi_{\mathrm{s,mp}}$, we can perform the approximation $S_{\mathrm{IF}}(\omega, T_m) = S_{\mathrm{IF}}(\omega, +\infty)$. We define the normalized spectral density as

$$\frac{S_{\mathrm{IF}}(\omega)}{S_{\mathrm{ref}}(\omega)} - 1 = \frac{G}{N_{\mathrm{n}}} S_{\mathrm{out}}(\omega_{\mathrm{LO}} - \omega). \tag{7.38}$$

Under the assumption that G/N_{n} is independent of ω (which is reasonable over the range $\omega \in [\omega_{\mathrm{IF}} - 2\chi_{\mathrm{s,mp}}, \omega_{\mathrm{IF}} + 10\chi_{\mathrm{s,mp}}]$), the normalized spectral density is proportional to the spectral density of the fluorescence field. Fig. 7.8 shows the measured normalized spectral density for various values of the drive strength Ω. The measurement can be reproduced using Eq. (7.29), in which the Dirac functions are replaced by a unique Lorentzian function, thereby taking into account the finite linewidth of the RF source, the filters, and the finite measurement time. Two parameters are free and can be used to adjust the theory: the global amplitude and the linewidth of the added Lorentzian function. We obtain a good agreement between the measured spectrum and the theory using an amplitude of 0.57 and a Lorentzian linewidth of 10 kHz. The color function used in the 2D map in Fig. 7.8 saturates at 0.04, as the contribution of the reflected drive to the spectral density is about 1,000 times bigger than the multiplexing qubit incoherent emission. Using a scale adapted to the reflected drive contribution would make the Mollow triplet invisible.

Next, we describe and measure the resonant fluorescence of the multiplexing qubit for the storage mode in vacuum; i. e. for a single resonant frequency, we will look at the multi-frequency resonance fluorescence that occurs when the storage mode is populated with various Fock states.

7.3.3 *Multi-frequency resonance fluorescence*

When the multiplexing qubit is probed with the frequency comb, the spectral density of the reflected comb becomes more complex than that given in Eq. (7.29). In the infinite frequency comb regime (see Sec. 7.2.2), the qubit does not undergo a Rabi oscillation. Every time $2\pi/\chi_{\mathrm{s,mp}}$, the qubit instantaneously rotates in the Bloch sphere, before relaxing until the next rotation. Thus, as the qubit dynamic is $2\pi/\chi_{\mathrm{s,mp}}$-periodic, we are expecting to measure new photon emissions at frequencies detuned from the multiplexing qubit frequency by multiple of $\chi_{\mathrm{s,mp}}$.

7.3.3.1 *Resonance fluorescence with a frequency comb*

First, we measure the normalized spectral density when the multiplexing qubit is probed by a frequency comb and the storage mode is empty. The IF signal is digitized over a duration of 8.192 µs for various constant drive strengths Ω. As most of the contribution made by the spectral density is due to the reflected comb, we use a trick to remove this trivial part. We thus perform the measurement a second time, starting from a storage mode with about 100 photons. Owing to the dispersive coupling, the normalized spectral density measured during this second measurement contains only the reflected drive spectrum. Noting that $S_{\mathrm{IF}}(\omega, \overline{n}_{\mathrm{s}})$ is the average power spectral density of the IF

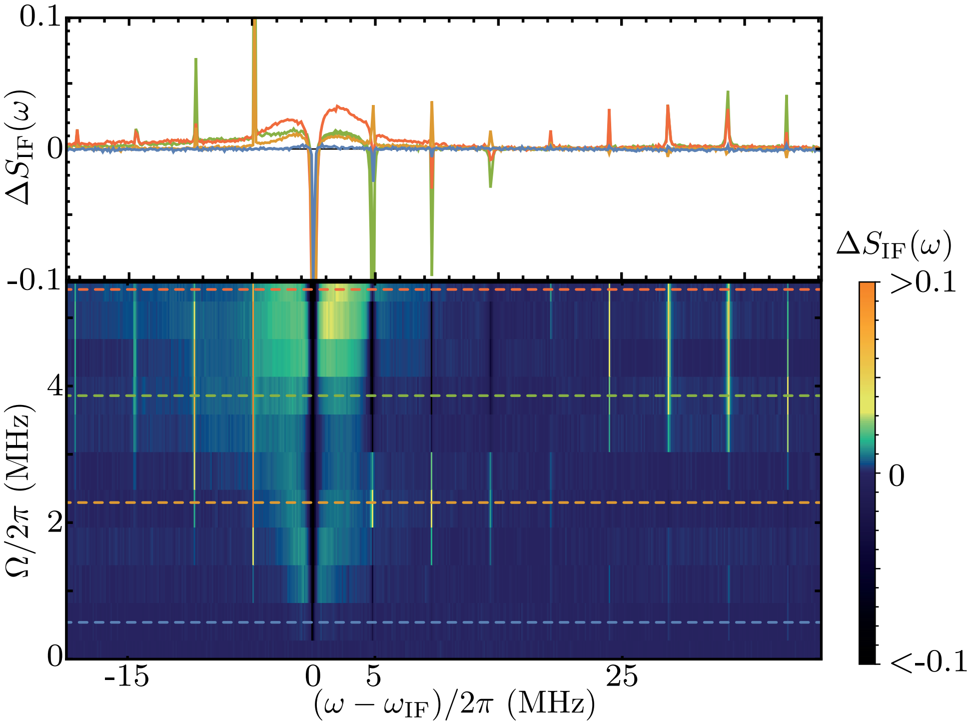

Figure 7.9: The difference $\Delta S_{\rm IF}$ between the normalized spectra of the multiplexing qubit that is probed by a frequency comb when the storage mode has 0 photon and when it has about 100 photons. The spectrum thereby obtained contains only the qubit absorption and emission. The lower graph shows the spectral difference $\Delta S_{\rm IF}$ for various drive strengths Ω. The upper graph shows four cuts of the lower graph, indicated by dashed lines.

signal when the storage mode has an average of $\overline{n}_{\rm s}$ photons, we look at the spectral difference $\Delta S_{\rm IF}$ between the two normalized spectral densities, as follows

$$\begin{aligned}\Delta S_{\rm IF}(\omega) &= \frac{S_{\rm IF}(\omega,\overline{n}_{\rm s}=0)}{S_{\rm ref}(\omega,\overline{n}_{\rm s}=0)} - \frac{S_{\rm IF}(\omega,\overline{n}_{\rm s}\sim 100)}{S_{\rm ref}(\omega,\overline{n}_{\rm s}\sim 100)} \\ &= \frac{G}{N_{\rm n}}\left(S_{\rm out}(\omega_{LO}-\omega,\overline{n}_{\rm s}=0) - S_{\rm out}(\omega_{LO}-\omega,\overline{n}_{\rm s}\sim 100)\right).\end{aligned} \tag{7.39}$$

Based on Eqs. (7.29) and (7.38), the spectral difference $\Delta S_{\rm IF}$ contains only the qubit absorption and emission which is what we were after. Fig. 7.9 shows this spectral difference as a function of the drive strength Ω. Here, it is important to note that the use of the lower sideband in the heterodyne detection (see Sec. 4.3) inverts the frequency axes (see Eq. 7.39).

As expected, the qubit absorption and emission spectrum exhibits a Mollow triplet that is centered on the IF frequency $\omega_{\rm IF}/2\pi = 75\,$MHz, with sidebands centered on $\omega_{\rm IF}\pm\Omega$. However this is only true for $\Omega < \chi_{\rm s,mp}$; for a large driving strength, the multi-frequency nature of the excitation modifies the incoherent emission of the qubit. The Mollow triplet sidebands seem to be localized at the angular frequencies $\omega_{\rm IF}\pm\chi_{\rm s,mp}/2$, and the upper sideband becomes larger than the lower sideband. This asymmetry in the Mollow triplet's amplitude is due to the comb's other frequencies, mainly the one at $\omega_{\rm IF}+\chi_{\rm s,mp}$, which corresponds to the drive that is resonant with the multiplexing qubit when the storage has 1 photon. For large Ω, this drive is able to drive the multiplexing qubit dynamics, even if the storage contains 0 photons. Thus, an incoherent emission is generated around this drive and is superposed on the incoherent emission of the ω_{IF} drive. This explains why the incoherent emission is stronger between the two angular frequencies ω_{IF} and $\omega_{\mathrm{IF}} + \chi_{\mathrm{s,mp}}$.

How the incoherent emission is affected by the frequency comb is not the only interesting information contained in the spectral difference ΔS_{IF}. For angular frequencies $\{\omega_{\mathrm{IF}} + k\chi_{\mathrm{s,mp}}\}_{k\in\mathbb{Z}}$, ΔS_{IF} contains information about the absorption and coherent emissions of the qubit. For small values of Ω (i. e. $\Omega < \chi_{\mathrm{s,mp}}$) the multiplexing qubit absorbs the photons that originate mainly from the drive at the intermediate angular frequency ω_{IF} (which corresponds to the radio frequency ω_{mp}), as it is the only frequency for which the spectral difference ΔS_{IF} is negative. At the intermediate frequencies, which correspond to 1 and 2 photons ($\omega_{\mathrm{IF}} + \chi_{\mathrm{s,mp}}$ and $\omega_{\mathrm{IF}} + 2\chi_{\mathrm{s,mp}}$), the spectral difference is negative for $\Omega/2\pi < 2\,\mathrm{MHz}$ and positive for $2\,\mathrm{MHz} < \Omega/2\pi < 3\,\mathrm{MHz}$, meaning that the multiplexing qubit either absorbs or emits photons at those frequencies. The surprising part lies in the qubit emission that occurs at the frequencies corresponding to negative photon numbers; e. g. $\omega_{\mathrm{IF}} - \chi_{\mathrm{s,mp}}$ and $\omega_{\mathrm{IF}} - 2\chi_{\mathrm{s,mp}}$. This photon emission does not come from the frequency comb, as we have removed the comb's contribution; rather, it comes from the multiplexing qubit. As we saw at the beginning of this section, when a qubit is probed by a frequency comb with the frequency step $\chi_{\mathrm{s,mp}}/2\pi$, the qubit dynamics is $2\pi/\chi_{\mathrm{s,mp}}$-periodic. Thus, the qubit coherence oscillates at $\chi_{\mathrm{s,mp}}/2\pi$, and its coherent emission spectrum should contain emission frequencies detuned by multiples of $\chi_{\mathrm{s,mp}}/2\pi$ from the resonant frequency $\omega_{\mathrm{mp}}/2\pi$. This multi-frequency excited coherent emission becomes even stronger for large values of Ω ($\Omega \sim \chi_{\mathrm{s,mp}}$). In this regime, we observe that the multiplexing qubit absorbs photons from the intermediate frequencies $\{\omega_{\mathrm{IF}} + k\chi_{\mathrm{s,mp}}\}_{k\in[\![0,3]\!]}$, and emits photons at the intermediate frequencies $\{\omega_{\mathrm{IF}} + k\chi_{\mathrm{s,mp}}\}_{k\in[\![-4,-1]\!]}$ and $\{\omega_{\mathrm{IF}} + k\chi_{\mathrm{s,mp}}\}_{k\in[\![4,8]\!]}$.

Compared the resonance fluorescence with a single drive, the resonance fluorescence with a frequency comb (multi-frequency excitation) already shows major differences in the incoherent emission (namely, asymmetric emission and frequency localization) and in the coherent absorption and emission (absorption over a larger spectrum than $\Gamma_{1,\mathrm{mp}}$, and emissions at all the angular frequencies, detuned by multiples of $\chi_{\mathrm{s,mp}}$).

In this section, we have restricted ourselves to a multi-frequency probe (excitation); however, as the multiplexing qubit is dispersively coupled to the storage mode, we can also study multiple-frequency resonance fluorescence, which corresponds to the resonance fluorescence of a qubit that has multiple possible resonant frequencies, simultaneously probing each of them. Here, these multiple resonances of the multiplexing qubit are incoherent, as they occur due to the entanglement with the storage mode. Thus, we can expect to see the superposition of multiple spectra, each corresponding to the spectrum of a qubit driven by a comb.

7.3.3.2 *Multiple-frequency resonance fluorescence with a coherent state*

Here, we study the multiple resonance fluorescence by preparing the storage mode in a coherent state $|\alpha = 3\rangle$ and probing the multiplexing qubit with a frequency comb $\{\omega_{\mathrm{mp}} - k\chi_{\mathrm{s,mp}}\}_{k\in[\![0,8]\!]}$ going from 0 to 8 photons. The IF signal is digitized over 4.096 µs,

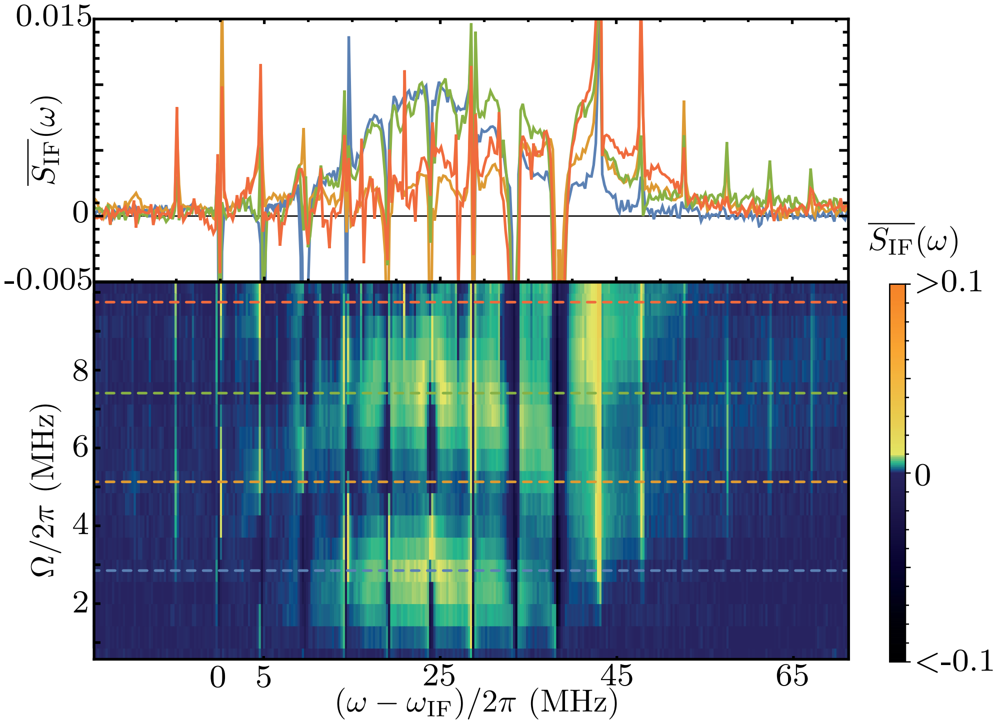

Figure 7.10: Measured normalized spectral density $\overline{S_{\mathrm{IF}}}(\omega)$ as a function of the frequency ω and the drive strength Ω when the storage mode is initialized in a coherent state $|\alpha=3\rangle$. Upper graph shows cuts of the lower graph for four values of Ω, as indicated by the dashed lines.

and the power spectral density $S_{\mathrm{IF}}(\omega,\overline{n}_{\mathrm{s}}=|\alpha|^2)$ is computed. To decrease the measurement time, the reference spectrum S_{ref} is not measured. This experiment is only performed a second time with a coherent-state storage that has about 100 photons[10]. The IF power spectral density $S_{\mathrm{IF}}(\omega,\overline{n}_{\mathrm{s}}=|\alpha|^2)$ is normalized using the spectral density $S_{\mathrm{IF}}(\omega,\overline{n}_{\mathrm{s}}\sim 100)$. In addition, we defined the normalized spectral density $\overline{S_{\mathrm{IF}}}(\omega,\overline{n}_{\mathrm{s}})$ as

$$\overline{S_{\mathrm{IF}}}(\omega,\overline{n}_{\mathrm{s}})=\frac{S_{\mathrm{IF}}(\omega,\overline{n}_{\mathrm{s}})}{S_{\mathrm{IF}}(\omega,\overline{n}_{\mathrm{s}}\sim 100)}-1=\frac{GS_{\mathrm{out}}(\omega-\omega_{LO},\overline{n}_{\mathrm{s}})+N_{\mathrm{n}}}{GS_{\mathrm{out}}(\omega-\omega_{LO},\overline{n}_{\mathrm{s}}\sim 100)+N_{\mathrm{n}}}-1. \quad (7.40)$$

This normalization process is less accurate than that used in Sec. 7.3.3.1 for the comb frequencies; however, it takes half less time to be measured. This is a non-negligible bonus, as each spectral density has to be averaged by over 4 million measurements.

The experiment and its normalization are carried out for various drive strengths Ω. The normalized spectral density $\overline{S_{\mathrm{IF}}}$, as a function of Ω, is shown in Fig. 7.10. The normalized spectral density shows a non-linear dependency on Ω. The multiplexing qubit incoherent emission reaches a maximum when $\Omega=\chi_{\mathrm{s,mp}}/2$ and $\Omega=3\chi_{\mathrm{s,mp}}/2$ (the blue and green lines in the upper graph in Fig. 7.10 respectively), and a minimum when $\Omega=\chi_{\mathrm{s,mp}}$ and $\Omega=2\chi_{\mathrm{s,mp}}$ (the yellow and red lines in the upper graph in Fig. 7.10, respectively). This behavior is easy to explain using the infinite comb

---

[10] When using the double calibration procedure, as in Sec. 7.3.3.1, we first calibrated the noise and gain of the amplifiers and then removed the drive contribution. However, in order to do so, the experiment must be performed four times.

approximation (see Sec. 7.2.2). With this approximation, the qubit undergoes discrete and instantaneous rotations in the Bloch sphere at an angle of $2\pi\Omega/\chi_{\mathrm{s,mp}}$ every time $2\pi/\chi_{\mathrm{s,mp}}$, relaxing between these rotations. Thus, when Ω is equal to a half integer of times $\chi_{\mathrm{s,mp}}$, the instantaneous rotations are π-pulses, and we can show that this specific value of Ω maximizes the qubit emission rate (see Sec. 7.2.2.2). In comparison, when Ω is equal to an integer times $\chi_{\mathrm{s,mp}}$, the instantaneous rotations are 2π-pulses, and the qubit stays more or less in its ground state $|g\rangle$. There, the drive has no effect on the qubit, and the qubit emission rate is equal to zero. Here, the normalized spectral density does not reach zero when Ω is equal to an integer times $\chi_{\mathrm{s,mp}}$, as the frequency comb is not large enough to be considered infinite. Specifically, the approximation is not valid on the border of the comb, which is where we observe a strong emission of the multiplexing qubit around the frequency corresponding to 9 photons.

7.3.3.3 *From the border to the center of the frequency comb*

The continuous evolution from the border to the center of the frequency comb can be studied by measuring the normalized spectral density $\overline{S_{\mathrm{IF}}}(\omega, |\alpha|^2)$ (defined in Eq. (7.40)) at a fixed driving strength Ω for various coherent states $|alpha\rangle$ in the storage mode and with a measurement time of 8.192 µs. For α smaller than 1, the multiplexing qubit only has one resonance at the angular frequency ω_{mp}, which corresponds to 0 photons in storage. When α increases, the number of resonances of the multiplexing qubit also increases. For $\alpha = 2$, the mean resonance frequency of the multiplexing qubit is in the middle of the frequency comb; thus, we expect to measure a spectral density that is in agreement with the infinite frequency comb approximation. When α becomes much bigger than 2, the resonances of the multiplexing qubit are far detuned, compared to the frequency comb, and the qubit emission should vanish. Figs. 7.11a and b show the measured evolution of the normalized spectral density $\overline{S_{\mathrm{IF}}}(\omega, |\alpha|^2)$ with α for Ω being equal to $\chi_{\mathrm{s,mp}}/2$ and $\chi_{\mathrm{s,mp}}$.

As expected, the multiplexing qubit emission is localized around the angular frequency ω_{IF} for α smaller than 1. When α increases, the multiplexing qubit dynamics becomes that described by the infinite comb approximation. For $\Omega = \chi_{\mathrm{s,mp}}$ the qubit emission vanishes around $\alpha = 3$, this value is a bit higher than the one expected ($\alpha = 2$) because of the relaxation of the storage mode during the measurement. If the storage is initialized in a state with an average of $\alpha^2 = 9$ photons, we expect that it has only 1 photon on average at the end of the measurement. In comparison, the qubit emission does not vanish when $\Omega = \chi_{\mathrm{s,mp}}/2$, which is as expected from the infinite comb approximation. When α is about 5, the qubit emission is not null, even for $\Omega = \chi_{\mathrm{s,mp}}$. In this case, the multiplexing qubit is mainly resonant with the border frequency of the comb during the measurement, and the infinite comb approximation is not valid. For higher values of α, the multiplexing qubit is resonant with none of the comb frequencies and, therefore, there is no photon emission.

To conclude this section about the fluorescence of a qubit with multiple resonances, we wish to note that the multi-resonance fluorescence of a qubit is a complex phenomenon that is only qualitatively described here. The infinite frequency comb approximation explains the dependence of the multiplexing qubit emission on the drive strength Ω. In addition, the Mollow triplet seems to disappear and is replaced by a

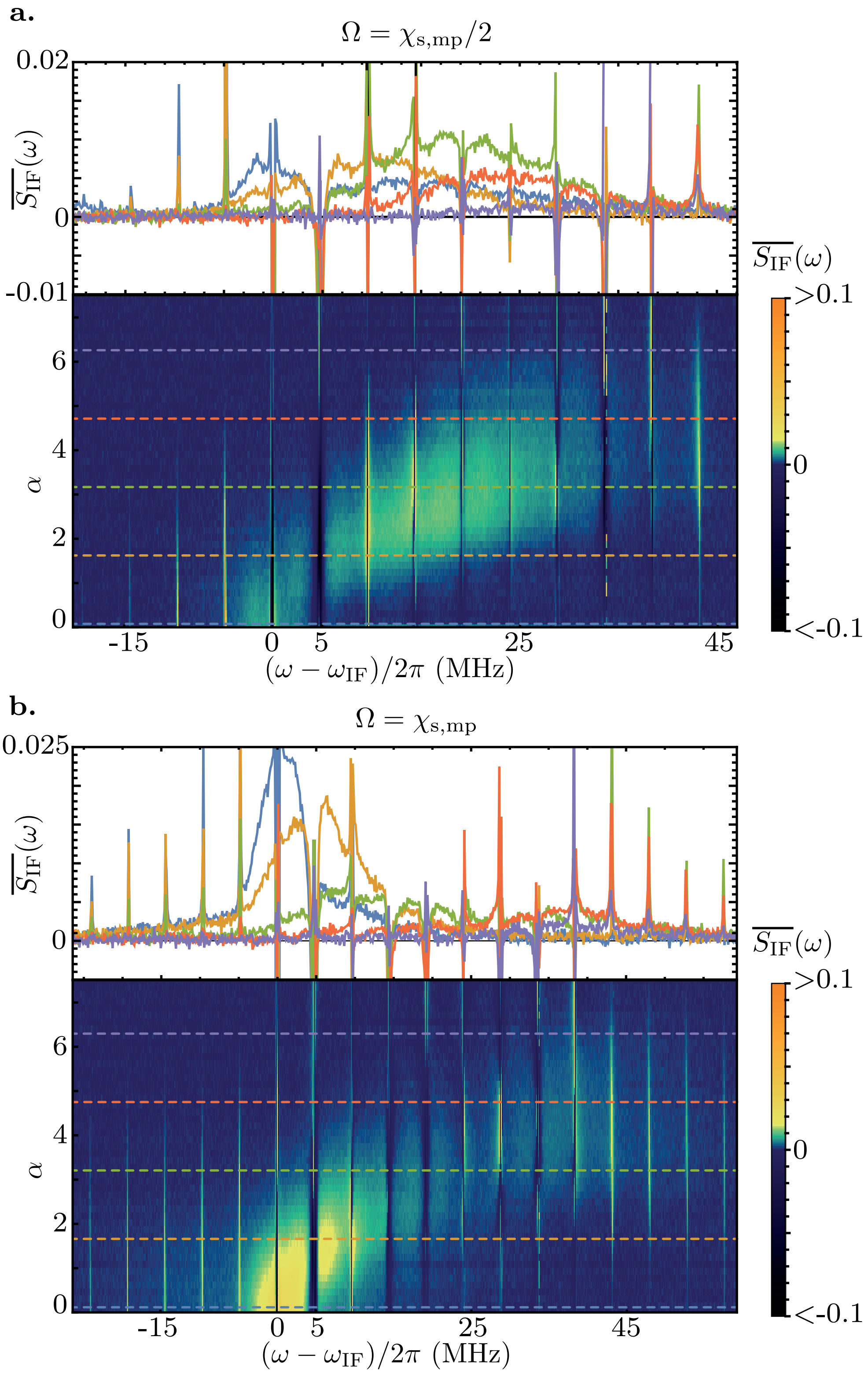

Figure 7.11: Measured normalized spectral density $\overline{S_{\mathrm{IF}}}(\omega, |\alpha|^2)$ as a function of the amplitude α of the storage mode coherent state $|\alpha\rangle$. The drive strength Ω is equal to **a.** $\chi_{\mathrm{s,mp}}/2$ and **b.** $\chi_{\mathrm{s,mp}}$. In each figure, the upper graph shows cuts of the lower graph for values of α, indicated by the colored dashed lines.

continuum of emissions between the comb frequencies. The multi-frequency excitation of the qubit entails a $2\pi/\chi_{\mathrm{s,mp}}$-periodic dynamic for the multiplexing qubit. This leads to a strong qubit emission at all frequencies, detuned by a multiple of $\chi_{\mathrm{s,mp}}$.

7.4 COMPARING THE INFORMATION IN THE COHERENT AND INCOHERENT EMISSIONS

7.4.1 *Raising the problem*

When a qubit is dispersively read out using a readout resonator, the probe used by the system, i. e. the readout resonator, is a linear system. Thus, the emission of the readout resonator is in theory always at the same frequency as its excitation (or drive). Moreover, assuming the output field is in a coherent state, the field is completely described by its amplitude. Thus, after a heterodyne detection, the second moment of the $\{I, Q\}$ quadrature distribution does not provide more information about the qubit state than the first moment. This means that we can recover all the information extracted by the measurement (up to the quantum efficiency) by measuring only the I and Q quadrature with a heterodyne detection at the excitation frequency.

When measuring the fluorescence of a qubit, the frequency of the fluorescence field can differ from the frequency of the excitation, due to the inelastic scattering. The output field is no longer a coherent state and, after a heterodyne detection, the first and second moments of the $\{I, Q\}$ quadrature distribution may contain different pieces of information. Moreover, if we perform only a heterodyne measurement at the drive frequency, we may not recover all the information up to the quantum efficiency. So, how can we quantify the amount of information we need to collect, compared to the total amount of information extracted by the multiplexing qubit (up to the quantum efficiency)?

To answer this question, we have to study the $\{I(\omega), Q(\omega)\}$ distribution at every demodulation frequency ω accessible through the heterodyne detection setup. These distributions contain all the information we can access. From a photon-counting perspective, we can define a photon-counting signal as the scalar product of the $\{I(\omega), Q(\omega)\}$ distributions of the reflected drive and the one we obtain when the storage mode is in a Fock state $|n\rangle$ and this for every frequency ω and Fock state $|n\rangle$.

If we assume that only the first and second moments of the distributions may differ (this implies that the amplification scheme does not affect the moments of order greater or equal than 3), comparing two distributions is equivalent to comparing the first moment (i. e. the mean value) and the second moment (i. e. the mean value of $I(\omega)^2 + Q(\omega)^2$) of the distributions. The average of these moments are easy to compute, as the first moment is equal to the coherent spectral density and the second moment is equal to the spectral density (or total spectral density), which contains both coherent and incoherent spectral densities and is defined by Eq. (7.25). The coherent spectral density reads

$$S_{\mathrm{coh}}(\omega) = \frac{1}{2\pi}\int \langle a_{\mathrm{out}}^{\dagger}(t+\tau)\rangle\langle a_{\mathrm{out}}(t)\rangle \mathrm{e}^{-i\omega\tau} = |\mathrm{FT}(\langle a_{\mathrm{out}}(t)\rangle)(\omega)|^2, \tag{7.41}$$

where FT is the Fourier transform.

In this thesis, we do not access the $\{I(\omega), Q(\omega)\}$ distributions, nor the spectral densities S_{coh} and S_{out}, when the storage is in a Fock state. However, we can detune the multiplexing qubit enough so that we have access to these spectral densities of the input drive by displacing the storage mode with 100 photons. We call these densities $S_{\text{coh}}(\omega, \overline{n}_s \sim 100)$ and $S_{\text{out}}(\omega, \overline{n}_s \sim 100)$, respectively. When subtracting these reference densities from measured spectral densities of the resonant reflected drive, we obtain the coherent and total spectral densities of the absorption and emission of the qubit. Thus, the ratio η_c, which is defined as coherent spectral density divided by the total spectral density of the qubit absorption and emission

$$\eta_c = \frac{\int_0^{+\infty} |S_{\text{coh}}(\omega) - S_{\text{coh}}(\omega, \overline{n}_s \sim 100)| \mathrm{d}\omega}{\int_0^{+\infty} |S_{\text{out}}(\omega) - S_{\text{out}}(\omega, \overline{n}_s \sim 100)| \mathrm{d}\omega}, \tag{7.42}$$

is the difference at every frequency ω of the first moment of the $\{I(\omega), Q(\omega)\}$ distribution for resonant and non-resonant drives, divided by the difference at every frequency ω of the second moment of the same distributions. Interestingly, the numerator of η_c is the number of photons emitted or absorbed by the multiplexing qubit and that can be resolved by looking only at the first moment of the $\{I(\omega), Q(\omega)\}$ distribution (i. e., by looking at the coherent part of the emission). In the same way, the denominator is the number of emitted and absorbed photons resolved by looking at the second moment of the $\{I(\omega), Q(\omega)\}$ distribution (i. e.by looking at the coherent and incoherent part of the emission). The ratio η_c can thus be called a *collecting ratio*; that is, it is the percentage of photons we collect when measuring the coherent emission alone compared to the full emission.

If the quantum efficiency η gives the fraction of information we recover after the total amplification process, the ratio η_c says nothing about the fraction of the information missing in the first moment compare to the second. In order to define a *collecting efficiency*, the fraction of information we collect by only analyzing the first moment of the $\{I(\omega), Q(\omega)\}$ distribution, we will need a more complex discussion, one that is out of the range of this thesis. However, we can easily convince ourselves that the collecting efficiency is strongly correlated to the collecting ratio we defined and that the bigger η_c is, the bigger the collecting efficiency should be. For example, if η_c is equal to 0, the coherent part of the drive should not resolve any of the photons absorbed or emitted by the qubit, and the coherent spectral density is the same whether the qubit is resonant or non-resonant. In such a case, we can convince ourselves that there is no information to recover from the coherent emission, as it does not depend on the multiplexing qubit frequency[11].

Here, we propose to study the collecting ratio in order to determine whether we might miss pieces of information stored in the second moment of the $\{I(\omega), Q(\omega)\}$ distribution (i. e. stored in the incoherent spectral density) and to examine whether we might improve our measurement speed by measuring the full photon emission spectrum.

---

[11] In practice, this situation will never happen.

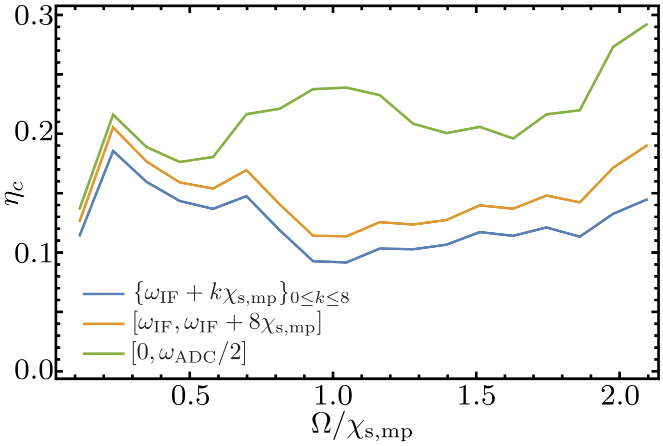

Figure 7.12: Measured collecting ratio η_c for various frequency spans $\mathcal{C}_{\mathrm{coh}}$ equal to $\{\omega_{IF} + k\chi_{\mathrm{s,mp}}\}_{0\leq k\leq 8}$, $[\omega_{IF}, \omega_{IF} + 8\chi_{\mathrm{s,mp}}]$, and $[0, \omega_{ADC}/2]$ as a function of the drive strength Ω, expressed in units of the cross-Kerr rate $\chi_{\mathrm{s,mp}}$.

7.4.2 *Measuring the collecting ratio*

In order to measure the collecting ratio as a function of the drive strength Ω, we probe the multiplexing qubit with a frequency comb and digitize the IF signal of the heterodyne detection setup over 4.096 µs. The (total) spectral density is related to the IF signal by Eq. (7.35). In the same way, the coherent spectral density is related to the IF signal through

$$|\langle \tilde{s}_{\mathrm{IF}}(\omega)\rangle|^2 = \frac{\hbar\omega_{\mathrm{mp}} Z_0}{2} G S_{\mathrm{coh}}(\omega_{\mathrm{LO}} - \omega), \tag{7.43}$$

with Z_0 being the impedance of the transmission line and G being the TWPA gain. Thus, the collecting ratio reads

$$\eta_c(\mathcal{C}_{\mathrm{coh}}) = \frac{\int_{\mathcal{C}_{\mathrm{coh}}} \left| |\langle \tilde{s}_{\mathrm{IF}}(\omega)\rangle|^2 - |\langle \tilde{s}_{\mathrm{IF}}(\omega)\rangle_{\overline{n}_{\mathrm{s}}\sim 100}|^2 \right| \mathrm{d}\omega}{\int_0^{\omega_{\mathrm{ADC}}/2} |\langle |\tilde{s}_{\mathrm{IF}}(\omega)|^2\rangle - \langle |\tilde{s}_{\mathrm{IF}}(\omega)|^2\rangle_{\overline{n}_{\mathrm{s}}\sim 100}| \,\mathrm{d}\omega}, \tag{7.44}$$

where the subscript $\overline{n}_{\mathrm{s}} \sim 100$ means that the IF signal was recorded with a storage mode containing about 100 photons. The integral of the numerator is performed over the ensemble $\mathcal{C}_{\mathrm{coh}}$, which is the ensemble of the frequencies probed with the heterodyne detection setup when measuring only the coherent emission. In the experiments of this thesis, $\mathcal{C}_{\mathrm{coh}}$ is always equal to $\{\omega_{IF} + k\chi_{\mathrm{s,mp}}\}_{0\leq k\leq 8}$. The upper boundary of the denominator integral is replaced by half of the ADC frequency ω_{ADC}, due to frequency aliasing. In our case, as the IF signal is filtered with a low-pass filter that has a frequency cut-off below ω_{ADC}, there is no frequency aliasing; we are only probing the photons absorbed and emitted by the multiplexing qubit in a spectral range of about 200 MHz around its resonance frequency. As $\Gamma_{1,\mathrm{mp}}$ and $\chi_{\mathrm{s,mp}}$ are smaller than 100 MHz, we can assume that there is no photon absorbed or emitted by the qubit outside of the spectral range probed and that replacing the boundary $+\infty$ with $\omega_{\mathrm{ADC}}/2$ changes nothing.

Fig. 7.12 shows the collecting ratio η_c for various drive strengths Ω and for $\mathcal{C}_{\mathrm{coh}}$ equal to $\{\omega_{IF} + k\chi_{\mathrm{s,mp}}\}_{0\leq k\leq 8}$, $[\omega_{IF}, \omega_{IF} + 8\chi_{\mathrm{s,mp}}]$ and $[0, \omega_{ADC}/2]$. The first observation is that the collecting ratio is always strictly smaller than 1. Thus, we believe that the coherent emission does not contain all the information extracted by the multiplexing qubit.

We observe that the collecting ratio is as low as 10–15% when we probe only the coherent emission at the comb frequencies (the blue line in Fig. 7.12). In this case, as the collecting ratio is smaller than the quantum efficiency (about 19%), measuring the total emission instead of the coherent emission may lead to an increase in the measurement rate, even if the total emission is more sensitive to the quantum efficiency[12]. When probing the coherent emission at all the frequencies between ω_{IF} and $\omega_{\mathrm{IF}} + 8\chi_{\mathrm{s,mp}}$ (the orange line in Fig. 7.12) the collecting ratio does not increase significantly. This means that the coherent emission mostly occurs at the comb frequency peaks in this frequency range. However, when probing the coherent emission at all frequencies (the green line in Fig. 7.12), we observe an increase in the collecting ratio of up to 20–25%. Thus, we can conclude that half of the coherent emission occurs at frequencies outside of the frequency comb. However, even when probing all the frequencies, the coherent part contains only a quarter of the photons absorbed and emitted by the multiplexing qubit.

An interesting feature is the dependence of η_c on $\Omega/\chi_{\mathrm{s,mp}}$. When probing the coherent emission at all frequencies, the collecting ratio shows an oscillation with $\Omega/\chi_{\mathrm{s,mp}}$. The collecting ratio is minimal when $\Omega/\chi_{\mathrm{s,mp}}$ is a half integer. According to the infinite comb approximation, the multiplexing qubit occurs during quasi-instantaneous π-pulses and, on average, its coherence is close to zero. These specific values of $\Omega/\chi_{\mathrm{s,mp}}$ maximize the qubit excited population and thus maximize the qubit's incoherent emission. In comparison, when $\Omega/\chi_{\mathrm{s,mp}}$ is an integer, the qubit emission occurs during the 2π-pulse, and the qubit's incoherent emission is minimal.

From a coherent-emission perspective, there is a trade-off that we need to find. Maximizing the qubit emission (and thus the measurement strength, see Sec. 8.2.1) minimizes the collecting ratio and, in the same way, maximizing the collecting ratio minimizes the qubit emission (and thus the measurement strength).

CONCLUSION

Here are this chapter's main conclusions.

- The reflection coefficient of a qubit can be measured simultaneously and at multiple frequencies using a multiplexing protocol.
- The multiplexed measurement of the reflection coefficient enables us to recover information about all storage photon numbers simultaneously.
- The multiplexed photon number measurement shows a measurement time scaling as a logarithm of the maximum photon number, as the state-of-the-art protocol: the binary decimation.

---

[12] This is because, to compute the total emission, we take the square of our signal before averaging it; thus, it is more sensible to the noise.

- The multiplexed photon number measurement is continuous in both strength and time. Conversely, standard protocols are continuous in strength and discrete in time. Thus, the multiplexed photon number measurement is the first photocounting protocol that is continuous in time.

- The qubit dynamics under a frequency comb differs significantly from Rabi oscillations. The qubit periodically undergoes quasi-instantaneous rotations in the Bloch sphere.

- The resonance fluorescence of the multiplexing qubit when the latter is probed by a frequency comb differs significantly from that of the Mollow triplet. The infinite comb approximation enables a qualitative description of the qubit emission spectrum.

- The collecting ratio (i. e. the percentage of photons emitted or absorbed by the multiplexing qubit we detect in the coherent emission) is smaller than 1. We believe that this means that the coherent emission does not contain all the information extracted by the multiplexing qubit. The second moment of the quadrature distribution (i. e. the incoherent emission of the qubit) may contain information absent from the first moment; namely, the coherent emission.

8

MULTIPLEXED PHOTON NUMBER MEASUREMENT BACK-ACTION

A quantum measurement, continuous in time and strength, can be characterized by its back-action. The back-action can be quantified either by looking at the dephasing rate of the measurement induced on the system [40, 193] or by the correlation it generates between a weak measurement and the system tomography [74]. The back-action of the dispersive readout and fluorescence measurement of a qubit is a well-known subject [162, 194]. However, as the multiplexed photon number measurement is the first photon number measurement to be continuous in time, its back-action was never studied. In this chapter, we will look at the back-action of the multiplexed photon number measurement and see how it can differ from the back-action of the fluorescence photon number measurement (see Sec. 6.3.4). We will introduce the protocol we used to measure the dephasing rate induced by the measurement and study its dependence with the drive strength. The infinite comb approximation (see Sec. 7.2.2.2) was used to derive an analytic expression of the induced dephasing rate between two Fock states of the storage mode that reproduces the same dependence with the drive strength. Interestingly, from this analytic expression one can prove that the multiplexed approach can reach a measurement that is time independent of the number of probed Fock states.

Moreover, the photocounting abilities of the multiplexed photon number measurement can be highlighted by the measurement of the correlations between a weak multiplexed photon number measurement and a strong measurement of the Fock state population. Using a qualitative analysis of the measurement operator, one can predict the sign of the correlations and observe a good agreement with the measured correlations.

Remarks: Most of the results shown in this chapter are published in Ref. [155]

8.1 PROBE THE STORAGE MODE DECOHERENCE

The measurement strength of the multiplexing measurement can be characterized using the yes-no qubit to observe the dynamics of the cavity coherences under the action of the continuous multiplexed measurement. The advantage of this method is that it does not require a single-shot measurement of the photon number, which we could not reach owing to the limited efficiency of our amplifier, and the too short lifetime of the storage mode. In the reciprocal case of measuring a qubit using a cavity as a probe, the measurement rate is bounded by the measurement-induced dephasing rate of the qubit, which grows as the square of the cavity driving strength [8, 94]. Thus, characterizing the measurement rate of our multiplexed photon-counting can be done by observing how the storage mode dephases for a given driving strength Ω. Indeed, owing to the inherent quantum back-action of the photon number measurement, the measurement rate is bounded by how fast the conjugated operator, here the phase,

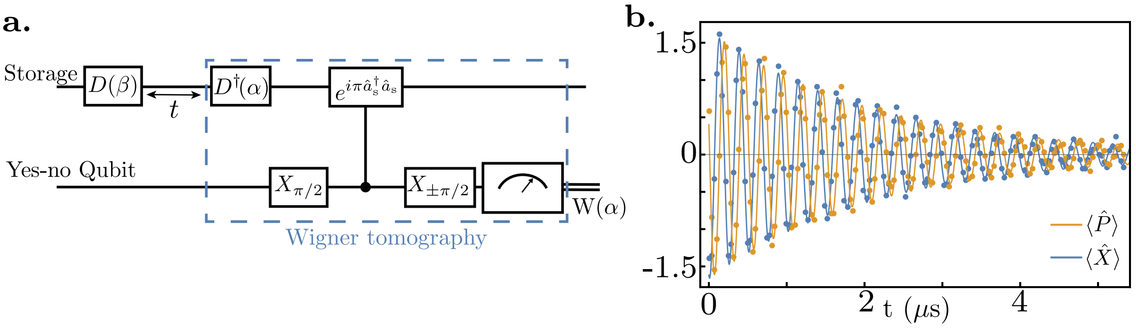

Figure 8.1: Ramsey oscillations of the storage mode **a.** Circuit diagram for Ramsey oscillations of a harmonic oscillator. In this experiment, the amplitude of the prepared coherent state β is set to -1.55. The detuning between displacement pulse and bare storage frequencies is $\delta f_s^0 = 3.96$ MHz. **b.** Measured (dots) and expected (lines) signals for $\langle\hat{X}\rangle$ (blue) and $\langle\hat{P}\rangle$ (orange). The expected signals are matched to the experiment using Eq. (8.1) with a frequency detuning $\delta f_s = 3.96$ MHz and a decay rate $\Gamma_{2,s} = 2\,\mu s^{-1}$.

diffuses. As the probe is based on a qubit driven by a frequency comb, one expects a different dependence of the measurement rate on Ω than for standard dispersive qubit readout and fluorescence measurement (see Sec. 6.3.4).

In order to measure this dephasing rate, we perform the analogous experiment as the qubit Ramsey oscillations for an harmonic mode.

8.1.1 *"Ramsey oscillations" of an harmonic oscillator*

For a qubit, Ramsey oscillations correspond to the evolution of the real and imaginary parts of the coherence $\langle g|\rho|e\rangle$ between the $|g\rangle$ and $|e\rangle$ states. A typical sequence starts by a $\pi/2$ pulse detuned from resonance by δf to create a coherent superposition of $|g\rangle$ and $|e\rangle$ states. Then the qubit evolves freely before its state tomography. Both σ_x and σ_y oscillate at δf while decaying at the decoherence rate Γ_2.

We decided to realize an analogous sequence based on the same idea for a harmonic oscillator (a similar sequence was recently performed in Ref. [195]). The first $\pi/2$ pulse is replaced by a detuned displacement pulse $D(\beta)$ on the storage mode. This displacement creates coherences between the Fock states of the storage mode in the same way as the $\pi/2$ pulse create coherences between the qubit number states $|g\rangle$ and $|e\rangle$. The field then evolves over a time t (during which the multiplexing measurement could be applied) before a Wigner tomography is realized (see Fig. 8.1a and App. c for the definition of a Wigner tomography). The expectation value of $\hat{X} = (\hat{a}_s + \hat{a}_s^\dagger)/2$ and $\hat{P} = (\hat{a}_s - \hat{a}_s^\dagger)/2i$ quadratures are computed from the Wigner tomography (see App. c). The time trace of $\langle\hat{X}\rangle$ and $\langle\hat{P}\rangle$ is what we call the Ramsey oscillations for the storage mode. As in the qubit case, the frequency of the oscillations is set by the detuning δf_s between the drive and the resonant frequency of the mode, which also allows us to extract the frequency of the storage mode. At this point, a distinction has to be made between the detuning $\delta f_s^0 = f_{\text{drive}} - f_s$ between the drive and the bare storage mode frequency (the resonant frequency when the multiplexed qubit and the storage are undriven) and the detuning

δf_s between the drive and the resonant frequency of the storage mode, which depends on the multiplexed measurement strength in perfect analogy with the AC-Stark effect for a qubit readout. Note that the Wigner tomography sequence uses the same detuned frequency δf_s for its displacement pulse $D^\dagger(\alpha)$ in order to keep the same phase reference. The measurement of Ramsey oscillations of a harmonic oscillator takes longer than the ones of a qubit because we fully determine the quantum state of an oscillator at each time step instead of a simple Bloch vector. From Eq. (5.2), one finds that $\langle\hat{X}\rangle$ and $\langle\hat{P}\rangle$ evolve as

$$\begin{aligned}\langle\hat{X}\rangle &= |\beta|\cos(2\pi\delta f_\mathrm{s}t+\phi)e^{-t\Gamma_{\mathrm{d,s}}}\\ \langle\hat{P}\rangle &= |\beta|\sin(2\pi\delta f_\mathrm{s}t+\phi)e^{-t\Gamma_{\mathrm{d,s}}}\end{aligned} \tag{8.1}$$

where $\beta = |\beta|e^{i\phi} = \langle\hat{a}_s\rangle(t=0)$. We define the storage mode dephasing rate as $\Gamma_{\mathrm{d,s}}$ which contains the intrinsic decoherence rate $\Gamma_{\varphi,\mathrm{s}}$. The Fig. 8.1b shows an example of measured Ramsey oscillations

8.1.2 *Storage mode frequency shift and induced dephasing rate by driving the multiplexing qubit with a comb*

In analogy with the ac-Stark shift of the frequency of a qubit coupled to a driven resonator, we also call ac-Stark shift the frequency shift of the storage mode induced by driving the multiplexing qubit. In order to measure this frequency shift and the dephasing rate that is induced by the multiplexing qubit on the storage mode, we realize the reciprocal protocol for a qubit measured by a cavity. We use the Ramsey interferometry sequence, defined in the former section, on the storage mode during which the multiplexing qubit is driven with a frequency comb (see Fig. 8.2a). The drive pulse is given by the sum of nine sine functions at the frequencies $[f_\mathrm{mp}, f_\mathrm{mp}-\chi_{\mathrm{s,mp}}/2\pi, ..., f_\mathrm{mp}-8\chi_{\mathrm{s,mp}}/2\pi]$ multiplied by a Gaussian envelope of duration t and width $t/4$.

For small measurement strength $\Omega/\chi_{\mathrm{s,mp}} < 0.9$, we generated the Ramsey sequence with a displacement pulse of amplitude $\beta = -1.55$ detuned from the base storage mode by $\delta f_\mathrm{s}^0 = 3.96$ MHz. We fit the time evolution of $\langle\hat{X}\rangle$ and $\langle\hat{P}\rangle$ (see Fig. 8.2b) using the damped sine function

$$\begin{aligned}\langle\hat{X}\rangle &= A\cos(2\pi\delta f_\mathrm{s}t+\phi)e^{-t\Gamma_{\mathrm{d,s}}}\\ \langle\hat{P}\rangle &= A\sin(2\pi\delta f_\mathrm{s}t+\phi)e^{-t\Gamma_{\mathrm{d,s}}}\end{aligned}\quad . \tag{8.2}$$

The parameters A, δf_s, ϕ, and $\Gamma_{\mathrm{d,s}}$ are determined altogether by fitting the model to the measured oscillations. δf_s is the sum of the detuning from the bare storage mode frequency δf_s^0 and of the ac-Stark shift of the storage mode.

For larger measurement strength $\Omega/\chi_{\mathrm{s,mp}} > 0.9$, we generated the Ramsey sequence with a displacement pulse detuning of $\delta f_\mathrm{s}^0 = 5.96$ MHz, an amplitude of $\beta = -1.27$, and we model the time evolution of $\langle\hat{X}\rangle$ and $\langle\hat{P}\rangle$ by the sum of two sine functions with an exponential decay

$$\begin{aligned}\langle\hat{X}\rangle &= A(\cos(2\pi\delta f_\mathrm{s}t+\phi)+\zeta\cos(2\pi\nu t+\psi_\mathrm{X}))e^{-t\Gamma_{\mathrm{d,s}}}\\ \langle\hat{P}\rangle &= A(\sin(2\pi\delta f_\mathrm{s}t+\phi)+\zeta\sin(2\pi\nu t+\psi_\mathrm{P}))e^{-t\Gamma_{\mathrm{d,s}}}\end{aligned}\quad . \tag{8.3}$$

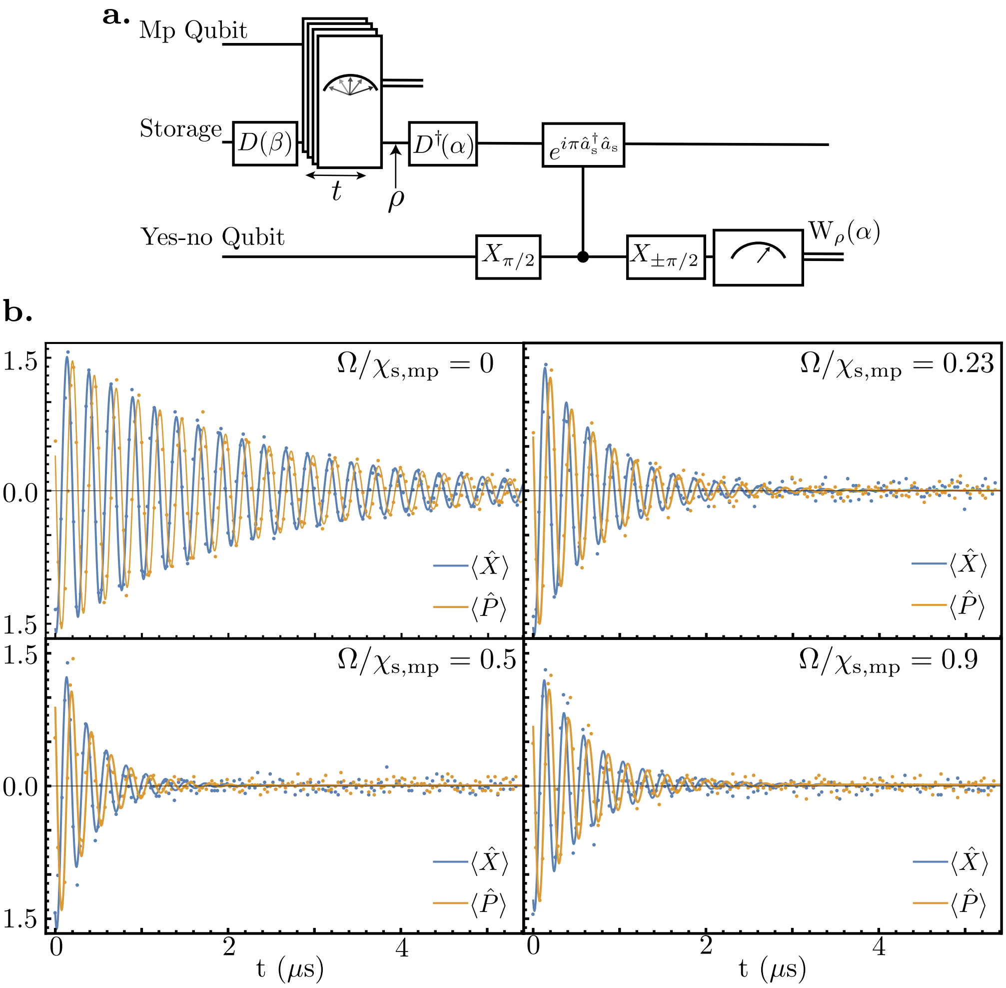

Figure 8.2: **a.** Circuit diagram of the protocol used to determine the dephasing rate and frequency shift of the storage mode induced by the multiplexed photocounting measurement. The blocks linking the multiplexing qubit and the storage mode represent the multiplexed measurement during a time t made by the qubit on the storage mode. This measurement is realized by driving the qubit with a frequency comb $[f_{\text{mp}}, f_{\text{mp}} - \chi_{\text{s,mp}}/2\pi, ..., f_{\text{mp}} - 8\chi_{\text{s,mp}}/2\pi]$ within a Gaussian envelope. **b.** Ramsey oscillations of the storage mode (dots) and theory (lines) for “small" measurement amplitude $\Omega/\chi_{\text{s,mp}} < 1$. One can observe that the dephasing rate of $\langle\hat{X}\rangle$ and $\langle\hat{P}\rangle$ is non-monotonic with the drive strength Ω.

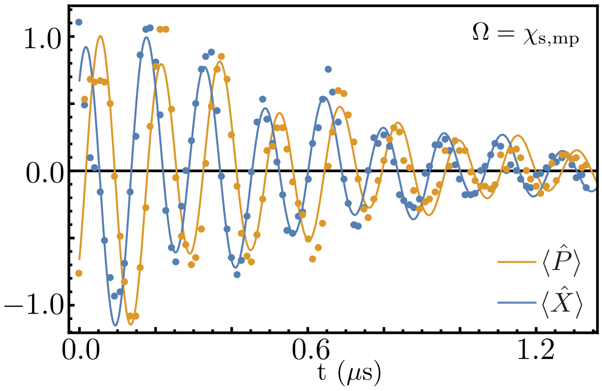

Figure 8.3: Ramsey oscillations of the storage mode for “large" measurement amplitude $\Omega/\chi_{\mathrm{s,mp}} = 1$. One can observe that the dynamics $\langle\hat{X}\rangle$ and $\langle\hat{P}\rangle$ are not governed by a simple decaying sine function. The theory does not reproduce quantitatively the measurement when using the naive version of the model Eq. (8.2). we use the simple model Eq. (8.3) to capture this modulation.

This empirical model is motivated by three reasons. The first term is identical to the simple model in Eq. (8.2). Second, the measured Ramsey oscillations seem to show a small modulation in amplitude, which we try to capture with a second sine function. Third we try to keep the model as simple as possible.

Fig. 8.3 shows an example of Ramsey oscillations of the storage mode with a large amplitude of measurement. The two signals are fitted simultaneously to extract the parameters A, δf_{s}, ν, ϕ, ψ_{X}, ψ_{P}, and $\Gamma_{\mathrm{d,s}}$ for various drive amplitude Ω. The frequency ν varies from 2.15 MHz to 2.5 MHz when Ω varies from 5 MHz to 10 MHz. The parameter ζ is roughly constant, it varies between 0.2 to 0.27 when Ω varies from 5 MHz to 10 MHz. The Fig. 8.3 shows measurement induced detuning as a function of measurement drive amplitude.

The ac-Stark shift and the storage dephasing rate measured for drive strength Ω going from 0 to $2\chi_{\mathrm{s,mp}}$ are shown on Fig. 8.4. We observe a strong non-linear dependence of both quantities with Ω and a small dependence with the initial coherent state amplitude β. Noticeably, the dephasing rate reaches a maximum when $\Omega = \chi_{\mathrm{s,mp}}/2$ for which information is extracted at a rate approximately 5 times larger than the natural dephasing rate. It is possible to understand this behavior by considering the infinite frequency comb approximation (see Sec. 7.2.2.2). The drive performs sudden rotations by an angle $2\pi\Omega/\chi_{\mathrm{s,mp}}$ of the Bloch vector of the qubit every time step $2\pi/\chi_{\mathrm{s,mp}}$. When $\Omega/\chi_{\mathrm{s,mp}}$ is integer, the comb does not affect the qubit and thus $\Gamma_{\mathrm{d,s}}$ vanishes. Conversely, the maximum measurement rate corresponds to half-integer $\Omega/\chi_{\mathrm{s,mp}}$ for which the effect of the comb on the qubit dynamics is maximum and leads to the strongest qubit emission. With the finite comb used in the experiment, this maximum persists and is reproduced by a model based on a master equation without any free parameter (line in Fig. 8.4, see App. d for more information about the simulation). The small dependence of the dephasing rate and the ac-Stark shift on the coherent state amplitude β comes from the finite size of the comb. As the comb is not infinite, the dephasing rate between Fock states $|n_1\rangle$ and $|n_2\rangle$ will not only depend on the difference $|n_1 - n_2|$ (which is the case for an infinite comb, see next section) but also on the value of n_1 and n_2. Thus, the storage

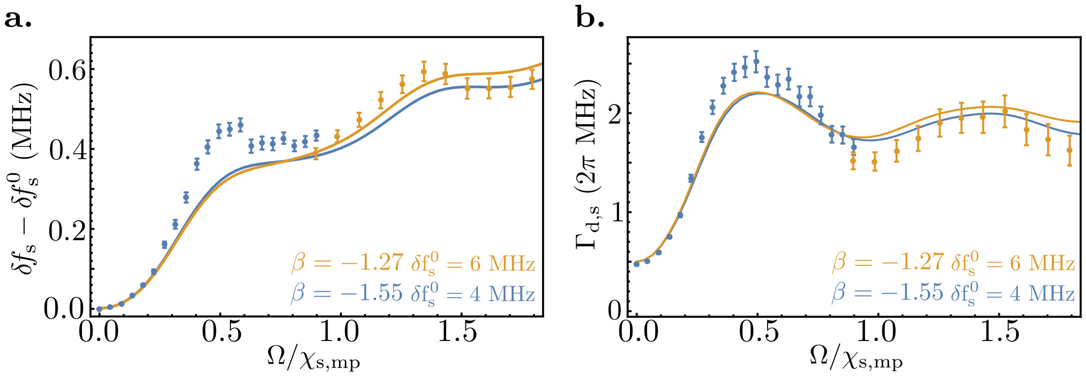

Figure 8.4: **c.** and **d.** ac-Stark shift and dephasing rate measured (dots) and simulated (line) as a function of multiplexing qubit drive amplitude Ω in units of $\chi_\mathrm{s,mp}$. The evolution of the detuning and dephasing rate are strongly non linear with drive amplitude.

dephasing rate will depend on its photon number distribution. Simulation shows that this dependence disappears when using a larger comb $\{f_\mathrm{mp} - k\chi_\mathrm{s,mp}/2\pi\}_{k\in[\![-4,8]\!]}$ (see App. d).

While the measurement-induced dephasing rate can be simulated, we currently do not know how to derive an analytical expression of the dephasing rate for a finite frequency comb. However the infinite comb approximation simplifies the problem enough to enable an analytical description of the multiplexing qubit-storage mode bipartite system and derive the storage dephasing rate. In the next section, we will describe this derivation and show how it explains the maximum and minimum of the storage dephasing rate. Interestingly, we will be able to study the dephasing rate as a function of the parameter Γ_1, $\chi_\mathrm{s,mp}$ and the maximum photon number allowed in the storage mode N_max.

8.2 MEASUREMENT-INDUCED DEPHASING IN THE INFINITE COMB APPROXIMATION

The derivation described in this section follows the study of the multiplexing qubit dynamics under a frequency comb (see Sec. 7.2.2). We only consider the relaxation of the multiplexing qubit and the dispersive coupling between the storage mode and the multiplexing qubit. The Lindblad master equation of the bipartite system, described by the density matrix $\rho_\mathrm{s,mp}$ is

$$\begin{aligned}\dot{\rho}_\mathrm{s,mp} = -i &\left[-\chi_\mathrm{s,mp} a_\mathrm{s}^\dagger a_\mathrm{s} \frac{\sigma_\mathrm{z,mp}}{2} + \frac{\Omega}{2}\sum_{k=-p}^{p}\cos(k\chi_\mathrm{s,mp}t)\sigma_\mathrm{x,mp}, \rho_\mathrm{s,mp}\right] \\ &+ \Gamma_\mathrm{1,mp}\mathcal{D}(\sigma_{-,\mathrm{mp}})\rho_\mathrm{s,mp}.\end{aligned} \tag{8.4}$$

8.2.1 *Dynamics of the multiplexing qubit-storage mode bipartite system*

For the sake of simplicity, we consider a lossless storage mode in this section. In this case, each 2 by 2 sub-matrix $\rho_{n_1,n_2} = \langle n_1|\rho_\mathrm{s,mp}|n_2\rangle$, with $|n_i\rangle$ the Fock state n_i, evolves independently of the others ρ_{m_1,m_2} similarly to a collection of qubit-like system. The sub-matrix ρ_{n_1,n_2} is non-normalized because it is an off-diagonal sub-matrix of the storage-qubit system $\rho_{\mathrm{s,mp}}$. For this sub-matrix, the Lindblad master equation of Eq. (8.4) becomes

$$\begin{aligned}\dot\rho_{n_1,n_2} =& -i\chi_{\mathrm{s,mp}}\tfrac{n_1+n_2}{2}[\frac{\sigma_z}{2},\rho_{n_1,n_2}] - i\chi_{\mathrm{s,mp}}\tfrac{n_1-n_2}{2}\{\frac{\sigma_z}{2},\rho_{n_1,n_2}\}\\ &- i[\frac{\Omega}{2}\sum_{k=-p}^{p}\cos(k\chi_{\mathrm{s,mp}}t)\sigma_x,\rho_{n_1,n_2}] + \Gamma_{1,\mathrm{mp}}\mathcal{D}(\sigma_-)\rho_{n_1,n_2}.\end{aligned} \tag{8.5}$$

8.2.1.1 *Computing the decoherence rate of the n_1, n_2 component*

The infinite comb approximation again helps. We view the frequency comb drive as applying a Rabi pulse of angle $\theta = 2\pi\frac{\Omega}{\chi_{\mathrm{s,mp}}}$ at each period $T = 1/\chi_{\mathrm{s,mp}}$, without any effect for the rest of the time. Over one period, we thus have

$$\rho_{n_1,n_2}(kT+T) = \mathcal{K}_0\circ\mathcal{K}_1\rho_{n_1,n_2}(kT), \tag{8.6}$$

where the Kraus map $\mathcal{K}_0$ applies the Rabi pulse, while $\mathcal{K}_1$ contains dynamics associated to the dispersive coupling and to the multiplexing qubit decay. During each period between Rabi jumps, denoting[1] $\rho_{n_1,n_2} = \frac{x\sigma_x+y\sigma_y+z\sigma_z+\eta I}{2}$, the dynamics $\mathcal{K}_1$ corresponds to the integration of the set of equations

$$\begin{cases}\frac{\mathrm{d}}{\mathrm{d}t}x = -\frac{\Gamma_{1,\mathrm{mp}}}{2}x - \frac{\chi_{\mathrm{s,mp}}(n_1+n_2)}{2}y\\ \frac{\mathrm{d}}{\mathrm{d}t}y = -\frac{\Gamma_{1,\mathrm{mp}}}{2}y + \frac{\chi_{\mathrm{s,mp}}(n_1+n_2)}{2}x\\ \frac{\mathrm{d}}{\mathrm{d}t}z = -\Gamma_{1,\mathrm{mp}}(z+\eta) - i\frac{\chi_{\mathrm{s,mp}}(n_1-n_2)}{2}\eta\\ \frac{\mathrm{d}}{\mathrm{d}t}\eta = -i\frac{\chi_{\mathrm{s,mp}}(n_1-n_2)}{2}z\end{cases}. \tag{8.7}$$

Our goal is to derive the dynamics of the variable η, it will give us access to the dephasing rate between the Fock states $|n_1\rangle$ and $|n_2\rangle$. After one period T, since the peaks in the comb are exactly separated by the dispersive shift $\chi_{\mathrm{s,mp}}$, the effect of the precession at a frequency $\chi_{\mathrm{s,mp}}(n_1+n_2)/2$ is canceled out[2]. Note that the infinite comb approximation differs from the usual rotating wave approximation that would lead to a similar disabling of the precession for $\chi_{\mathrm{s,mp}} \gg \Gamma_1$. We then obtain, in the above coordinates, the matrix expression

$$\mathcal{K}_1 = (-1)^{n_1+n_2}\begin{pmatrix} e^{-\Gamma_{1,\mathrm{mp}}T/2} & 0 & 0 & 0\\ 0 & e^{-\Gamma_{1,\mathrm{mp}}T/2} & 0 & 0\\ 0 & 0 & (e^{-\Gamma_{1,\mathrm{mp}}T}-G) & (e^{-\Gamma_{1,\mathrm{mp}}T}-1-G)\\ 0 & 0 & G & (G+1)\end{pmatrix} \tag{8.8}$$

with $G = \dfrac{-i\chi_{\mathrm{s,mp}}\dfrac{n_1-n_2}{2}(1-e^{-\Gamma_{1,\mathrm{mp}}T})}{\Gamma_{1,\mathrm{mp}}+i\chi_{\mathrm{s,mp}}(n_1-n_2)}$. Besides, the Rabi rotation corresponds to

$$\mathcal{K}_0 = \begin{pmatrix} 1 & 0 & 0 & 0\\ 0 & \cos\theta & -\sin\theta & 0\\ 0 & \sin\theta & \cos\theta & 0\\ 0 & 0 & 0 & 1\end{pmatrix}, \tag{8.9}$$

---

[1] Here η is the coherence between Fock states $|n_1\rangle$ and $|n_2\rangle$

[2] modulo a possible phase flip every period when $n_1 + n_2$ is odd

where $\theta = 2\pi\Omega/\chi_{\mathrm{s,mp}}$. This expression further simplifies for the two drive strengths $\Omega = (k+1/2)\chi_{\mathrm{s,mp}}$ or $\Omega = k\chi_{\mathrm{s,mp}}$, which respectively lead to $\theta = 0$ (no qubit emission) and $\theta = \pi$ (maximal qubit emission), since the (z, η) variables of interest decouple from (x, y).

- For $\theta = 0$, we tend to a stationary regime $(z, \eta)_{kT+T} = (z, \eta)_{kT}$. This steady value thus confirms the intuition developed in the single qubit case (see Sec. 7.2.2.2): there is no change in the coherences η between Fock states in the resonator for $\theta = 0$, which means that no measurement is performed (this corresponds to the minima in $\Gamma_{\mathrm{d,s}}$ in Fig. 8.4b).

- For $\theta = \pi$, we can compute an analytical expression for the factor R by which the trace η decreases every period T in the permanent regime[3]. Thus the average dephasing rate is given by $-\log(|R|)/T$ with

$$\begin{aligned} R = &\frac{1}{2(\Gamma_{1,\mathrm{mp}} + i\chi_{\mathrm{s,mp}}(n_1 - n_2))}\Bigg[\Gamma_{1,\mathrm{mp}}(1 - e^{-\Gamma_{1,\mathrm{mp}}T}) \\ &+ 2\sqrt{B}\left(\sqrt{\sqrt{1+A^2}+A} + i\sqrt{\sqrt{1+A^2}-A}\right)\Bigg] \\ &\text{where } A = \frac{\Gamma_{1,\mathrm{mp}}^2(1+e^{-\Gamma_{1,\mathrm{mp}}T})^2 - 4\chi_{\mathrm{s,mp}}^2(n_1-n_2)^2 e^{-\Gamma_{1,\mathrm{mp}}T}}{8B} \\ &\qquad B = \chi_{\mathrm{s,mp}}(n_1 - n_2)\Gamma_{1,\mathrm{mp}} e^{-\Gamma_{1,\mathrm{mp}}T} \\ &\text{and we recall } T = 1/\chi_{\mathrm{s,mp}} \ . \end{aligned} \tag{8.10}$$

We now analyze this last expression.

8.2.1.2 *Optimal decoherence rate of the coherence between Fock states $|n_1\rangle$ and $|n_2\rangle$*

The average dephasing rate $-\log(|R|)\chi_{\mathrm{s,mp}}/2\pi$ only depends on the ratio $\chi_{\mathrm{s,mp}}/\Gamma_{1,\mathrm{mp}}$ and on the photon numbers n_1 and n_2. In Fig. 8.5 are shown the rates corresponding to several values of $n_1 - n_2$ for a driving amplitude $\Omega = \chi_{\mathrm{s,mp}}/2$ (maximal measurement strength). As expected, the decoherence is stronger when the photon numbers are further apart. Besides, when the effective cross-Kerr rate is much larger than the multiplexing qubit relaxation rate, i. e. $\chi_{\mathrm{s,mp}}|n_1 - n_2| \gg \Gamma_{1,\mathrm{mp}}$, the rate saturates to $\Gamma_{1,\mathrm{mp}}/2$ similarly to the emission rate of a qubit driven by a single frequency. In this regime, the qubit stays close to the Bloch sphere center as it does not have the time to relax between two Rabi jumps. This leads to an average population of 1/2 and an average qubit emission of $\Gamma_{1,\mathrm{mp}}/2$.

However we have to be careful when comparing to the gedanken experiment (of Sec. 5.3.2). In the gedanken experiment, after the π-pulse, the qubit relaxes, the excited population p_e decreases and there is no drive to increases it back. Thus, the emission rate at time t is $\Gamma_{1,\mathrm{mp}} \exp(-\Gamma_{1,\mathrm{mp}}t)$ and decreases exponentially with time t. On the contrary, in the multiplexed experiment with the frequency comb, the latter acts on

---

[3] We find two solutions where z/η is stationary, one stable and one unstable. Considering the stable solution only, we compute R such that $\eta(kT + T) = R\,\eta(kT)$. The computation boils down to solving order-two polynomials.

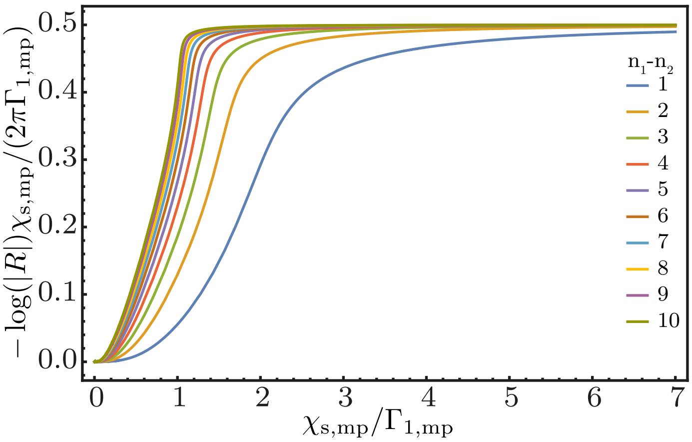

Figure 8.5: Decoherence rate between Fock states $|n_1\rangle$ and $|n_2\rangle$ in units of $\Gamma_{1,\mathrm{mp}}$ for a driving amplitude $\Omega = \chi_{\mathrm{s,mp}}/2$ as a function of $\chi_{\mathrm{s,mp}}/\Gamma_{1,\mathrm{mp}}$ and for various values of $n_1 - n_2$.

the qubit and excites it again. In particular, when $\Omega = \chi_{\mathrm{s,mp}}$ and $\chi_{\mathrm{s,mp}} \gg \Gamma_{1,\mathrm{mp}}$, the qubit excited population is always 1/2 and the emission rate is always $\Gamma_{\mathrm{s,mp}}/2$.

8.2.2 *Maximal reachable measurement rate*

8.2.2.1 *Modeling of the entanglement process*

Beyond the determination of the decoherence rate between two Fock states, we are interested in the maximal information extraction rate of the storage state photon number in the multiplexed measurement scheme. In particular, we will discuss how this maximal total measurement rate depends on the maximum number of photons N_{max} that are probed by the multiplexed scheme. In the following, we assume a perfect measurement apparatus, giving us access to all the information extracted by the measurement process, i. e. the measurement rate is equal to the measurement-induced dephasing rate, which is not necessarily the case for heterodyne measurements on each peak of the comb (see Sec. 7.4). In Sec. 5.3.2, we propose such a measurement apparatus.

We assume the number-resolved regime $\chi_{\mathrm{s,mp}} \gg \Gamma_{2,\mathrm{mp}}, \Gamma_{1,\mathrm{mp}}$. Thus, the decoherence rate between two Fock states is independent of the Fock state numbers and is equal to $\Gamma_{1,\mathrm{mp}}/2$ (see Fig. 8.5). In the following, we show that under these assumptions, the total measurement rate does not depend on N_{max}.

Since the multiplexed measurement operates by entangling the storage mode with $N_{\mathrm{max}} + 1$ wavelet modes of the transmission line[4], we can describe the system and the extraction of information without the multiplexing qubit and only consider its effect, which is the entanglement operation. Each Fock state $|n\rangle$ in the storage mode ($0 \leq n \leq N_{\mathrm{max}}$) is associated with one out of the $N_{\mathrm{max}} + 1$ wavelet modes of the transmission line with a carrier frequency $\omega_{\mathrm{mp}} - n\chi_{\mathrm{s,mp}}$. Every mode is driven so that

---

[4] Due to the periodic dynamics of the qubit, the storage mode is entangled with more than $N_{\mathrm{max}} + 1$ frequency modes of the transmission line. However, when choosing the proper wavelet basis [188] to describe the propagating modes of the transmission line, the storage mode is entangled with only $N_{\mathrm{max}} + 1$ wavelet modes

the input is in a coherent state (it can even be a vacuum as in the Gedanken experiment). At the output, if we change the reference frame by displacing the outgoing modes $a_{\mathrm{out},n}$ by the opposite of the input coherent state, a single mode will be excited and all the non-resonant modes will be in the vacuum state when the storage mode is in a Fock state. Therefore, any quantum state of the outgoing modes can be expressed as a superposition of $N_{\max}+2$ states only. States $|n\rangle_m$ correspond to all transmission line modes in the vacuum except the one with a carrier frequency $\omega_{\mathrm{mp}} - n\chi_{\mathrm{s,mp}}$, and $|\perp\rangle_m$ is the vacuum state of the line.

Thus, we can describe the system using two modes only: the storage mode and a simplified measurement mode. The storage mode is described using the Fock state basis $\{|n\rangle_{\mathrm{s}}\}_{0\leq n\leq N_{\max}}$. The measurement mode has the $N_{\max}+2$ states discussed above. During a multiplexed measurement, the bipartite system starts in the state

$$|\Psi_{\mathrm{s,mp}}(0)\rangle = |\Psi_{\mathrm{storage}}\rangle_s \otimes |\Psi_{\mathrm{meas}}\rangle_m = \left(\sum_{n=0}^{N_{\max}} \psi_n |n\rangle_{\mathrm{s}}\right) \otimes |\perp\rangle_{\mathrm{m}}. \tag{8.11}$$

After a measurement time t, the storage mode and the measurement mode become entangled, and the readout of the measurement mode extracts information about the storage photon number. As the decoherence rate between every storage Fock state pair is $\Gamma_{1,\mathrm{mp}}/2$, one can write the state of the bipartite system as

$$|\Psi_{\mathrm{s,mp}}(t)\rangle = \sqrt{e^{-\Gamma_{1,\mathrm{mp}}t/2}}|\Psi(0)\rangle + \sqrt{1-e^{-\Gamma_{1,\mathrm{mp}}t/2}} \sum_{n=0}^{N_{\max}} \psi_n |n\rangle_{\mathrm{s}} \otimes |n\rangle_{\mathrm{m}}. \tag{8.12}$$

As expected, if we trace over the measurement mode, the diagonal of the density matrix of the storage mode remains unchanged while the off-diagonal terms decrease at a rate $\Gamma_{1,\mathrm{mp}}/2$.

8.2.2.2 *Extracted information and mutual information*

How can the amount of information we gained during the measurement of duration t be derived from the state $|\Psi_{\mathrm{s,mp}}(t)\rangle$? One can look at the system as a noisy communication channel between Alice, who sent information by toggling the storage state, and Bob, who recovers the information by measuring the state of the measurement mode. The noisy-channel coding theorem of Shannon [196] enables us to say that the maximum amount of information that can be shared through a classical communication channel is given by the maximum of the *mutual information* [197] of the bipartite system over the input state. However, in quantum mechanics one has to distinguish the mutual information $I(s,m)$ from the *locally accessible* mutual information $J(s,\{m,\mathcal{B}_m\})$ [198, 199]. They are defined as

$$\begin{aligned} I(s,m) &= S(\rho_{\mathrm{s}}) + S(\rho_{\mathrm{m}}) - S(\rho_{\mathrm{s,m}}),\\ J(s,\{m,\mathcal{B}_m\}) &= S(\rho_{\mathrm{s}}) - S(\rho_{\mathrm{s,m}}|\{\rho_{\mathrm{m}},\mathcal{B}_m\}) \end{aligned} \tag{8.13}$$

where $S(\rho)$ is the von Neumann entropy (see Sec. 2.2.2), $\rho_{\mathrm{s,m}}$ is the bipartite density matrix, ρ_{s} (respectively, ρ_{m}) is the density matrix of the storage mode (respectively, measurement mode) obtained by tracing out the other mode, and $S(\rho_{\mathrm{s,m}}|\{\rho_{\mathrm{m}},\mathcal{B}_m\})$

is the entropy of the storage mode when the measurement mode state is projectively measured in the basis of $\mathcal{B}_m$. Due to the back-action of the measurement, the mutual information and the locally accessible mutual information differ by a quantity called the quantum discord [198, 199]. From the point of view of measurement, the mutual information is the amount of information one can recover from the system using measurements of both input and output states (the storage and the measurement mode states), whereas the locally accessible mutual information is the amount of information one can recover when measuring only the output state (the measurement mode state). Thus, in the case of the multiplexed measurement, for which we only measure the measurement mode, the amount of information C extracted is given by the maximum of the locally accessible mutual information over the storage state [200, 201, 8].

8.2.2.3 *Measurement time*

To derive C, we first have to choose the basis $\mathcal{B}_m$ on which the measurement mode is measured. As we are considering a measurement apparatus recovering all the information, the basis is simply $\mathcal{B}_m = \{|\perp\rangle_m, |0\rangle_m, |1\rangle_m, ..., |N_{\max}\rangle_m\}$. Then, we have to choose the storage state that maximizes $J(s, \{m, \mathcal{B}_m\})$: it is the one for which the storage finishes at the end of the measurement in the most entropic state. This is the case when considering an initially uniform photon number distribution, such as $\psi_n = (N_{\max}+1)^{-1/2}$, for all n. Thus, the amount of information C extracted by the measurement reads

$$\begin{aligned} C =& S(\rho_{\mathrm{s}}) - \sum_{n=0}^{N_{\max}} \mathrm{Tr}(\rho_{\mathrm{s,m}}|n\rangle\langle n|_{\mathrm{m}}) S\left(\frac{\mathrm{Tr}_m(\rho_{\mathrm{s,m}}|n\rangle\langle n|_{\mathrm{m}})}{\mathrm{Tr}(\rho_{\mathrm{s,m}}|n\rangle\langle n|_{\mathrm{m}})}\right) \\ &- \mathrm{Tr}(\rho_{\mathrm{s,m}}|\perp\rangle\langle\perp|_{\mathrm{m}}) S\left(\frac{\mathrm{Tr}_m(\rho_{\mathrm{s,m}}|\perp\rangle\langle\perp|_{\mathrm{m}})}{\mathrm{Tr}(\rho_{\mathrm{s,m}}|\perp\rangle\langle\perp|_{\mathrm{m}})}\right), \end{aligned} \tag{8.14}$$

where $\frac{\mathrm{Tr}_m(\rho_{\mathrm{s,m}}|n\rangle\langle n|_{\mathrm{m}})}{\mathrm{Tr}(\rho_{\mathrm{s,m}}|n\rangle\langle n|_{\mathrm{m}})}$ is the storage density matrix after the measurement of the measurement mode with outcomes $|n\rangle$ and probability $\mathrm{Tr}(\rho_{\mathrm{s,m}}|n\rangle\langle n|_{\mathrm{m}})$.

For the measurement basis $\mathcal{B}_m$, the storage density matrix after the measurement of the measurement mode is always a pure state. Thus, C reads

$$C = S(\rho_{\mathrm{s}}) \tag{8.15}$$

and the storage density matrix ρ_{s}, for the uniform photon number distribution is

$$\rho_{\mathrm{s}} = \frac{e^{-\Gamma_{1,\mathrm{mp}}t/2}}{N_{\max}+1} \sum_{n,l=0}^{N_{\max}} |n\rangle_{\mathrm{s}}\langle l|_{\mathrm{s}} + \frac{1-e^{-\Gamma_{1,\mathrm{mp}}t/2}}{N_{\max}+1} \sum_{n=0}^{N_{\max}} |n\rangle_{\mathrm{s}}\langle n|_{\mathrm{s}}. \tag{8.16}$$

The eigenvalues of ρ_{s} are $e^{-\Gamma_1 t/2} + (1-e^{-\Gamma_1 t/2})/(N_{\max}+1)$ with degeneracy 1 and $(1-e^{-\Gamma_1 t/2})/(N_{\max}+1)$ with degeneracy $N_{\max}$. Thus, one can derive the amount of extracted information C

$$C = -\left(r + \frac{1-r}{N_{\max}+1}\right)\log_2\left(r + \frac{1-r}{N_{\max}+1}\right) - \frac{N_{\max}(1-r)}{N_{\max}+1}\log_2\left(\frac{1-r}{N_{\max}+1}\right), \tag{8.17}$$

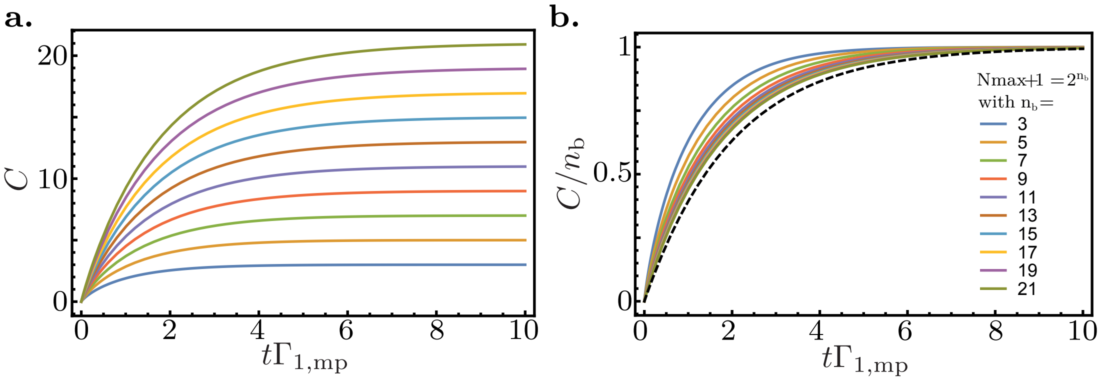

Figure 8.6: Extracted information C for various maximum photon numbers $N_{\max} = 2^{n_b} - 1$ as a function of measurement time t. **a.** Mutual information in bits. **b.** Extracted information C divided by the number of bits n_b as a function of time. The dashed black curve is the lower bound $(1 - e^{-\Gamma_1 t/2})$.

with $r = e^{-\Gamma_{1,\mathrm{mp}}t/2}$. The time evolution of the extracted information C is shown in Fig. 8.6. At short time, the extracted information increases with time t at a speed that depends on $N_{\max} + 1$. The time derivative of the extracted information at short time scales gives the rate at which information is extracted (i.e., the total measurement rate)[8, 201]. However, in this model, it diverges for finite $N_{\max}$. This divergence is due to the fact that we did not consider the dynamics of the measurement mode. In our model the measurement mode can evolve instantaneously from the state $|\perp\rangle$ to the state $|n\rangle$. In reality, it would take time of about $1/(p\Omega)$ where p is the number of frequency in the drive. If the derivative at short time scales is not a good quantity to look at for this model, one can still look at the time needed to extract 98% of the photon number information. To do so, we look at the extracted information per bit of information $n_b = \log_2(N_{\max} + 1)$. Here, n_b is the number of bits we have to extract in order to fully determine the storage photon number. The extracted information per bit decreases with n_b for small photon numbers but converges to a lower bound when n_b goes to infinity (see Fig. 8.6b)

$$\lim_{n_b \to +\infty} \frac{C}{n_b} = (1 - e^{-\Gamma_1 t/2}). \tag{8.18}$$

As the extracted information per bit is always bigger than $(1-r)$, the total measurement time to extract 98% of the photon number information is always smaller than $8/\Gamma_{1,\mathrm{mp}} = 8T_{1,\mathrm{mp}}$. Thus, the best achievable measurement time for the multiplexing protocol is independent of the maximum photon number $N_{\max}$.

8.3 CORRELATION BETWEEN MULTIPLEXED MEASUREMENT AND STRONG PHOTON NUMBER MEASUREMENT

Similarly to the correlations studied in Secs. 4.4 and 6.3.2, we can study the correlations between a weak and a strong measurement in the case of the multiplexing photon number measurement. The weak measurement will be the multiplexed measurement, and the strong measurement will be a binary question asked and read out using the yes-no qubit and its dedicated readout resonator.

Before describing the experiment and its results in detail, we will derive the measurement operators of the multiplexing photon number measurement. We will use the same approximation as in Sec. 6.3.1, i. e. we will describe the output field reflected by the multiplexing qubit as a coherent field.

8.3.1 *Measurement operator*

Here we will generalize the simple measurement operator model described in Sec. 6.3.1 to the multiplexed photon number measurement. In this case, instead of having only one record $I^{(k)} + iQ^{(k)}$ corresponding to the fluorescence measurement at the angular frequency $\omega_{\text{mp}} - k\chi_{\text{s,mp}}$, we have nine records $\{I^{(k)} + iQ^{(k)}\}_{0\leq k\leq 8}$ corresponding to the multiplexed fluorescence measurement at all the frequencies $\{\omega_{\text{mp}} - k\chi_{\text{s,mp}}\}_{0\leq k\leq 8}$. When preparing a Fock state $|n\rangle$ in the storage mode, the multiplexing qubit fluorescence will oscillate at the frequency $\omega_{\text{mp}} - n\chi_{\text{s,mp}}$ with a $2\pi/\chi_{\text{s,mp}}$-periodic amplitude. Thus, all the transmission line propagating modes oscillating at $\{\omega_{\text{mp}} - k\chi_{\text{s,mp}}\}_{0\leq k\leq 8}$ are displaced compared to the amplitude α_{in} of the reflected frequency comb. One can define the matrix $\underline{\alpha}$ of elements α_{kn} equal to the amplitude of the transmission line propagating mode oscillating at $\omega_{\text{mp}} - k\chi_{\text{s,mp}}$ when the storage mode state is the Fock state $|n\rangle$.

For each record $I^{(k)} + iQ^{(k)}$, we define the measurement operator $M^{(k)}(I^{(k)}, Q^{(k)})$ as

$$M^{(k)}(I^{(k)}, Q^{(k)}) = \sum_{n=0}^{8} \xi(\alpha_{kn}, I^{(k)}, Q^{(k)})\Pi_n + \xi(\alpha_{in}, I^{(k)}, Q^{(k)})(\mathbb{1} - \sum_{n=0}^{8} \Pi_n), \quad (8.19)$$

where the function $\xi(\beta, I, Q)$ is defined in Sec. 6.3.1 and Π_n is the projector on the storage Fock state $|n\rangle$. The measurement operator $M(\{I^{(k)} + iQ^{(k)}\}_{0\leq k\leq 8})$ of the multiplexed measurement reads

$$M(\{I^{(k)} + iQ^{(k)}\}_{0\leq k\leq 8}) = \prod_{k=0}^{8} M^{(k)}(I^{(k)}, Q^{(k)}), \quad (8.20)$$

which can be written in the form

$$\begin{aligned} M(\{I^{(k)} + iQ^{(k)}\}_{0\leq k\leq 8}) \; &= \\ \sum_{n=0}^{8} \frac{1}{(4\pi\sigma_0^2)^{9/4}} &\exp\left(-\sum_{k=0}^{8} \frac{|\alpha_{kn}|^2 + (I^{(k)} + iQ^{(k)} - 2\alpha_{kn})(I^{(k)} - iQ^{(k)})}{2(2\sigma_0)^2}\right)\Pi_n \\ + \frac{1}{(4\pi\sigma_0^2)^{9/4}} &\exp\left(-\sum_{k=0}^{8} \frac{|\alpha_{in}|^2 + (I^{(k)} + iQ^{(k)} - 2\alpha_{in})(I^{(k)} - iQ^{(k)})}{2(2\sigma_0)^2}\right)(\mathbb{1} - \sum_{n=0}^{8} \Pi_n) \end{aligned} \quad (8.21)$$

The situation can be simplified either by inverting the matrix $\underline{\alpha}$ or by using an advanced waveform for the demodulation of the IF signal (see supplementary information of Ref. [187]). In this case, one can remove correlations between records $I^{(k)} + iQ^{(k)}$ and we get new uncorrelated records $I_{uc}^{(k)} + iQ_{uc}^{(k)}$. If the waveforms are normalized or if we normalize the inverse matrix, the records $I_{uc}^{(k)} + iQ_{uc}^{(k)}$ are all affected by a Gaussian noise of amplitude $2\sigma_0$ and the average records, when the storage state is a Fock state $|n\rangle$, are equal to $\alpha_{in} + \delta_{kn}\alpha$. One can displace all records by α_{in} and thus, the measurement operators using the uncorrelated records $I_{uc}^{(k)} + iQ_{uc}^{(k)}$ read

$$\begin{aligned} &M(\{I^{(k)} + iQ^{(k)}\}_{0\leq k\leq 8}) \;= \\ &\sum_{n=0}^{8} \frac{1}{(4\pi\sigma_0^2)^{9/4}} \mathrm{e}^{-\dfrac{|\alpha|^2 + (I_{uc}^{(n)} + iQ_{uc}^{(n)} - 2\alpha)(I_{uc}^{(n)} - iQ_{uc}^{(n)})}{2(2\sigma_0)^2}} \mathrm{e}^{-\sum_{k\neq n} \dfrac{((I_{uc}^{(k)})^2 + (Q_{uc}^{(k)})^2)}{2(2\sigma_0)^2}} \Pi_n \\ &+ \frac{1}{(4\pi\sigma_0^2)^{9/4}} \mathrm{e}^{-\sum_{k=0}^{8} \dfrac{((I_{uc}^{(k)})^2 + (Q_{uc}^{(k)})^2)}{2(2\sigma_0)^2}} (\mathbb{1} - \sum_{n=0}^{8} \Pi_n) \end{aligned} \tag{8.22}$$

Now that we have derived the measurement operators, let us discuss the correlation between a weak multiplexed measurement and a strong binary question.

8.3.2 *Correlations*

8.3.2.1 *Description of the experiment*

The correlations between the multiplexing qubit and the yes–no qubit photon number measurement can be seen through the following experiment We initialize the storage mode in a coherent state $|\alpha\rangle$ and then probe the multiplexing qubit with a frequency comb during 2 µs with an amplitude $\Omega/2\pi = 1.1$ MHz. A π-pulse of 1.335 µs is performed on the yes–no qubit at the frequency f_{drive} at the same time as the multiplexing qubit measurement. The π-pulse is long enough compared to the cross-Kerr rate $\chi_{\mathrm{s,yn}}$ to consider it as conditional with respect to the storage photon number. The pulse sequence finishes by a readout of the yes–no qubit state leading to a record Q_{yn}. Thus, for each repetition of the experiment, we have 10 records $\{Q_{\mathrm{yn}}, I^{(0)} + iQ^{(0)}, ..., I^{(8)} + iQ^{(8)}\}$ that depend on α and f_{drive}. In order to obtain positive correlation between records giving the same information, we multiply[5] all the records $I^{(k)} + iQ^{(k)}$ by -1. The mean value of the yes–no readout quadrature $\overline{Q_{\mathrm{yn}}}$ depends linearly on the yes–no qubit excited state probability p_e. One can first look at the dependence of $p_e(\alpha, f_{\mathrm{drive}})$. Fig. 8.7 shows this dependence. We retrieve the same map as the one in Sec. 5.2.1. Each spot of large p_e corresponds to a resonance of the yes–no qubit for a specific photon number. Thus, the probabilities $\{p_e(\alpha, f_{\mathrm{drive}} = f_{\mathrm{yn}} - n\chi_{\mathrm{s,yn}}/2\pi)\}_n$ reveal the storage photon distribution when it is initialized in the coherent state $|\alpha\rangle$.

8.3.2.2 *Measuring the correlations*

The correlations between a record $I^{(k)}$ or $Q^{(k)}$ and the record Q_{yn} due to the measurement back-action can be seen using the same analysis as the one carried out in Sec. 4.4. For any choice of quadrature $I_{\mathrm{ps}} + iQ_{\mathrm{ps}}$, we select all the realizations for

---

[5] This is equivalent to a change of phase reference. With this reference, the records reads $I^{(k)} + iQ^{(k)} = -\alpha_{\mathrm{in}} + \sqrt{\Gamma_{1,\mathrm{mp}}}\langle\sigma_{-,\mathrm{mp}}\rangle$

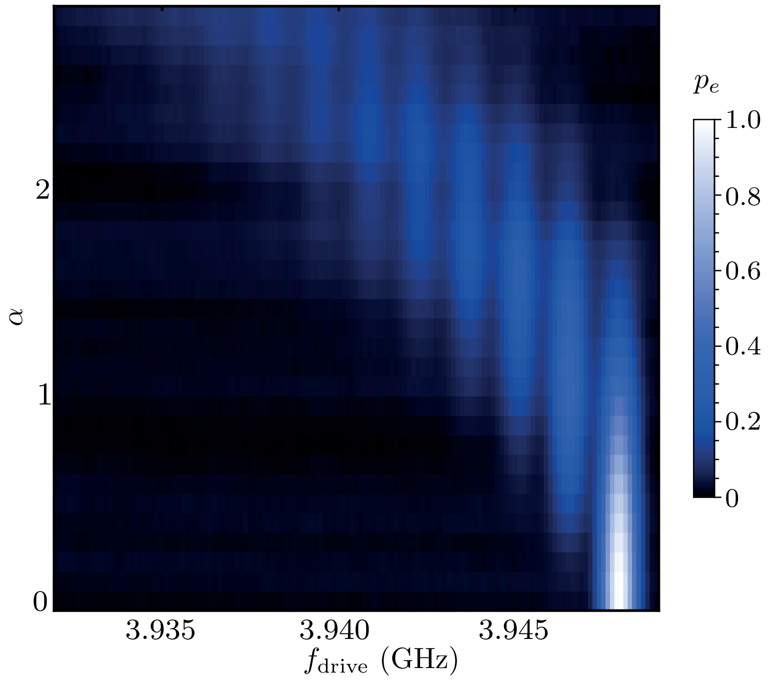

Figure 8.7: Yes–no qubit excited state population p_e as a function of the π-pulse frequency f_{drive} on the yes-no qubit and the storage mode amplitude α. The excited state population is obtained by averaging the records Q_{yn} over all realizations of the experiment.

which $I^{(k)} + iQ^{(k)} = I_{\mathrm{ps}} + iQ_{\mathrm{ps}}$ and compute the yes–no excited state population $p(e|I^{(k)} + iQ^{(k)} = I_{\mathrm{ps}} + iQ_{\mathrm{ps}})$ by averaging Q_{yn}over these realizations only.

For each value of yes-no drive frequency f_{drive} and coherent amplitude α of the storage mode, $p(e|I^{(k)} + iQ^{(k)} = I_{\mathrm{ps}} + iQ_{\mathrm{ps}})$ can be fit by the function

$$p(I_{\mathrm{ps}}, Q_{\mathrm{ps}}) = c_I^{(k)} I_{\mathrm{ps}} + c_Q^{(k)} Q_{\mathrm{ps}} + c_0 \tag{8.23}$$

where $c_I^{(k)}$ and $c_Q^{(k)}$ are respectively the correlation slopes between the records $I^{(k)}$ and Q_{yn} and the records $Q^{(k)}$ and Q_{yn} (see Fig. 8.8).

8.3.2.3 *Correlation slopes*

Here, we did not remove the correlations between the fluorescence records $\{I^{(k)} + iQ^{(k)}\}_{0\leq k\leq 8}$ as explained in Sec. 8.3.1. Thus, to discuss the dependence of the correlation slopes with f_{drive} and α, we have to determine the matrix $\underline{\alpha}$ (see Sec. 8.3.1). Using the master equation model already used to simulate all photon-counting experiments (see App. d), we simulate the matrix $\underline{\alpha}$ displaced by α_{in} by initializing the storage mode in a Fock state and looking at the multiplexing qubit fluorescence. In the model, we set the relaxation rate of the storage mode to 0 to obtain a correlation matrix $\underline{\alpha'}$

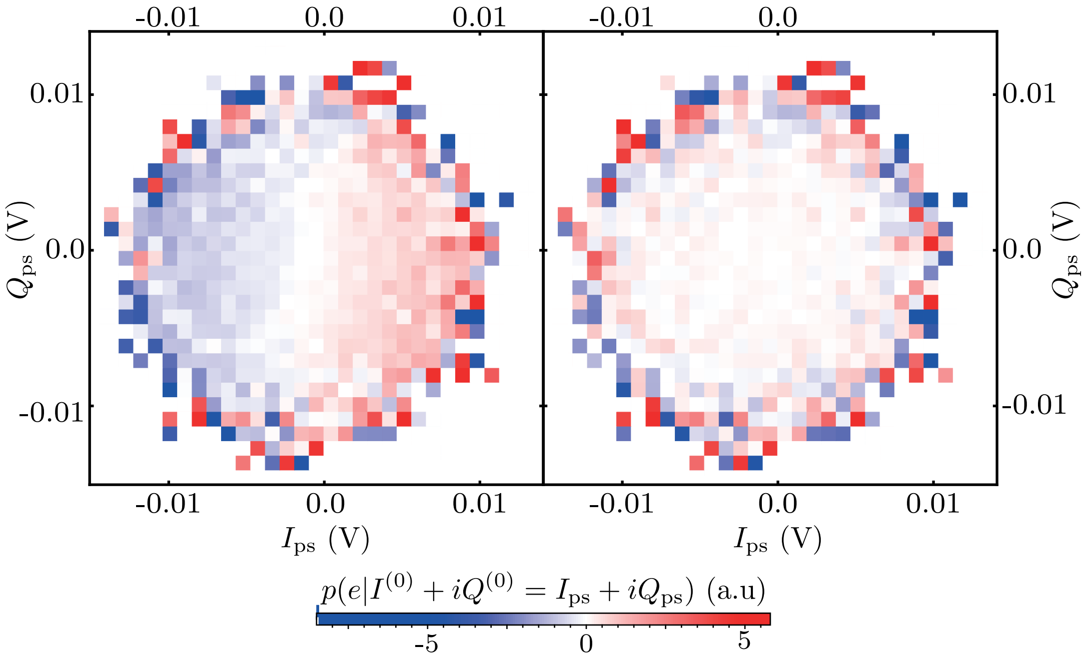

Figure 8.8: **left:** yes–no excited state population $p(e|I^{(0)} + iQ^{(0)} = I_{\mathrm{ps}} + iQ_{\mathrm{ps}})$ as a function of the post-selected value $I_{\mathrm{ps}} + iQ_{\mathrm{ps}}$. **right:** Difference between the yes–no excited state population $p(e|I^{(0)} + iQ^{(0)} = I_{\mathrm{ps}} + iQ_{\mathrm{ps}})$ and the fit function $p(I_{\mathrm{ps}}, Q_{\mathrm{ps}})$ (see Eq. (8.23)). The outskirts of the distributions are averaged on very few realizations and thus are very noisy.

containing only the correlations due to the demodulation and channel cross-talk. The correlation matrix $\underline{\alpha'}$ reads in units of $\sqrt{\Gamma_{1,\mathrm{mp}}}$

$$\underline{\alpha'} = 0.01\times \begin{pmatrix} 18-4i & 5+6i & 2+3i & 2+2i & 1+2i & 1+i & 1+i & i & i \\ 2-\ 6i & 17-4i & 4+5i & 2-3i & 1+2i & 1+2i & 1+i & i & i \\ -3i & 2-6i & 16-3i & 3+5i & 1+3i & 1+2i & 2i & i & i \\ -2i & -3i & 2-6i & 15-2i & 3+5i & 1+3i & 1+2i & 2i & i \\ -2i & -2i & 1_3i & 2-6i & 15 & 2+6i & 1+3i & 2i & 2i \\ -i & -2i & 1_2i & 1_3i & 3-5i & 15+2i & 2+6i & 3i & 2i \\ -i & -i & -2i & 1_2i & 1-3i & 4-5i & 16+3i & 2+6i & 3i \\ -i & -i & 1-i & 1-2i & 1-2i & 2-3i & 4-5i & 16+4i & 2+6i \\ -i & -i & 1-i & 1-i & 1-2i & 2-2i & 2-3i & 5-6i & 18+4i \end{pmatrix} \tag{8.24}$$

We now discuss this matrix at the same time as the correlation slopes.

Let us first look at the correlation slopes $c_I^{(0)}$ and $c_Q^{(0)}$ (see Fig. 8.9). The correlation slopes are non-zero only for frequencies f_{drive} and amplitudes α, which are compatible, i. e. when the drive is resonant with the yes–no qubit and the yes–no qubit probes a Fock state that has a non-zero population. The correlation slope $c_I^{(0)}$ shows that the record $I^{(0)}$ and the yes–no record are correlated ($c_I^{(0)} > 0$) when the yes–no qubit is probing if the storage mode contains 0 photons and anti-correlated ($c_I^{(0)} < 0$) when the yes–no qubit is probing if the storage mode contains 1 or 2 photons.

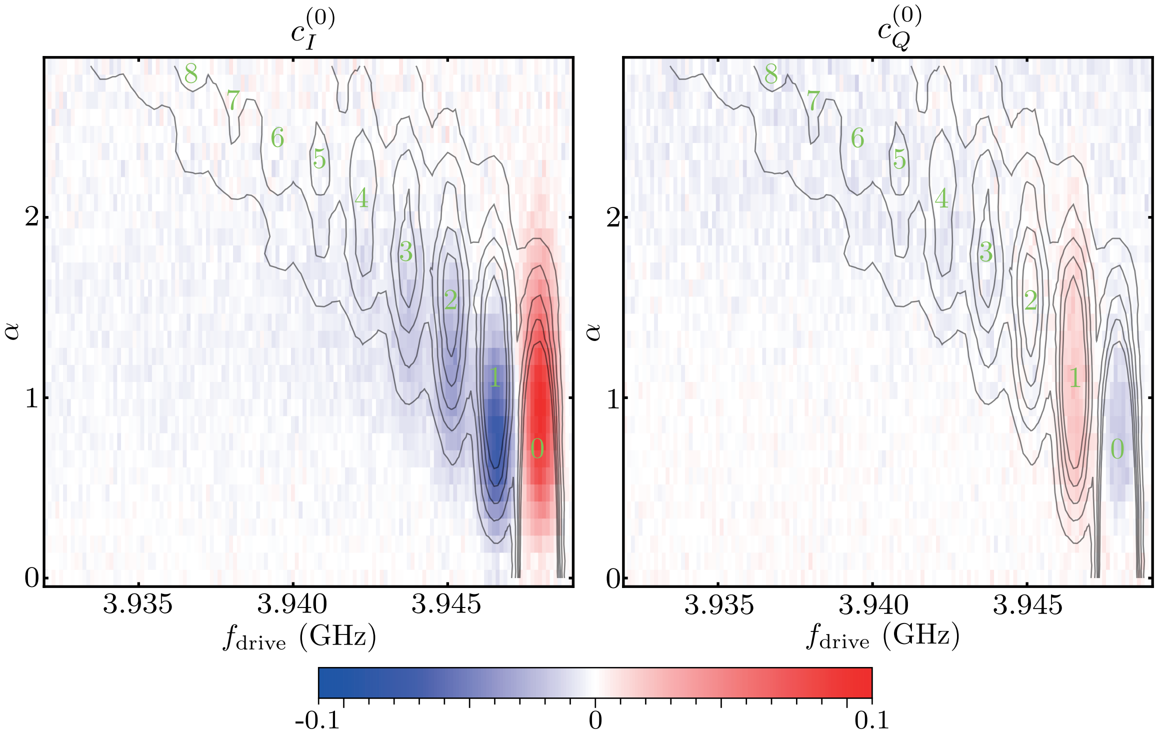

Figure 8.9: Correlation slopes $c_I^{(0)}$ (left) and $c_Q^{(0)}$ (right) as a function of the yes–no qubit π-pulse frequency f_{drive} and the storage mode coherent state amplitude α. The black solid lines correspond to the contour lines of dressed yes-no qubit spectroscopy in Fig. 8.7 and indicates the regions of response of the yes-no photocounting. The green numbers in theses contour lines are the storage photon numbers probed by the yes–no qubit for the π-pulse frequency f_{drive}.

The mean record $\overline{I^{(0)} + iQ^{(0)}}$ is equal to $-\alpha_{\mathrm{in}} + \sqrt{\Gamma_{1,\mathrm{mp}}}\alpha'_{0n}.p_s(n)$, where $p_s(n)$ is the storage mode photon number distribution and . denote a vector product. Thus, according to the measurement operator of Eq. (8.21), the closer $I^{(0)} + iQ^{(0)}$ is to $-\alpha_{\mathrm{in}} + \sqrt{\Gamma_{1,\mathrm{mp}}}\alpha'_{0n}$, the bigger the probability $p_s(n)$ is. From the real part of α'_{0n}, one can deduce the expected sign of the correlation slopes $c_I^{(0)}$. The storage Fock state $|0\rangle$ corresponds to a high average record $\overline{I^{(0)}} = -\alpha_{\mathrm{in}} + 0.18\sqrt{\Gamma_{1,\mathrm{mp}}}$, whereas other Fock states correspond to small values of $\overline{I^{(0)}} \leq -\alpha_{\mathrm{in}} + 0.05\sqrt{\Gamma_{1,\mathrm{mp}}}$. Thus, as observed, we are expecting a positive correlation slope between $I^{(0)}$ and Q_{yn} (as the higher $I^{(0)}$ is, the higher $p_s(0)$ should be) when probing if there are 0 photons in the storage mode. For other Fock states, we are expecting a negative correlation slope. The amplitude of this negative correlation slope must decrease with the support of the storage photon number distribution. Indeed, if there are only 0 or 1 photons in the storage mode, a small value of $I^{(0)}$ can be associated to the Fock state $|1\rangle$ without ambiguity, and we would expect a strong anti-correlation. However, if the photon distribution is spread over many photon numbers, a small value of $I^{(0)}$ cannot be associated to a single Fock state but only to the fact that there are not 0 photons. Thus, the anti-correlation should be small. For the correlation slope $c_I^{(0)}$, we indeed observe that the anti-correlation when probing if there are 1 photon and 2 photons is maximal for small coherent states $\alpha \sim 0.75$ compared to the yes–no resonance corresponding to 1 photon (see the black lines in Fig. 8.9).

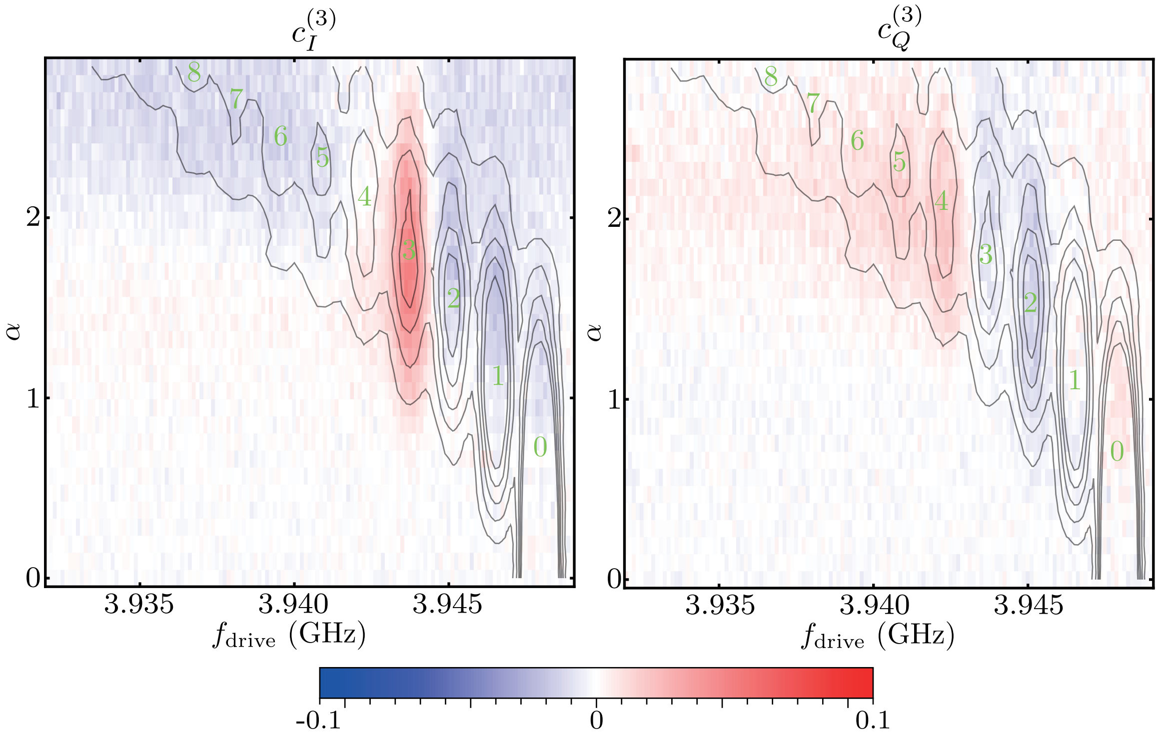

Figure 8.10: Correlation slopes $c_I^{(3)}$ (left) and $c_Q^{(3)}$ (right) as a function of the yes–no qubit π-pulse frequency f_{drive} and the storage mode coherent state amplitude α. The black solid lines correspond to the contour lines of dressed yes-no qubit spectroscopy in Fig. 8.7 and indicates the regions of response of the yes-no photocounting. The green numbers in theses contour lines are the storage photon numbers probed by the yes–no qubit for the π-pulse frequency f_{drive}.

In the same way, looking at the imaginary part of α'_{0n}, one can deduce the expected sign of the correlation slopes. With the imaginary parts being negative for α'_{00} and positive for α'_{0n} with $n \neq 0$, one would expect negative correlations when using the yes–no qubit probe if there are 0 photons and positive correlations when probing other Fock states. This is indeed what we observe, taking into account the fact that the positive correlation is observable only if the photon distribution is narrow, i. e. only if the information “no 0 photons” is equivalent to “there is 1 photon”.

The correlation slopes $c_I^{(3)}$ and $c_Q^{(3)}$ (see Fig. 8.10) can be analyzed using the same approach. We observe a strong correlation between $I^{(3)}$ and Q_{yn} when using the yes–no qubit to probe whether there are 3 photons and a small anti-correlation when a different photon number is probed. The anti-correlation is smaller than the one observed with $I^{(0)}$, as the photon number distribution is broader. Looking at $c_Q^{(3)}$, $Q^{(3)}$ and Q_{yn} are anti-correlated when the yes–no qubit probe photon number is equal to or below 3 and is correlated in other cases. These observations are in good agreement with the real and imaginary part of α'_{3n}. The real part is high for $n = 3$ and small for $n \neq 3$. The imaginary part is negative for $n \leq 3$ and positive for $n > 3$. The same study can be applied to the other correlation slopes, and we always obtain a good agreement between the sign of the correlation slope (i. e. if we have a correlation or an anti-correlation) and the value of the real and imaginary parts of α'_{kn}. All the correlation slopes can be found in App. f. The existence of these correlations between the multiplexed records and the storage photon number probability is proof that the multiplexed measurement extracts information about the storage photon number and that the record k extracts mainly information about the storage Fock state $|k\rangle$ population.

CONCLUSION

Here are the main conclusions of this section.

- We demonstrate how to measure the decoherence rate of a harmonic oscillator through an experiment inspired by the Ramsey interference experiment.
- The dephasing rate of the multiplexing measurement shows a maximum when the drive strength Ω is equal to half the cross-Kerr rate $\chi_{\mathrm{s,mp}}$ and a minimum when the drive strength is equal to the cross-Kerr rate.
- The infinite frequency comb is used to derive the dephasing rate between two storage Fock states. This dephasing rate shows maximum and minimum rates for the same drive strength values as the experimental observation.
- From the infinite frequency comb and the derived dephasing rate, one can prove that the best measurement rate that is accessible using a measurement apparatus recovering all the information is $N_{\mathrm{max}}\Gamma_{1,\mathrm{mp}}/2$, meaning that 98% of the storage photon number information is always extracted in $8T_{1,\mathrm{mp}}$ no matter what is the maximal photon number N_{max} looked for in the storage mode.
- The photon-counting ability of the multiplexed measurement can be studied through the correlations between the multiplexed records and a strong measurement performed with the yes–no qubit.

Part III

TOWARD THE SINGLE SHOT MEASUREMENT

9

SINGLE-SHOT MULTIPLEXED PHOTON NUMBER MEASUREMENT

A major part of this thesis has been dedicated to the improvement of multiplexing photon number measurement, which makes it possible to photocount using a single-shot measurement. The single-shot ability of the multiplexed measurement is governed by the ratio $\eta\frac{\Gamma_{1,\mathrm{mp}}}{\Gamma_{1,\mathrm{s}}}$; the larger it is, the larger the signal-to-noise ratio of the measurement. This ratio can be viewed as the number of photons emitted by the multiplexing qubit and detected by the heterodyne detection setup during the lifetime of the storage mode. The circuit used in the previous chapters had a ratio of about 17; increasing this by an order of magnitude should make single-shot multiplexed photon number measurements possible.

The main difficulty boils down to preventing the desired strong coupling of the qubit to the measurement line to deteriorate the quality factor of the storage mode. In the first attempt, we used a tunable Purcell filter, which was added to the transmission line. The design and performance of this filter will be discussed in this chapter; overall, however, the improvement on the storage lifetime was only by a factor of 2.5. In the second attempt, a new experiment was designed using a $\lambda/4$ coaxial cavity instead of a coplanar waveguide resonator for the storage mode. The design of this new experiment and preliminary results will be discussed in this chapter.

9.1 TUNABLE PURCELL FILTER

9.1.1 *Design*

The goal of the Purcell filter is to protect the storage mode from the Purcell effect through its hybridization with the multiplexing qubit. In this experiment, a storage lifetime of 3.8 µs was limited by the Purcell emission of the storage mode in the multiplexing qubit transmission line (see Sec. 3.3 for more information about the Purcell effect). The Purcell filter has been designed in such a way that it has a close-to-1 and flat transmission coefficient around the multiplexing qubit frequency and a close-to-1 reflection coefficient at the storage frequency. We decided to use a 3D geometry to make the fabrication easier, designing the filter in such a way that the frequency of the notch is tunable, enabling us to match the notch frequency with the storage frequency.

Pictures of the Purcell filter are given in Fig. 9.1. The filter is a 3D rectangular cavity with a superconducting inner conductor connected to the left and right faces of the rectangular cavity. Two microwave pins are added, which define the input/output ports of the filter. The superconducting inner conductor was added in order to obtain a non-simply connected geometry, allowing the existence of a transverse electromagnetic (TEM) mode coupling the two ports. The filter can be viewed as a coaxial cable with

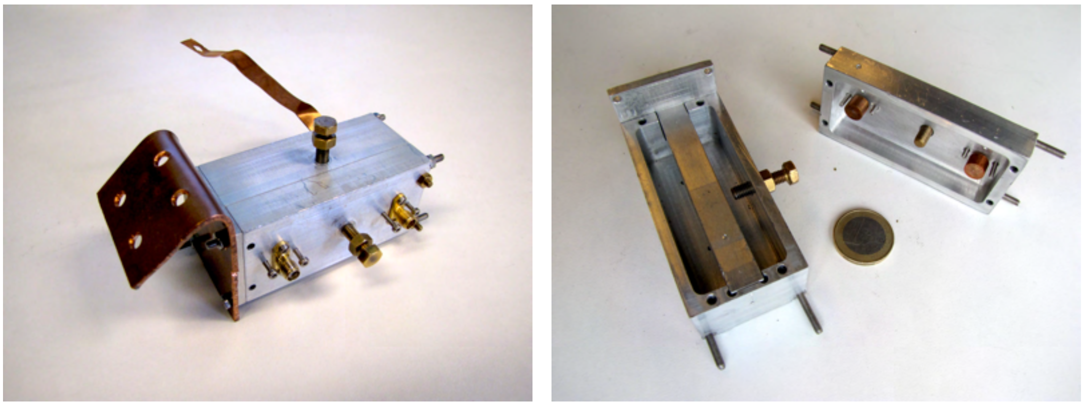

Figure 9.1: Pictures of the tunable Purcell filter. Left: filter closed. Right: filter open. The two large brass screws allow us to tune the notch band frequency. The small stainless-steel screw allows us to tune the impedance of the two ports. A coin of 1 euro gives the scale.

a square structure instead of a circular one. Without the superconducting inner conductor, the filter is a rectangular waveguide with a frequency cut-off that is above the multiplexing qubit frequency.

In order to create a notch band, we added two screws. The notch frequency is set by the penetration length of the screws inside the filter.

The microwave pins in the filter are made of large copper cylinders, in order make the transmission coefficient higher and flatter around the multiplexing qubit and to enable us to reach a close to 1 transmission coefficient on a larger frequency band. The distance between the two pins is also chosen because it increases the transmission coefficient at the multiplexing qubit frequency.

Two small screws were added from each side of each pin. The length of the screws penetrating inside the cavity enable us to tune the impedance the port but only by a small factor.

9.1.2 *Results*

The reflection and transmission coefficients of the ports were measured for various screw configurations (see Fig. 9.2). When the screws controlling the notch band frequency are removed, the filter shows a close-to-1 transmission amplitude around the multiplexing qubit frequency 4.238 GHz. We identify a parasitic mode around 4.6 GHz (see the purple line in Fig. 9.2), which can hybridize with the multiplexing qubit and thereby change its relaxation rate. One of the two screws controls the frequency of the parasitic mode and enables it to decrease to below 3 GHz (see the red line in Fig. 9.2). The second screw enables us to create a notch band and to control the notch frequency over a range larger than 1 GHz. Due to the contraction of the cavity during the cool down, the notch frequency decreases by 18 MHz from room temperature to 20 mK. This value is reproducible over several cool downs and enables us to tune the filter at room temperature, such that the notch frequency is equal to the storage mode frequency

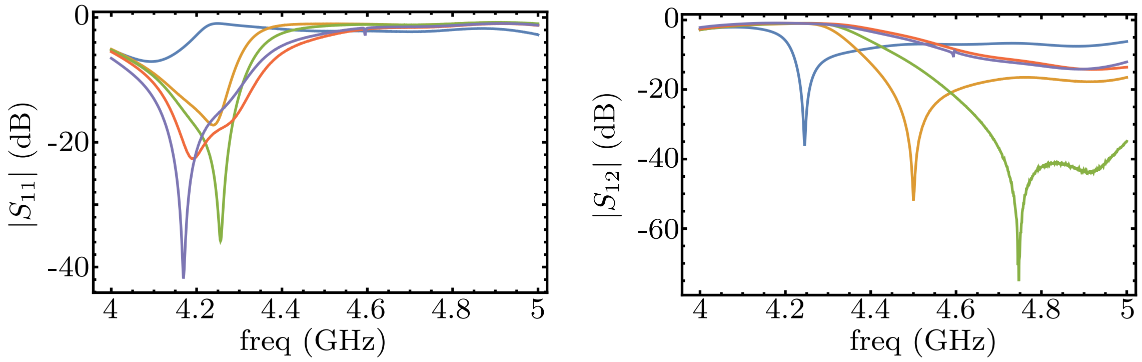

Figure 9.2: Amplitude of the reflection (left) and transmission (right) coefficients of the tunable Purcell filter for various screw penetration lengths (the blue, orange, and green lines). When the two screws are removed (the purple line) a parasitic mode appears at 4.6 GHz. The frequency of the parasitic mode can be controlled with only one of the two screws and decreased to below 3 GHz (red line).

4.558 GHz. At this frequency, the filter shows a transmission coefficient below −30 dB over 40 MHz.

Experimentally, we observed an increase in the storage mode lifetime: from 3.8 µs to 10 µs. The multiplexing qubit relaxation was fluctuating between 30 ns and 120 ns. This was due to an impedance mismatch between the filter and the transmission line, leading to a Fabry–Perot–like effect in the cable connecting the multiplexing qubit to the filter.

The improvement of the storage lifetime by a factor of 2.5 being too small to perform a single-shot measurement, we decided instead to design a new version of the experiment.

9.2 NEW CIRCUIT WITH A COAXIAL CAVITY

A major part of this thesis has been dedicated to the design and fabrication of a new version of the circuit—one that is based on a 3D cavity, instead of on a coplanar waveguide resonator. Indeed, $\lambda/4$ coaxial cavities have shown a lifetime that is larger by orders of magnitude than that of the $\lambda/2$ coplanar waveguide (CPW) resonator [46, 66, 202]. The goal of the new design is to obtain a cavity mode with a lifetime of above 200 µs, coupled dispersively to a qubit with a lifetime of 50 ns (dominated by its coupling to the transmission line) through a cross-Kerr rate of 6 MHz. To reach these parameters, we have to add a filter in order to protect the cavity mode from the decay that results from to its coupling to the lossy qubit.

9.2.1 *Design*

9.2.1.1 *Design of the cavity*

The cavity is a $\lambda/4$ coaxial cavity with a rectangular base (see Fig. 9.3). The bottom part of the cavity can be viewed as a coaxial line, while the top part can be viewed as a rectangular waveguide. The dimension of the cavity (10 mm, 18 mm, 30 mm) and the post height (13.9 mm) define the cavity's resonant frequency (4.5 GHz) and the frequency cut off of the waveguide (80 GHz). The frequency cut off of the waveguide is chosen such that the field of the $\lambda/4$ coaxial mode is evanescent above the post, thus protecting the cavity mode from the loss of the seal at the top of the waveguide [46]. Two "arms" enable us to introduce two chips, each of which contains a qubit.

9.2.1.2 *Design of the yes–no qubit*

The yes–no qubit is designed as a transmon qubit dispersively coupled to a $\lambda/2$ microstrip resonator dedicated to the yes–no qubit readout. The readout resonator is coupled to a transmission line through a Purcell filter (a $\lambda/2$ microstrip resonator), which acts as a band pass filter. The Purcell filter protects the yes–no qubit from the decay induced by its hybridization with the readout resonator.

9.2.1.3 *Design of the multiplexing qubit*

The multiplexing qubit design was the hardest part of this new circuit; it has to be strongly coupled to a transmission line in such a way that its lifetime is about 50 ns, and sufficiently dispersively coupled to the cavity mode to reach the photon number-resolved regime, without decreasing the cavity mode quality factor.

We decided to capacitively couple the multiplexing qubit to a microstrip transmission line. The end of the microstrip transmission line is galvanically coupled to a coaxial transmission line through a *pogopin* (see Fig. 9.3.a). The pogopin is a microwave pin mounted on a string. The string presses the microwave pin against the microstrip transmission line and ensures a galvanic (instead of a capacitive) coupling. On the other side of the pogopin, the microwave pin is galvanically connected to a SubMiniature A (SMA) port (see Fig. 9.3.c).

The cavity mode is protected from the Purcell effect through the addition of two stubs to the microstrip transmission line. These stubs act as a $\lambda/4$ resonator, resonant at the cavity mode frequency (these are described in detail in Ref. [203]). The stubs have a simple "L"-shape geometry (see Fig. 9.3.d); the length of the stub controls the stub frequency and the width controls the impedance of the stub.

9.2.2 *First characterizations*

We started by characterizing the cavity separately. The cavity was fabricated in 4N aluminum, without mirror polish. It was first cleaned with acetone and isopropanol and blow-dried with nitrogen, then etched at 50 °C with a type-A Transene aluminum etchant for 40 min, corresponding to etching a depth of 25 µm. Following the etching, the cavity was cleaned again with acetone and isopropanol, blow-dried with nitrogen, and backed at 50 °C for 30 min. A first cool down of the cavity was then performed. Next, we carried out a spectroscopy of the cavity in transmission through the ports dedicated to driving the cavity and the yes–no qubit. The transmission coefficient and its fit are both shown in Fig. 9.4. As the resonance shows Fano features [204], we fitted

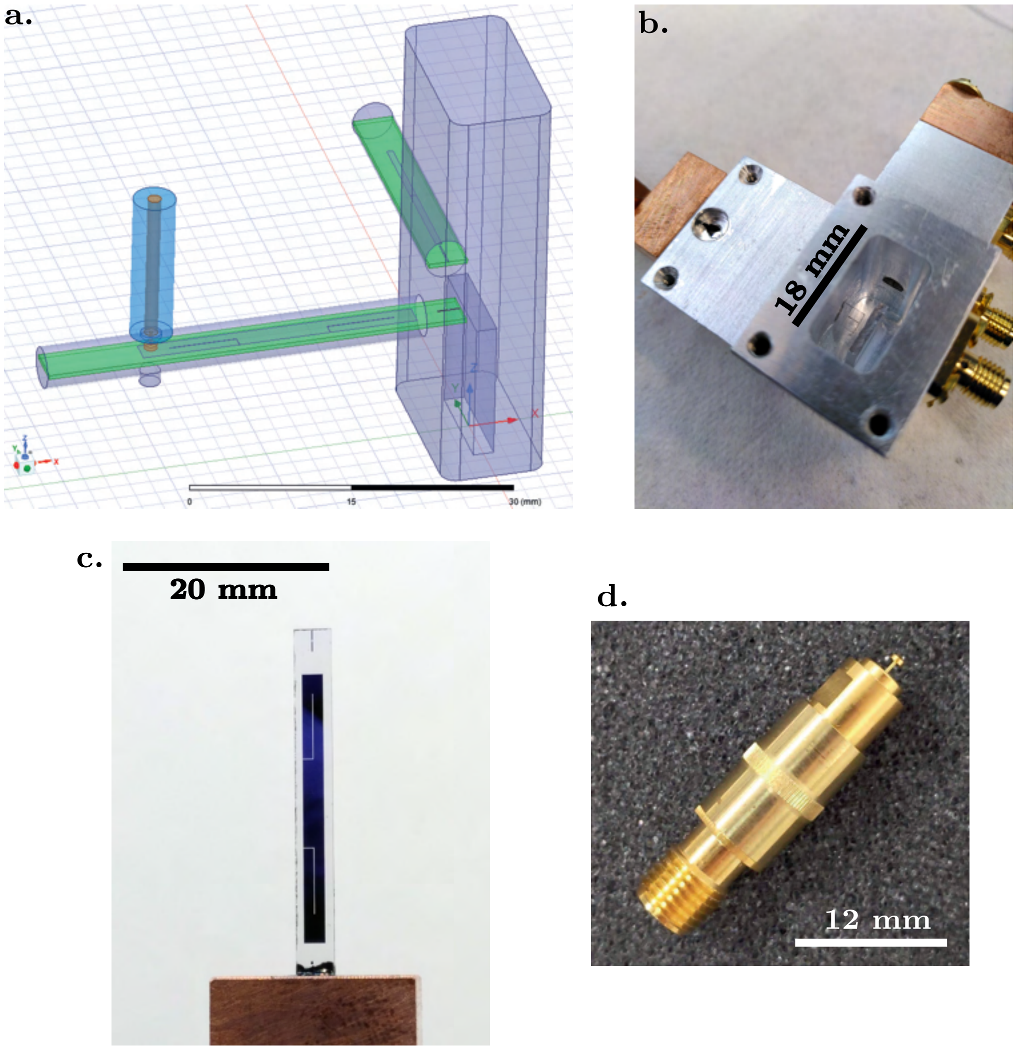

Figure 9.3: Multiplexing photon-counting experiment based on a $\lambda/4$ coaxial cavity. **a.** High-frequency structure simulator (HFSS) simulation of the experiment. The storage mode (first cavity mode) is coupled to two qubits. The multiplexing qubit (left arm) is capacitively coupled to both a microstrip transmission line containing two $\lambda/4$ stubs (identifiable by their "L" shape) and to a *pogopin*. The yes–no qubit (arm in the back) is coupled to a microstrip resonator and protected by a microstrip Purcell filter. **b.** Picture of the cavity with the multiplexing qubit inside. **c.** Picture of the multiplexing qubit chip. The multiplexing qubit antennas are visible at the top of the chip, while the microstrip transmission line with the $\lambda/4$ stubs can be seen below. **d.** Picture of the pogopin POGO-PIN-19.0-1 (non-magnetic) by EmulationTechnologie. The pin (at the top-right corner) is mounted on a spring, allowing enough pressure between the pin and the microstrip transmission line to create a galvanic contact.

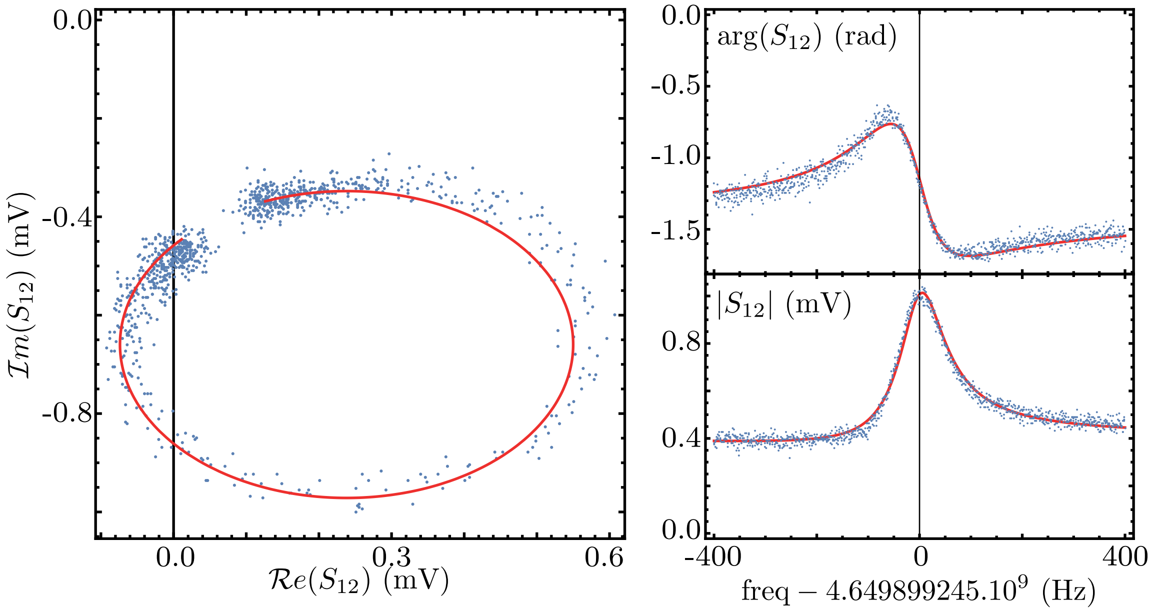

Figure 9.4: Spectroscopy of a coaxial high-Q cavity. Left: measured transmission coefficient in the complex plane (dots) and its fit (red line). Right: Phase and absolute value of the transmission coefficient as a function of the spectroscopy frequency. The absolute value of the transmission coefficient is asymmetric because of a Fano effect [204]. The total Q factor of the resonance is about 52×10^6.

it using Eq. (2.36) and added a parasitic transmission channel characterized by the transmission coefficient t_f, as follows:

$$S_{21}(\omega) = \sqrt{1 - |t_\mathrm{f}|^2}\frac{-2\sqrt{\kappa_1\kappa_2}}{\kappa_\mathrm{tot} - 2i(\omega - \omega_r)} + t_\mathrm{f}. \tag{9.1}$$

We then obtained a total loss rate κ_tot of 90 Hz, corresponding to a total Q factor of about 52×10^6. Using spectroscopy in reflection, we estimated the value of the coupling rates κ_1 and κ_2 to be about 1 Hz, meaning that most of the losses are internal.

When the quality factor is limited by coupling to parasitic two-level systems, a high probe power saturates the two-level systems and the quality factor increases [205]. For the purpose of our experiment, we are interested in the quality factor in the single photon regime (i. e. at a probe power low enough that we can consider the cavity to contain only one photon). We estimate that the probe power after attenuation is about −115 dBm, leading to a cavity mean photon number of 2000. In Ref. [206], the authors show that the critical photon number (i. e. the number of photons we need to add to see a modification of the quality factor) is about 1100 for a 3D cavity. Thus, the quality factor measured should be closed to the single photon quality factor and we will confirm its value with another independent measurement.

The second step was to characterize the cavity/yes–no qubit system. We obtained a desirable cross-Kerr rate between the yes–no qubit and the cavity mode of 0.8 MHz. The yes–no qubit lifetime is 38 µs and its coherence lifetime is 2.5 µs. We believe that the coherence lifetime is limited due to the poor thermalization of the dilution fridge lines. The storage lifetime is measured by probing the time evolution of the zero photon

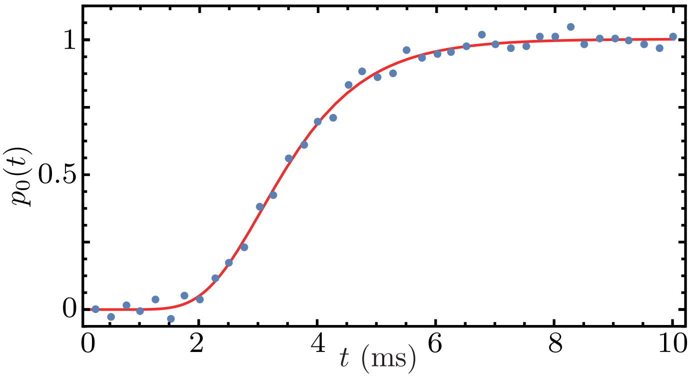

Figure 9.5: Time evolution of the probability that the storage mode contains 0 photons after a displacement. The probability is measured using a π-pulse that is resonant with the yes–no qubit only if the cavity contains 0 photons. The red line is a fit of the measured probabilities (the blue points) using the expression $p_0(t) = \exp(-n_0 \exp(-t/T_{1,\mathrm{cav}}))$, with $n_0 = 24$ being the mean photon number after the displacement and $T_{1,\mathrm{cav}} = 0.96\,\mathrm{ms}$ the lifetime of the cavity.

probability after a displacement of the cavity (see Fig. 9.5); by doing so, we obtain a cavity lifetime of 0.96 ms, corresponding to a quality factor of 25×10^6.

The last part we had to characterize was the multiplexing qubit/cavity system. As of the date of this writing, we were not able to observe the fluorescence of the multiplexing qubit. We have identified two main reasons for this. First, it took us several cool downs before we could obtain a multiplexing qubit with the targeted frequency (up to 200 MHz). Second, the length of the pogopin was too short during the first cool downs, leading to a multiplexing qubit with a lifetime that was 20 times higher than the one targeted (we have recently corrected this).

From the point of view of the cavity mode, the highest lifetime measured with the multiplexing qubit was about 70 µs. In order to investigate this short lifetime, we probed the microstrip transmission line/stubs/pogopin/TWPA transmission coefficient, as shown in Fig. 9.6. The ratio of the transmission coefficient at the targeted multiplexing qubit frequency (5.7 GHz) and at the cavity frequency (targeted 4.54 GHz, measured 4.585 GHz) is about 45 dB. Thus, the Purcell decay of the storage mode when there is no stubs should be divided by at least 10000 due the presence of the stubs. For the multiplexing qubit frequency targeted and the cavity multiplexing qubit cross-Kerr rate targeted (6.3 MHz), the Purcell effect should limit the cavity lifetime to 5 µs without stubs (see Eq. (3.20)); thus, with the stub filter, the cavity lifetime should be limited by the Purcell effect to more than 50 ms. We therefore conclude that the low lifetime measured for the cavity is not due to an error in the stubs' design and that we will need to investigate the situation further if we are to understand it.

9.3 PERSPECTIVES

To conclude this manuscript, we would like to offer some perspectives for the future of multiplexing photon number measurement.

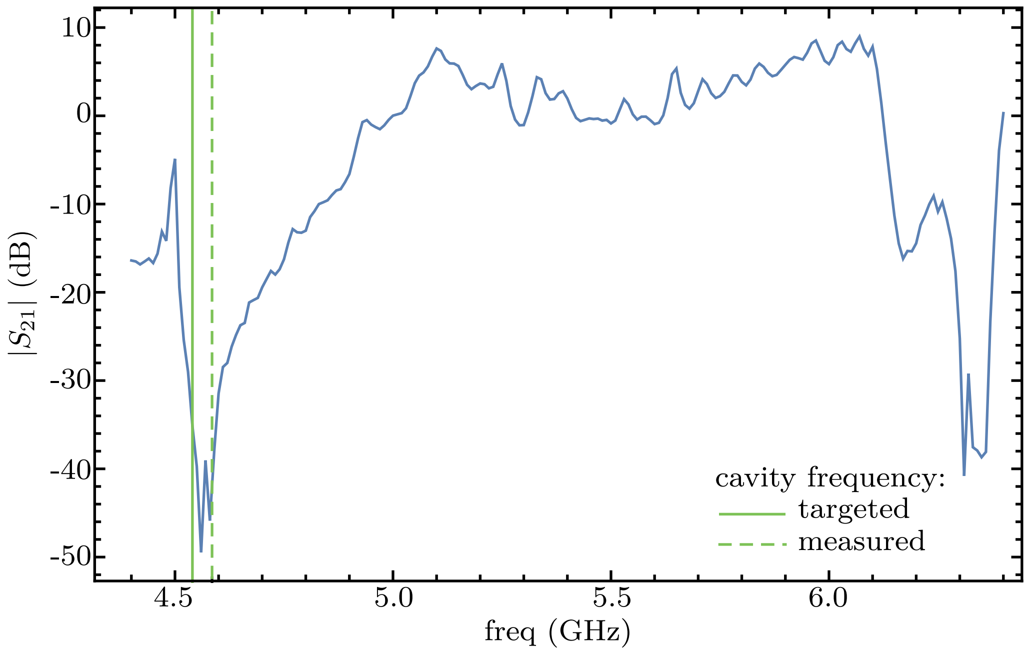

Figure 9.6: Measured transmission coefficient of the microstrip transmission line with the stubs, the pogopin, and the TWPA. The measurement was performed by inserting an antenna inside the cavity trough the cavity cap. The transmission amplitude is measure between this antenna and the pogopin port. The features above 6 GHz are the TWPA gap. The targeted and measured cavity resonant frequencies are close to the stub frequency. Compared to the multiplexing qubit frequency (targeted 5.7 GHz), the stubs offer a protection of about 45 dB.

9.3.1 *After the single-shot measurement*

Our continuous measurement opens new possibilities in terms of feedback control of the quantum state of a cavity. It can readily be applied to stabilize quantum states by feedback control [40, 207], probe quantum trajectories of microwave modes [7], observe quantum Zeno dynamics [208], or engineer desired decoherence channels by varying in time the amplitude of the probe tones. This measurement scheme enables the future implementation of a large class of measurement operators that would be useful to stabilize bosonic codes [209], to stabilize a Fock state parity by autonomous feedback [189], or to extend the reach of simultaneous probing of a single quantum system by multiple observers [210, 163] to larger systems and arbitrarily many observers. Our photocounter for stationnary modes can also be converted into a photocounter for propagating modes using a catch and count protocol [27]. Moving further, one could extend this frequency domain measurement to more complex probes than a single qubit and many possible physical systems beyond superconducting circuits.

9.3.2 *Going further with the pogopin*

The galvanic coupling that was created thanks to the pogopin gave us the idea of studying whether we could use the pogopin to create a fast-flux line for a frequency-

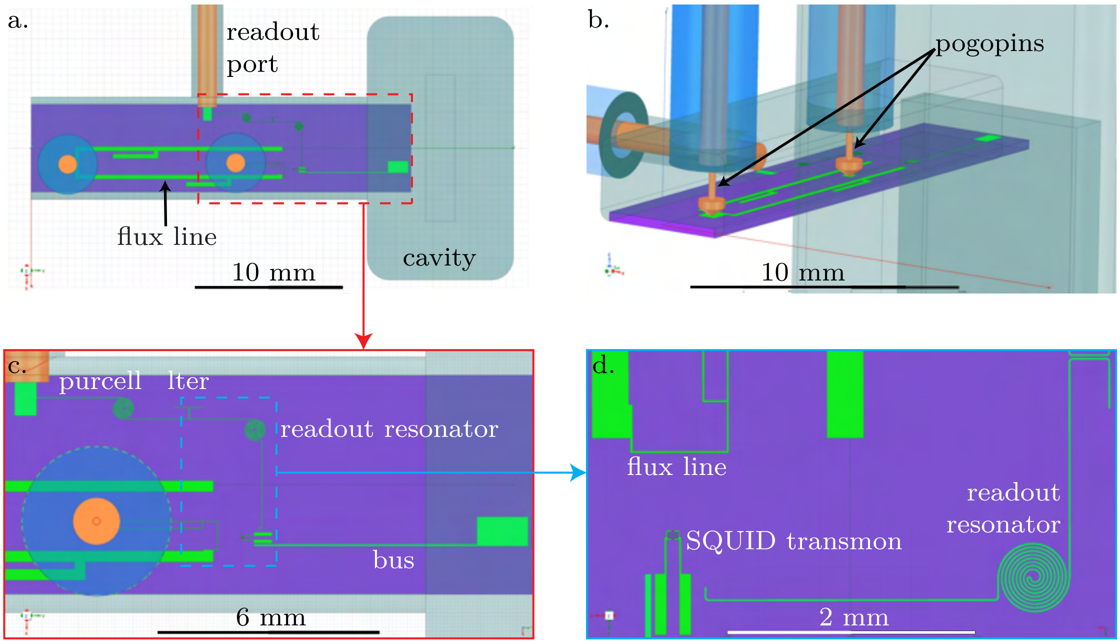

Figure 9.7: Design of a SQUID transmon coupled to a superconducting cavity and a DC current line or flux line. The flux line allows the SQUID transmon frequency to be controlled. **a. and b.** The flux line is galvanically connected to two pogopins, and a readout port is used to read out the qubit state. The superconducting cavity is a $\lambda/4$ coaxial cavity. **c. and d.** Zoom-in on the SQUID transmon. A readout resonator is used to read out the qubit state, and the qubit is protected by a Purcell filter. The filter and the readout resonator are *snail* resonators (inspired by [108]), and a bus is used to mediate the interaction between the qubit and the cavity.

tunable qubit in a superconducting cavity. A superconducting quantum interference device (SQUID) transmon qubit is a transmon qubit in which the single Josephson junction is replaced by two Josephson junctions, forming a loop [20]. The magnetic flux through the loop allows the frequency of the qubit to be controlled. How to control the flux of a frequency-tunable qubit in a superconducting cavity is still an open challenge. The main difficulty comes from the fact that the superconducting cavity screens any external magnetic field. The current approach consists in replacing a part of the superconducting cavity with either vacuum [211], a non-superconducting metal such as copper [212] or a magnetic hose that can be used to guide the magnetic field inside the cavity [213]. Here, we propose to use the pogopin to create an interface between a coaxial DC transmission line and a microstrip DC transmission line, using the microstrip transmission line (or flux line) to control the magnetic flux inside the SQUID transmon loop.

The circuit we propose to use is represented in Fig. 9.7. The superconducting cavity is a $\lambda/4$ coaxial cavity of the same design as the one used for the 3D version of the multiplexing photon-counting experiment. It is dispersively coupled to a SQUID transmon, with the coupling being mediated by a *bus* (see Fig. 9.7a and c). In the DC regime, the SQUID transmon is coupled to a flux line, which allows us to control the flux in the SQUID loop. The flux line is galvanically connected to two pogopins, which allow us to bring a DC current inside the cavity (see Fig. 9.7b, c, and d). The flux line contains three stub filters, which act as a $\lambda/4$ resonator, in order to protect the cavity from decaying in the flux line. These filters are identifiable by their “L” shape. The SQUID transmon is also dispersively coupled to a readout resonator, whose *snail* shape (inspired by Ref. [108]) permits to decrease its coupling to the flux line (see Fig. 9.7d). A readout port enables us to probe the readout resonator through the Purcell filter that protects the SQUID transmon from Purcell decay (see Fig. 9.7a and c).

The goal of this experiment has been to demonstrate the following points:

- the control of the flux inside the SQUID transmon loop
- the long lifetime and coherence time of the SQUID transmon
- the long lifetime of the cavity mode
- the ability to perform a fast-flux gate on the SQUID transmon
- the ability to deterministically prepare the cavity mode in non-classical states (such as Fock or cat states).

Part IV

APPENDIX

a

JOSEPHSON JUNCTION FABRICATION PROCESS

The JJs are fabricated using a Dolan bridge technique [214] that is based on shadow evaporation. The wafer/chip is recovered using a bi-layer resist polymethylglutarimide (PMGI) and PMMA mask (with the PMMA on top of the PMGI). An electrical lithography is performed using a *scanning electron microscope* (SEM) enabling a sub-10 nm resolution to be reached. A layer of 10 nm of aluminum is added on top of the PMMA in order to avoid charge accumulation during the electrical lithography. We first develop the PMMA, which is electron-sensitive, and then the PMGI, which is not electron-sensitive. Thus, everywhere the PMMA has been removed, the PMGI is as well, causing an undercut to appear below the PMMA. The goal of this lithography is to create a bridge. Fig. a.1a shows the typical pattern exposed during the electrical lithography and two horizontal cuts, one of which shows the bridge obtained following the PMMA and PMGI development (Fig. a.1b).

Two aluminum evaporations are then performed using a Plassys®evaporator with angles at 30° and 0° along the vertical green dashed line in Fig. a.1a, separated by a control oxidation. Fig. a.1c shows a cut along the evaporation line, while Fig. a.1d shows the resulting aluminum pattern following the evaporations. An Al/$\mathrm{AlO_x}$/Al JJ, as indicated by the red boxes in Figs. a.1c and d, is created. Its area is given by the two "finger-width " w_1 and w_2 (see Fig. a.1a), while the thickness of the oxide barrier is controlled by the oxidation parameters (pressure and duration).

A SEM image of a JJ is shown in Fig. a.2a. We observe that, due to the large size of the transmon antennas required by the cavity multiplexed photocounting experiment, the JJ is very sensitive to electrical discharge (see Fig. a.2b and c). To protect the JJ against such discharges, we electrically connect the two antennas together with a 15 µm-wide aluminum line, which is evaporated at the same time as the JJ. This is equivalent to shorting the JJ. The shorting line protects the junction during both the lift-off and the first manipulation of the chip. Once the chip is ready to be introduced into the cavity and only the resistance of the junction needs to be measured (see the next section), we cut the shorting line using the needle of a probe station while keeping the JJ under an ionized air flow that is generated by an air ionizer fan. The ionized air flow evacuates any charge that has started to accumulate on the transmon antennas, thus protecting the JJ against electrical discharge. We keep the JJ under the ionized air flow until the chip is mounted in the cavity.

The protocol for the fabrication of the JJ is as follows.

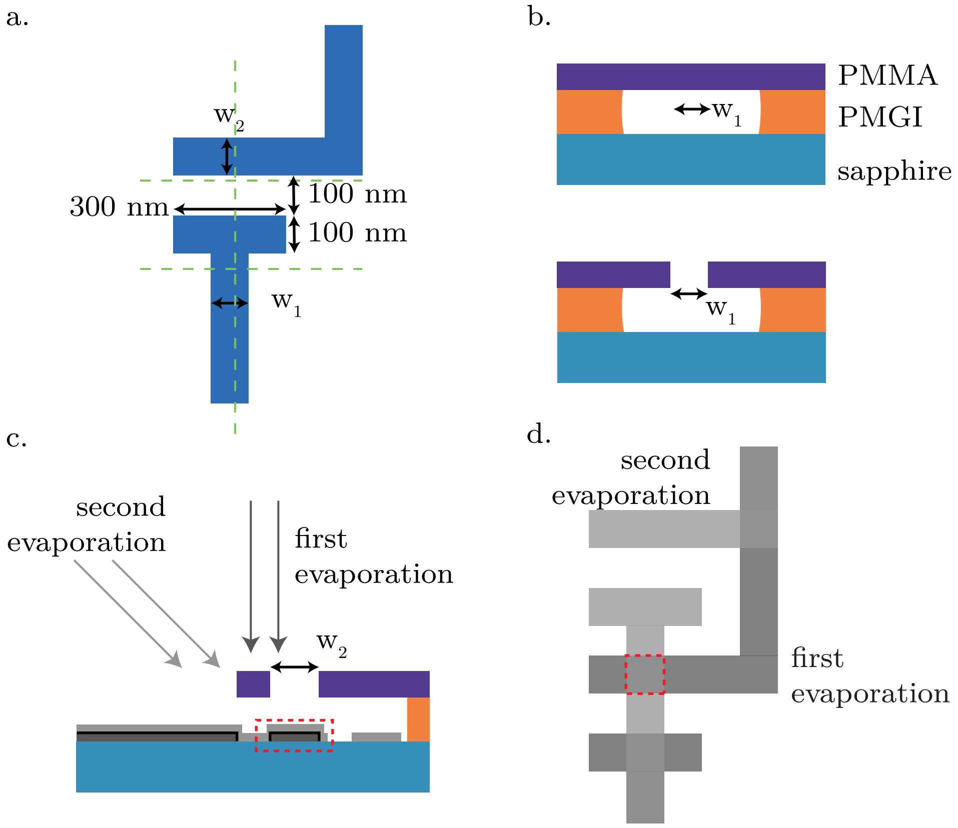

Figure a.1: Junction fabrication through shadow evaporation using a Dolan bridge. **a.** Pattern exposed during the electrical lithography. The finger-width w_1 and w_2 determine the future JJ area. **b.** A cut along the two horizontal axes, indicated by a green dashed line in **a**. Top: cut showing the Dolan bridge made of PMMA. Bottom: cut showing the undercut of the PMGI, below the PMMA. **c.** Cut along the axes, as indicated by the vertical dashed line in **a**. Two aluminum evaporation (grey) layers with different angles are performed and separated through a control oxidation step, generating an oxide layer (black line). We obtain a JJ in which the two types of evaporation are superposed (red dashed box). **d.** Aluminum pattern after the two evaporations. The JJ is indicated by the red dashed box.

A.0.0.1 *Cleaning*

The cleaning step contains two sub-processes: a toluene-methanol-acetone-IPA (TAMI) cleaning and a piranha cleaning. **Remarks:** Toluene and methanol are toxic solvents and piranha is a powerful acid. All must, therefore, be used with caution.

- Clean with toluene in a sonicator for 5 min
- Clean with methanol in a sonicator for 5 min
- Clean with acetone in a sonicator for 5 min
- Clean with IPA in a sonicator for 5 min
- Blow dry with nitrogen

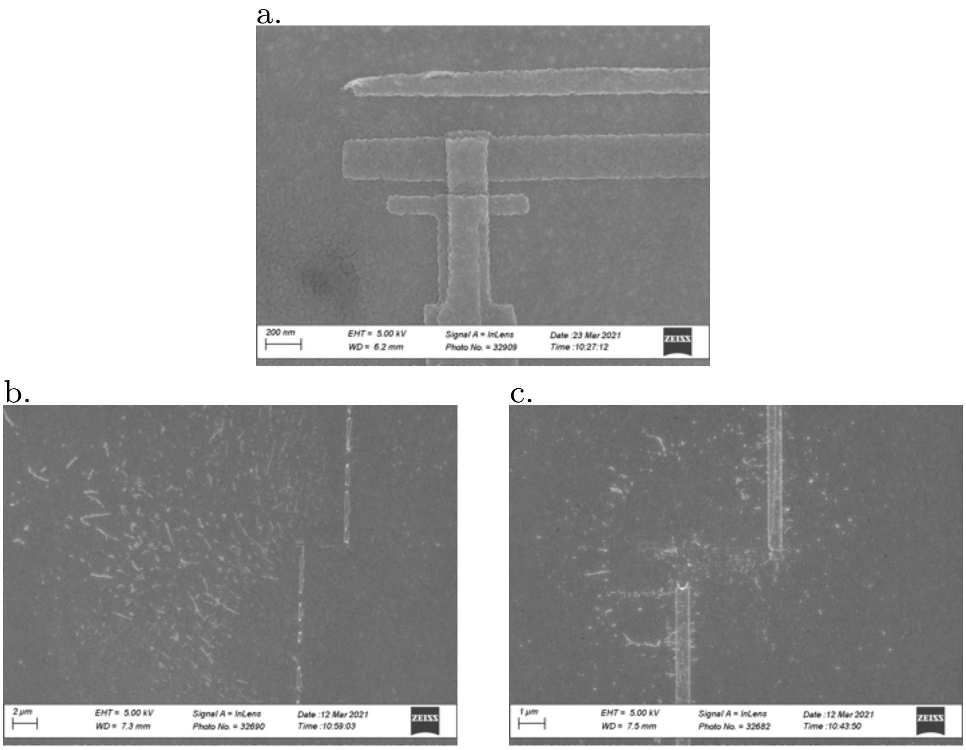

Figure a.2: SEM pictures of a JJ. **a.** Regular JJ; the image shows the overlap between the two evaporations that defines the junction. **b. and c.** JJ after an electrical discharge.

- Clean with piranha solution for 5 min (do not agitate)
- Rinse with DI water
- Blow dry with nitrogen

A.0.0.2 *Resist spin coat*

- Rinse with DI water
- Blow dry with nitrogen
- Heat at 200 °C for 5 min
- Let the wafer/chip cool down for 1 min
- Re-cover entirely with PMGI resist and spin coat:
  - 500 rpm 5 s (500 rpm/s)
  - 2000 rpm 55 s (4000 rpm/s)
- Heat at 200 °C for 5 min
- Let the wafer/chip cool down for 1 min
- Re-cover entirely with PMMA resist and spin coat:

  - 500 rpm 5 s (500 rpm/s)
  - 4000 rpm 55 s (4000 rpm/s)
- Heat at 180 °C for 15 min
- Let the wafer/chip cool down for 1 min
- Evaporate 10nm of aluminum on top of the PMMA:
  - angle = 0°
  - rate = 0.3 nm/s

A.0.0.3 *Electrical lithography*

The electrical lithography is performed using a SEM. The relevant parameters of the lithography are as follows:

- Tension 30 keV
- Working distance 7 mm
- Aperture 7.5 µm
- Dose 380 µC μm^{-1}

The development of the electrical lithography is achieved using the following protocol. The MIBK/IPA solution only develops the PMMA resist, while the MF319 only develops the PMGI resist.

- Soak the wafer/chip in a potassium hydroxide (KOH) solution (2% in mass) for 1 min to remove the aluminum on top of the PMMA
- Rinse with DI water for 20 s
- Blow dry with nitrogen
- Stir in the MIBK/IPA (1:3 in volume) for 60 s
- Rinse in DI water for 20 s
- Blow dry with nitrogen
- Stir in the MF319 for 35 s (for a 4 mm x 30 mm chip) or 60 s (for a 2-inch wafer)
- Rinse in IPA for 20 s
- Blow dry with nitrogen

A.0.0.4 *Evaporation*

The evaporation is performed using a Plassys evaporator, as follows:

- Insert the sample in the evaporator
- Pump the chamber at least overnight, so that it reaches a pressure below 1×10^{-7} mbar
- Perform ion milling for 30 s (400 V, 22 mA, Ar, tilt = 0°)
- Perform ion milling for 30 s (400 V, 22 mA, Ar, tilt = 30°)
- Protect the sample with a shutter
- Evaporate the titanium to decrease the O_2 pressure:
  - rate 0.2 nm/s
  - duration 2 min
- Remove the shutter
- Evaporate the aluminum:
  - rate 0.5 nm/s
  - thickness 20 nm
  - tilt 0°
- Perform static oxidation:
  - duration 25 min
  - pressure P_{O_2} for a few (0.5 to 10) mbar
- Evaporate the aluminum:
  - rate 0.5 nm/s
  - thickness 40 nm
  - tilt 30°
- Perform static oxidation:
  - duration 10 min
  - pressure 10 mbar.

A.0.0.5 *Lift off*

- Remove the resist with NMP in the sonicator for 1 h at 60 °C
- Rinse with IPA
- Blow dry with nitrogen

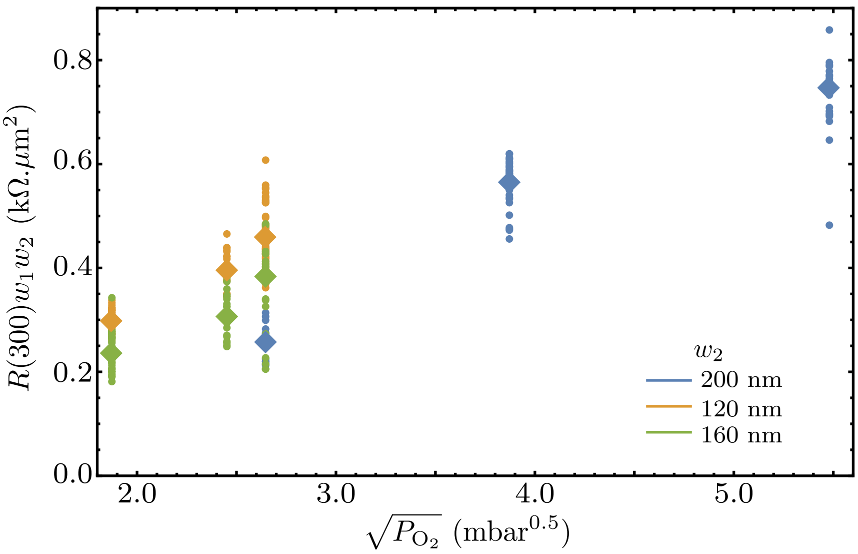

Figure a.3: Resistance of the JJ at 300 K, times the finger widths $R(300)w_1w_2$, as a function of the square root of the oxidation pressure $\sqrt{P_{O_2}}$. We observe that $R(300)$ depends almost linearly on w_1 w_2 and $\sqrt{P_{O_2}}$. The diamond corresponds to the median of $R(300)w_1w_2$ for values of w_2 and P_{O_2}.

A.1 JUNCTION RESISTANCE

The Josephson energy E_J of the junction can be deduced by measuring the normal resistance of the junction. The Ambegaokar–Baratoff relationship links the normal-state resistance of a junction at zero temperature $R(0)$ to the critical current of the junction $I_0 = E_J/\varphi_0$, as follows:

$$R(0) = \frac{\pi\Delta}{2eI_0} = \frac{\pi\Delta\varphi_0}{2eE_J}, \tag{a.1}$$

where $\Delta \sim 180\,\mu\text{eV}$ is the aluminum superconducting gap. The resistance of the junction $R(300)$ is measured at 300 K, and we estimate that $R(0)$ is $15-20\%$ smaller.

The resistance $R(300)$ should be proportional to $1/w_1$, $1/w_2$ and almost proportional to $\sqrt{P_{O_2}}$ [215]. Fig. a.3 shows the resistance of 270 junctions made with a width w_1 from 100 nm to 200 nm, a width w_2 equal to 120 nm, 160 nm or 200 nm, and pressure P_{O_2} equal to $\{3.5, 5.8, 6, 7, 15, 30\}$ mbar. This shows how $R(300)w_1w_2$ depends on $\sqrt{P_{O_2}}$. We obtain a close-to-linear relationship. Assuming that the linear relationship is exact, we compute the value of P_{O_2}, which we will use during the evaporation process in order to reach the targeted resistance $R(300)$, working always with the same finger widths.

b

MEASUREMENT SETUP

B.1 TWPA CHARACTERIZATION

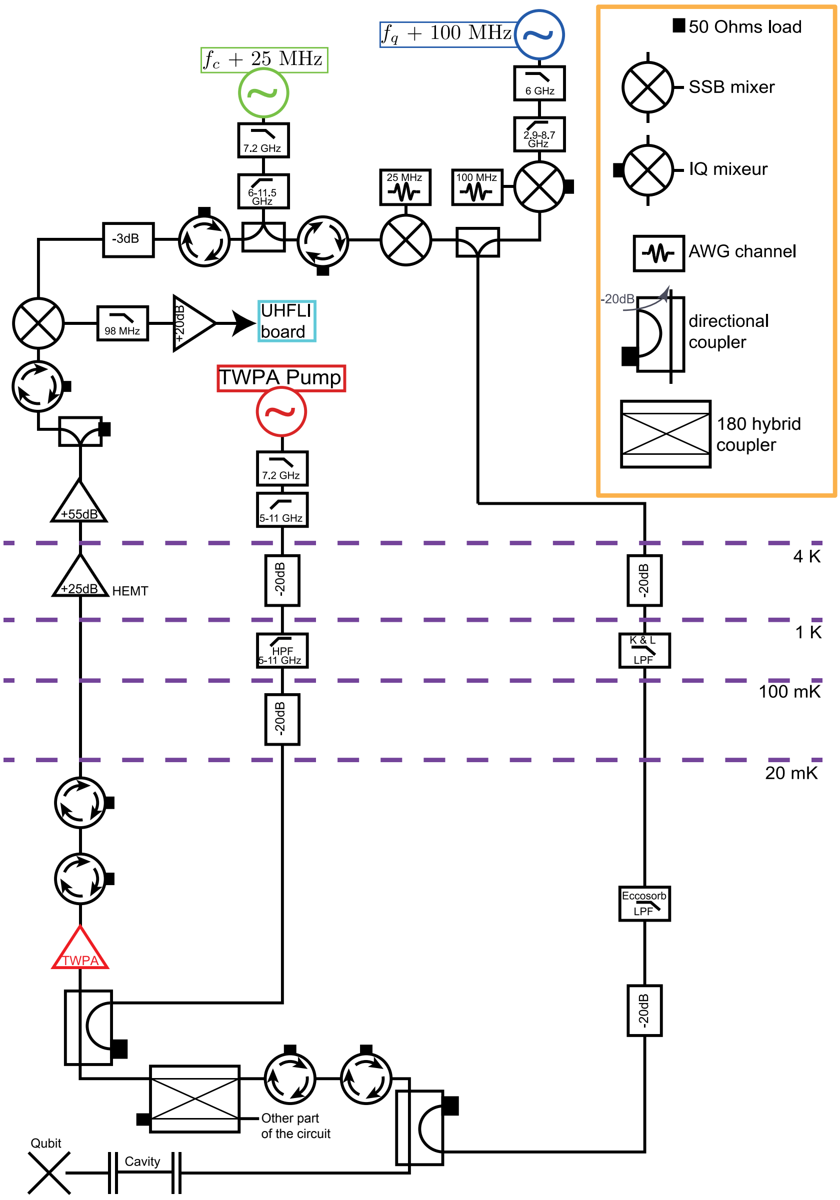

Figure b.1: Cabling for the Josephson travelling wave parametric amplifier characterization.

B.2 PHOTOCOUNTING EXPERIMENTS

The readout resonator, the yes-no qubit and the multiplexing qubit are driven by pulses that are generated using a Tektronix® Arbitrary Waveform Generator (AWG) AWG5014C with a sample rate of 1 GS/s. Storage mode pulses are generated using a Zurich Instruments® UHFLI with a sample rate of 1.8 GS/s. The UHFLI allows us to change the pulse amplitude and phase without recompiling the sequence. This feature decreases the time needed for Wigner tomography compared to a standard AWG and makes the pulse sequence simple with the drawback of having to synchronize the two AWGs. AWG pulses are modulated at a frequency 25 MHz for readout, 100 MHz for yes-no qubit, and 75 MHz for storage and multiplexing qubit. They are up-converted using single sideband mixers for readout resonator and multiplexing qubit and regular mixers for the storage resonator and yes-no qubit, with continuous microwave tones produced respectively by AnaPico® APSIN12G, Agilent® E8257D, WindFreak® SynthHD, and AnaPico® APSIN20G sources that are set at the frequencies $f_{\mathrm{ro}} + 25$ MHz, $f_{\mathrm{mp}} + 75$ MHz, $f_{\mathrm{s}} + 75$ MHz and $f_{\mathrm{yn}} + 100$ MHz.

The two reflected signals from the readout and multiplexing qubit are combined with a diplexer and then amplified with a Travelling Wave Parametric Amplifier (TWPA) provided by Lincoln Labs. We tuned the pump frequency ($f_{\mathrm{TWPA}} = 5.998$ GHz) and power in order to reach a gain of 20.7 dB at 7.138 GHz and 18.2 dB at 4.238 GHz. The quantum efficiency of the yes-no readout signal was measured to be $18.7 \pm 0.4\%$, and should be close to the efficiency η of the multiplexing detection. We estimate that this efficiency is the product of the efficiency of the microwave components before the TWPA (25 to 60%), the efficiency of the TWPA itself (33% to 83%) and the (90 to 95%) efficiency coming from what is above the HEMT amplifier. The follow-up amplification is performed by a High Electron Mobility Transistor (HEMT) amplifier from Low Noise Factory (LNF®) at 4 K and by two room temperature amplifiers. The two signals are down-converted using image reject mixers before digitization by an Alazar® acquisition board and numerical demodulation. Actually for the multiplexed signal, nine demodulation operations are performed at each of the down-converted frequencies 75 MHz $+ k\chi_{\mathrm{s,mp}}$ for $0 \leq k \leq 8$. The full setup is shown in Fig. b.2. The Tektronix® AWG is used as the master that triggers the UHFLI and the Alazar® board.

The frequency comb that is used for the multiplexing measurement is generated and demodulated using the following method. Nine cosine functions at frequencies $\{75\ \mathrm{MHz} + k\chi_{\mathrm{s,mp}}\}_{0\leq k\leq 8}$ are summed and multiplied by a Gaussian envelop numerically with a sampling rate of 1 GHz/s over the duration of the pulse. A waveform is then generated by the AWG following this list of values. This method ensures a good phase coherence between all the comb frequencies. The AWG output is up-converted using a single side band mixer whose LO port is driven at frequency $f_{\mathrm{mp}} + 75$ MHz.

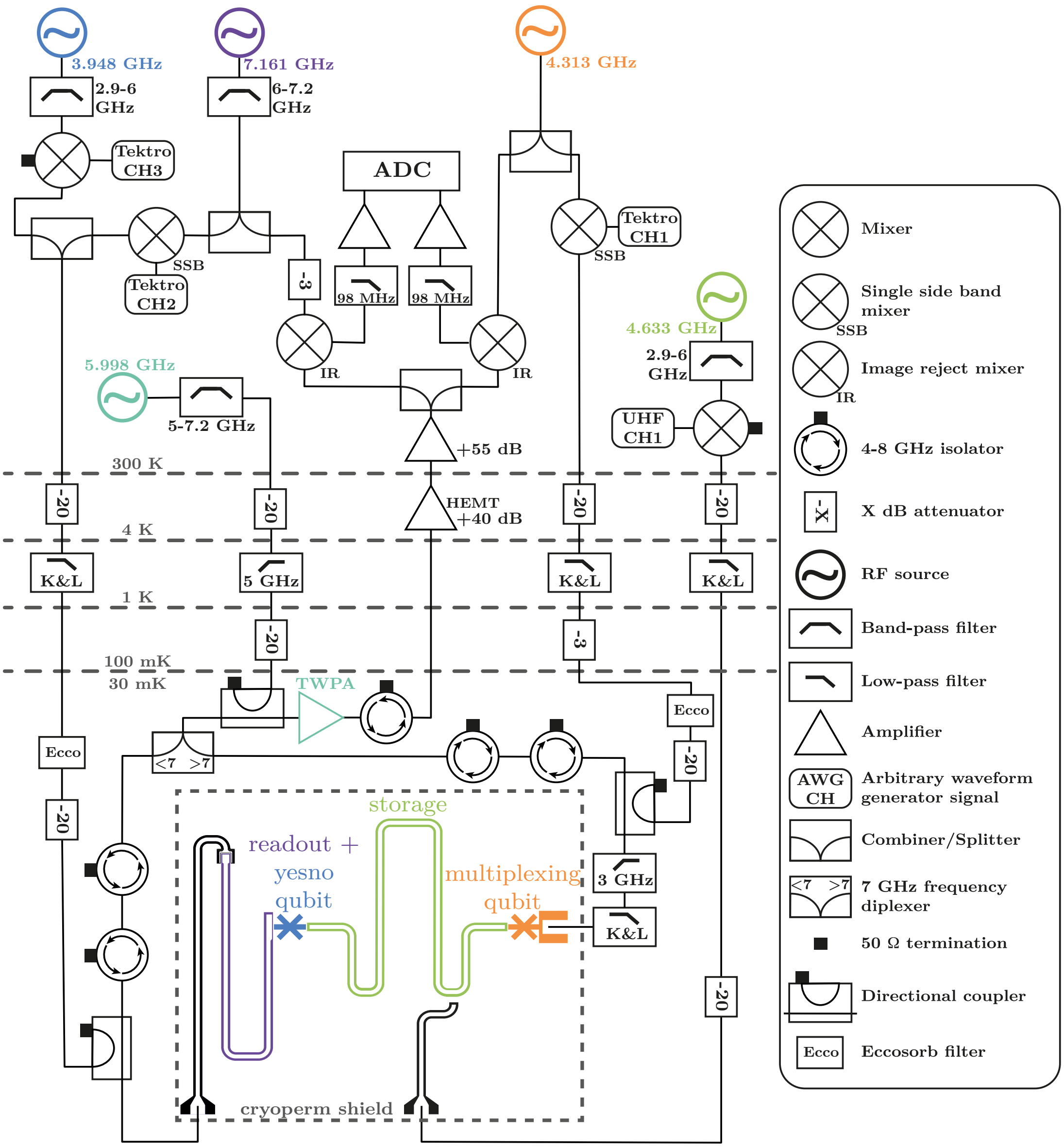

Figure b.2: **Schematic of the setup.** Each electromagnetic mode of the experiment is driven by a RF generator detuned by the modulation frequency and whose color matches the color of the corresponding mode in Fig. 5.1. Room temperature isolators are not represented for the sake of clarity.

C

WIGNER TOMOGRAPHY AND DENSITY MATRIX RECONSTRUCTION

The Wigner tomography is the tomography process that is most often used with a harmonic oscillator, giving access to the Wigner function or Wigner quasiprobability distribution of the quantum state. This appendix will define the Wigner tomography and the experimental processes used to measure and calibrate it. It will then discuss the Wigner–Weyl transformations, where we will see that the Wigner tomography is simply the Wigner transformation of the density matrix and, reciprocally, that the density matrix is the Weyl transformation of the Wigner function. We will also see that the Weyl transformation is not straightforward to apply, as well as determining the different approaches we can use to reconstruct the density matrix from the Wigner function. One of these approaches is based on the Wigner map, which allows the mean value of any observable to be measured using the Wigner function. When using this approach, therefore, the computation is directly performed in the Wigner function phase space, instead of through the use of the density matrix.

In this appendix, we will use the hat notation with the quantum operator to distinguish the classical coordinates x and p of the phase space from the quantum Hermitian operators $\hat{x}$ and $\hat{p}$, thereby defining $\hat{a} = \hat{x} + i\hat{p}$. We also introduce the quadrature $\hat{x}_\theta = \cos(\theta)\hat{x} + i\sin(\theta)\hat{p}$ so that $\hat{x}_{\pi/2} = \hat{p}$.

C.1 THE WIGNER TOMOGRAPHY

C.1.1 *Definition*

The Wigner tomography is a process leading to the measurement of the Wigner function. The Wigner function of a harmonic oscillator with the density matrix ρ is defined as $W(\alpha) = \frac{2}{\pi}\mathrm{Tr}(\hat{D}^\dagger(\alpha)\rho\hat{D}(\alpha)\hat{\mathcal{P}})$, where $\hat{D}(\alpha) = e^{\alpha\hat{a}^\dagger - \alpha^*\hat{a}}$ is the displacement operator of the harmonic mode by the coherent field α, and $\hat{\mathcal{P}} = e^{i\pi\hat{a}^\dagger\hat{a}}$ is the photon number parity operator. A Wigner function is thus the expectation value of the photon number parity operator after displacement by the amplitude $-\alpha$.

The Wigner function is a quasiprobability distribution as, once it is integrated along the quadrature $\hat{x}_{\theta+\pi/2}$ direction, it leads to the probability distribution of the $\hat{x}_\theta$ quadrature of the field. It is the unique quasiprobability distribution that exhibits this simple property [7]. Compared to classical quasiprobability distributions (which are always positive) the Wigner quasiprobability distribution can be negative; this negativity is the sign of a "non classical" quantum state. For example, the Wigner function of a coherent state, a thermal state, and a squeezed state are all positive Gaussian functions. Those states are considered as "classical", as we can generate them using a classical source of light. In comparison, the Wigner function of the Fock state $|1\rangle$ contains a

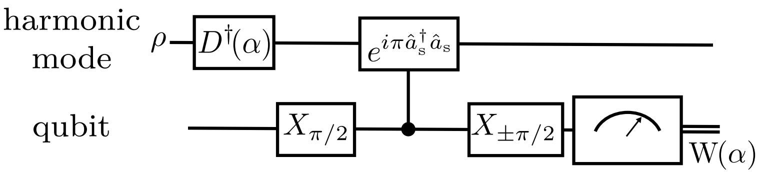

Figure c.1: A circuit diagram of a direct Wigner tomography using a parity measurement based on dispersive interaction. After a displacement pulse on the harmonic mode, an unconditional $\pi/2$ pulse is applied to the qubit. The qubit evolves freely during the time $\Delta\tau = \pi/\chi$, before a new $\pm\pi/2$ pulse is sent and its state is read out.

negativity; this is expected, as we need a quantum source of light in order to generate a single photon. The Wigner tomography is a powerful tool with which to study the quantum state, as an equivalence exists between the Wigner function and the density matrix.

C.1.2 *Pulse sequence*

There are various ways to measure a Wigner function [7]; however, most of these are not direct measurements. In circuit QED, we usually use a technique that was proposed by Lutterbach and Davidovich in 1997[1] [32, 180, 181] which enables the direct measurement of the Wigner function. The Lutterbach and Davidovich proposal is based on the measurement of the parity operator, which is made possible thanks to the dispersive coupling χ shared between the harmonic mode and a qubit. We will discuss the implementation of this measurement in Sec.c.1.3.

The Wigner tomography sequence is represented in Fig. c.1. It starts by performing a displacement on the harmonic mode, following which two successive $\pi/2$ pulses are applied to the qubit, separated by the waiting time $\Delta\tau = \pi/\chi$. The sequence thus implements a parity measurement and maps the parity of the harmonic mode onto the z-axis on the qubit. It is then terminated by a readout of the qubit state.

C.1.2.1 *Pulse characteristics*

The pulses of the Wigner tomography sequence have to comply with some constraints. Due to the dispersive coupling, the harmonic mode inherits some self-Kerr rate. Thus, the displacement must be achieved in an amount of time that is shorter than the inverse of the self-Kerr rate, otherwise the harmonic mode will not be displaced by a coherent state but instead by a squeezed state. The $\pi/2$ pulses applied to the qubit must be independent of the photon number of the harmonic mode. To do so, the duration of these pulses has to be much shorter than the inverse cross-Kerr rate χ between the harmonic mode and the qubit. In this thesis, the displacement pulses are Gaussian pulses of 100 ns, with a width of 25 ns, while the $\pi/2$ pulse is a Gaussian pulse of 18 ns, with a width of 4.5 ns.

Depending on the system, the readout of the qubit state can be achieved using a dedicated readout resonator or by using the same harmonic mode as the one studied.

---

[1] This technique was initially proposed for use in cavity QED.

In the first case, as the readout resonator is dispersively coupled to the qubit, there exists a parasitic cross-Kerr rate between the harmonic mode and the readout mode. Thus, the heterodyne detection of the readout field contains an offset that depends on the harmonic mode state. The Q quadrature of the readout reads as

$$Q_{\pi/2} = p_g Q_g + p_e Q_e + Q_\rho, \tag{c.1}$$

where $p_{g/e}$ is the qubit probability in the state $|g\rangle \,/\, |e\rangle$, $Q_{g/e}$ is the value of the record for the qubit state $|g\rangle \,/\, |e\rangle$, and Q_ρ the offset that depends on the harmonic mode state[2]. The easiest way to remove this offset is to perform the experiment a second time, replacing the second $\pi/2$ pulse with a $-\pi/2$ pulse. Thus, the Q quadrature reads

$$Q_{-\pi/2} = p_e Q_g + p_g Q_e + Q_\rho, \tag{c.2}$$

where $p_{g/e}$ are the same weight as the one in Eq. (c.1). The difference between the two records is independent of the harmonic mode state, as follows

$$Q_{\pi/2} - Q_{-\pi/2} = (p_g - p_e)(Q_g - Q_e). \tag{c.3}$$

This technique is even more powerful as it enables us to remove any offset in the Wigner tomography. Calibrating the Q_g and Q_e quadratures using the amplitude of the qubit's Rabi oscillation, the Wigner function reads

$$W(\alpha) = \frac{\pi}{2}\frac{Q_{\pi/2} - Q_{-\pi/2}}{Q_g - Q_e}. \tag{c.4}$$

If the readout is performed in the same harmonic mode, we have to wait until the latter relaxes to its ground state before performing a readout, otherwise the readout will be strongly modified by the existing harmonic mode field. Even so, it is recommended that the experiment be performed a second time, this time with a $-\pi/2$ pulse, in order to remove any offset.

C.1.2.2 *Noise and averaging*

A Wigner tomography is a measurement that can take from minutes to hours to be performed. During the measurement process, the setup can be sensitive to the amplifier phase and gain drift, as well as to temperature drift and qubit parameter drift (such as frequency drift or relaxation and dephasing-rate drift). A Wigner function is measured pixel by pixel, thus the harmonic mode quadrature phase space is meshed. We then have two choices: either average the measurement of one pixel before moving on to the next one, or measure each pixel of the mesh once only and repeat this mesh measurement in order to obtain the average. The first approach is highly sensitive to low-frequency noise and drifts. The averaging of one pixel measurement is long enough such that the low-frequency noise and the system drifts have different amplitude when measuring the next pixel. Thus, each pixel are measured with different setup and system parameters

---

[2] Q_g and Q_e are modified for higher photon numbers, and the contrast $Q_g - Q_e$ decreases with photon numbers. We can counter this effect either by correcting the readout frequency or by flushing the harmonic mode before the readout.

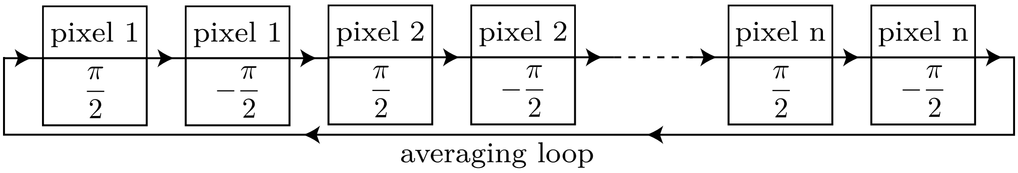

Figure c.2: Wigner tomography averaging. Each pixel of the Wigner function is measured twice (once with the $\pi/2$ pulse sequence and once with the $-\pi/2$ pulse sequence) before moving to the next pixel. Once all the pixels have been measured, we repeat the sequence to obtain the average.

and the Wigner function is distorted. In the second approach, the Wigner tomography is insensible to low-frequency noise or drift, at the expense of being more sensitive to noise or drift that is of a frequency equal to the mesh measurement's repetition frequency. As the mesh measurement can be obtained in a few seconds, which corresponds with frequencies that have relatively low noise and drifts, using the second approach is advised. For the same reason, it is recommended to interleave sequences that have $\pi/2$ pulses with sequences that have $-\pi/2$ pulses. The interleaved sequences, together with their mesh averaging, are represented in Fig. c.2.

C.1.3 *Parity measurement*

The duration $\Delta\tau$ can be calibrated using qubit state revival during Ramsey interferometry (see supplementary material of Ref. [208]). The Ramsey interferometry sequence is represented on Fig. c.3a. The only difference compared to a usual Ramsey interferometry sequence is that the harmonic mode starts in a coherent state instead of the vacuum. Due to the dispersive interaction, revivals happen every multiple of $2\pi/\chi$ which allows us to set $\Delta\tau$ as half of the revival time in Fig. c.3b. Indeed, the qubit acquires a phase $n\chi t$ for each Fock state $|n\rangle$. Thus for large coherent state, the phase of the qubit becomes random, leading to a drop of its coherence, except for specific times equal to $2k\pi\chi$ with k integer for which the phase acquired by the qubit is a multiple of 2π.

For the same reason as for the Wigner function, the experiment has to be repeated twice with a final pulse of either $\pi/2$ or $-\pi/2$. The signal difference between the final $-\pi/2$ and $+\pi/2$ pulses can be expressed as

$$\begin{aligned} S(t) &= \frac{Q_{\pi/2} - Q_{-\pi/2}}{Q_g - Q_e} \\ &= e^{|\alpha|^2(\cos(\chi t)-1)}\cos(|\alpha|^2\sin(\chi t))e^{-t\Gamma_2-\gamma|\alpha|^2 t}. \end{aligned} \tag{c.5}$$

This expression is derived in the supplementary material of Ref. [208] under the assumption of a harmonic oscillator with infinite lifetime and a qubit excited state population equals to zero. The last exponential decay factor was added to take into account the intrinsic decoherence of the qubit and the measurement-induced dephasing rate of the harmonic mode on the qubit during the waiting time. It is also possible to take into

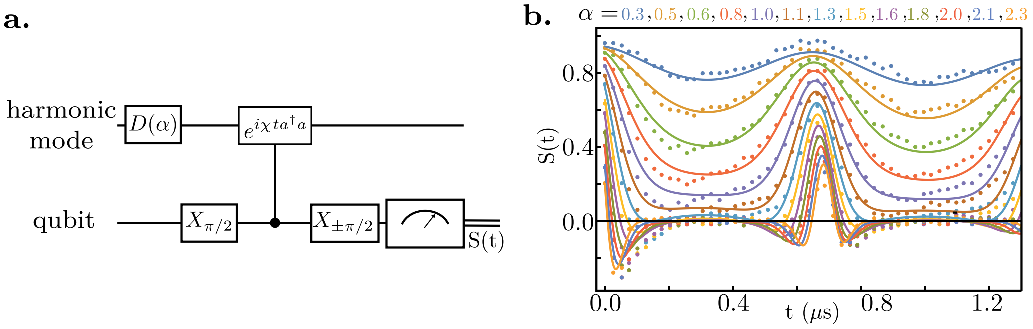

Figure c.3: Revival of the Ramsey interferences on the yes-no qubit **a.** Circuit diagram for Ramsey interferometry in the presence of harmonic mode photons. After displacement pulse, an unconditional $\pi/2$ pulse is applied to the qubit. We then let the qubit evolve freely during a time t before doing a new $\pm\pi/2$ pulse and measure its state. **b.** Measured (dots) and predicted (lines) signal S as a function of waiting time t for the storage mode and the yes-no qubit. Predicted signal is computed from Eq. (c.5). Yes-no qubit revivals occur every $2\pi/\chi_{\mathrm{s,yn}} \approx 0.7\mu$s.

account a second order Kerr correction that shifts the revival time with the amplitude of the coherent state [208]. At first order this shift is given by

$$t_{\mathrm{revival}} = 2\Delta\tau \left(1 - 2|\alpha|^2 \chi_{\mathrm{ho,ho,q}} \Delta\tau\right). \tag{c.6}$$

This experiment was performed to calibrate the Storage mode Wigner tomography, by adjusting the above parameters to allow the model to match the measured signal shown in Fig. c.3b, we find $\Delta\tau = 337$ ns, $\gamma = 0.23\ \mu\mathrm{s}^{-1}$ and $\chi_{\mathrm{s,s,yn}} = -14$ kHz. However, this simple expression does not take into account the finite lifetime of the storage mode and we prefer to only use it as a calibration of $\Delta\tau$ and not as a calibration of $\chi_{\mathrm{s,s,yn}}$.

c.1.4 *Axis calibration*

The axes x and p of the phase space of the Wigner function $W(\alpha = x + ip) = W(x, p)$ have to be calibrated. They correspond to the real and imaginary parts of the displacement $-\alpha$ and thus can be calibrated using any calibration of the harmonic mode displacement. In this thesis, the axes of the phase space x, p are calibrated using the same pulse sequence as the Wigner tomography. The photon number calibration realized before (see section 5.2.2) cannot be used here for two reasons. First, in order to measure the measurement back-action of the multiplexed photon number measurement (see Sec. 8.1), we have to play the Wigner sequence with displacement pulses detuned from the storage mode frequency, while the photon number calibration is only valid for resonant pulses. Second, high order Kerr interaction affects the calibration when the harmonic mode hosts a large number of photons. Thus, we decided to use the width of the Wigner function when the storage mode is in the thermal equilibrium state to calibrate the phase space axes. For a thermal state with a thermal photon number n_{th} the Wigner function is a 2D Gaussian function with a width $\sqrt{n_{\mathrm{th}} + 1/2}$ [7]

$$W_{\rho(n_{\mathrm{th}})}(\alpha = x + ip) = \frac{2}{\pi} \frac{1}{2n_{\mathrm{th}} + 1} e^{-2|\alpha|^2/(2n_{\mathrm{th}}+1)}. \tag{c.7}$$

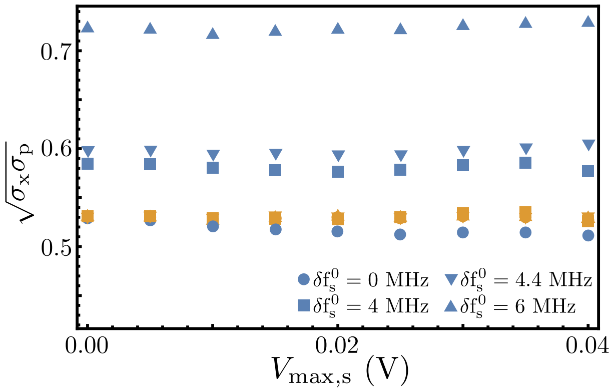

Figure c.4: Calibration of the quadrature axis for Wigner tomography. Blue dots represent the standard deviation of the quadratures of the displaced thermal equilibrium state of the storage mode as a function of drive amplitude for various detuning using only the photon number calibration (see section 5.2.2). In contrast, yellow dots show the same standard deviation with the noise based quadrature calibration.

For a thermal state displaced by an amplitude β the Wigner function is still a 2D Gaussian function with a width $\sqrt{n_{\text{th}}+1/2}$ but centered on β. In thermal equilibrium, the storage mode has an average photon number $n_{\text{th}} = 0.03$, which is measured using the standard photon-counting experiment (see Sec. 5.2.1). We calibrated the quadrature axes in order to get the expected geometrical mean $\sqrt{\sigma_x\sigma_p} = 0.53$ of the spread along the quadratures x and p when the storage mode is at thermal equilibrium. To take into account high order Kerr effects, we displace the storage mode equilibrium state and measure its Wigner function. We adjust the calibration to still find a spread of $\sqrt{\sigma_x\sigma_p} = 0.53$. The function used for the calibration is a third order polynomial function which gives $|\alpha|$ as a function of the pulse amplitude $V_{\text{max,s}}$. We repeat this protocol for 3 detuning values δf_{s} between the displacement pulse and storage mode frequencies. Fig. c.4 shows the mean quadrature spread of the displaced storage mode thermal state Wigner function as a function of drive amplitude $V_{\text{max,s}}$ for the photon number calibration and the Wigner phase space calibration. For example, the polynomial function for a detuning of 4 MHz reads $\alpha = x + ip = e^{i\phi_{\text{s}}}(77.3V_{\text{max,s}} + 86.7V_{\text{max,s}}^2 - 1343V_{\text{max,s}}^3)$ where $V_{\text{max,s}}$ is expressed in Volts and ϕ_{s} is the phase of the pulse. For a typical value $V_{\text{max,s}} = 20$ mV, the second order term is a correction of about 2% and the third one is a correction of about 0.07%.

C.2 THE WIGNER–WEYL TRANSFORMATION

C.2.1 *Definition*

The Wigner function is in fact the Wigner transformation of the density matrix and is a part of the Wigner–Weyl transformation, which creates a bijection between the real function of the phase space and the quantum operator of the Hilbert space. The Wigner transform $W_{\hat{O}}$ of a quantum operator $\hat{O}$ is defined as

$$W_{\hat{O}}(\alpha = x+ip) = \frac{1}{\pi}\int_{-\infty}^{+\infty} \mathrm{e}^{-2ipy}\langle x+y/2|\hat{O}|x-y/2\rangle \mathrm{d}y = \frac{2}{\pi}\mathrm{Tr}(\hat{D}^{\dagger}(\alpha)\hat{O}\hat{D}(\alpha)\hat{\mathcal{P}}), \quad \text{(c.8)}$$

where $\{|x\rangle\}$ is the eigenbasis of the quadrature operator $\hat{x}$. The inverse transform $\hat{O}_f$, which is the Weyl transform of the real function $f(x,p)$, is defined as

$$\begin{aligned} \hat{O}_f &= \frac{1}{4\pi}\iiiint f(x,p)\mathrm{e}^{ik_x(\hat{x}-x)+ik_p(\hat{p}-p)}\mathrm{d}x\mathrm{d}p\mathrm{d}k_x\mathrm{d}k_p \\ &= \pi\iint \tilde{f}(k_x,k_p)\mathrm{e}^{ik_x\hat{x}+ik_p\hat{p}}\mathrm{d}k_x\mathrm{d}k_p \end{aligned}, \quad \text{(c.9)}$$

where $\tilde{f}(k_x,k_p)$ is the Fourier transform of $f(x,p)$. Thus, the Weyl transform can be seen as the replacement of the real variables x and p by the quantum operators $\hat{x}$ and $\hat{p}$, defined as

$$\begin{cases} \hat{x} = \dfrac{\hat{a}+\hat{a}^{\dagger}}{2}, \\ \hat{p} = \dfrac{\hat{a}-\hat{a}^{\dagger}}{2i}. \end{cases} \quad \text{(c.10)}$$

C.2.2 *Density matrix reconstruction*

As the Wigner transform admits a reverse transformation, the Weyl transform can be used to reconstruct the density matrix from the Wigner function [216, 217, 218]. However, it leads to an expression of the density operator in the $\hat{x}$ and $\hat{p}$ basis that is not straightforward to use. In addition, this calculation can be significantly simplified [219]. In this section, we will discuss two other ways to reconstruct the density matrix.

C.2.2.1 *Maximum likelihood reconstruction*

The maximum likelihood (MaxLike) approach consists of finding the physical[3] density matrix with the closest Wigner function to the one measured [220, 221, 219]. This approach is robust against the noise and imperfection of the measurement and ensures that a Hermitian density matrix is obtained that is both positive and normalized. A review of MaxLik methods in quantum mechanics can be found in Ref. [222].

C.2.2.2 *Reconstruction using the Wigner map*

For any operator $\hat{O}$, we can apply the Wigner transform (see Eq. (c.8)) to obtain the operator's Wigner map $W_{\hat{O}}$. The mean value of the operator $\hat{O}$ can be derived from the integral over the phase space of the product of the Wigner map $W_{\hat{O}}$ and the Wigner

---

[3] density matrix ρ such that $\rho \geq 0$ and $\mathrm{Tr}(\rho) = 1$.

function $W(\alpha)$ (namely, the Wigner map of the density matrix) multiplied by π, as follows:

$$\begin{array}{l} \pi \int \mathrm{d}x \int \mathrm{d}p\, W_\rho(x,p) W_{\hat{O}}(x,p) \\ = \frac{1}{\pi} \int \mathrm{d}x \int \mathrm{d}p \int \mathrm{d}y \int \mathrm{d}y'\, e^{-2ip(y+y')} \langle x+y/2|\rho|x-y/2\rangle \langle x+y'/2|\hat{O}|x-y'/2\rangle \\ = \int \mathrm{d}x \int \mathrm{d}y \int \mathrm{d}y'\, \delta(y+y') \langle x+y/2|\rho|x-y/2\rangle \langle x+y'/2|\hat{O}|x-y'/2\rangle \\ = \int \mathrm{d}x \int \mathrm{d}y\, \langle x+y/2|\rho|x-y/2\rangle \langle x-y/2|\hat{O}|x+y/2\rangle \\ = \int \mathrm{d}u \int \mathrm{d}v\, \langle u|\rho|v\rangle \langle v|\hat{O}|u\rangle \\ = \mathrm{Tr}(\rho\hat{O}) = \langle \hat{O}\rangle_\rho \end{array} . \tag{c.11}$$

This is a powerful tool, as it enables us to compute the mean value of any operator without reconstructing the density matrix. For example, for $\hat{x}$ and $\hat{p}$ operators, Wigner maps take the simple expression

$$\begin{array}{l} W_{\hat{x}}(\alpha = x+ip) = x/\pi \\ W_{\hat{p}}(\alpha = x+ip) = p/\pi \end{array} , \tag{c.12}$$

and their mean value can be easily computed as

$$\begin{array}{l} \langle \hat{x}\rangle = \int \mathrm{d}x \int \mathrm{d}p\, W(x,p)x \\ \langle \hat{p}\rangle = \int \mathrm{d}x \int \mathrm{d}p\, W(x,p)p \end{array} . \tag{c.13}$$

We can use the same approach to reconstruct the density matrix, as any element ρ_{nm} of the density matrix is the mean value of the operator $|n\rangle\langle m|$. The Wigner map for every operator $|n\rangle\langle m|$ reads

$$W_{|n\rangle\langle m|}(x,p) = \frac{1}{\pi} \int \mathrm{d}y e^{-2ipy} \psi_n(x+y/2)\overline{\psi_m}(x-y/2), \tag{c.14}$$

where ψ_n is the wavefunction of $|n\rangle$

$$\langle x|n\rangle = \psi_n(x) = \left(\frac{2}{\pi}\right)^{1/4} \frac{1}{\sqrt{2^n n!}} \mathcal{H}_n(\sqrt{2}x) e^{-x^2} \tag{c.15}$$

and $\mathcal{H}_n(x) = (-1)^n e^{x^2} \frac{d^n}{dx^n} e^{-x^2}$ is the Hermite polynomial function of order n. Thus, the matrix element ρ_{nm} of the harmonic mode is given by

$$\rho_{nm} = \pi \iint \mathrm{d}x\mathrm{d}p W_{|n\rangle\langle m|}(x,p) W(x,p). \tag{c.16}$$

This approach requires the Wigner function to be properly calibrated. Specifically, the Wigner function must be normalized $\iint \mathrm{d}^2\alpha W(\alpha) = 1$, as its integral is equal to the density matrix trace $\iint \mathrm{d}^2\alpha W(\alpha) = \mathrm{Tr}(\rho)$. Each Wigner map $W_{|n\rangle\langle m|}(x,p)$ can be easily computed using any formal calculation software[4]; additionally, it is necessary to check that the mesh of the phase space is thin enough, compared to the pattern size of $W_{|n\rangle\langle m|}(x,p)$, that the integral of $W_{|n\rangle\langle m|}(x,p)W(x,p)$ can be well approximated by the discrete sum over the phase-space pixel.

For the diagonal element of the density matrix, the Wigner map $W_{|n\rangle\langle n|}$ can easily be expressed, as it is equal to the Wigner function of the Fock state $|n\rangle$,

$$W_{|n\rangle\langle n|} = (-1)^n \frac{2}{\pi} \mathrm{e}^{-2(x^2+p^2)} L_n(4(x^2+p^2)), \tag{c.17}$$

where $L_n(x)$ is the Laguerre polynomial function of order n.

---

[4] We recommend the use of Mathematica

d

SIMULATION OF PHOTOCOUNTING EXPERIMENTS

In this appendix, we describe the master equation simulations used to reproduce the experimental results of Chaps. 5,6, 7 and 8. We simulated the three photon-counting experiments, the standard (see App. d.1.1),the fluorescence (see App. d.1.1.1) and the multiplexed (see App. d.1.3) photocounting; the photon number calibration (see App. d.1.2) of the storage mode, and the dephasing rate induced by the multiplexed measurement of the storage mode photon number (see App. d.1.4).

All simulations were performed using the Python package *QuTiP* [223]. We simulated the complete system composed of the storage mode, the yes-no qubit and the multiplexing qubit with all couplings, except in the simulation of the measurement-induced dephasing rate for which we only took into account the storage mode and the multiplexing qubit. The storage mode was modeled as an harmonic oscillator while the transmon qubits were replaced by two-level systems. The Hilbert space of the storage mode was truncated at a photon number ranging from 10 to 25 photons depending on the simulation.

D.1 PHOTOCOUNTING SIMULATIONS

D.1.1 *Photocounting with the yes-no qubit*

Both photon-counting approaches are simulated in a very similar manner. The first simulation (yes-no simulation) describes the use of conditional operations on the yes-no qubit. This experiment serves as a calibration of the number of photons in the storage mode and of all relevant parameters. This experiment starts with a displacement of the storage mode followed by a conditional π pulse on the yes-no qubit at frequency $f_{\mathrm{yn}} - \delta f_{\mathrm{yn}}$ before detecting the expectation value of the Pauli operator $\sigma_{\mathrm{z,yn}}$.

We write the Hamiltonian of the system in a frame rotating at $\omega_{\mathrm{s}} - \chi_{\mathrm{s,mp}}/2 - \chi_{\mathrm{s,yn}}/2$ for storage mode, $\omega_{\mathrm{yn}} - 2\pi\delta f_{\mathrm{yn}}$ for yes-no qubit mode and ω_{mp} for multiplexing qubit mode as follows

$$\begin{aligned}\hat{H}_1/\hbar \quad = \quad & 2\pi\delta f_{\mathrm{yn}}\frac{\hat{\sigma}_{\mathrm{z,yn}}}{2} - \chi_{\mathrm{s,yn}}\hat{n}_{\mathrm{s}}\frac{\hat{\sigma}_{\mathrm{z,yn}}}{2} - \chi_{\mathrm{s,mp}}\hat{n}_{\mathrm{s}}\frac{\hat{\sigma}_{\mathrm{z,mp}}}{2} - \chi_{\mathrm{s,s}}\hat{n}_{\mathrm{s}}(\hat{n}_{\mathrm{s}}-1) \\ & -\chi_{\mathrm{s,s,yn}}\hat{n}_{\mathrm{s}}(\hat{n}_{\mathrm{s}}-1)\frac{\hat{\sigma}_{\mathrm{z,yn}}}{2} - \chi_{\mathrm{s,s,mp}}\hat{n}_{\mathrm{s}}(\hat{n}_{\mathrm{s}}-1)\frac{\hat{\sigma}_{\mathrm{z,mp}}}{2} + \epsilon_{\mathrm{yn}}(t)\hat{\sigma}_{\mathrm{x,yn}} \\ & +\lambda(t)(\epsilon_{\mathrm{max}}e^{i(\chi_{\mathrm{s,mp}}+\chi_{\mathrm{s,yn}})t/2}\hat{a}_{\mathbf{s}} + \epsilon^{*}_{\mathrm{max}}e^{-i(\chi_{\mathrm{s,mp}}+\chi_{\mathrm{s,yn}})t/2}\hat{a}^{\dagger}_{\mathbf{s}})\end{aligned}, \tag{d.1}$$

where $\lambda(t)$ is a Gaussian function with duration 100 ns, width 25 ns and a maximum of 1 so that the storage mode displacement pulse reads $\epsilon_{\mathrm{s}}(t) = \lambda(t)\epsilon_{\mathrm{max}}$ and $\epsilon_{\mathrm{yn}}(t)$ is the time envelope of a Gaussian pulse with duration 1.9 μs and width 475 ns. The amplitude of the pulse is chosen to obtain a π rotation on the yes-no qubit. The term $-\delta f_{\mathrm{yn}}\frac{\hat{\sigma}_{\mathrm{z,yn}}}{2}$ takes into account the detuning between the π pulse and the yes-no qubit frequency. $\epsilon_{\mathrm{yn}}(t)$ is delayed with respect to $\lambda(t)$ to match the experimental pulse sequence. In comparison with the Hamiltonian (5.1) this simulation adds higher order cross-Kerr interactions between each qubit and the storage mode and a self-Kerr term on the storage mode but it does not take into account the readout resonator.

In addition to the Hamiltonian (d.1), we supply the solver with eight collapse operators to simulate the dynamics of the following master equation

$$\begin{aligned}\dot{\rho} \;=\; & -\frac{i}{\hbar}[\hat{H}_1, \rho] + 2\Gamma_{\phi,\mathrm{s}}\mathcal{L}(\hat{n}_\mathrm{s})\rho \\ & +(1+n_{\mathrm{th,s}})\Gamma_{1,\mathrm{s}}\mathcal{L}(\hat{a}_\mathrm{s})\rho + n_{\mathrm{th,s}}\Gamma_{1,\mathrm{s}}\mathcal{L}(\hat{a}_\mathrm{s}^\dagger)\rho \\ & +\frac{1}{2}\Gamma_{\phi,\mathrm{yn}}\mathcal{L}(\hat{\sigma}_{\mathrm{z,yn}})\rho + \Gamma_{1,\mathrm{yn}}\mathcal{L}(\hat{\sigma}_{\mathrm{yn}}^-)\rho \\ & +\frac{1}{2}\Gamma_{\phi,\mathrm{mp}}\mathcal{L}(\hat{\sigma}_{\mathrm{z,mp}})\rho + \Gamma_{1,\mathrm{mp}}\mathcal{L}(\hat{\sigma}_{\mathrm{mp}}^-)\rho\end{aligned}\quad, \tag{d.2}$$

with $n_{\mathrm{th,s}}$ the expectation values of $\hat{n}_\mathrm{s}$ when the system is at rest due to thermal occupation. All decoherence and relaxation rates are measured using previously explained calibration.

The master equation is solved using the function “mesolve” of QuTiP starting from a thermal state with $n_{\mathrm{th,s}}$ average photons in the storage mode, the yes-no qubit in the ground state $|g\rangle$ and the multiplexing qubit also in the ground state $|g\rangle$. The solver iteratively computes the density matrix with a 10 ns time step during the displacement pulse and the π pulse. We compute the expectation value $\langle\hat{\sigma}_{\mathrm{z,yn}}\rangle$ at the end of the sequence and convert it into a probability $\mathbb{P}_e$ of finding the yes-no qubit in the $|e\rangle$ state.

This simulation can be used to reproduce the experiment in Fig. 5.2 by adjusting the following parameters $\{\mu = \epsilon_{\max}/V_{\max,\mathrm{s}}, \chi_{\mathrm{s,yn}}, \chi_{\mathrm{s,s}}, \chi_{\mathrm{s,s,yn}}, n_{\mathrm{th,s}}\}$ where $V_{\max,\mathrm{s}}$ is the maximum amplitude in Volts of the storage pulse. Note that we need to run the simulation for every couple of parameters $(V_{\max,\mathrm{s}},\ \delta f_{\mathrm{yn}})$. Tab. d.1 compiles the values of fitted parameters.

D.1.1.1 *Photocounting with the multiplexing qubit*

A second simulation (fluorescence simulation) was carried out to compare the photon-counting experiment in Fig. 6.3 using a single drive on the multiplexing qubit with theory. This experiment also starts with a storage mode displacement but it is followed by a 2 μs Gaussian pulse on the multiplexing qubit at the frequency $f_{\mathrm{mp}} - \delta f_{\mathrm{mp}}$ with an amplitude expressed as a Rabi frequency $\Omega = \chi_{\mathrm{s,mp}}/4$. The measured reflection coefficient of the multiplexing qubit $r(\delta f_{\mathrm{mp}})$ is given by Eq. (2.61) and since the Rabi frequency is given by $\Omega = 2\sqrt{\Gamma_{1,\mathrm{mp}}}|\langle a_{\mathrm{in}}\rangle|$ we get an emission coefficient

$$1 - \mathcal{R}e\left(r(\delta f_{\mathrm{mp}})\right) = \frac{2\Gamma_{1,\mathrm{mp}}}{\Omega}\mathcal{R}e\left(e^{-i\arg(\langle a_{\mathrm{in}}\rangle)}\langle\hat{\sigma}_{-,\mathrm{mp}}\rangle\right) \tag{d.3}$$

in the frame rotating at $f_{\mathrm{mp}} - \delta f_{\mathrm{mp}}$ for the multiplexing qubit. If we set the phase of the drive so that $i\langle a_{\mathrm{in}}\rangle = 0$, meaning we drive the qubit along $\sigma_{\mathrm{y,mp}}$, the emission coefficient becomes

$$1 - \mathcal{R}e\left(r(\delta f_{\mathrm{mp}})\right) = \frac{\Gamma_{1,\mathrm{mp}}}{\Omega}\langle\hat{\sigma}_{\mathrm{x,mp}}\rangle \tag{d.4}$$

The Hamiltonian of the problem in the frame rotating at $\omega_{\mathrm{s}} - \chi_{\mathrm{s,mp}}/2 - \chi_{\mathrm{s,yn}}/2$ for storage mode, ω_{yn} for yes-no qubit and $\omega_{\mathrm{mp}} - 2\pi\delta f_{\mathrm{mp}}$ for multiplexing qubit reads

$$\begin{aligned}\hat{H}_2/\hbar \quad = \quad & 2\pi\delta f_{\mathrm{mp}}\frac{\hat{\sigma}_{\mathrm{z,mp}}}{2} - \chi_{\mathrm{s,yn}}\hat{n}_{\mathrm{s}}\frac{\hat{\sigma}_{\mathrm{z,yn}}}{2} - \chi_{\mathrm{s,mp}}\hat{n}_{\mathrm{s}}\frac{\hat{\sigma}_{\mathrm{z,mp}}}{2} - \chi_{\mathrm{s,s}}\hat{n}_{\mathrm{s}}(\hat{n}_{\mathrm{s}} - 1) \\ & -\chi_{\mathrm{s,s,yn}}\hat{n}_{\mathrm{s}}(\hat{n}_{\mathrm{s}} - 1)\frac{\hat{\sigma}_{\mathrm{z,yn}}}{2} - \chi_{\mathrm{s,s,mp}}\hat{n}_{\mathrm{s}}(\hat{n}_{\mathrm{s}} - 1)\frac{\hat{\sigma}_{\mathrm{z,mp}}}{2} - \frac{\Omega}{2}\epsilon_{\mathrm{mp}}(t)\hat{\sigma}_{\mathrm{y,mp}} \\ & +\lambda(t)(\epsilon_{\mathrm{max}}e^{i(\chi_{\mathrm{s,mp}}+\chi_{\mathrm{s,yn}})t/2}\hat{a}_{\mathbf{s}} + \epsilon^*_{\mathrm{max}}e^{-i(\chi_{\mathrm{s,mp}}+\chi_{\mathrm{s,yn}})t/2}\hat{a}^\dagger_{\mathbf{s}})\end{aligned} \quad , \quad \text{(d.5)}$$

where $\epsilon_{\mathrm{mp}}(t)$ is a Gaussian function of duration 2 μs, width 250 ns and amplitude 1. $\epsilon_{\mathrm{mp}}(t)$ is delayed compare to $\lambda(t)$ to reproduce the experimental pulse sequence. We add to this Hamiltonian the same relaxation and decoherence channels as for the yes-no simulation (see Eq. (d.2)) for which the decoherence and relaxation rates were measured independently. The resulting master equation only differs from the yes-no simulation by the Rabi drive that addresses the multiplexing qubit instead of the yes-no qubit. The master equation is solved using the "mesolve" function of QuTiP with a time step of 5.25 ns starting from a thermal state with $n_{\mathrm{th,s}}$ average photons for storage and the yes-no qubit and the multiplexing qubit in the ground state $|g\rangle$. Finally, the expectation value $\langle\hat{\sigma}_{\mathrm{x,mp}}\rangle$ is computed and integrated during the 2 μs of the pulse.

We compare the measured emission coefficient in Fig. 6.3 to the simulated signal $A\langle\hat{\sigma}_{\mathrm{y,mp}}\rangle$ where A is left as a free parameter due to a small parasitic reflection in the measurement setup and thermal population. The parameters $\{\mu, \chi_{\mathrm{s,t}}, \chi_{\mathrm{s,s}}, \chi_{\mathrm{s,s,t}}, n_{\mathrm{th,s}}\}$ is already set by the calibration above using the simulation of the yes-no qubit. From the fluorescence simulation, we thus extract the parameters $\{\chi_{\mathrm{s,mp}}, \chi_{\mathrm{s,s,mp}}, A\}$ by comparing the experimental observations in Fig. 6.3 with the simulation for various $V_{\mathrm{max,s}}$ and δf_{mp}. Fitted values are given in Tab. d.1. Finally, we ran the yes-no simulation again taking into account the updated multiplexing qubit parameters. As expected only small changes in the results of the yes-no qubit simulation are observed.

parameter	fitted values
μ	1.45 (mV μs)$^{-1}$
$\chi_{\mathrm{s,yn}}$	1.42 MHz
$\chi_{\mathrm{s,mp}}$	4.9 MHz
$\chi_{\mathrm{s,s}}$	-0.02 MHz
$\chi_{\mathrm{s,s,yn}}$	-0.003 MHz
$\chi_{\mathrm{s,s,mp}}$	-0.08 MHz
$n_{\mathrm{th,s}}$	0.03

Table d.1: Parameters extracted from the photocounting simulations using the multiplexing or yes-no qubit. All parameters except those related to the multiplexing qubit are determined using a fit of the yes-no qubit simulation to the Fig. 5.2. Parameters related to multiplexing qubit are obtained using a fit of the simulation to Fig. 6.3.

D.1.2 *Evolution of the average photon number in the storage mode*

We simulated the filling of the storage mode by a displacement pulse on the resonator. We simulated the same master equation used for the photocounting simulations with parameters obtained from the photocounting simulations (see Tab. d.1) but without applying any drive on the qubits. Only the displacement pulse on the storage mode is modeled i.e. $\epsilon_{\mathrm{mp}}(t) = 0$, $\delta f_{\mathrm{mp}} = 0$, $\epsilon_{\mathrm{yn}}(t) = 0$, and $\delta f_{\mathrm{yn}} = 0$.

The "mesolve" function of QuTiP computes the density matrix with a time step of 10 ns and returns the mean number of photons in the storage mode at the end of the displacement pulse for various drive amplitudes. Fig. 5.3 shows the square root of the expected mean photon number as a function of the amplitude $\epsilon_{\max}$. We obtain a scaling factor $\sqrt{\langle n_{\mathrm{s}} \rangle} = 85.9\ \mathrm{V}^{-1} V_{\mathrm{max,s}}$ used in the photon number calibration of the storage mode, where $V_{\mathrm{max,s}}$ is the maximum voltage output by the pulse generator that drives the displacement.

D.1.3 *Simulation of multiplexed readout*

In this subsection, we simulate how a frequency comb reflects off the multiplexing qubit. We write the Hamiltonian in the frame rotating at $\omega_{\mathrm{s}} - \chi_{\mathrm{s,mp}}/2 - \chi_{\mathrm{s,yn}}/2$ for the storage mode and at the qubit frequencies for the qubits as

$$\begin{aligned}\hat{H}_3/\hbar = &- \chi_{\mathrm{s,yn}} \hat{n}_{\mathrm{s}} \frac{\hat{\sigma}_{\mathrm{z,yn}}}{2} - \chi_{\mathrm{s,mp}} \hat{n}_{\mathrm{s}} \frac{\hat{\sigma}_{\mathrm{z,mp}}}{2} - \chi_{\mathrm{s,s}} \hat{n}_{\mathrm{s}} (\hat{n}_{\mathrm{s}} - 1) - \chi_{\mathrm{s,s,yn}} \hat{n}_{\mathrm{s}} (\hat{n}_{\mathrm{s}} - 1) \frac{\hat{\sigma}_{\mathrm{z,yn}}}{2} \\ &- \chi_{\mathrm{s,s,mp}} \hat{n}_{\mathrm{s}} (\hat{n}_{\mathrm{s}} - 1) \frac{\hat{\sigma}_{\mathrm{z,mp}}}{2} + \frac{\Omega}{2} (\epsilon^*_{\mathrm{comb}}(t) \hat{\sigma}^-_{\mathrm{mp}} + \epsilon_{\mathrm{comb}}(t) \hat{\sigma}^+_{\mathrm{mp}}) \\ &+ \lambda(t) (\epsilon_{\max} e^{i(\chi_{\mathrm{s,mp}} + \chi_{\mathrm{s,yn}})t/2} \hat{a}_{\mathbf{s}} + \epsilon^*_{\max} e^{-i(\chi_{\mathrm{s,mp}} + \chi_{\mathrm{s,yn}})t/2} \hat{a}^\dagger_{\mathbf{s}})\end{aligned}, \quad (\mathrm{d.6})$$

where $\Omega = \chi_{\mathrm{s,mp}}/2$ and $\epsilon_{\mathrm{comb}}(t)$ is the product of a Gaussian function with the sum of nine complex tones $\sum_{k=0}^{8} \exp(i\chi_{\mathrm{s,mp}} k t)$. The Gaussian envelope of $\epsilon_{\mathrm{comb}}(t)$ has a duration of 2 μs, a width of 250 ns, and a maximum amplitude of 1 and the delay between $\epsilon_{\mathrm{comb}}(t)$ and $\lambda(t)$ reproduces the experimental sequence. The master equation (d.2) is used with a time step of 1 ns for various amplitudes $\epsilon_{\max}$. We obtain the time evolution of $\langle \sigma_{y,mp} \rangle$ enabling us to compare the experimental measurements of Fig. 7.4 to the model. To do so, we integrate the simulated function $\langle \sigma_{y,mp} \rangle \times \cos(\chi_{\mathrm{s,mp}} k t)$ for each integer k, similarly to the demultiplexing processing we perform on the multiplexed experimental signal. Note that, in the case $k = 0$, we need to divide the integral by 2 in order to perform a proper demultiplexing. By combining this simulation with the photon number calibration, we get the expected values of the 9 multiplexing readout signals as a function of the mean number of photons in the storage mode used in Fig. 7.4.

D.1.4 *Simulation of measurement-induced dephasing on the storage mode*

In this part, we only simulate the multiplexing qubit and the storage mode to decrease the computational cost of the simulation. The Hamiltonian of the simulation in the frame rotating at the multiplexing qubit resonant frequency and at $\omega_{\mathrm{s}} + 2\pi\delta f^0_{\mathrm{s}}$ for the storage mode is

$$\begin{aligned}\hat{H}_4/\hbar = &- \chi_{\mathrm{s,mp}} \frac{\hat{\sigma}_{\mathrm{z,mp}} + \mathbb{1}}{2} \hat{n}_{\mathrm{s}} - \delta f^0_{\mathrm{s}} \hat{n}_{\mathrm{s}} - \chi_{\mathrm{s,s,mp}} \hat{n}_{\mathrm{s}} (\hat{n}_{\mathrm{s}} - 1) \frac{\hat{\sigma}_{\mathrm{z,mp}} + \mathbb{1}}{2} \\ &+ \frac{\Omega}{2} (\epsilon_{\mathrm{comb}}(t) \hat{\sigma}^+_{\mathrm{mp}} + \epsilon^*_{\mathrm{comb}}(t) \hat{\sigma}^-_{\mathrm{mp}}),\end{aligned} \quad (\mathrm{d.7})$$

where $\epsilon_{\mathrm{comb}}(t)$ is the product of a Gaussian function with the sum of nine complex exponential $\sum_{k=0}^{8}\exp(i\chi_{\mathrm{s,mp}}k\tau)$. The width of the Gaussian function is equal to one quarter of the duration t of the pulse. We add four dephasing and relaxation channels to this Hamiltonian to obtain the master equation

$$\begin{aligned}\dot{\rho} = &-\frac{i}{\hbar}[\hat{H}_4, \rho] + 2\Gamma_{\phi,\mathrm{s}}\mathcal{L}(\hat{n}_{\mathrm{s}})\rho + \Gamma_{1,\mathrm{s}}\mathcal{L}(\hat{a}_{\mathrm{s}})\rho \\ &+ \frac{1}{2}\Gamma_{\phi,\mathrm{mp}}\mathcal{L}(\hat{\sigma}_{\mathrm{z,mp}})\rho + \Gamma_{1,\mathrm{mp}}\mathcal{L}(\hat{\sigma}^{-}_{\mathrm{mp}})\rho.\end{aligned} \tag{d.8}$$

The storage is initialized in a coherent state of amplitude $\beta = 1.55$ and the multiplexing qubit is initialized in state $|g\rangle$. We simulate the dynamics of the system for a pulse duration t going from 100 ns to 5 μs and for Ω ranging from 0 to $2\chi_{\mathrm{s,mp}}$. We compute the expectation value of $\hat{X} = (\hat{a}_{\mathrm{s}}+\hat{a}_{\mathrm{s}}^{\dagger})/2$ at the end of each simulation. For a given Ω, we extract the time evolution of $\langle\hat{X}\rangle$ under the influence of the multiplexed measurement as shown on Fig. d.1a. This decaying sinusoid is fitted using Eq. (8.2) to obtain the oscillation frequency δf_{s} and the decay rate $\Gamma_{\mathrm{d,s}}$ and compare it to the same measured quantities (see Fig. 8.4)

We repeat the simulation using a square pulse envelope instead of Gaussian pulse for ϵ_{comb} to make the simulation faster for several values of $\chi_{\mathrm{s,mp}}$ from 1.5 to 8.8 MHz by steps of 1.4 MHz. We observe that $\delta f_{\mathrm{s}}(\Omega)$ and $\Gamma_{\mathrm{d,s}}(\Omega)$ increase as $\chi_{\mathrm{s,mp}}$ becomes larger but that the maxima and minima of the curve are always found for the same $\Omega/\chi_{\mathrm{s,mp}}$ ratio (Fig. d.1b) as predicted by the theory (see Sec. 8.2.1).

Varying the initial coherent state amplitude β (see Fig. d.1c), we observe that the dephasing $\Gamma_{\mathrm{d,s}}$ depends on the amplitude of the initial coherent state. As the frequency comb contains only a finite number of frequencies $f_{\mathrm{mp}} - n\chi_{\mathrm{s,mp}}$ with $0 \leq k \leq 8$, we are not exactly in the infinite frequency comb approximation and due to "border" effect, the decoherence between two Fock states $|n\rangle$ and $|m\rangle$ does not depends only of the differences $|n-m|$ but also of the value of n and m.

However, when using a larger comb probing the frequencies $\{\omega_{\mathrm{mp}} - k\chi_{\mathrm{s,mp}}\}_{-4\leq k\leq 12}$, the dephasing rate $\Gamma_{\mathrm{d,s}}$ shows lower minimum, closer from $\Omega/\chi_{\mathrm{s,mp}}$ integer (see Fig. d.1d). The curve $\Gamma_{\mathrm{d,s}}(\Omega)$ also becomes more $\chi_{\mathrm{s,mp}}$ periodic as the theory predicts with the infinite comb approximation. Moreover, the dephasing rate $\Gamma_{\mathrm{d,s}}$ becomes independent of the initial coherent state (for amplitude smaller than 1.8) as for any Fock state initially populated, one can consider the infinite frequency comb valid and there is no "boarder" effect in particular for the Fock state $|0\rangle$ (see Fig. d.1e).

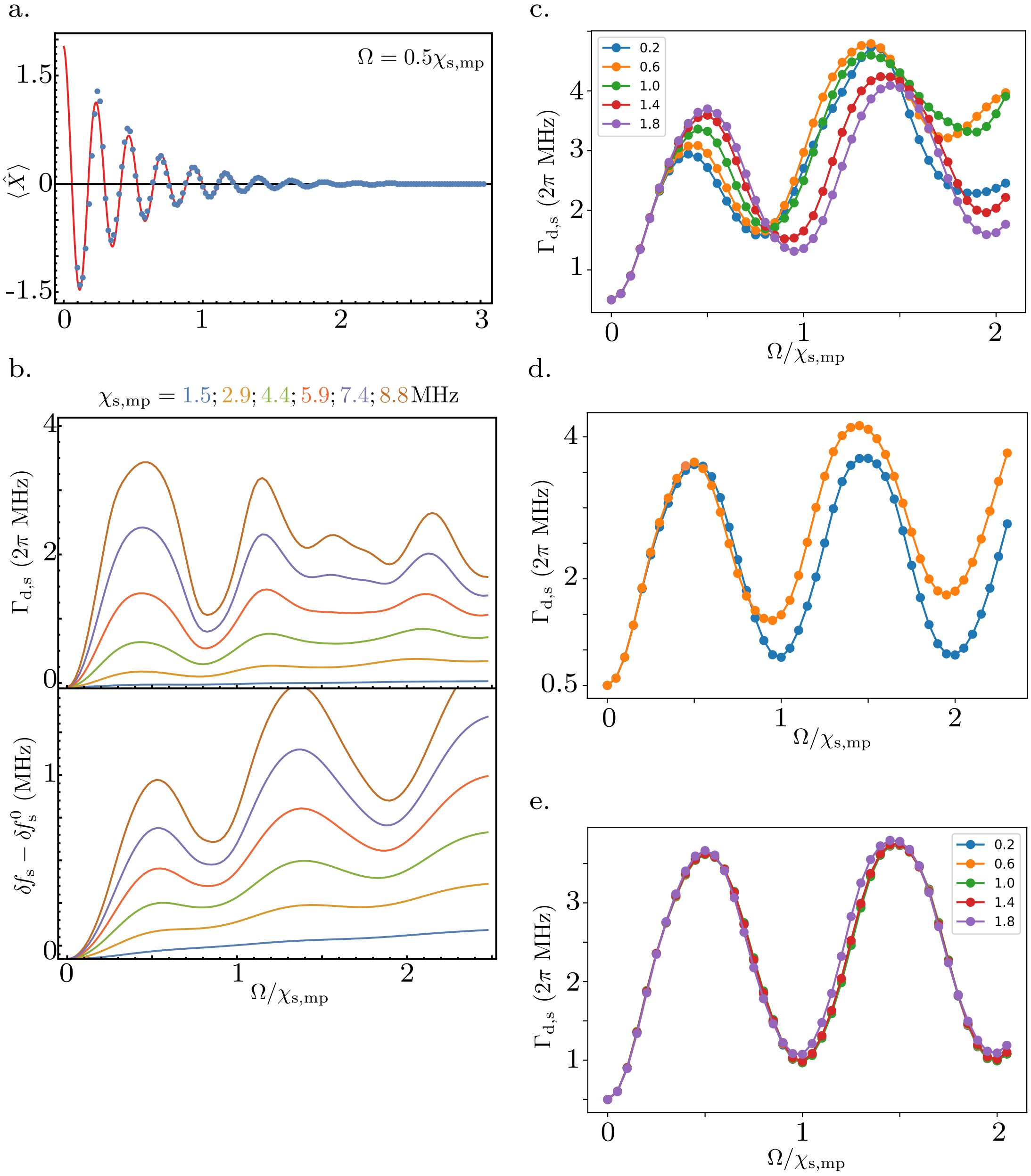

Figure d.1: Simulations of the measurement-induced dephasing rate and of the ac-Stark shift induced by a frequency comb. **a.** Ramsey-like oscillations of the storage mode for $\Omega = \chi_{s,mp}/2$ and an initial coherent field amplitude $\beta = -1.55$. Blue dots are the simulated expectation values of $\hat{X}$ and red line is the theory given by the Eq. (8.2). **b.** Simulated measurement-induced dephasing rate $\Gamma_{\mathrm{d,s}}$ and ac-Stark shift as a function of $\Omega/\chi_{s,mp}$ for various values of $\chi_{\mathrm{s,mp}}$. Simulations show the same pattern with maxima and minima for some specific values of $\Omega/\chi_{s,mp}$ as in the experiment in Fig. 8.4. **c.** Simulated measurement-induced dephasing rate as a function of $\Omega/\chi_{s,mp}$ for various initial coherent state amplitudes β in the storage mode and comb probing from 0 to 8 photons. **d.** Simulated measurement-induced dephasing rate as a function of $\Omega/\chi_{s,mp}$ for a frequency comb probing from 0 to 8 photons (yellow line) and a frequency comb probing from -4 to 12 photons (i. e. probing at frequencies $\{\omega_{\mathrm{mp}} - k\chi_{\mathrm{s,mp}}\}_{-4\leq k\leq 12}$). **e.** Simulated measurement-induced dephasing rate as a function of $\Omega/\chi_{s,mp}$ for various initial coherent state amplitudes β in the storage mode and comb probing from -4 to 8 photons (i. e. probing at frequencies $\{\omega_{\mathrm{mp}} - k\chi_{\mathrm{s,mp}}\}_{-4\leq k\leq 8}$).

e

DERIVATION OF THE CORRELATIONS FUNCTIONS OF THE COMPLEX RECORD AND IF SIGNAL

The complex record $s_0(t) = I(t)+iQ(t)$ is related to the IF signal $s_{\mathrm{IF}}(t) = I(t)\cos(\omega_{\mathrm{IF}}t) - Q(t)\sin(\omega_{\mathrm{IF}}t)$ by the equation

$$s_0(t) = \lim_{f_{\mathrm{IF}}\to+\infty} 2f_{\mathrm{IF}} \int_{t-1/(2f_{\mathrm{IF}})}^{t+1/(2f_{\mathrm{IF}})} s_{\mathrm{IF}}(t')\mathrm{e}^{-\mathrm{i}\omega_{\mathrm{IF}}t'}\mathrm{d}t' \tag{e.1}$$

Thus, using the notation $T_{\mathrm{IF}} = 1/f_{\mathrm{IF}}$, the correlation function $g_{s_0}(\tau)$ of the complex record can be written as

$$\begin{aligned} g_{s_0}(\tau) &= \langle s_0^*(t+\tau)s_0(t)\rangle \\ &= \lim_{f_{\mathrm{IF}}\to+\infty} 4f_{\mathrm{IF}}^2 \int_{t-T_{\mathrm{IF}}/2}^{t+T_{\mathrm{IF}}/2} \mathrm{d}t' \int_{t+\tau-T_{\mathrm{IF}}/2}^{t+\tau+T_{\mathrm{IF}}/2} \mathrm{d}t'' \langle s_{\mathrm{IF}}(t'')s_{\mathrm{IF}}(t')\rangle \mathrm{e}^{i\omega_{\mathrm{IF}}(t''-t')}. \end{aligned} \tag{e.2}$$

By making the change of variable $t'' \to \tau' = t'' - t'$, the correlation function becomes

$$g_{s_0}(\tau) = \lim_{f_{\mathrm{IF}}\to+\infty} 4f_{\mathrm{IF}}^2 \int_{t-T_{\mathrm{IF}}/2}^{t+T_{\mathrm{IF}}/2} \mathrm{d}t' \int_{t+\tau-t'-T_{\mathrm{IF}}/2}^{t+\tau-t'+T_{\mathrm{IF}}/2} \mathrm{d}\tau' \langle s_{\mathrm{IF}}(\tau'+t')s_{\mathrm{IF}}(t')\rangle \mathrm{e}^{i\omega_{\mathrm{IF}}\tau'}. \tag{e.3}$$

We recognize at the center of the integrals, the correlation function $g_{s_{\mathrm{IF}}}(\tau') = \langle s_{\mathrm{IF}}(\tau'+t')s_{\mathrm{IF}}(t')\rangle$ of the IF signal. Using the rectangular function $\Pi_T(t)$ defined as

$$\begin{cases} \Pi_T(t) = 0 \text{ if } |t| > T/2 \\ \Pi_T(t) = 1 \text{ if } |t| \leq T/2 \end{cases}, \tag{e.4}$$

we can write the correlation function $g_{s_0}(\tau)$ as

$$g_{s_0}(\tau) = \lim_{f_{\mathrm{IF}}\to+\infty} 4f_{\mathrm{IF}}^2 \int_{-\infty}^{+\infty} \mathrm{d}t' \int_{-\infty}^{+\infty} \mathrm{d}\tau' g_{s_{\mathrm{IF}}}(\tau')\Pi_{T_{\mathrm{IF}}}(t'-t)\Pi_{T_{\mathrm{IF}}}(\tau'-(t+\tau-t'))\mathrm{e}^{i\omega_{\mathrm{IF}}\tau'}. \tag{e.5}$$

The integral over τ' is the Fourier transform of the function $g_{s_{\mathrm{IF}}}(\tau')\Pi_{T_{\mathrm{IF}}}(\tau'-(t+\tau-t'))$ evaluated in $-\omega_{\mathrm{IF}}$. Thus, this integral is equal to the convolution product of the $g_{s_{\mathrm{IF}}}(\tau')$ Fourier transform, noted $\tilde{g}_{s_{\mathrm{IF}}}(\omega)$ and the Fourier transform of $\Pi_{T_{\mathrm{IF}}}(\tau'-(t+\tau-t'))$. Replacing the integral over τ' by the integral over ω of the convolution product, the correlation function reads

$$g_{s_0}(\tau) = \lim_{f_{\mathrm{IF}}\to+\infty} \frac{2f_{\mathrm{IF}}}{\pi} \iint_{-\infty}^{+\infty} \mathrm{d}t'\mathrm{d}\omega \tilde{g}_{s_{\mathrm{IF}}}(-\omega_{\mathrm{IF}}-\omega)\mathrm{sinc}\left(\pi\frac{\omega}{\omega_{\mathrm{IF}}}\right)\Pi_{T_{\mathrm{IF}}}(t'-t)\mathrm{e}^{-i\omega(t+\tau-t')}. \tag{e.6}$$

The integral over t' is the Fourier transform of the translated rectangular function $\Pi_{T_{\mathrm{IF}}}(t'-t)$ evaluated in $-\omega$. Thus, the correlation function reads

$$g_{s_0}(\tau) = \lim_{f_{\mathrm{IF}}\to+\infty} \frac{1}{\pi^2} \int_{-\infty}^{+\infty} \mathrm{d}\omega \tilde{g}_{s_{\mathrm{IF}}}(-\omega_{\mathrm{IF}}-\omega)\mathrm{sinc}\left(\pi\frac{\omega}{\omega_{\mathrm{IF}}}\right)^2 \mathrm{e}^{-i\omega\tau}. \tag{e.7}$$

Taking the Fourier transform of this last equation, we finally obtain the relation between the Fourier transforms of the complex record and IF correlation functions

$$\begin{aligned}\tilde{g}_{s_0}(\omega) &= \lim_{f_{\mathrm{IF}}\to+\infty} \frac{1}{2\pi^3}\iint_{-\infty}^{+\infty} \mathrm{d}\omega'\mathrm{d}\tau\tilde{g}_{s_{\mathrm{IF}}}(-\omega_{\mathrm{IF}}-\omega')\mathrm{sinc}\left(\pi\frac{\omega'}{\omega_{\mathrm{IF}}}\right)^2 \mathrm{e}^{-i(\omega'+\omega)\tau} \\ &= \lim_{f_{\mathrm{IF}}\to+\infty} \frac{1}{\pi^2}\tilde{g}_{s_{\mathrm{IF}}}(\omega-\omega_{\mathrm{IF}})\mathrm{sinc}\left(\pi\frac{\omega}{\omega_{\mathrm{IF}}}\right)^2 \\ &= \frac{1}{\pi^2}\tilde{g}_{s_{\mathrm{IF}}}(\omega-\omega_{\mathrm{IF}})\end{aligned} \tag{e.8}$$

Thus, the spectrum $\tilde{g}_{s_0}(\omega)$ is equal to the spectrum $\tilde{g}_{s_{\mathrm{IF}}}(\omega)$ shifted by ω_{IF}. This make sense as the complex envelope s_0 is obtained by demodulating the IF signal at the frequency $-\omega_{\mathrm{IF}}$.

f

CORRELATION BETWEEN A WEAK MULTIPLEXED PHOTON NUMBER MEASUREMENT AND THE STORAGE FOCK STATE POPULATION

This appendix contains the correlation slopes $c_I^{(k)}$ and $c_Q^{(k)}$ for each record k of the multiplexed measurement. The protocol used to measure these correlation slopes and their definitions is given in Sec. 8.3.2.2. The measurement operator defined in Eq. 8.21 enables us to predict the sign of the correlation slope with the matrix $\underline{\alpha}$ is equal to[1]

$$\underline{\alpha} = -\alpha_{\text{in}}\mathbb{1} + \sqrt{\Gamma_{1,\text{mp}}}\alpha' \tag{f.1}$$

and

$$\underline{\alpha'} = 0.01\times \begin{pmatrix} 18-4i & 5+6i & 2+3i & 2+2i & 1+2i & 1+i & 1+i & i & i \\ 2-6i & 17-4i & 4+5i & 2-3i & 1+2i & 1+2i & 1+i & i & i \\ -3i & 2-6i & 16-3i & 3+5i & 1+3i & 1+2i & 2i & i & i \\ -2i & -3i & 2-6i & 15-2i & 3+5i & 1+3i & 1+2i & 2i & i \\ -2i & -2i & 1_3i & 2-6i & 15 & 2+6i & 1+3i & 2i & 2i \\ -i & -2i & 1_2i & 1_3i & 3-5i & 15+2i & 2+6i & 3i & 2i \\ -i & -i & -2i & 1_2i & 1-3i & 4-5i & 16+3i & 2+6i & 3i \\ -i & -i & 1-i & 1-2i & 1-2i & 2-3i & 4-5i & 16+4i & 2+6i \\ -i & -i & 1-i & 1-i & 1-2i & 2-2i & 2-3i & 5-6i & 18+4i \end{pmatrix}, \tag{f.2}$$

which is obtain by simulating the circuit with the storage mode initializes in a Fock state and looking at the multiplexing qubit fluorescence (see Sec. 8.3.2.3).

When examining the real and imaginary parts of $\underline{\alpha'}$, we observe that, for each line k, the highest real part, which is equal to about 0.15–0.18, is obtained for the column $n = k$. For the other columns $n \neq k$, the real part is almost the same: between 0 and 0.05. Thus, based on the measurement operators of the multiplexing measurement, the real part of the record k must encode information that answers the question "Are there k photons?". The higher the record $I^{(k)}$ is, the higher the back-action on the Fock state k (i. e. the higher the probability that the storage mode will contains k photons). Thus, we expect to observe strong correlations between $I^{(k)}$ and $p_s(k)$ (the probability of having k photons). This is also equivalent to saying that we expect to observe a strong anti-correlation between $I^{(k)}$ and the probability of not having k photons. In our experiment, this means we expect to observe an anti-correlation between $I^{(k)}$ and each

---

[1] We multiply the fluorescence records by -1 to have positive correlation between records giving the same information. This is equivalent to a change of phase reference.

photon probability $p_s(n \neq k)$, with an amplitude that decreases when we increase the extent of the initial storage photon distribution. Indeed, for narrow photon distributions, the information "there are not k photons" may be equivalent to saying "there are k' photons" with $k' \neq k$.

We do indeed observe these expected correlations and anti-correlations between $I^{(k)}$ and $p_s(n)$. In Figs. f.1,f.2, and f.3, the correlation slope $c_I^{(k)}$ is always positive when the yes–no qubit probes whether there are k photons, indicating that there is a correlation between $I^{(k)}$ and $p_s(k)$. The amplitude of the slope when probing $p_s(k)$ is the highest among all the values of the $c_I^{(k)}$ and $c_Q^{(k)}$ slopes, which indicates a strong correlation between $I^{(k)}$ and $p_s(k)$. When k increases, the amplitude of the correlation slope when probing $p_s(k)$ decreases, because the initial storage state is a coherent state with a larger amplitude and, therefore, a smaller initial probability of having k photons. Moreover, the correlation slope $c_I^{(k)}$ is always negative when the yes–no qubit probes whether there are $n \neq k$ photons, indicating an anti-correlation, with an amplitude that decreases quickly when the initial storage photon distribution width increases; i. e. when the initial coherent state amplitude α increases.

When looking at the imaginary part of α', we observe that, for each line k, the imaginary part is positive for $n > k$ and negative for $n \leq k$ and has an absolute value that is higher when n is close to k. Thus, we are expecting a correlation between $Q^{(k)}$ and $p_s(n)$ for $n > k$, and an anti-correlation when $n \leq k$, with a larger amplitude when n is close to k, which decreases quickly when the initial photon distribution width increases; i. e. when the initial coherent state amplitude α increases. The correlation slopes $c_Q^{(k)}$ in Figs. f.1,f.2 and f.3 show this behavior. There is a positive (negative) correlation slope $c_Q^{(k)}$ when the yes–no qubit is probing $p_s(n)$ with $n > k$ $(n \leq k)$.

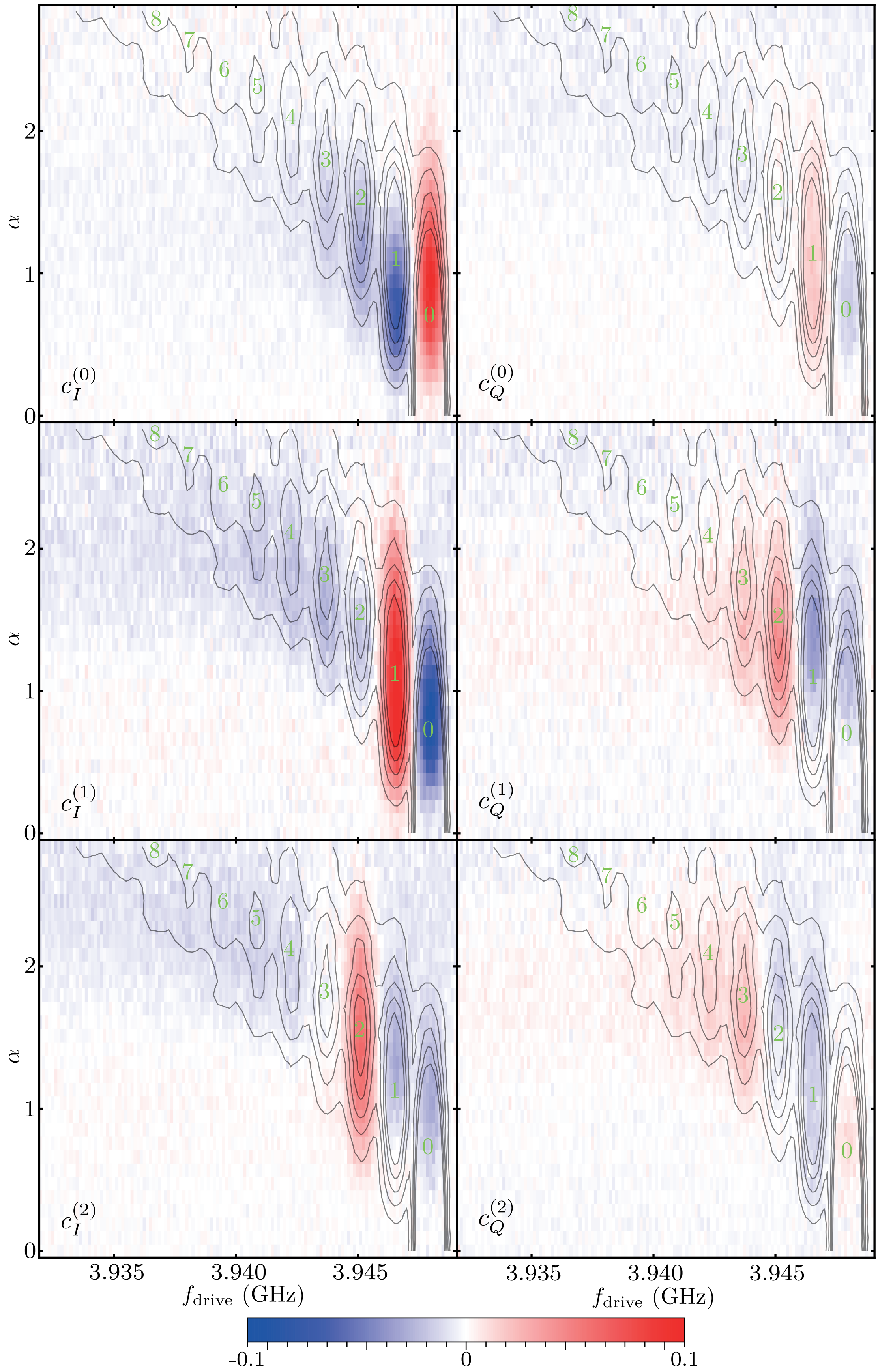

Figure f.1: Correlation slopes $c_I^{(k)}$ (left) and $c_Q^{(k)}$ (right) for $k = 0, 1, 2$ (top, middle, bottom) as a function of the yes–no qubit π-pulse frequency f_{drive} and the storage mode's coherent state amplitude α. The black line corresponds to the contour lines in Fig. 8.7, while the numbers in green are the storage photon numbers probed by the yes–no qubit for a π-pulse frequency f_{drive}.

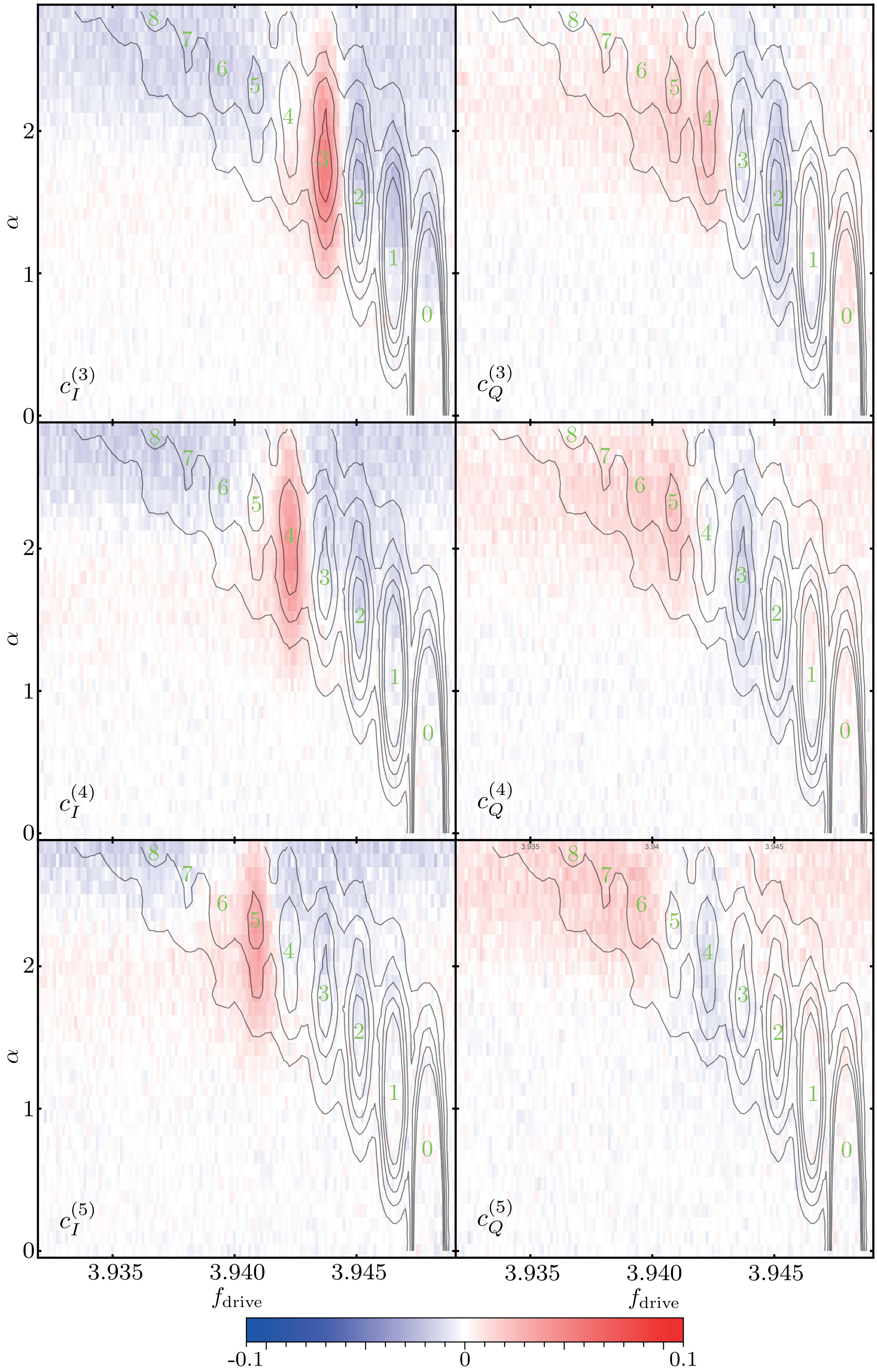

Figure f.2: Correlation slopes $c_I^{(k)}$ (left) and $c_Q^{(k)}$ (right) for $k = 3, 4, 5$ (top, middle, bottom) as a function of the yes–no qubit π-pulse frequency f_{drive} and the storage mode's coherent state amplitude α. The black line corresponds to the contour lines in Fig. 8.7, while the numbers in green are the storage photon numbers probed by the yes–no qubit for a π-pulse frequency f_{drive}.

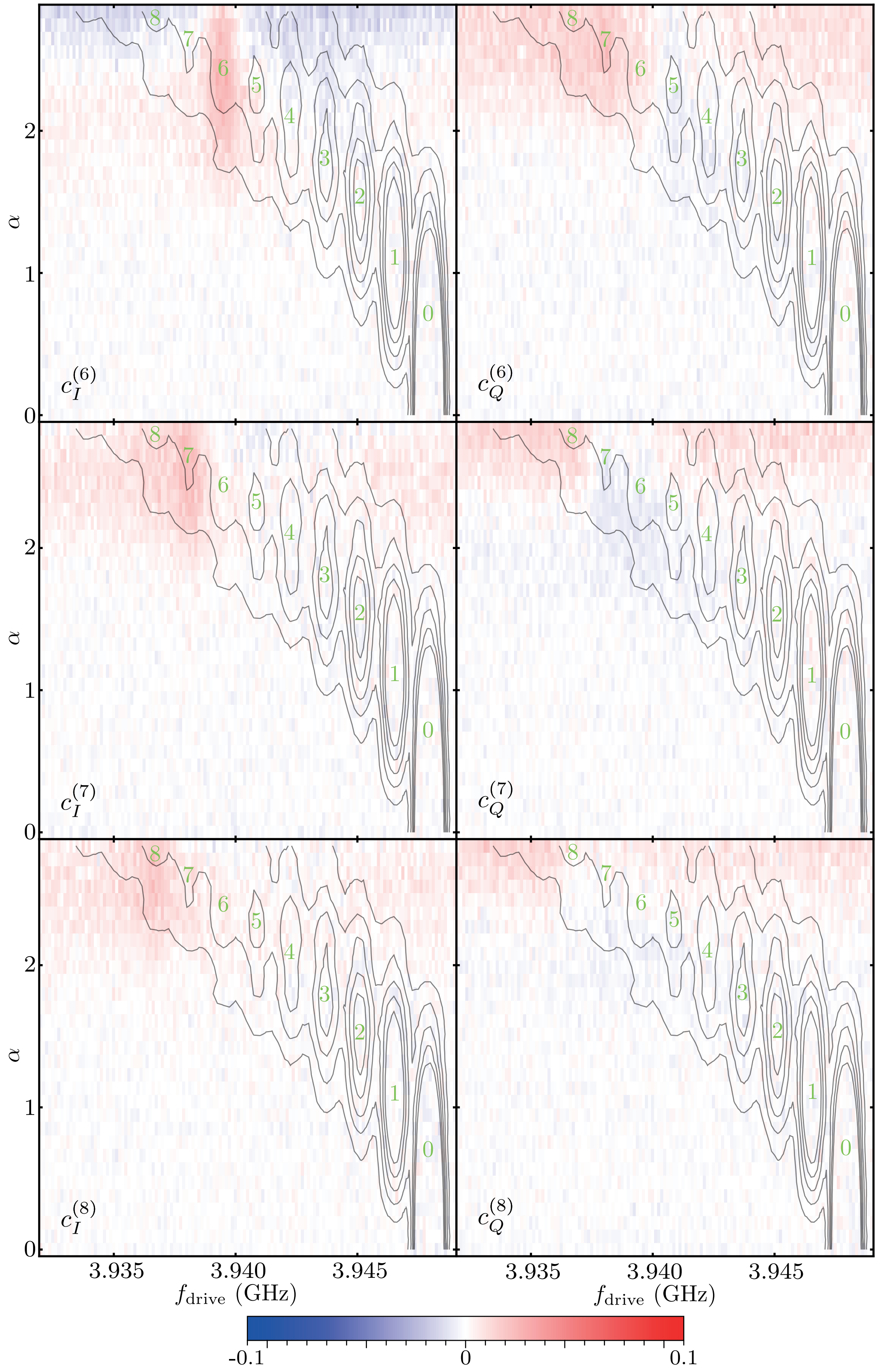

Figure f.3: Correlation slopes $c_I^{(k)}$ (left) and $c_Q^{(k)}$ (right) for $k = 6, 7, 8$ (top, middle, bottom) as a function of the yes–no qubit π-pulse frequency f_{drive} and the storage mode's coherent state amplitude α. The black line corresponds to the contour lines in Fig. 8.7, while the numbers in green are the storage photon numbers probed by the yes–no qubit for a π-pulse frequency f_{drive}.

Part V

BIBLIOGRAPHY

[1] A. Einstein, B. Podolsky, and N. Rosen. "Can Quantum-Mechanical Description of Physical Reality Be Considered Complete?" In: *Phys. Rev.* 47 (10 1935), pp. 777–780 (Cited on page 3).

[2] David Bohm. "A Suggested Interpretation of the Quantum Theory in Terms of "Hidden" Variables. I." In: *Phys. Rev.* 85 (2 1952), pp. 166–179 (Cited on page 3).

[3] J. S. Bell. "On the Einstein Podolsky Rosen paradox." In: *Physics Physique Fizika* 1 (3 1964), pp. 195–200 (Cited on page 3).

[4] Alain Aspect, Jean Dalibard, and Gérard Roger. "Experimental Test of Bell's Inequalities Using Time-Varying Analyzers." In: *Phys. Rev. Lett.* 49 (25 1982), pp. 1804–1807 (Cited on page 3).

[5] W. Heisenberg. "Über den anschaulichen Inhalt der quantentheoretischen Kinematik und Mechanik." In: *Zeitschrift für Physik* 43.3 (1927), pp. 172–198 (Cited on page 3).

[6] Guth. "J. v. Neumann, Mathematische Grundlagen der Quantenmechanik." In: *Monatshefte für Mathematik und Physik* 40.1 (1933), A31–A32 (Cited on page 3).

[7] Serge Haroche, Jean-Michel Raimond, and Pierre Meystre. "Exploring the Quantum: Atoms, Cavities, and Photons." In: *Physics Today* 60.8 (Jan. 2007), p. 61 (Cited on pages 3, 12, 20–22, 24, 53, 106, 180, 195, 196, 199).

[8] A. A. Clerk et al. "Introduction to quantum noise, measurement, and amplification." In: *Reviews of Modern Physics* 82.2 (Apr. 2010). Publisher: American Physical Society, pp. 1155–1208 (Cited on pages 3, 41, 58, 67, 81, 134, 138, 151, 161, 162).

[9] *The Nobel Prize in Physics 2012.* URL: `https://www.nobelprize.org/prizes/physics/2012/summary/` (Cited on page 3).

[10] Wojciech Hubert Zurek. "Decoherence, einselection, and the quantum origins of the classical." In: *Rev. Mod. Phys.* 75 (3 2003), pp. 715–775 (Cited on page 4).

[11] Haocun Yu et al. "Quantum correlations between light and the kilogram-mass mirrors of LIGO." In: *Nature* 583 (7814 July 2020), pp. 43–47 (Cited on page 4).

[12] F. Acernese et al. "Quantum Backaction on kg-Scale Mirrors: Observation of Radiation Pressure Noise in the Advanced Virgo Detector." In: *Physical Review Letters* 125 (13 Sept. 2020), p. 131101 (Cited on page 4).

[13] Rainer Blatt and David Wineland. "Entangled states of trapped atomic ions." In: *Nature* 453.7198 (2008), pp. 1008–1015 (Cited on page 4).

[14] Marcus W. Doherty et al. "The nitrogen-vacancy colour centre in diamond." In: *Physics Reports* 528.1 (2013). The nitrogen-vacancy colour centre in diamond, pp. 1–45 (Cited on page 4).

[15] M. Califano. “Quantum dots.” In: *Quantum Wells, Wires and Dots*. John Wiley & Sons, Ltd, 2016. Chap. 9, pp. 279–302. eprint: `https://onlinelibrary.wiley.com/doi/pdf/10.1002/9781118923337.ch9` (Cited on page 4).

[16] Serge Haroche. “Nobel Lecture: Controlling photons in a box and exploring the quantum to classical boundary *.” In: (2013) (Cited on pages 4, 12).

[17] Markus Aspelmeyer, Tobias J. Kippenberg, and Florian Marquardt. “Cavity optomechanics.” In: *Rev. Mod. Phys.* 86 (4 2014), pp. 1391–1452 (Cited on page 4).

[18] M. H. Devoret and R. J. Schoelkopf. “Superconducting circuits for quantum information: An outlook.” In: *Science* 339 (6124 Mar. 2013), pp. 1169–1174 (Cited on pages 4, 12).

[19] A. Wallraff et al. “Strong coupling of a single photon to a superconducting qubit using circuit quantum electrodynamics.” In: *Nature* 431.7005 (2004), pp. 162–167 (Cited on pages 5, 12, 54).

[20] Jens Koch et al. *Charge insensitive qubit design derived from the Cooper pair box*. 2007 (Cited on pages 5, 17, 28, 59, 97, 181).

[21] D I Schuster et al. “Resolving photon number states in a superconducting circuit.” In: *Nature* 445.7127 (2007), pp. 515–518 (Cited on pages 5, 39, 85–87).

[22] S. Haroche, M. Brune, and J.M. Raimond. “Measuring photon numbers in a cavity by atomic interferometry: optimizing the convergence procedure.” In: *J. Phys. II France* 2.4 (1992), pp. 659–670 (Cited on pages 5, 85, 86, 91).

[23] Christine Guerlin et al. “Progressive field-state collapse and quantum non-demolition photon counting.” In: *Nature 2007 448:7156* 448 (7156 Aug. 2007), pp. 889–893 (Cited on pages 5, 85, 86, 90).

[24] B. Peaudecerf et al. “Adaptive Quantum Nondemolition Measurement of a Photon Number.” In: *Physical Review Letters* 112.8 (2014), p. 080401 (Cited on pages 5, 85, 91).

[25] Bruno Peaudecerf. “Mesure adaptative non destructive du nombre de photons dans une cavité.” Theses. Université Pierre et Marie Curie - Paris VI, Sept. 2013 (Cited on pages 5, 85, 91).

[26] B. R. Johnson et al. “Quantum non-demolition detection of single microwave photons in a circuit.” In: *Nature Physics 2010 6:9* 6 (9 June 2010), pp. 663–667 (Cited on pages 5, 85–87, 90).

[27] R. Dassonneville et al. “Number-Resolved Photocounter for Propagating Microwave Mode.” In: *Physical Review Applied* 14 (4 Oct. 2020), p. 044022 (Cited on pages 5, 85, 91, 94, 180).

[28] Jacob C. Curtis et al. “Single-shot number-resolved detection of microwave photons with error mitigation.” In: *Physical Review A* 103 (2 Feb. 2021), p. 023705 (Cited on pages 5, 85, 92).

[29] Mario F. Gely et al. “Observation and stabilization of photonic Fock states in a hot radio-frequency resonator.” In: *Science* (2019). arXiv: `1901.07267` (Cited on pages 5, 85, 97, 100).

[30] C. Macklin et al. "A near–quantum-limited Josephson traveling-wave parametric amplifier." In: *Science* 350 (6258 Oct. 2015), pp. 307–310 (Cited on pages 6, 66, 72–74, 93, 124).

[31] J.G. Proakis and M. Salehi. *Communication Systems Engineering*. Pearson Education. Prentice Hall, 2002 (Cited on page 6).

[32] L. G. Lutterbach and L. Davidovich. "Method for Direct Measurement of the Wigner Function in Cavity QED and Ion Traps." In: *Physical Review Letters* 78 (13 Mar. 1997), p. 2547 (Cited on pages 7, 104, 196).

[33] Frank Pobell and James Brooks. "Matter and Methods at Low Temperatures." In: *Physics Today* 45.10 (Oct. 1992), p. 116 (Cited on page 11).

[34] David J Wineland. "Nobel Lecture: Superposition, entanglement, and raising Schrö dinger's cat *." In: (2013) (Cited on page 12).

[35] Y Nakamura, Yu A Pashkin², and J S Tsai. *Coherent control of macroscopic quantum states in a single-Cooper-pair box*. 1999 (Cited on pages 12, 17).

[36] Jukka P. Pekola. "Towards quantum thermodynamics in electronic circuits." In: *Nature Physics* 11 (2 Jan. 2015), pp. 118–123 (Cited on page 12).

[37] J P Pekola and I M Khaymovich. *Thermodynamics in Single-Electron Circuits and Superconducting Qubits*. 2018 (Cited on page 12).

[38] Nathanaël Cottet. "Énergie et information dans la fluorescence de circuits supraconducteurs." 2018PSLEE064. PhD thesis. 2018 (Cited on pages 12, 35, 97).

[39] C. L. Degen, F. Reinhard, and P. Cappellaro. "Quantum sensing." In: *Reviews of Modern Physics* 89 (3 July 2017), p. 035002 (Cited on page 12).

[40] Howard M. Wiseman and Gerard J. Milburn. *Quantum Measurement and Control*. Cambridge University Press, 2009 (Cited on pages 12, 151, 180).

[41] Alberto Barchielli and Matteo Gregoratti. *Quantum Trajectories and Measurements in Continuous Time*. Vol. 782. Springer-Verlag Berlin Heidelberg, 2009 (Cited on page 12).

[42] He-Liang Huang et al. "Superconducting quantum computing: a review." In: *Science China Information Sciences* 63.8 (2020), p. 180501 (Cited on page 12).

[43] David Pozar. *Microwave Engineering*. Wiley, 2011 (Cited on pages 13, 48).

[44] Hanhee Paik et al. "Observation of high coherence in Josephson junction qubits measured in a three-dimensional circuit QED architecture." In: *Physical Review Letters* 107 (24 Dec. 2011), p. 240501 (Cited on page 13).

[45] Matthew Reagor et al. "Reaching 10 ms single photon lifetimes for superconducting aluminum cavities." In: *Applied Physics Letters* 102 (19 May 2013), p. 192604 (Cited on page 13).

[46] Matthew James Reagor. *Superconducting Cavities for Circuit Quantum Electrodynamics*. 2015 (Cited on pages 13, 27, 175, 176).

[47] M H Devoret. *Quantum fluctuations in electrical circuits*. 1997 (Cited on pages 13, 17).

[48] Uri Vool and Michel Devoret. "Introduction to quantum electromagnetic circuits." In: vol. 45. John Wiley and Sons Ltd, July 2017, pp. 897–934 (Cited on pages 13, 14, 25, 133).

[49] S. E. Rasmussen et al. *The superconducting circuit companion – an introduction with worked examples*. 2021. arXiv: `2103.01225 [quant-ph]` (Cited on page 15).

[50] N. E. Frattini et al. "3-wave mixing Josephson dipole element." In: *Applied Physics Letters* 110 (22 May 2017), p. 222603 (Cited on page 15).

[51] Fei Yan et al. *Engineering Framework for Optimizing Superconducting Qubit Designs*. 2020 (Cited on page 15).

[52] Raphaël Lescanne et al. "Exponential suppression of bit-flips in a qubit encoded in an oscillator." In: *Nature Physics* 16 (5 May 2020), pp. 509–513 (Cited on page 15).

[53] Frank Arute et al. "Quantum supremacy using a programmable superconducting processor." In: *Nature* 574 (7779 Oct. 2019), pp. 505–510 (Cited on pages 15, 119).

[54] Petar Jurcevic et al. "Demonstration of quantum volume 64 on a superconducting quantum computing system." In: *Quantum Sci. Technol* 6 (2021), p. 25020 (Cited on page 15).

[55] P. W. Anderson and J. M. Rowell. "Probable observation of the Josephson superconducting tunneling effect." In: *Physical Review Letters* 10 (6 Mar. 1963), pp. 230–232 (Cited on page 16).

[56] V. Bouchiat et al. "Quantum coherence with a single cooper pair." In: *Physica Scripta T* 76 (T76 Jan. 1998), pp. 165–170 (Cited on page 17).

[57] Daoquan Zhu et al. "Quantum Computing with Superconducting Circuits in the Picosecond Regime." In: *Phys. Rev. Applied* 16 (1 2021), p. 014024 (Cited on page 18).

[58] Claude Cohen-Tannoudji, Bernard Biu, and Franl Laloë. *Quantum Mechanics*. Vol. I & II. Wiley, 1991 (Cited on page 18).

[59] Pascal Degiovanni et al. *Physique quantique, Information et Calcul: des concepts aux applications*. Jan. 2020 (Cited on pages 19, 20).

[60] Philip Taranto et al. *Landauer vs. Nernst: What is the True Cost of Cooling a Quantum System?* 2021. arXiv: `2106.05151 [quant-ph]` (Cited on page 19).

[61] Claude Cohen-Tannoudji, Jacques Dupont-Roc, and Gilbert Grynberg. *Atom-Photon Interactions: Basic Processes and Applications*. 1998 (Cited on pages 22, 24, 69, 131, 135).

[62] Alexandre Blais et al. *Circuit Quantum Electrodynamics*. 2020 (Cited on pages 25, 26, 30, 34, 36, 38, 67, 70, 133).

[63] M. Virginia P. Altoé et al. *Localization and reduction of superconducting quantum coherent circuit losses*. 2020. arXiv: `2012.07604 [quant-ph]` (Cited on page 27).

[64] J. Verjauw et al. "Investigation of Microwave Loss Induced by Oxide Regrowth in High-Q Niobium Resonators." In: *Phys. Rev. Applied* 16 (1 2021), p. 014018 (Cited on page 27).

[65] S Ohya et al. "Room temperature deposition of sputtered TiN films for superconducting coplanar waveguide resonators." In: *Superconductor Science and Technology* 27.1 (2013), p. 015009 (Cited on page 27).

[66] Srivatsan Chakram et al. *Seamless high-Q microwave cavities for multimode circuit QED.* 2020 (Cited on pages 27, 175).

[67] B. R. Mollow. "Power Spectrum of Light Scattered by Two-Level Systems." In: *Physical Review* 188 (5 Dec. 1969), p. 1969 (Cited on pages 35, 131, 133–135).

[68] O. Astafiev et al. "Resonance fluorescence of a single artificial atom." In: *Science* 327 (5967 Feb. 2010), pp. 840–843 (Cited on pages 35, 97, 100, 131, 135).

[69] Vladimir E. Manucharyan et al. "Fluxonium: Single cooper-pair circuit free of charge offsets." In: *Science* 326 (5949 Oct. 2009), pp. 113–116 (Cited on page 35).

[70] Alexandre Blais et al. "Cavity quantum electrodynamics for superconducting electrical circuits: An architecture for quantum computation." In: *Physical Review A - Atomic, Molecular, and Optical Physics* 69 (6 June 2004), p. 062320 (Cited on pages 35, 42, 54, 66).

[71] Christian Kraglund Andersen and Alexandre Blais. "Ultrastrong coupling dynamics with a transmon qubit." In: *New Journal of Physics* 19 (2 Feb. 2017), p. 023022 (Cited on page 37).

[72] A. Stockklauser et al. "Strong coupling cavity QED with gate-defined double quantum dots enabled by a high impedance resonator." In: *Physical Review X* 7 (1 Mar. 2017), p. 11030 (Cited on page 37).

[73] C. C. Bultink et al. "General method for extracting the quantum efficiency of dispersive qubit readout in circuit QED." In: *Applied Physics Letters* 112 (9 Mar. 2018), p. 092601 (Cited on pages 41, 72).

[74] K. W. Murch et al. "Observing single quantum trajectories of a superconducting quantum bit." In: *Nature* 502 (7470 Oct. 2013), pp. 211–214 (Cited on pages 41, 64, 67, 68, 80, 151).

[75] Jay Gambetta et al. "Quantum trajectory approach to circuit QED: Quantum jumps and the Zeno effect." In: *Phys. Rev. A* 77 (1 2008), p. 012112 (Cited on page 41).

[76] Raphaël Lescanne et al. "Escape of a Driven Quantum Josephson Circuit into Unconfined States." In: *Physical Review Applied* 11 (1 Jan. 2019), p. 014030 (Cited on pages 42, 85, 88, 94).

[77] T. Walter et al. "Rapid High-Fidelity Single-Shot Dispersive Readout of Superconducting Qubits." In: *Physical Review Applied* 7 (5 May 2017), p. 054020 (Cited on page 42).

[78] Simon E. Nigg et al. "Black-box superconducting circuit quantization." In: *Physical Review Letters* 108 (24 June 2012), p. 240502 (Cited on pages 44, 46).

[79] Firat Solgun, David W. Abraham, and David P. DiVincenzo. "Blackbox quantization of superconducting circuits using exact impedance synthesis." In: *Phys. Rev. B* 90 (13 2014), p. 134504 (Cited on page 45).

[80] Moein Malekakhlagh and Hakan E. Türeci. "Origin and implications of an A^2-like contribution in the quantization of circuit-QED systems." In: *Phys. Rev. A* 93 (1 2016), p. 012120 (Cited on page 45).

[81] Zlatko K. Minev et al. "Energy-participation quantization of Josephson circuits." 15 Figures, 39 pages, 4 tables; See also http://github.com/zlatko-minev/pyEPR; Send feedback to zlatko.minev [@] aya.yale.edu. Dec. 2020 (Cited on pages 47, 48).

[82] Z. Leghtas et al. "Confining the state of light to a quantum manifold by engineered two-photon loss." In: *Science* 347 (6224 Feb. 2015), pp. 853–857 (Cited on page 48).

[83] Z. K. Minev et al. "Planar Multilayer Circuit Quantum Electrodynamics." In: *Physical Review Applied* 5 (4 Apr. 2016), p. 044021 (Cited on page 48).

[84] S. Touzard et al. "Coherent Oscillations inside a Quantum Manifold Stabilized by Dissipation." In: *Physical Review X* 8 (2 Apr. 2018), p. 21005 (Cited on page 48).

[85] Nathanaël Cottet et al. "Electron shelving of a superconducting artificial atom." In: (Aug. 2020) (Cited on pages 48, 97).

[86] R.N. Simons. *Coplanar Waveguide Circuits, Components, and Systems*. Wiley Series in Microwave and Optical Engineering. Wiley, 2004 (Cited on page 51).

[87] E. M. Purcell. *Spontaneous Emission Probabilities at Radio Frequencies*. Springer, Boston, MA, 1995, pp. 839–839 (Cited on page 53).

[88] Eyob A. Sete, Jay M. Gambetta, and Alexander N. Korotkov. "Purcell effect with microwave drive: Suppression of qubit relaxation rate." In: *Physical Review B - Condensed Matter and Materials Physics* 89 (10 Mar. 2014), p. 104516 (Cited on pages 53, 55).

[89] A. Bienfait et al. "Controlling spin relaxation with a cavity." In: *Nature* 531 (7592 Mar. 2016), pp. 74–77 (Cited on page 54).

[90] A. A. Houck et al. "Controlling the spontaneous emission of a superconducting transmon qubit." In: *Physical Review Letters* 101 (8 Aug. 2008), p. 080502 (Cited on pages 55, 56).

[91] Daniel Esteve, Michel H. Devoret, and John M. Martinis. "Effect of an arbitrary dissipative circuit on the quantum energy levels and tunneling of a Josephson junction." In: *Physical Review B* 34 (1 July 1986), pp. 158–163 (Cited on page 55).

[92] Moein Malekakhlagh, Alexandru Petrescu, and Hakan E. Türeci. "Cutoff-Free Circuit Quantum Electrodynamics." In: *Physical Review Letters* 119 (7 Aug. 2017), p. 073601 (Cited on page 56).

[93] Jerome Bourassa. "Non-linearite et couplages lumiere-matiere en electrodynamique quantique en circuit." PhD thesis. Universite de Sherbrooke (Canada), Jan. 2012 (Cited on page 56).

[94] Maxime Boissonneault, J. M. Gambetta, and Alexandre Blais. "Dispersive regime of circuit QED: Photon-dependent qubit dephasing and relaxation rates." In: *Physical Review A - Atomic, Molecular, and Optical Physics* 79 (1 Jan. 2009), p. 013819 (Cited on pages 57, 59, 151).

[95] M. D. Reed et al. "Fast reset and suppressing spontaneous emission of a superconducting qubit." In: *Applied Physics Letters* 96 (20 May 2010), p. 203110 (Cited on page 57).

[96] Evan Jeffrey et al. "Fast accurate state measurement with superconducting qubits." In: *Physical Review Letters* 112 (19 May 2014), p. 190504 (Cited on page 57).

[97] Walther Gerlach and Otto Stern. "Der experimentelle Nachweis der Richtungsquantelung im Magnetfeld." In: *Zeitschrift für Physik* 9.1 (1922), pp. 349–352 (Cited on page 61).

[98] François Mallet et al. "Single-shot qubit readout in circuit quantum electrodynamics." In: *Nature Physics 2009 5:11* 5 (11 Sept. 2009), pp. 791–795 (Cited on pages 63, 73).

[99] N. Roch et al. "Widely Tunable, Nondegenerate Three-Wave Mixing Microwave Device Operating near the Quantum Limit." In: *Physical Review Letters* 108 (14 Apr. 2012), p. 147701 (Cited on pages 66, 72).

[100] B. Yurke et al. "Observation of parametric amplification and deamplification in a Josephson parametric amplifier." In: *Physical Review A* 39 (5 Mar. 1989), p. 2519 (Cited on pages 66, 72).

[101] Alexandru Petrescu, Moein Malekakhlagh, and Hakan E. Türeci. "Lifetime renormalization of driven weakly anharmonic superconducting qubits. II. The readout problem." In: *Physical Review B* 101 (13 Apr. 2020), p. 134510 (Cited on page 66).

[102] R. Vijay, D. H. Slichter, and I. Siddiqi. "Observation of Quantum Jumps in a Superconducting Artificial Atom." In: *Physical Review Letters* 106 (11 Mar. 2011), p. 110502 (Cited on pages 67, 68).

[103] M. Hatridge et al. "Quantum Back-Action of an Individual Variable-Strength Measurement." In: *Science* 339 (6116 Jan. 2013), pp. 178–181 (Cited on pages 68, 103).

[104] N. Bergeal et al. "Analog information processing at the quantum limit with a Josephson ring modulator." In: *Nature Physics* 6.4 (2010), pp. 296–302 (Cited on page 72).

[105] I. Siddiqi et al. "RF-Driven Josephson Bifurcation Amplifier for Quantum Measurement." In: *Physical Review Letters* 93 (20 Nov. 2004), p. 207002 (Cited on page 73).

[106] V. E. Manucharyan et al. "Microwave bifurcation of a Josephson junction: Embedding-circuit requirements." In: *Physical Review B* 76 (1 July 2007), p. 014524 (Cited on page 73).

[107] M. A. Castellanos-Beltran and K. W. Lehnert. "Widely tunable parametric amplifier based on a superconducting quantum interference device array resonator." In: *Applied Physics Letters* 91 (8 Aug. 2007), p. 083509 (Cited on page 73).

[108] Byeong Ho Eom et al. "A wideband, low-noise superconducting amplifier with high dynamic range." In: *Nature Physics 2012 8:8* 8 (8 July 2012), pp. 623–627 (Cited on pages 73, 74, 181, 182).

[109] O. Yaakobi et al. "Parametric amplification in Josephson junction embedded transmission lines." In: *Physical Review B* 87 (14 Apr. 2013), p. 144301 (Cited on pages 73, 74).

[110] A. B. Zorin. "Josephson Traveling-Wave Parametric Amplifier with Three-Wave Mixing." In: *Physical Review Applied* 6 (3 Sept. 2016), p. 034006 (Cited on page 74).

[111] V. A. Vysloukh. "Nonlinear fiber optics." In: *Phys. Usp.* 33.5 (1990), pp. 400–400 (Cited on page 74).

[112] Kevin O'Brien et al. "Resonant Phase Matching of Josephson Junction Traveling Wave Parametric Amplifiers." In: *Physical Review Letters* 113 (15 Oct. 2014), p. 157001 (Cited on page 74).

[113] C. Bockstiegel et al. "Development of a Broadband NbTiN Traveling Wave Parametric Amplifier for MKID Readout." In: *Journal of Low Temperature Physics 2014 176:3* 176 (3 Jan. 2014), pp. 476–482 (Cited on page 74).

[114] L. Ranzani et al. "Kinetic inductance traveling-wave amplifiers for multiplexed qubit readout." In: *Applied Physics Letters* 113 (24 Dec. 2018), p. 242602 (Cited on page 74).

[115] M. R. Vissers et al. "Low-noise kinetic inductance traveling-wave amplifier using three-wave mixing." In: *Applied Physics Letters* 108 (1 Jan. 2016), p. 012601 (Cited on page 74).

[116] Saptarshi Chaudhuri et al. "Broadband parametric amplifiers based on nonlinear kinetic inductance artificial transmission lines." In: *Applied Physics Letters* 110 (15 Apr. 2017) (Cited on page 74).

[117] A. A. Adamyan et al. "Superconducting microwave parametric amplifier based on a quasi-fractal slow propagation line." In: *Journal of Applied Physics* 119 (8 Feb. 2016), p. 083901 (Cited on page 74).

[118] Samuel Goldstein et al. "Four wave-mixing in a microstrip kinetic inductance travelling wave parametric amplifier." In: *Applied Physics Letters* 116 (15 Apr. 2020), p. 152602 (Cited on page 74).

[119] M. Malnou et al. "Three-Wave Mixing Kinetic Inductance Traveling-Wave Amplifier with Near-Quantum-Limited Noise Performance." In: *PRX Quantum* 2 (1 Jan. 2021), p. 010302 (Cited on page 74).

[120] Luca Planat et al. "Photonic-Crystal Josephson Traveling-Wave Parametric Amplifier." In: *Physical Review X* 10 (2 Apr. 2020), p. 021021 (Cited on page 74).

[121] T. C. White et al. "Traveling wave parametric amplifier with Josephson junctions using minimal resonator phase matching." In: *Applied Physics Letters* 106 (24 June 2015), p. 242601 (Cited on page 74).

[122] Arpit Ranadive et al. "A reversed Kerr traveling wave parametric amplifier." In: () (Cited on page 74).

[123] Martina Esposito et al. "Perspective on traveling wave microwave parametric amplifiers." In: (July 2021) (Cited on page 74).

[124] Hoi-Kwong Lo, Marcos Curty, and Bing Qi. "Measurement-Device-Independent Quantum Key Distribution." In: *Physical Review Letters* 108 (13 Mar. 2012), p. 130503 (Cited on page 85).

[125] Hua-Lei Yin et al. "Measurement-Device-Independent Quantum Key Distribution Over a 404 km Optical Fiber." In: *Physical Review Letters* 117 (19 Nov. 2016), p. 190501 (Cited on page 85).

[126] Sheng-Kai Liao et al. "Satellite-to-ground quantum key distribution." In: *Nature 2017 549:7670* 549 (7670 Aug. 2017), pp. 43–47 (Cited on page 85).

[127] Marco Cattaneo, Matteo G. A. Paris, and Stefano Olivares. "Hybrid quantum key distribution using coherent states and photon-number-resolving detectors." In: *Physical Review A* 98 (1 July 2018), p. 012333 (Cited on page 85).

[128] E. Knill, R. Laflamme, and G. J. Milburn. "A scheme for efficient quantum computation with linear optics." In: *Nature 2001 409:6816* 409 (6816 Jan. 2001), pp. 46–52 (Cited on page 85).

[129] Pieter Kok et al. "Linear optical quantum computing with photonic qubits." In: *Reviews of Modern Physics* 79 (1 Jan. 2007), p. 135 (Cited on page 85).

[130] L.-M. Duan et al. "Long-distance quantum communication with atomic ensembles and linear optics." In: *Nature 2001 414:6862* 414 (6862 Nov. 2001), pp. 413–418 (Cited on page 85).

[131] R. Ursin et al. "Entanglement-based quantum communication over 144 km." In: *Nature Physics 2007 3:7* 3 (7 June 2007), pp. 481–486 (Cited on page 85).

[132] H. J. Kimble. "The quantum internet." In: *Nature 2008 453:7198* 453 (7198 June 2008), pp. 1023–1030 (Cited on page 85).

[133] T. E. Northup and R. Blatt. "Quantum information transfer using photons." In: *Nature Photonics 2014 8:5* 8 (5 Apr. 2014), pp. 356–363 (Cited on page 85).

[134] Jian-Yong Hu et al. "Experimental quantum secure direct communication with single photons." In: *Light: Science & Applications 2016 5:9* 5 (9 Apr. 2016), e16144–e16144 (Cited on page 85).

[135] Wei Zhang et al. "Quantum Secure Direct Communication with Quantum Memory." In: *Physical Review Letters* 118 (22 May 2017), p. 220501 (Cited on page 85).

[136] Jian-Peng Dou et al. "A broadband DLCZ quantum memory in room-temperature atoms." In: *Communications Physics 2018 1:1* 1 (1 Sept. 2018), pp. 1–7 (Cited on page 85).

[137] Christoph Simon et al. "Quantum Repeaters with Photon Pair Sources and Multimode Memories." In: *Physical Review Letters* 98 (19 May 2007), p. 190503 (Cited on page 85).

[138] Max Tillmann et al. "Experimental boson sampling." In: *Nature Photonics 2013 7:7* 7 (7 May 2013), pp. 540–544 (Cited on page 85).

[139] Chris Sparrow et al. "Simulating the vibrational quantum dynamics of molecules using photonics." In: *Nature 2018 557:7707* 557 (7707 May 2018), pp. 660–667 (Cited on page 85).

[140] Justin B. Spring et al. "Boson Sampling on a Photonic Chip." In: *Science* 339 (6121 Feb. 2013), pp. 798–801 (Cited on page 85).

[141] Marco Bentivegna et al. "Experimental scattershot boson sampling." In: *Science Advances* 1 (3 Apr. 2015), e1400255 (Cited on page 85).

[142] Joonsuk Huh et al. "Boson sampling for molecular vibronic spectra." In: *Nature Photonics 2015 9:9* 9 (9 Aug. 2015), pp. 615–620 (Cited on page 85).

[143] Craig S. Hamilton et al. "Gaussian Boson Sampling." In: *Physical Review Letters* 119 (17 Oct. 2017), p. 170501 (Cited on page 85).

[144] William R Clements et al. "Approximating vibronic spectroscopy with imperfect quantum optics." In: *Journal of Physics B: Atomic, Molecular and Optical Physics* 51 (24 Nov. 2018), p. 245503 (Cited on page 85).

[145] Regina Kruse et al. "Detailed study of Gaussian boson sampling." In: *Physical Review A* 100 (3 Sept. 2019), p. 032326 (Cited on page 85).

[146] Robert H. Hadfield. "Single-photon detectors for optical quantum information applications." In: *Nature Photonics 2009 3:12* 3 (12 Dec. 2009), pp. 696–705 (Cited on page 85).

[147] Y.-F. Chen et al. "Microwave Photon Counter Based on Josephson Junctions." In: *Physical Review Letters* 107 (21 Nov. 2011), p. 217401 (Cited on pages 85, 94).

[148] Kunihiro Inomata et al. "Single microwave-photon detector using an artificial Lambda-type three-level system." In: *Nature Communications 2016 7:1* 7 (1 July 2016), pp. 1–7 (Cited on pages 85, 94).

[149] A. Narla et al. "Robust Concurrent Remote Entanglement Between Two Superconducting Qubits." In: *Physical Review X* 6 (3 Sept. 2016), p. 031036 (Cited on pages 85, 94).

[150] Jean-Claude Besse et al. "Single-Shot Quantum Nondemolition Detection of Individual Itinerant Microwave Photons." In: *Physical Review X* 8 (2 Apr. 2018), p. 021003 (Cited on pages 85, 93, 94).

[151] S. Kono et al. "Quantum non-demolition detection of an itinerant microwave photon." In: *Nature Physics 2018 14:6* 14 (6 Mar. 2018), pp. 546–549 (Cited on pages 85, 94).

[152] Emanuele Albertinale et al. "Detecting spins with a microwave photon counter." In: (2021) (Cited on page 85).

[153] Arne L. Grimsmo et al. "Quantum Metamaterial for Broadband Detection of Single Microwave Photons." In: *Physical Review Applied* 15 (3 Mar. 2021), p. 034074 (Cited on page 85).

[154] Victor V Albert et al. "Pair-cat codes: autonomous error-correction with low-order nonlinearity." In: *Quantum Science and Technology* 4.3 (2019), p. 035007 (Cited on page 86).

[155] Antoine Essig et al. "Multiplexed Photon Number Measurement." In: *Phys. Rev. X* 11 (3 2021), p. 031045 (Cited on pages 86, 97, 119, 151).

[156] Christopher S. Wang et al. "Efficient Multiphoton Sampling of Molecular Vibronic Spectra on a Superconducting Bosonic Processor." In: *Physical Review X* 10 (2 June 2020), p. 021060 (Cited on page 92).

[157] Suman Kundu et al. "Multiplexed readout of four qubits in 3D circuit QED architecture using a broadband Josephson parametric amplifier." In: *Applied Physics Letters* 114 (17 May 2019), p. 172601 (Cited on pages 93, 119).

[158] V. Schmitt et al. "Multiplexed readout of transmon qubits with Josephson bifurcation amplifiers." In: *Physical Review A* 90 (6 Dec. 2014), p. 062333 (Cited on pages 93, 119).

[159] Johannes Heinsoo et al. "Rapid High-fidelity Multiplexed Readout of Superconducting Qubits." In: *Physical Review Applied* 10.3 (2018), pp. 1–13. arXiv: `1801.07904` (Cited on pages 93, 119).

[160] Yong Lu et al. "Characterizing decoherence rates of a superconducting qubit by direct microwave scattering." In: *npj Quantum Information 2021 7:1* 7 (1 Feb. 2021), pp. 1–9 (Cited on page 97).

[161] A. A. Abdumalikov et al. "Dynamics of Coherent and Incoherent Emission from an Artificial Atom in a 1D Space." In: *Physical Review Letters* 107 (4 July 2011), p. 043604 (Cited on pages 97, 100).

[162] Quentin Ficheux. "Quantum Trajectories with Incompatible Decoherence Channels." Theses. École normale supérieure - ENS PARIS, Dec. 2018 (Cited on pages 97, 151).

[163] Q. Ficheux et al. "Dynamics of a qubit while simultaneously monitoring its relaxation and dephasing." In: *Nature Communications* 9 (1 Dec. 2018), pp. 1–6 (Cited on pages 97, 180).

[164] P. Campagne-Ibarcq et al. "Observing Interferences between Past and Future Quantum States in Resonance Fluorescence." In: *Physical Review Letters* 112 (18 May 2014), p. 180402 (Cited on pages 97, 100).

[165] P. Campagne-Ibarcq et al. "Using Spontaneous Emission of a Qubit as a Resource for Feedback Control." In: *Physical Review Letters* 117 (6 Aug. 2016), p. 060502 (Cited on page 97).

[166] P. Campagne-Ibarcq et al. "Observing Quantum State Diffusion by Heterodyne Detection of Fluorescence." In: *Physical Review X* 6 (1 Jan. 2016), p. 011002 (Cited on page 97).

[167] Naghiloo M et al. "Mapping quantum state dynamics in spontaneous emission." In: *Nature communications* 7 (May 2016) (Cited on page 97).

[168] M. Naghiloo et al. "Quantum caustics in resonance-fluorescence trajectories." In: *Physical Review A* 96 (5 Nov. 2017), p. 053807 (Cited on page 97).

[169] Nathanaël Pierre Cottet. "Energy and information in fluorescence with superconducting circuits." Theses. Université Paris sciences et lettres, Nov. 2018 (Cited on pages 97, 133).

[170] Jeremy Stevens et al. *Energetics of a Single Qubit Gate*. 2021. arXiv: `2109.09648 [quant-ph]` (Cited on page 97).

[171] D. M. Toyli et al. "Resonance Fluorescence from an Artificial Atom in Squeezed Vacuum." In: *Physical Review X* 6 (3 July 2016), p. 031004 (Cited on pages 97, 131, 135).

[172] M. Baur et al. "Measurement of Autler-Townes and Mollow Transitions in a Strongly Driven Superconducting Qubit." In: *Physical Review Letters* 102 (24 June 2009), p. 243602 (Cited on page 97).

[173] Io-Chun Hoi et al. "Giant Cross–Kerr Effect for Propagating Microwaves Induced by an Artificial Atom." In: *Physical Review Letters* 111 (5 Aug. 2013), p. 053601 (Cited on page 97).

[174] I.-C. Hoi et al. "Probing the quantum vacuum with an artificial atom in front of a mirror." In: *Nature Physics 2015 11:12* 11 (12 Sept. 2015), pp. 1045–1049 (Cited on page 97).

[175] P. Y. Wen et al. "Large Collective Lamb Shift of Two Distant Superconducting Artificial Atoms." In: *Physical Review Letters* 123 (23 Dec. 2019), p. 233602 (Cited on page 97).

[176] Arjan F. van Loo et al. "Photon-Mediated Interactions Between Distant Artificial Atoms." In: *Science* 342 (6165 Dec. 2013), pp. 1494–1496 (Cited on page 97).

[177] A. A. Houck et al. "Generating single microwave photons in a circuit." In: *Nature 2007 449:7160* 449 (7160 Sept. 2007), pp. 328–331 (Cited on pages 97, 100).

[178] Alain Sarlette et al. "Quantum adiabatic elimination at arbitrary order for photon number measurement." In: *IFAC-PapersOnLine* 53 (2 Jan. 2020), pp. 250–256 (Cited on pages 97, 113, 114).

[179] Claude Cohen-Tannoudji, Jacques Dupont-Roc, and Gilbert Grynberg. *Atom-Photon Interactions: Basic Processes and Applications*. 2001 (Cited on page 100).

[180] P Bertet et al. "Direct Measurement of the Wigner Function of a One-Photon Fock State in a Cavity." In: *Physical Review Letters* 89.20 (2002), p. 200402 (Cited on pages 104, 196).

[181] Brian Vlastakis et al. "Deterministically Encoding Quantum Information Using 100-Photon Schrödinger Cat States." In: *Science* 342 (6158 Nov. 2013), pp. 607–610 (Cited on pages 104, 196).

[182] Jack Carr. *Applications of Centre Manifold Theory.* 1982 (Cited on page 114).

[183] R. Azouit et al. "Towards generic adiabatic elimination for bipartite open quantum systems." In: *Quantum Science and Technology* 2 (2017), p. 044011 (Cited on page 114).

[184] Luc Bouten and Andrew Silberfarb. "Adiabatic Elimination in Quantum Stochastic Models." In: *Communications in Mathematical Physics 2008 283:2* 283 (2 May 2008), pp. 491–505 (Cited on page 114).

[185] Paolo Zanardi, Jeffrey Marshall, and Lorenzo Campos Venuti. "Dissipative universal Lindbladian simulation." In: *Phys. Rev. A* 93 (2 2016), p. 022312 (Cited on page 114).

[186] Anirban DasGupta, S.N. Lahiri, and Jordan Stoyanov. "Sharp fixed n bounds and asymptotic expansions for the mean and the median of a Gaussian sample maximum, and applications to the Donoho–Jin model." In: *Statistical Methodology* 20 (2014). Re-sampling and Contemporary Inference: A tribute to Kesar Singh, pp. 40–62 (Cited on page 125).

[187] T. Peronnin et al. "Sequential Dispersive Measurement of a Superconducting Qubit." In: *Phys. Rev. Lett.* 124 (18 2020), p. 180502 (Cited on pages 130, 163).

[188] "Front Matter." In: *A Wavelet Tour of Signal Processing (Third Edition).* Ed. by Mallat Stéphane. Third Edition. Boston: Academic Press, 2009 (Cited on pages 130, 159).

[189] Jeffrey M. Gertler et al. "Protecting a Bosonic Qubit with Autonomous Quantum Error Correction." In: *Nature* 590 (7845 Apr. 2020), pp. 243–248 (Cited on pages 131, 180).

[190] C. Lang et al. "Observation of Resonant Photon Blockade at Microwave Frequencies Using Correlation Function Measurements." In: *Physical Review Letters* 106 (24 June 2011), p. 243601 (Cited on pages 131, 135).

[191] Simone Gasparinetti et al. "Two-photon resonance fluorescence of a ladder-type atomic system." In: *Physical Review A* 100 (3 Sept. 2019), p. 033802 (Cited on pages 131, 135).

[192] Marcus P Da Silva et al. "Schemes for the observation of photon correlation functions in circuit QED with linear detectors." In: *PHYSICAL REVIEW A* 82 (2010), p. 43804 (Cited on page 136).

[193] Jay Gambetta et al. "Qubit-photon interactions in a cavity: Measurement-induced dephasing and number splitting." In: *Phys. Rev. A* 74 (4 2006), p. 042318 (Cited on page 151).

[194] Philippe Campagne-Ibarcq. "Quantum backaction and feedback in superconducting circuits." Thèse de doctorat dirigée par Huard, Benjamin et Devoret, Michel Physique Paris, Ecole normale supérieure 2015. PhD thesis. 2015 (Cited on page 151).

[195] P. Campagne-Ibarcq et al. "Quantum error correction of a qubit encoded in grid states of an oscillator." In: *Nature* 584.7821 (2020), pp. 368–372 (Cited on page 152).

[196] Thomas M. Cover and Joy A. Thomas. *Elements of Information Theory (Wiley Series in Telecommunications and Signal Processing)*. USA: Wiley-Interscience, 2006 (Cited on page 160).

[197] Michael A. Nielsen and Isaac L. Chuang. *Quantum Computation and Quantum Information: 10th Anniversary Edition*. Cambridge University Press, 2010 (Cited on page 160).

[198] Harold Ollivier and Wojciech H. Zurek. "Quantum Discord: A Measure of the Quantumness of Correlations." In: *Physical Review Letters* 88 (1 Dec. 2001), p. 017901 (Cited on pages 160, 161).

[199] Wojciech Hubert Zurek. "Quantum discord and Maxwell's demons." In: *Physical Review A* 67 (1 Jan. 2003), p. 012320 (Cited on pages 160, 161).

[200] A.S. Holevo. "Quantum channel capacities." In: *Quantum Electronics* 50 (5 May 2020), p. 440 (Cited on page 161).

[201] A. A. Clerk, S. M. Girvin, and A. D. Stone. "Quantum-limited measurement and information in mesoscopic detectors." In: *Physical Review B* 67 (16 Apr. 2003), p. 165324 (Cited on pages 161, 162).

[202] A. Megrant et al. "Planar superconducting resonators with internal quality factors above one million." In: *Applied Physics Letters* 100 (11 Mar. 2012), p. 113510 (Cited on page 175).

[203] *Filters Using Planar Transmission Lines*. John Wiley and Sons, Ltd, 2016. Chap. 19, pp. 541–575. eprint: `https://onlinelibrary.wiley.com/doi/pdf/10.1002/9781118936160.ch19` (Cited on page 176).

[204] U. Fano. "Effects of Configuration Interaction on Intensities and Phase Shifts." In: *Phys. Rev.* 124 (6 1961), pp. 1866–1878 (Cited on pages 176, 178).

[205] G. Calusine et al. "Analysis and mitigation of interface losses in trenched superconducting coplanar waveguide resonators." In: *Applied Physics Letters* 112 (6 Feb. 2018), p. 062601 (Cited on page 178).

[206] David Niepce et al. *Stability of superconducting resonators: motional narrowing and the role of Landau-Zener driving of two-level defects*. 2020. arXiv: `2008.07038 [cond-mat.supr-con]` (Cited on page 178).

[207] Riccardo Porotti et al. *Deep Reinforcement Learning for Quantum State Preparation with Weak Nonlinear Measurements*. 2021. arXiv: `2107.08816 [quant-ph]` (Cited on page 180).

[208] L. Bretheau et al. "Quantum dynamics of an electromagnetic mode that cannot contain N photons." In: *Science* 348 (6236 May 2015), pp. 776–779 (Cited on pages 180, 198, 199).

[209] Weizhou Cai et al. "Bosonic quantum error correction codes in superconducting quantum circuits." In: *Fundamental Research* 1.1 (2021), pp. 50–67 (Cited on page 180).

[210] Shay Hacohen-Gourgy et al. "Quantum dynamics of simultaneously measured non-commuting observables." In: *Nature* 538.7626 (2016), pp. 491–494 (Cited on page 180).

[211] M Stammeier, S Garcia, and A Wallraff. "Applying electric and magnetic field bias in a 3D superconducting waveguide cavity with high quality factor." In: *Quantum Science and Technology* 3 (4 Aug. 2018), p. 045007 (Cited on page 181).

[212] Yarema Reshitnyk, Markus Jerger, and Arkady Fedorov. "3D microwave cavity with magnetic flux control and enhanced quality factor." In: *EPJ Quantum Technology 2016 3:1* 3 (1 Oct. 2016), pp. 1–6 (Cited on page 181).

[213] O. Gargiulo et al. "Fast flux control of 3D transmon qubits using a magnetic hose." In: *Applied Physics Letters* 118 (1 Jan. 2021), p. 012601 (Cited on page 181).

[214] G. J. Dolan. "Offset masks for lift-off photoprocessing." In: *Applied Physics Letters* 31 (5 Aug. 2008), p. 337 (Cited on page 185).

[215] L J Zeng et al. "Direct observation of the thickness distribution of ultra thin AlOx barriers in Al/AlOx/Al Josephson junctions." In: *Journal of Physics D: Applied Physics* 48 (39 Sept. 2015), p. 395308 (Cited on page 190).

[216] M. Beck, D. T. Smithey, and M. G. Raymer. "Experimental determination of quantum-phase distributions using optical homodyne tomography." In: *Phys. Rev. A* 48 (2 1993), R890–R893 (Cited on page 201).

[217] D T Smithey et al. "Complete experimental characterization of the quantum state of a light mode via the Wigner function and the density matrix: application to quantum phase distributions of vacuum and squeezed-vacuum states." In: *Physica Scripta* T48 (1993), pp. 35–44 (Cited on page 201).

[218] D. T. Smithey et al. "Measurement of the Wigner distribution and the density matrix of a light mode using optical homodyne tomography: Application to squeezed states and the vacuum." In: *Phys. Rev. Lett.* 70 (9 1993), pp. 1244–1247 (Cited on page 201).

[219] A. I. Lvovsky and M. G. Raymer. "Continuous-variable optical quantum-state tomography." In: *Rev. Mod. Phys.* 81 (1 2009), pp. 299–332 (Cited on page 201).

[220] A I Lvovsky. "Iterative maximum-likelihood reconstruction in quantum homodyne tomography." In: *Journal of Optics B: Quantum and Semiclassical Optics* 6 (6 May 2004), S556 (Cited on page 201).

[221] Jaromír Fiurášek and Zdeněk Hradil. "Maximum-likelihood estimation of quantum processes." In: *Physical Review A* 63 (2 Jan. 2001), p. 020101 (Cited on page 201).

[222] Zdeněk Hradil et al. "3 Maximum-Likelihood Methodsin Quantum Mechanics." In: *Quantum State Estimation*. Ed. by Matteo Paris and Jaroslav Řeháček. Berlin, Heidelberg: Springer Berlin Heidelberg, 2004, pp. 59–112 (Cited on page 201).

[223] J.R. Johansson, P.D. Nation, and Franco Nori. "QuTiP 2: A Python framework for the dynamics of open quantum systems." In: *Computer Physics Communications* 184.4 (2013), pp. 1234–1240 (Cited on page 203).